INFORMATION TO USERS

This manuscript has been reproduced from the microfilm master. UMI films the text directly from the original or copy submitted. Thus, some thesis and dissertation copies are in typewriter face, while others may be from any type of computer printer.

The quality of this reproduction is dependent upon the quality of the copy submitted. Broken or indistinct print, colored or poor quality illustrations and photographs, print bleedthrough, substandard margins, and improper alignment can adversely affect reproduction.

In the unlikely event that the author did not send UMI a complete manuscript and there are missing pages, these will be noted. Also, if unauthorized copyright material had to be removed, a note will indicate the deletion.

Oversize materials (e.g., maps, drawings, charts) are reproduced by sectioning the original, beginning at the upper left-hand corner and continuing from left to right in equal sections with small overlaps.

Photographs included in the original manuscript have been reproduced xerographically in this copy. Higher quality 6" x 9" black and white photographic prints are available for any photographs or illustrations appearing in this copy for an additional charge. Contact UMI directly to order.

ProQuest Information and Learning
300 North Zeeb Road, Ann Arbor, MI 48106-1346 USA
800-521-0600

UMI®

Nonlinear Finite Element Modeling and Incremental Analysis of A Composite Truck Tire Structure

Xiong Zhang

A Thesis

in

The Department

of

Mechanical Engineering

Presented in Partial Fulfillment of the Requirements
for the Degree of Doctor of Philosophy at
Concordia University
Montreal, Quebec, Canada

March 2001

National Library of Canada
Bibliothèque nationale du Canada

Acquisitions and Bibliographic Services
Acquisitions et services bibliographiques

395 Wellington Street
Ottawa ON K1A 0N4
Canada

395, rue Wellington
Ottawa ON K1A 0N4
Canada

Your file Votre référence

Our file Notre référence

0-612-63993-2

Canada

ABSTRACT

Nonlinear Finite Element Modeling and Incremental Analysis of A Composite Truck Tire Structure

Xiong Zhang, Ph.D.
Concordia University, 2001

The performance of a road vehicle is directly related to the static and dynamic properties of tires, which provide support and control for vehicles and which must possess good durability under various tire-road interactions and loading conditions. The tire characteristics are inherently dependent on various structural and geometric parameters, the material properties of the individual layers of a tire and the loading conditions. In view of the simulation and analysis of tire response, in terms of deformation and stress fields, and vibration properties, extensive analytical studies had been conducted in the past based on the linear analysis of the multi-layered tire structure, assuming negligible shear interactions between the layers. In this dissertation, a nonlinear finite element model of a radial truck tire is developed based on its composite structural elements to analyze the various stress fields, with focus on the inter-ply shear stresses between the belt and carcass layers as functions of normal loads and inflation pressures. The model is validated through a comparison of the normal force-deflection characteristics and the contact patch geometry derived from the model with the laboratory-measured data in a qualitative sense. The tire model is used to conduct a parametric study on the shear interactions in the multiple layers under a wide range of loading conditions, to derive a more desirable set of structural parameters that can lead to lower values of maximum shear stresses within the loaded multi-layered tire structure. A polynomial function has been derived to estimate the two-dimensional tire-road contact pressure distribution as a function of the inflation pressure and the normal load. The tire model is further used to study the free-vibration behavior of the inflated tire structure. The influences of the individual structural parameters on the load and pressure-dependent natural frequencies of a radial truck tire are also investigated. The results show that the proposed finite element tire model based on adequately measured geometric and material properties of a tire structure can yield considerable benefits in the tire design and heavy vehicle performance.

Acknowledgements

The author wishes to thank sincerely the thesis supervisors, Dr. S. Rakheja and Dr. R. Ganesan for their guidance and efforts during the course of this investigation.

The author wishes to acknowledge Concordia University and Concordia Center for Advanced Vehicle Engineering (CONCAVE) for their Graduate Fellowship and Research Assistantship, respectively.

The author also wishes to thank the colleagues, faculty and staff of CONCAVE Research Center for their contributions to this study.

Finally, the author would like to express a deep appreciation to his parents, wife and the other family members for their continuous concerns, encouragement and supports.

TABLE OF CONTENTS

Page

LIST OF FIGURES

LIST OF TABLES

NOMENCLATURE

a_i	Interpolation coefficients of the polynomial $p_c(x)$
C_1, C_2	Material constants in Mooney-Rivlin material model, unit: N/m^2
${}_0^tC$	Matrix that equal to ${}_0^tX^T\,{}_0^tX$
${}_t^0C_{kl}$	Inverse of the right Cauchy-Green deformation tensor ${}_0^tC_{kl}$
${}_0^tC_{mn}$	Right Cauchy-Green deformation tensor at time t with respect to the configuration at t=0
${}_0\overline{C}_{ijrs}$	Tensor of the constants of constitutive equations due to displacement
$\tilde{C}$	Matrix obtained from ${}_0^tC$ with all elements in the ith row except C_{ij} are zeros
${}_0CPP$	Term used to compute the element in the force vector due to pressure ${}^tFP$
${}_0CUU_{klrs}$	Term used to compute the element in the stiffness matrix ${}^tKUU$
${}_0CUP_{kl}$	Term used to compute the element in the stiffness matrix ${}^tKUP$
D	Determinant of order n
D'	Derivative of a determinant D
$D_{(j)}$	Determinant obtained from D by differentiating its entries in the j-th row
dz_{nm}	Average normal deflection of the element, unit: m
E	Young's modulus E, unit: psi
E_1	Longitudinal (along cord's direction) Young's modulus for individual layer, unit: psi
E_2	Transverse (to the cord's direction) Young's modulus for individual layer, unit: psi
e_V	The volumetric strain

e_{ii}	The normal strains along the coordinate axes.
e_{ij}	The components of the Cauchy strain tensor corresponding to τ_{ij}
$e^{\cdot}_{ij}$	The deviatoric strain components
epc	The amount of cord ends per unit centimeter
F	Force vector
F_z	Normal load applied on the tire, unit: kN
F_z	Resultant normal load, unit: kN
$\overline{F}_z$	Normalized normal load applied on the tire
[F]	Column matrix formed by the normal load variables
${}^{t}FU$	Force vector resulted from displacement at time t
${}^{t}FP$	Force vector resulted from pressure at time t
F_{zn}	Distributed tire-road contact force due to elements in row n, unit: kN
f_i	Natural frequency of mode i, unit: Hz
f_i^B	The Cartesian components of the body force vector
G	The shear modulus, unit: psi
G_1	Shear Modulus in belt plane, unit: psi
G_2	Shear Modulus in transverse plane vertical to the cords, unit: psi
G_3	Shear Modulus in transverse plane along the cords direction, unit: psi
g_i	The i-th interpolation function for pressure
h_L	Interpolation function for displacement at node L
${}_{0}^{t}I_i$	The i-th invariant given in terms of the components of the Cauchy-Green deformation tensor.

${}_{0}^{t}J_{i}$	The i-th reduced invariant in Mooney-Rivlin material model
K_i	Column matrix formed by the interpolation coefficients k_j
k	Maximum number of element columns in the contact patch
k	Bulk modulus, unit: N/ m^2
k_j	Interpolation coefficients of the polynomial $a_i(F_z)$
${}^{t}KUP$	Stiffness matrix resulted from both displacement and pressure at time t
${}^{t}KPU$	Stiffness matrix resulted from both displacement and pressure at time t
${}^{t}KUU$	Stiffness matrix resulted from displacement at time t
${}^{t}KPP$	Stiffness matrix resulted from pressure at time t
[K]	Element stiffness matrix
[K]	Stiffness matrix
l	Maximum number of element rows in the contact patch
L_n	Length of the elements in row n, measured along x direction, unit: m
[M]	Mass matrix
P_{nm}	Centralized force acting on the element in row n and column m of the contact patch, unit: N
p	The hydrostatic pressure, unit: Pa
$p_c(x)$	Contact pressure as a function of longitudinal coordinate x, unit: Pa
$\overline{p}_c(x)$	Normalized contact pressure as a function of longitudinal coordinate x
p$_{I}$, p_I	Inflation pressure of a tire, unit: psi
$\overline{p}_I$	Normalized inflation pressure of a tire
p_n	Equivalent two-dimensional contact pressure due to elements in row n, unit: Pa

p_{nm}	Average contact pressure at the element in row n and column m, unit: Pa
$\hat{p}$	Pressure vectors containing increments in pressure
${}^{t}\hat{p}_{i}$	The i-th nodal pressure at time t, unit: N/m^2
${}^{t}\bar{p}$	Hydrostatic pressure computed directly from the displacements at time t, unit: N/m^2
${}^{t}\tilde{p}$	Hydrostatic pressure computed from the separately interpolated pressure variables at time t, unit: N/m^2
${}^{t}\hat{p}_{k}$	Increments in k-th pressure variables, unit: N/m^2
${}_{0}P(\cdot)$	Operator representing a differentiation with respect to strains
q	Order of the polynomial $p_c(x)$
${}_{0}^{t}Q$	Potential energy density due to displacements and the separately interpolated pressure at time t with respect to configuration at t=0, unit: Nm/m^3
r	Order of the polynomial $a_i(F_z)$
${}^{t}R$	External virtual work at time t, unit: Nm
${}_{0}^{t}R$	Orthogonal (rotation) matrix
${}^{t+\Delta t}R$	Nodal point forces corresponding to the external loading at time t + Δt, unit: N
S_{nm}	Element area, unit: m^2
S_{xy}	Shear stress in wheel plane, developed in belt and carcass layers, unit: Pa
S_{xz}	Shear stress in transverse plane of a tire, developed in belt and carcass layers, unit: Pa
S_{yz}	Shear stresses in the belt plane, unit: Pa
${}_{0}^{t}\bar{S}_{ij}$	The components of the second Piola-Kirchhoff stress tensor due to displacement
${}_{0}^{t}S_{kl}$	Second Piola-Kirchhoff stress tensor at time t due to both the displacement and hydrostatic pressure, with respect to the configuration at t=0

s	Order of the polynomial $k_j(p_l)$
${}_0^tU$	Symmetric stretch matrix
u_i	The components of the displacement vector for the considered point P, unit: m
${}^tu_i^L$	Displacement at node L of an element along the i-th direction, unit: m
$\hat{u}$	Displacement vector containing increments of displacement
${}^t\hat{u}_k$	Increments in displacement variables in k-th direction, unit: m
${}^0V$	Reference volume of the configuration at time $t = 0$, unit: m^3
W	Total potential energy per unit volume in materials, unit: Nm/m^3
W_H	Strain energy density due to hydrostatic pressure unit: Nm/m^3
${}_0^t\overline{W}$	Potential energy density due to displacement at time t with respect to configuration at t=0, unit: Nm/m^3
${}_0^t\tilde{\tilde{W}}$	Strain energy density estimated using ${}_0^tI_i$, unit: Nm/m^3
W_{nm}	Work done by centralized force P_{nm}, unit: Nm
w_l	Interpolation coefficients of the polynomial $k_j(p_l)$
x	Longitudinal coordinate of a point in the contact patch, unit: m
$\bar{x}$	Normalized longitudinal coordinate of a point in the contact patch
X	Column matrix formed by the longitudinal coordinate variables
${}_0^tX$	Deformation gradient tensor at time t with respect to configuration at t=0
x_i	The coordinates of the displacement vector for the considered point P
${}_0^tx_{i,j}$	Differentiation of the i-th displacement variable at time t, with respect to the j-th displacement variable at time t=0
δ_{kl}	Kronecker delta

Δy_n	Width of the elements in row n, measured along y direction, unit: m
ΔZ	Normal deflection of a tire, unit: mm
ΔV	Change of volume, unit: m^3
$\hat{\varepsilon}_{ijk}$	Permutation tensor
${}_0^t\varepsilon_{mn}$	Green-Lagrange strain tensor at time t with respect to the configuration at t=0
$\{\Phi_i\}$	Mode shape vector (eigenvector) of mode i
ω_i	Natural circular frequency of mode i, unit: Hz
ν	Poisson's ratio
ν_1	Poisson's ratio associated with the movement in belt plane
ν_2	Poisson's ratio associated with the movement in the transverse plane vertical to the cords
ν_3	Poisson's ratio associated with the movement in the transverse plane along the cords direction
θ	Cord angle in layer, unit: degree
ρ	Density, unit: kg/m^3
τ_{ij}	The Cartesian components of the Cauchy stress tensor
$(\cdot)^{\bullet}_{ij}$	Operator representing $\frac{1}{2}\left(\frac{\partial(\cdot)}{\partial\,{}_0^t\varepsilon_{ij}}+\frac{\partial(\cdot)}{\partial\,{}_0^t\varepsilon_{ji}}\right)$

CHAPTER 1 INTRODUCTION AND LITERATURE REVIEW

1.1 GENERAL

The pneumatic tires are the most widely used composite structures of commercial importance and have functioned as an integral part of the wheeled-vehicle systems, since their inception [1]. The dominant use of pneumatic rubber tires in vehicles is attributed to their various properties, such as ability to support and guide the vehicle, and to provide adequate traction and braking with good durability under widely varying tire-road interactions and loading conditions. The ride quality, handling, and directional control and stability performance requirements of a vehicle thus strongly rely upon properties of the tires. The characteristics of tires, however, are not easily predictable and comprehensible due to the complexity of the tire structure and the lack of effective analysis methods. The tire properties are mostly characterized through laboratory experiments in terms of total forces and moments developed at the tire-road interface. The experimental methods not only involve highly complex fixtures and measurement systems; the development of relationships between the measured data and the structural properties of tires poses many challenges. Moreover, in view of the nonlinear nature of the tire forces and moments, the measured quantities can be considered to be valid only in the vicinity of the test conditions employed. The analysis methods involving structural properties of a pneumatic tire are considered desirable to study the influence of tire design and operating factors on its response characteristics. Such tire models can yield considerable insight into the tire design and response in terms of deformation, stress and strain fields, tire-road contact pressure distribution, oscillation modes, etc.

A number of tire models have been developed to study the vehicle characteristics related to the vertical load carrying properties, traction and braking forces, cornering forces and the cushioning ability of the vehicle over rough roads [2, 3, 4]. The tire models, derived from the measured data, are widely employed in analysis of the vehicle system performance. These models have served as simple yet effective tools for enhancement of understanding of the tire properties. The models, however, cannot analyze the contributions due to structural features and material properties of the layers in a tire. An analysis of the tire properties over a wide range of operating conditions requires the knowledge of deformation and stress fields for a loaded tire that must be determined in the design stage. A number of models of the tire structure have thus been developed on the basis of material properties and geometry of the multi-layered tire system [4, 5]. However, the techniques used to compute tire stress and deformation fields have remained limited for decades due to lack of adequate computing resources and analysis software. Today, one of the main challenging tasks encountered by tire designers is to understand the underlying causes of the tire delamination failures, which may be resulted from a combination of factors involving the tire structural parameters and geometric dimensions, tire loads, vehicles and driving conditions. Such investigation can be initiated by performing static analyses followed by modal analysis of a specific tire, and then, the dynamic analyses concerning the real operating conditions of a tire in service. Special attention has been concentrated on the effective prediction of the various stress fields, especially the shear stress fields developed in the multi-layered system of a pneumatic tire due to various loads and operating conditions. Implementation of this goal can be facilitated through the application of the commercial finite element (FE) analysis code ANSYS® for the multi-layered composite structure of a loaded tire.

In this dissertation, a nonlinear finite element model of a radial truck tire is developed on the basis of its composite structural elements to analyze the various stress fields, with particular focus on the inter-ply shear stresses in the belt and carcass layers as functions of the structural parameters and the normal load. The established tire model incorporates the geometry and orientation of the cords in belt and carcass layers, stacking sequence of different layers, large magnitude and nonlinear deformations of the multiple layers and the nearly incompressible property of the tread rubber block. The influences of the structural and geometric parameters, and the configuration and material properties of the individual belt and carcass layers on the shear interactions in the individual layers are investigated under non-rolling conditions. The results of the parametric study are used to derive a more desirable set of structural parameters that can lead to lower maximum shear stresses within a loaded tire body. The computed three-dimensional pressure fields in the tire-road interface are analyzed to derive a polynomial function to effectively estimate the contact pressure distribution as a function of the inflation pressure and the axle load. The model is further used to perform modal analysis to investigate the influence of the design parameters and the loads on the vibration characteristics of the tire.

1.2 REVIEW OF THE LITERATURE

The reported relevant studies are reviewed and briefly discussed in this section to enhance the knowledge and to build the scope of the dissertation research.

1.2.1 Tire Structure and Modeling Considerations

A pneumatic tire is a toroidal shaped structure filled with air. There are two kinds of tires that can be distinguished by their structural features: bias-ply tires and radial-ply tires. The design of a radial-ply tire differs considerably from that of a bias-ply tire. The radial tires are increasingly being implemented for automobiles and heavy road and off-road vehicles. The essential structural elements of a pneumatic radial tire include the carcass, belts, tread and beads, as shown in Figure 1.1.

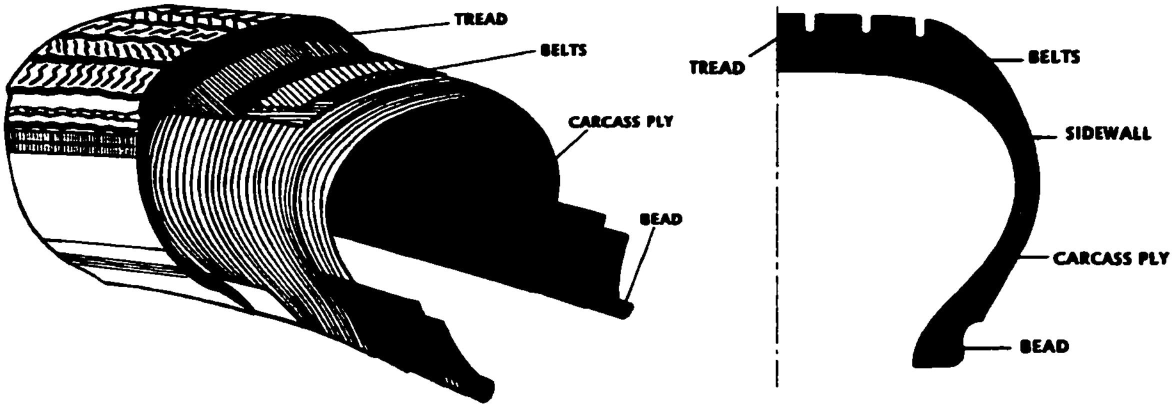

Figure 1.1: Primary structural elements of a radial tire.

The carcass is a molding of rubber reinforced by one or more cord-reinforced layers in a matrix of low modulus rubber material (natural or synthetic rubber). The cords embedded in the layer(s) are disposed in a radial direction running directly across the crown at 90° to the circumferential centerline of a radial tire. The carcass, inflated with air, forms the toroidal tire structure as a sealed body and that supports the vehicle load. The carcass construction plays a dominant role in determining the tire characteristics and vehicle performances [6]. The belts or breaker are made up of several plies of cords fitted on the top of the casing and laid at various low crown angles. The belt layers enhance rigidity to the tire in the lateral direction and help to stabilize the tire in radial direction.

The exterior tread layer of a tire is patterned with grooves and slots to provide gross drainage of water from the tire-road contact patch in wet conditions. The tread also serves as a wear resistant layer in addition to protecting the tire casing. Furthermore, tread provides sufficient frictional contact with the road to develop and transmit adequate driving, braking and cornering forces, and assists cooling in dry conditions. The beads, made up of many turns of high modulus cords, are located at the inner edges of the sidewall. The main function of the beads is to secure the tire casing at the wheel rim firmly.

The mechanics of pneumatic tires has been extensively investigated through experimental as well as analytical means. The objectives of the majority of these studies have included the characterization of the load-deflection properties, rolling resistance and skid resistance properties, the tire-road contact patch geometry and the forces and moments generated in the tire-road contact patch. Owing to the strong nonlinear properties of the tires, experimental studies have attempted to define tire characteristics as functions of various operating conditions, with little or no consideration of the material and structural parameters [3, 6-8].

The forces and moments generated by a tire are known to be strongly nonlinear functions of many operating (speed, load, road surface, inflation pressure, temperature, tread condition, etc.) and design (geometry, structure, material properties of layers, etc.) parameters. Estimation of tire forces and moments, therefore, requires consideration of the majority or all of these parameters. The characterizations through experimental means, in general, do not permit the influence of all of the design and operating variables due to extensively large test matrix, nonlinear material properties and measurement difficulties associating with the rolling tires [3, 6, 9].

The analytical studies on tires have attempted to develop tire models of varying complexities. The tire modeling generally involves the elastic deformation of the tire structure subjected to a normal load, tire-road interactions between the tread and the road surface in the contact region, and the related three-dimensional geometry. The deformation and loading properties are considered to be mutually interactive. The stress-strain fields generated in a tire depend on the contact conditions, the structural parameters, geometric configuration of the cross section and the material properties of the layers making up the tire. It is generally agreed that the tire modeling and analysis tasks represent a very complex problem that requires either extensive calculations or warrants considerable simplifications for obtaining solutions to meet various design and analysis objectives.

A vast number of tire models have been developed since the 1950's, which differ considerably in complexity, structure and purpose of use. Classical models were developed on the basis of a string or a beam supported on an elastic foundation representing the tread band and the tire body [6-8]. The results derived from these relatively simple models have provided considerable knowledge leading to understanding of the development of the shear forces and moments generated in the tire-road contact patch. A number of empirical models have also been developed on the basis of experimentally measured forces and moments [10-11]. These models are mostly used for simulation of coupled tire-vehicle models [3, 8]. Semi-empirical models, combining the features of both the classical and the empirical models, have also been proposed [12-14]. Both the empirical and semi-empirical models are considered useful in predicting the overall tire properties affecting the vehicle performance, such as traction, braking, cornering and the ride quality, while the influence of structural and geometric parameters are mostly ignored in vehicle performance analysis codes. The models derived on the basis of structural parameters and geometric configurations of individual layers form another category of tire models. These models are, in general, quite complex due to complex tire geometry, multi-layered tire structure, material properties of different layers and cords embedded in the layers. Such models are developed and used by the tire designers for stress related analyses to enhance the tire characteristics, such as tire durability [4-5, 15]. The models reported in the recent years are mostly based on the finite element analyses and are capable of predicting the stress-strain fields within the individual layers. These models contain detailed representations of the tire structure and the related material properties of layers. In the subsequent sections, the tire models are grouped into two categories on the basis of their potential use and objective: (i) the models for vehicle dynamics analyses, which include those derived from the measured data and the classical methods; (ii) the models for tire design and analyses, which emphasize the structural and material features of the tire.

1.2.2 Analytical Tire Models

While the contact forces generated in the tire-road contact patch are of fundamental importance for preservation of stability, control and guidance of road vehicles, the deformation and stress fields developed in a loaded tire have significant influence on the fatigue life, durability, wear and failure of a tire. The mechanics of the stress or force generation processes of a tire under various loading conditions are of particular interest to the tire designers, the vehicle dynamists, and pavement and bridge designers. The application of tire mechanics in different fields, however, involves different perspectives and performance objectives.

The vehicle dynamists, in general, are concerned with overall tire properties affecting the vehicle performance characteristics, such as response to the side slip and/or longitudinal slip (braking and traction efforts) and road surface irregularity. The classical and semi-empirical/empirical tire models developed on the basis of measured data under well defined operating conditions are thus considered adequate to characterize the total forces and moments developed by the tires. The forces and moments developed by a pneumatic tire are known to be related to the material properties, structural features, tire-road contact geometry, inflation pressure and the frictional interaction in the contact patch. Input parameters for these models usually include vertical load, side-slip angle, longitudinal slip ratio, camber angle, vehicle speed, free rolling angular speed, while the outputs are normally the resultant shear force and moment generated in the tire-road contact region. The pavement and bridge designers, on the other hand, are mostly concerned with the magnitudes of static and dynamic tire forces transmitted to the road and bridge structures. The tire models characterizing the static and dynamic force-deflection properties may thus be considered adequate for such studies. Both the classical and regression function (empirical/semi-empirical) models are considered adequate and economical for analysis of vehicle dynamics performance and dynamic pavement/bridge loads [3, 6, 8, 16-18]. Since these regression-based models are derived on the basis of measured data under carefully controlled conditions, they can be considered valid in the vicinity of the selected operating conditions. Moreover, the contributions due to material and structural properties are mostly ignored [19].

A pneumatic tire is a complex system of multiple layers of carcass and belts, which are made of components with considerably different properties. The properties of the anisotropic cord-rubber composite layers in the carcass structure play a dominant role in controlling the overall performance characteristics of the pneumatic tire. Moreover, the stress and strain fields within the tire structure determine the characteristics of tire forces and tire durability. The finite element techniques are widely employed to derive elaborate models of the tire structure incorporating the detailed material properties and structural features of each individual component, such as the nearly-incompressible behavior of the tread rubber and the anisotropic material properties of the carcass and belt layers. The outputs of these models, in general, are the stress fields in the individual layers. The tire responses, such as the load deflection characteristics, shear force generated in the tire-road contact patch, etc., are derived from the stress fields through post-processing of the model results. Various reported tire models are reviewed and grouped in two broad classes on the basis of the analyses objectives and applications. The models within each group are briefly described in the following sections.

1.2.3 Tire Models for Vehicle Dynamics Analyses

Apart from the aerodynamic and gravitational forces, almost all other forces and moments affecting the motion of a road vehicle are applied through the tire-road contact interface. The handling, directional control and stability, and ride performance of vehicles are thus primarily dependent upon the overall static and dynamic properties of the tires. It is generally convenient to distinguish between symmetric and anti-symmetric modes of tire performance, with reference to the rolling plane of a tire in the vehicle dynamics analysis [20]. While a tire supports the vertical load and transmits longitudinal braking or driving forces, it is also required to supply adequate cornering and camber forces that are essential for the directional control of the vehicle. Linear tire models are often applied, when only small deviations in the vehicle response are considered. In this case, the symmetric and anti-symmetric motions of the assumed wheel-tire system are usually assumed uncoupled. The in-plane and out-of-plane tire models are frequently used to analyze symmetric and anti-symmetric motions of the tire-wheel system [20].

In-plane Tire Models

The in-plane tire models are mainly concerned with the response of a tire to a disturbance input that stems from the motions of the wheel relative to the road in the wheel plane. The in-plane tire models are used to study the symmetric behavior of tires, arising from the steady state or slowly varying motions to high frequency and non-steady-state behavior of a tire [21]

The simple in-plane tire models describe the linear and nonlinear normal load-deflection properties of tires [22-27], which are widely used to study the in-plane vibrations of a tire and the effects of tire vibration characteristics on the vehicle performance in terms of ride quality [28-33]. The in-plane tire models, have also been applied to study the radial and longitudinal tire force responses to in-plane variations in the wheel axle position, road irregularities, tire radius and tire radial stiffness, assuming linear analysis of the in-plane motions [3].

The inertia effects of a tire are mostly neglected, assuming that predominant motions occur at frequencies well below the lowest natural frequency of the tire, which is estimated near 20 Hz for road vehicle tires [3]. Under high frequency excitations, above 30 Hz, a pneumatic tire exhibits number of natural frequencies in the in-wheel plane and out-of-wheel plane motions, resulting in continuously distributed vibrations of the side wall and the tread band [3]. The tires also exhibit coupled in-plane and out-of-plane motions involving complex three-dimensional deformation modes, which can not be obtained from both the in-plane and out-of-plane tire models. The development of an effective three-dimensional tire model is thus considered desirable to study the coupled motion of the tire. The experiments performed to study the frequency response characteristics of tires revealed considerably small amplitude ratio of the hub oscillation to the sinusoidal platform oscillation at higher frequencies, above 110 Hz [21]. At even higher frequencies, the tire exhibits the standing wave phenomenon, which has been extensively investigated by many researchers [34-41].

Out-of-plane Tire Models

The out-of-plane tire models are widely used to study the response of a tire in the transverse plane of the tire-wheel system related to the cornering properties of tires [42-50], which are of fundamental importance in view of the handling and stability characteristics of the road vehicles. In these models, the road is assumed to be undeformable with smooth surface, while the tire is represented by combination of elastic or visco-elastic elements. The majority of the out-of-plane tire models considered the contact patch as either a straight line or a two-dimensional idealized shape, such as rectangular and elliptical [42]. These models mostly provide qualitative descriptions of the tire behavior to facilitate the understanding of the mechanism related to shear force generation in the tire-road contact patch.

The use of an elastic continuous structure representing the carcass is essential in both the steady state and the non-steady state tire models. Many investigations have attempted to incorporate elastic continuous carcass structure in formulating these out-of-plane tire models. Some of the models are based on the assumption that the tread of a tire is equivalent to a stretched string restrained by lateral springs that are representative of the side wall, with the wheel rim acting as the base of the springs [3, 6]. Some of the other models consider the tread as an elastic beam with continuous lateral support [8, 51], while the others assume that the carcass flexibility is associated entirely with independently acting radial spokes representing both the carcass and the tread block flexibility [52-53]. None of these models, however, could describe the structural and geometric features of the tire. Their applications are limited to the fundamental understanding of the shear force generation in the tire-road contact patch and the investigation of the overall tire properties as functions of the various vehicle parameters, such as slip angle, tire load and speed.

The most widely used out-of-plane tire model is the regression-based model, proposed by Pacejka [10-12]. The model, referred to as the 'magic formula' tire model, comprises a set of analytical functions, whose coefficients are identified by curve fitting the data acquired from full-scale tire experiments [43-44]. The model describes the forces and moments as functions of different operating conditions, such as normal load, side slip, slip ratio and speed. The need to perform additional work to adequately incorporate the effects of the camber force and moment as well as the spin force into the model has been recognized [51]. The 'magic formula' tire model has been widely adopted by tire manufactures as an industry standard. The measured data are, therefore, frequently reported in terms of the model coefficients, rather than the conventional graphical or tabular forms. Although the 'magic formula' model has been proven as an effective tool for analyses of directional performance of vehicles, it does not allow the consideration of material and structural properties of the tires. The applications of these models, however, is limited by the fact that they require extensive experiments for evaluating the equivalent parameters and that the range of their validity is limited to specific ranges of those parameters.

1.2.4 Tire Models Based upon Structure and Geometry

Models used in tire stress analysis are normally called structural tire models and are based on the composite material or layer theories. These models are normally developed using finite element techniques, where the governing equations of motion of a typical element are derived using the energy method. The primary feature of these models is the ability to determine the tire responses to a prescribed set of applied loads and operating conditions under given boundary conditions. Consequently, the structural models are used to predict the displacement, strain or stress at any chosen location within the tire structure, when the geometry configurations, the relevant properties of its component materials, the applied loads and the constraints from boundary conditions are known. The response of a loaded tire is mostly governed by the properties of the anisotropic cord-rubber composite layers. A vast number of structural models have been developed with different considerations or simplifications of the configuration of the carcass and the belt layers, resulting in varying levels of complexity. The reported models can be grouped into four different classes on the basis of complexity or modeling simplifications. They are the netting analysis models, the membrane models, the thin shell models and the finite element models, as illustrated in Figure 1.2.

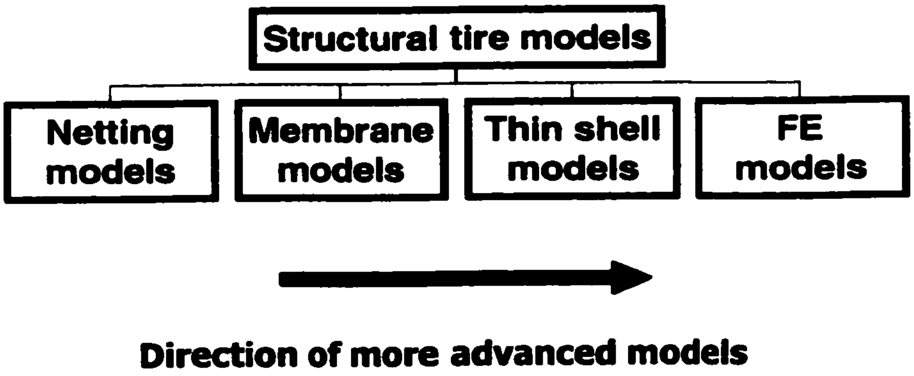

Figure 1.2: Classification of structural tire models.

Early structural tire models were based on elementary structural analysis, which were called the cord and rubber models or netting models [54-60]. The netting models assume that the tensile forces in the cords exclusively balance the inflation pressure. The models, therefore, fail to include the bending and stiffening effects of the rubber surrounding the cords and the bending effect of the tire. Despite these limitations, cord-network models allow the determination of the inflated profile of some bias-ply tires with reasonably good accuracy. The cord-network model has also been applied to study the response behavior of aircraft tires [57]. The study concluded that such models often yield unacceptable results in terms of the stresses in the cords.

Alternatively, the models based upon membrane and thin shell theory were developed to incorporate the effects of the rubber matrix [61-62]. These models, however, did not account for abrupt changes in the geometry, and material properties of different layers or loading. With the use of the membrane elements, the tire structure is treated like a thin film, where the bending effects of the rubber are also ignored and only the tensile forces within the membrane could be considered. The linear membrane analysis offers no more benefits than the netting analysis due to its independence of the elastic properties of the rubber material. The nonlinear membrane analysis, however, could be used to compute the profiles of the inflated membranes against flat surfaces [63-64]. DeEskinazi et al. [65] used the nonlinear membrane theory to solve the contact problem of an inflated toroidal membrane deflected against a flat surface, incorporating a general representation of the geometry, loading and boundary conditions. The more advanced membrane tire models based on the laminate theory can incorporate the differences in mechanical and geometric characteristics of the cord layers in addition to the elastic rubber property [66-67]. It had been established that nonlinear membrane theory in conjunction with the application of the maximum potential energy principle forms the essential basis for the finite element approach to deflecting a tire inner tube against a flat surface [68].

The tire models based upon shell theory include the bending effects that were neglected in the membrane theory and netting models. These models thus allow for analysis of local effects in the footprint and bead regions as well as the regions of significant curvature changes. Classical shell theory involves the solutions of the differential equations to obtain closed form expressions that relate the shell's deformations and stresses to the applied loads as functions of the shell dimensions and material properties [5]. Brewer [68-69] developed effective tire models using thin shell theory, which is based on the assumption that a straight line perpendicular to the plane of the plate is (i) inextensible; (ii) remains straight; and (iii) rotates, such that it remains normal to the tangent of the deformed surface. These assumptions are equivalent to specifying that the transverse shear strains are assumed to be zero. By using the shell theory to analyze an aircraft tire subjected to inflation loading, Brewer [68] modeled the tire as a thin laminate consisting of cord-rubber plies stacked in a specified sequence and derived the equations of equilibrium for the differential shell element using the composite laminate theory.

The tire models comprising multi-layered anisotropic shells have also been developed by Grigolyuk et al. [70-71] and Noor et al. [72] based on the Timoshenko-type theory, which assumes that a straight line perpendicular to the plane of the plate does not remain perpendicular to the tangent deformed surface after deformation. In these studies, a more general computational tire model was built using the higher-order Timoshenko-type theory of multi-layered anisotropic shells, which allows for describing the nonlinear dependence of the tangential stresses and strains on the thickness coordinate. More accurate computational models of tires have also been developed by the application of the discrete-layer theories of multi-layered anisotropic shells [73-79]. In these models, the order of the governing differential equations is dependent on the number of tire layers, which allows for the analysis of the distribution of transverse stresses along the tire thickness direction. The constitutive equations of the anisotropic elasticity theory for transverse shear stresses and strains, however, are satisfied in the integral sense for each layer, which may not agree well with the actual stress and strain distributions along the transverse direction.

The limitation of both the Timoshenko and Kirchhoff type models lies in the fact that the shell thickness is assumed to be small relative to the radii of the curvature of the shell surface. The displacements are assumed to be small relative to the shell dimensions, which may not be justifiable in the case of pneumatic tires comprising compliant rubber layers that experience large deformations. Furthermore, the thin shell models often ignore the contribution due to the tread block in order to simplify the tire structure as a shell shape, which results in the key limitation of these models. Although shell models have appeared as effective tools in stress analysis and profile determination for an inflated non-rolling or rolling tire, the analysis of tires deformed by external loads, to a large degree, still remains beyond their scope.

A vast number of finite-element-based computational models for pneumatic tires have been developed for analyses and design optimization studies. The finite element models could be effectively applied to study the stress and strain distributions in individual layers, contact pressure distributions in the tire-road interface, resultant contact forces, vibration characteristics, and dependence of the responses on various design and operating parameters (inflation pressure, geometry, loading, etc.). The highlights and limitations of the various reported finite element tire models are briefly discussed in the following sections.

1.2.5 Finite Element Tire Models

The early finite element models developed in 1970's chronologically used tetrahedrons and rectangular prisms, iso-parametric hexahedral elements and sub-parametric elements [80-88]. These elements remained difficult to implement and required a great deal of preparation and computational efforts due to the lack of powerful computers at the time. The iso-parametric elements used in these models, however, served as an efficient tool for the analysis of two dimensional and axisymmetric structures, which resulted in improved accuracy of the solution and the reduced computing time [89-92].

Since the 1970's, considerable advances have been made in the application of the finite element techniques in tire modeling. Three-dimensional finite element models have been developed and applied for the stress analysis of road vehicle and aircraft tires with appropriate consideration of large magnitude static deflections [93-94]. Some of these models have provided considerable information on characterization of the tire-road contact loads and the energy dissipation associated with the loading conditions [95-96], while others investigated the wear mechanism causing aircraft tire failure during a single landing operation [97-98]. The models have been used to study influence of variations in the material characteristics of the tire constituents due to the combined effects of material hysteresis and frictional heating [99-101]. The steady state dynamic and transient dynamic analyses have been performed to study the rolling, braking and cornering behavior of the tires [102-108]. These studies have mostly employed finite element modeling for nonlinear analysis of shells of revolution [109-111], reduced methods [112, 114], operating splitting techniques [115-116], etc. Applications of these techniques to the tire modeling are summarized in reference [117].

In recent years, the Finite Element Analysis (FEA) has been increasingly integrated into the tire design process [118]. The FEA has been used to study the general tire behavior and to perform parametric and comparative performance analyses. The FEA of tires is now increasingly being used in virtual vehicle dynamics simulation models and as a replacement for certain tire tests to reduce the development time. These models have been widely used to predict tire deformations and stresses due to inflation pressure loading, the load-deflection characteristics, footprint shape, global forces and moments, natural frequencies, etc. Considerable differences among the reported models, however, exist due to differences in objectives of the studies, modeling considerations, the orders of elements used, rubber elasticity and material models, representations of the cord-rubber layers, etc.

Compared to the analyses of statically loaded tires, dynamic simulations can be more computationally intensive due to asymmetric behavior and requirements of smaller load increments. The computational expense is considered as a major limitation of the 3-D tire analysis, and the primary reason for limited use of the dynamic finite element analysis within the tire design process [119]. The advances in high-performance computing together with more efficient numerical algorithms have facilitated the realization of high-density 3-D finite element analysis models of tires in recent years [120-123].

Stress Analysis

Vast majority of models for stress analysis are based upon either classical or finite element techniques as applied to the tire structures that are simplified as cylinders, membranes, or shells of revolution [4, 5, 12]. A large number of finite element based tire models have been reported during the past few years to analyze the stress, strain and deformation fields in the tire under various loading conditions [124-127]. While classical methods provide closed form solutions to sets of differential equations to gain insights into the tire behavior, the finite element techniques allow modeling of the geometry of the actual tire profile and considerations of representative material properties of individual layers. The importance of such studies may not lie in the quantitative values they present, but rather in the qualitative comparisons of the trends obtained for different design configurations involving variations in the geometric and structural properties. The reported tire stress analyses range from the use of simple axisymmetric models for the analysis of tire deformations due to curing stresses [128], to those involving application of advanced models for analysis of rolling tires with detailed considerations of friction, cornering and visco-elastic properties of the polymers [124].

While fiber stresses in a rolling tire relate to the cornering and traction properties of the tire, the shear stresses developed in different belt layers and the belts and carcass interfaces, directly affect the stability and integrity of the tire structure. The majorities of the reported tire models, however, do not reflect the complexity of a real tire and thus could not incorporate the concerned shear interactions. Too high a magnitude of inter-ply shear stress in the belts may cause delaminating damage. The analysis of structural integrity and stability characteristics of tires thus necessitates the shear stress analyses of the multi-layered loaded tire. Only limited efforts, however, have been made to analyze the inter-ply shear stress fields and distribution of fiber forces in the individual layers of tires [126-127, 129]. Most of the current finite element tire models, which could be found in the literature, are mainly based on linear analysis of the multi-layered system, assuming small deformations of layers and negligible shear interactions between the anisotropic layers.

A number of nonlinear finite element tire models, reported in the literature, consider the thickness of the individual rubber layers, while the fiber layers are considered as membranes to facilitate the large deformation analysis of the nearly incompressible rubber layers [126]. Wang et al. [127] introduced the Moire method to carry out in-plane strain and displacement analysis from the experimental stress-strain data for the tread and the belt regions. Nemeth et al. [126] described the use of a software package comprising finite element models for design purposes, which incorporated volume element modeling of the rubber layers and membrane element modeling of the fiber layers. Such studies thus do not consider the shear interactions between the individual anisotropic fiber layers and the large shear deformations of the fiber layers. The analysis of the shear stresses developed between the fiber layers necessitates the consideration of nonlinear analysis of such layers of finite thickness.

The above reported works are mostly concerned with car tires and only few of them have been used to investigate the responses of heavy-duty truck tires, whose geometry, material properties, and especially, the loading conditions, may differ considerably from those of the car tires. The tire response to an applied load, expressed in terms of stresses, strains and deformations of different layers, are inherently dependent on various tire structural parameters, such as the angle of cords in each layer, number of layers used in the belts and material properties of different layers [130]. The tire behavior under specific inflation pressure and normal load may be further influenced by its geometric features described by the aspect ratio, rim radius, tread depth, etc. [129]. The influences of various structural and geometric parameters on the shear interactions of a loaded truck tire, however, have not been investigated. The development of tire models capable of predicting inter-ply shear stress responses could provide information leading to improved design and reduced delamination failures.

Contact Pressure Distribution

The contact pressure field developed in the tire-road interface has been an integral part of the tire modeling programs and is of fundamental importance for both the tire design and vehicle performance studies. The contact pressure distribution of a rolling vehicle tire also determines the stresses induced in the pavement and bridge structures leading to their fatigue damage [16-18]. The contact pressure field is strongly related to the tire inflation pressure, vertical load and various structural properties. While a number of pressure sensing systems have been used to measure the tire-road contact pressure distribution [131], only limited efforts have been made to effectively estimate the contact pressure distributions as functions of the inflation pressure and the normal load. Sakai [131] employed an optical measurement system to characterize the stress distribution between a tire and the contact surface, which facilitates the image representing of the contact pressure distribution data and the contact area geometry in an experimental manner. Akasaka and Kabe [132] studied the 2-D contact pressure distribution for a bias tire loaded against a flat road surface. Assuming in-extensible cords in their study, however, ignored the variations in the cord tension. Trinko [133] derived a 2-D contact pressure distribution from a 3-D finite element analysis of a tire. The derived results, however, were not verified experimentally.

Although finite element tire models of varying complexities [134-138], have been used to derive the contact pressure distributions, only few studies have attempted to provide effective formulations for estimation of the 2-D contact pressure distribution that may be implemented into vehicle models. Akasaka et al. [139] reported the 2-D contact pressure distribution for a typical radial tire, by considering the tire as a ring with the embedded springs to simplify its complex structure. The study reported the high contact pressures along the shoulder regions and the relatively low pressures along the crown centerline for a statically loaded tire. Ishihara et al. [140] determined the 2-D contact pressure field due to a loaded tire through analysis of the model based upon membrane elements. While the results revealed good agreement with the measured data, the complexities of the related formulations used to derive the results deterred its general application. A comprehensive description of the tire-road contact geometry and the normal contact stresses developed due to tire-road interactions has been presented by Browne et al. [141]. The study presents the contact properties for various types of tire-road interactions based on both analytical models and experimental methodologies. Both Ishihara [140] and Browne et al. [141] have employed membrane elements in their investigations to solve for the large deformations experienced by the inflated tires. The majority of the reported models, however, are based on rather insufficient experimental evidence or relatively simple theoretical basis to establish the contact conditions.

Tanner et al. [142] employed an advanced computational procedure for the solution of frictional contact problem for the aircraft tires. The authors in their study modeled a space Shuttle nose-gear tire using the two-dimensional laminated anisotropic shell theory, incorporating the effects of variations in the material and geometric parameters, transverse shear deformation and the geometric nonlinearities [143, 144]. The contact algorithm was based on the perturbed Lagrangian formulation [145], and the preconditioned conjugate gradient (PCG) iteration procedure [146] was employed to compute the solutions of the nonlinear contact problem [147-150], the shape of the contact area and the normal force distributions in the contact region. In this investigation, the inflated tire was loaded against a rigid surface, and the static tire contact problem was thus treated as a unilateral contact problem. The numerical iteration was implemented with a mixed finite element formulation [151]. The contact forces were derived from the load intensities computed from the finite element program. The predicted normal and tangential contact load intensity distributions were observed to be in fair to good agreement with the experimental measurements. However, a possible drawback of this method lies in the fact that the shape functions used are computed only for the undeformed tire and may not reflect the contact area variations associated with the tire deformations at the tire-road interface.

The studies on pavement damage potentials of tire loads and ride dynamics of vehicles mostly consider the tire as an elastic element with a point contact with the road surface. Some of the reported studies have considered the contributions due to variations in normal load and inflation pressures through the development of equivalent spring rates of the point-contact tire models [152-154]. In these studies, the 3-D contact pressure field was represented by an equivalent force, acting at a point within the contact patch beneath the center of the tire. The contributions due to geometry of the tire enveloping the road surface were further ignored. The point-contact approach, although quite simple and convenient, yields the resultant tire force acting at a point on the road surface. This contact force, however, may yield an overestimate of the road damaging potentials of dynamic loads and exaggeration of the wheel-hop tendency [154]. Analysis of tire force transmitted to the pavement necessitates the development of adequate tire models to describe the contact patch geometry and the distribution of the contact forces on the road surface. It is believed that tire load distribution function can be formulated from the 3-D pressure field derived from an effective nonlinear finite element model incorporating the essential geometric, material and structural properties of a tire. The function may then be applied to the resultant tire force computed from the vehicle model comprising an equivalent point-contact spring to estimate the 2-D pressure distributions. The simplicity of the vehicle ride or pavement loading models could thus be retained through use of equivalent point-contact tire models in conjunction with the estimation function. This, however, would necessitate the derivation of an analytical function describing the 2-D tire-road contact pressure distributions as a function of the axle load, inflation pressure and contact patch length.

Modal Analysis

The vibration modes and the natural frequencies of a tire inherently determine the tire's dynamic response properties. The tires envelop the external input arising from the road irregularities and generate an input to the vehicle. The tire non-uniformities and unbalance may yield further inputs to the vehicle due to resulting self-excitations. The different modes of vibration of the tire interact with the dynamics of the vehicle and thus affect its vibration behavior and ride quality [3, 155]. The vibration characteristics of a tire design can be measured in the laboratory or computed numerically, in terms of the tire natural frequencies and the associated mode shapes in the radial, lateral and the circumferential directions [15]. The free and forced vibration response characteristics of pneumatic tires have been evaluated through both the experimental [21, 25, 156] and the computational means [157-159]. Majority of these studies, however, assumes uncoupled symmetric and anti-symmetric motions of the wheel-tire system. Moreover, the analytical models employed in these studies consider the tire structure as a circular string under tension and supported by an elastic foundation to facilitate the mathematical description. The finite element tire models based upon membrane or shell elements have also been employed to study the vibration responses of tires [160-161]. These models are considered to be considerably simple and can only provide the in-plane tire vibration characteristics. The majority of the reported modal analyses are primarily based on linear analyses of over-simplified tire structures, with the incompressible property of the rubber ignored. The contributions due to the large nonlinear deformations of the multi-layered system, and the variations in the inflation pressure and axle load thus have not been fully investigated. The in-plane tire models can be applied to study the radial (ride quality) and the longitudinal (braking or traction) force responses to in-plane variations in the wheel axle position, road irregularities, tire radius and tire radial stiffness. These models, however, do not yield the three-dimensional deflection modes comprising coupled in-plane and out-of-plane deformations. The vibration modes of a pneumatic tire containing the nearly incompressibility of rubber materials, the anisotropy of the multi-layered system and the structural features have been addressed in only few studies [162]. The analysis of deformation modes and the natural frequencies of a tire as functions of the anisotropy of the belt layers, axle load, and the inflation pressure have not been attempted. This necessitates the study of the influences of the anisotropy of belt layers on the vibration modes of a truck tire based on a nonlinear finite element analysis.

1.3 SCOPE AND OBJECTIVES OF THE THESIS

From the review of the literature, it is apparent that the dynamic performance characteristics of wheeled road and off-road vehicle are strongly influenced by the static and dynamic properties of tires. The deformation and stress/strain fields generated in the tire structure, and the forces and moments developed in the tire-road contact patch, are nonlinear and complex functions of many operating and design parameters. While empirical and semi-empirical tire models yield the forces and moments developed by tires for a limited range of operating variables, the continuous models provide significant information related to the design variables. Extensive analytical and experimental studies have been reported on the dynamics of road vehicles using either experimental tire data or empirical tire models. Only limited efforts, however, have been made to develop reliable analytical models for truck tires in view of the material properties and structural parameters of the tire. The development of an effective analytical tire model on the basis of its composite structural elements is thus highly desirable for the analysis and enhancement of heavy vehicle performance.

Owing to the complexity of the truck tire structure and geometry, it is quite difficult to determine the stress fields in a tire under normal working conditions through theoretical analysis. The majority of the reported models have neglected the effects of shear stresses in the multi-layered portions of the tire. Although a few models can incorporate the effects of transverse shear stress through the thickness direction, they are normally based on the thin shell theory. Their applications are thus limited to the inflation or rotational problems, while the analysis of deformations caused by other external loads can not be performed. The majority of the finite element models, which could be found in the literature, are mainly based on the linear analysis of the multi-layered system, assuming small deformations of the anisotropic layers and negligible shear interactions between the anisotropic layers. Some of the advanced finite element models, reported in the literature, consider the thickness of the individual rubber layers, where the fiber layers are considered as membranes. Such models thus do not adequately consider the interactions between the individual anisotropic fiber layers. Moreover, very few of the reviewed studies are related to the heavy-duty truck tires. The development of a detailed and efficient model for a truck tire that permits the analysis of the 3-D deformation and stress fields with emphasis on the shear interactions between the belt and carcass layers as a function of the tire load, is thus considered desirable.

The performance characteristics of tires, and thus the vehicle, are strongly influenced by many geometric, structural and material parameters. The effects of such parameters on the stress and strain fields of truck tires have not been reported, specifically, the influences of variations in structural parameters and material properties of individual layers and geometry of a loaded tire on the maximum shear stresses developed in the belt and carcass layers. A comprehensive parametric study is thus considered vital to derive a set of more desirable structural and geometric parameters for a truck tire, such that the maximum shear stresses in the belt and carcass layers could be reduced over a wide range of loading conditions.

The normal load distribution generated in the tire-road interface is dependent on the inflation pressure and the axle load. The contact pressure fields affect the operating properties of tires and offer essential information on how the road surfaces are loaded by vehicles through their tires. Owing to the complex nature of the tire-road contact problem, and wide variations in the operating conditions and pavement surfaces, the 3-D contact pressure field is often represented by a single nominal force acting at a point within the contact patch beneath the center of the tire. Such simplification yields an over estimation of the dynamic wheel load and pavement damage potential of tires. Although the contact pressure distributions have been quantified through experimental techniques, effective analytical functions describing the contact pressure distribution as functions of the inflation pressure and the normal load are not yet available. The identification of a tire-road contact pressure distribution function in the wheel plane as a function of the tire inflation pressure and normal load offers considerable potential for efficient analysis of the pavement damage potential of the tires. Moreover, the load-dependent vibration modes of a truck tire could provide considerable insight into its vibration behavior.

1.3.1 Objectives of the Dissertation Research

The overall objective of the dissertation research is to develop an effective tire design and analysis tool incorporating the nonlinear geometric and structural features of the multi-layered system of a truck tire. The dissertation research is focused on a non-rolling tire under static loading conditions. The study involves the nearly-incompressible property of the rubber block; large nonlinear deformation of both isotropic rubber and anisotropic layers; stress and strain fields in layers and normal stress distributions in the tire-road interface. The specific objectives of the study are described below:

a. Develop a nonlinear finite element model of a radial truck tire using 8-node layer and hyper-elastic elements representing each individual structure layer and the tire cross-section geometry to derive the deformation, stress, strain and inter-ply shear stress fields under a static load and specified inflation pressure.

b. Validate the tire model by comparing the computed tire-road contact patch geometry and the load-deflection characteristics, with those measured in the laboratory under a wide range of tire load and inflation pressure conditions.

c. Perform the analysis of the validated model and determine the tire response in terms of the radial deformations, tensile stresses, stresses in principal directions, inter-ply shear stress fields developed between the different belts and carcass layers, and the 3-D tire-road contact pressure fields, as functions of the normal load and the inflation pressure.

d. Perform a thorough parametric study on the effects of various structural parameters related to the tire geometry and cross-section, the geometry and anisotropic properties of the individual layers, on the maximum shear stresses developed between the belt and the carcass layers for a range of loads and inflation pressures.

e. Propose a more desirable set of structural parameters to reduce the maximum shear stresses in the belt layers for a loaded tire, and demonstrate the potential performance benefits of the proposed design parameters.

f. Estimate the 2-D tire-road contact pressure distribution with objective of enhancing the application of the point-contact tire models in the pavement damage studies. For this purpose, the so-called "equivalent work" concept is employed to propose an effective methodology to formulate the 2-D contact pressure distribution as a function of the inflation pressure and the axle load.

g. Perform modal analysis of the tire model to generate its natural modes and study the influence of the anisotropy related parameters, such as the cord angle, number of layers in the belt, number of cord ends per unit width of each layer and the inflation pressure, on the natural frequencies of the tire.

1.3.2 Organization of the Thesis

In chapter 2, the governing equations for the incremental analysis of the rubber element are derived based on the Total Lagrangian (TL) formulation and the modified Mooney-Rivlin material model. The general formulation for the finite element solution of the nonlinear elastic problem involving nearly incompressible materials has been derived using the mixed interpolation of the displacements and pressure (u/p) formulation, which are to be employed by the finite element model of a radial truck tire.

In chapter 3, a nonlinear finite element tire model is developed using ANSYS® to determine the deformation and stress fields in the belts and carcass layers, contact patch geometry and pressure distribution in the tire-road interface. The influence of normal load and thus the tire deflection on the above response parameters are discussed. The model is validated in a qualitative manner through comparison of the computed load-deflection characteristics and the footprint geometry with the measured data.

In chapter 4, a parametric study is performed to study the influence of selected structural and geometric parameters on the maximum shear stresses developed in the belt layers. The investigated parameters include the cord angle and number of twisted cords per unit width of an individual layer, total number of belt layers, the aspect ratio, rim radius and the tread depth. A more desirable set of these parameters is proposed to reduce the highest maximum shear stress to enhance the durability of a tire in service.

In chapter 5, the 3-D contact pressure data computed from the finite element model are analyzed to derive the 2-D pressure distribution using the equivalent work as the basis. Curve fitting techniques are applied to derive a polynomial function for the estimation of the 2-D contact pressure distribution as a function of the normal load and the inflation pressure. The validity of the proposed methodology is assessed through comparison of the estimated data with those computed from the finite element tire model.

In chapter 6, a model analysis is performed to derive the 3-D mode shapes and the corresponding natural frequencies below 112 Hz. The motions associated with each vibration mode of the tire under specific inflation pressures are discussed. The effects of variations in the inflation pressure and the anisotropy related structural parameters, such as cord angles and the number of layers in the belt, on the natural frequencies of a radial truck tire are investigated in a qualitative manner.

In chapter 7, the highlights of the research, major conclusions drawn and recommendations for future work are presented.

CHAPTER 2 FORMULATION FOR THE NONLINEAR FINITE ELEMENT TIRE MODEL

2.1 INTRODUCTION

A tire structure comprises of composite layers of different materials and exhibits strongly nonlinear deformation characteristics. The development of an effective and reliable tire model thus essentially involves the consideration of the nearly incompressible property of the tread rubber block in addition to the anisotrpic material properties of each layer. The nonlinear analysis of a body, in general, involves the determination of the state of equilibrium corresponding to the applied loads. The stress analysis of a pneumatic tire involves strong nonlinearities attributed to the material and the kinematics, and thus necessitates an incremental formulation and a time variable to conveniently describe the loading and the motion states of the body from its original to the final configuration. The Total Lagrangian (TL) formulation can be conveniently used to derive the governing equations for the rubber elements in the development of the finite element model of a pneumatic tire, where all the static and kinematic variables are related to the initial configuration of the considered body [163].

The displacement-based finite element method, due to its conceptual simplicity, is commonly used for the analysis of solids and structures [164]. Assuming that the nodal point displacements of the finite element mesh can be used to completely describe the displacements in the body, an application of the principle of virtual work generates a set of simultaneous equations with the nodal point displacements as unknowns. The displacements can then be used for the incremental nonlinear analysis, where the displacement increments are considered as the principal unknowns. For incompressible materials, however, the hydrostatic pressure is de-coupled from the displacement, which necessitates the use of the displacement/pressure (u/p) formulations to obtain the solution of the elastic problems involving the nearly-incompressible tread rubber materials.

In this chapter, the general FE stiffness matrices and force vectors of the rubber element for the incremental analysis are derived using the Total Lagrangian (TL) formulation and the modified Mooney-Rivlin material model. The general formulation for the FE solution of nonlinear elastic problem involving nearly incompressible materials has been derived using the mixed interpolation of the displacements and pressure (u/p) formulation, which are to be employed by the FE tire model developed using ANSYS® software for a typical truck tire.

2.2 BASIC EQUATIONS FOR THE LINEAR ISOTROPIC MATERIAL

Consider a three-dimensional element in a solid body of isotropic material that is described by the Young's modulus E and Poisson's ratio ν. Using indicial notation, the governing differential equations for any point within the considered solid body is given by

$$\tau_{ij,j} + f_i^B = 0 \tag{2.1}$$

where τ_{ij} are the Cartesian components of the Cauchy stress tensor and f_i^B are the Cartesian components of the body force vector. If the body is made of nearly incompressible material, the volumetric strains will be small in comparison to the deviatoric strains. Then the constitutive or stress-strain relations can be written as:

$$\tau_{ij} = \kappa e_V \delta_{ij} + 2Ge'_{ij} \tag{2.2}$$

where κ and G are given by the bulk modulus and shear modulus, respectively,

$$\kappa = \frac{E}{3(1-2\nu)} \tag{2.3}$$

$$G = \frac{E}{2(1+\nu)} \tag{2.4}$$

Further, e_V is the volumetric strain, expanded as:

$$e_V = e_{ii} = \frac{\Delta V}{V} = \frac{\partial u_1}{\partial x_1} + \frac{\partial u_2}{\partial x_2} + \frac{\partial u_3}{\partial x_3} = e_{11} + e_{22} + e_{33} \tag{2.5}$$

where x_i and u_i (i=1, 2, 3) are the coordinates and components of the displacement vector for the considered point P, respectively. e_{ii} (i=1, 2, 3) are the normal strains along the coordinate axes. ΔV and V describe the volume change and the original volume occupied by the considered material particles, respectively.

The δ_{ij} in Equation. (2.2) is the Kronecker delta, expanded as:

$$\delta_{ij} \begin{cases} = 1; & i = j \\ = 0; & i \neq j \end{cases} \tag{2.6}$$

and $e_{ij}^{\cdot}$ are the deviatoric strain components, which are related to the volumetric strain and the Cauchy strain tensor in the following manner:

$$e_{ij}^{\cdot} = e_{ij} - \frac{e_V}{3}\delta_{ij} \tag{2.7}$$

where e_{ij} are the components of the Cauchy strain tensor corresponding to τ_{ij}.

For a linear isotropic material, the pressure-strain relationship can be written:

$$p = -\kappa e_{ii} \tag{2.8}$$

where

$$p = -\frac{\tau_{kk}}{3} (= -\frac{\tau_{xx} + \tau_{yy} + \tau_{zz}}{3} \quad \textit{in Cartesian coordinates})$$

In the above equations, p is the hydrostatic pressure and κ is the bulk modulus. The e_{ii} are the volumetric strains, which diminish to zero for the incompressible materials as κ approaches to an infinite value. The hydrostatic pressure p, in this case, converges to a finite value. Obviously, Equation (2.8) cannot be used to numerically calculate p, since p is de-coupled from the displacements for a totally incompressible material and must be calculated directly from the equilibrium equations in an analytical solution.

2.3 NONLINEAR U/P FORMULATION FOR THE INCOMPRESSIBLE MATERIAL

A general u/p formulation is derived for analysis of elastic bodies involving nearly incompressible materials. The formulation is based on a mixed interpolation of the displacements and pressure, the so-called u/p formulation. The feature of the u/p formulation is that a separately interpolated pressure explicitly replaces the pressure computed from the displacement field. The displacement and pressure increments are solved during subsequent equilibrium iterations and are used to update the total displacements and pressures.

In the following sections, a general nonlinear formulation is derived upon the consideration of the material properties and/or geometric nonlinearities. The derivations employ many of the concepts and notations used in nonlinear analyses by Sussman et al. [163] and Bathe [164]. The finite element stiffness matrices and force vectors are derived from a modified potential using the Total Lagrangian (TL) formulation, which results in the incremental equations of motion that are used to develop the finite element tire model.

2.3.1 Basic Concepts Concerning TL Formulation

The most important idea in the nonlinear incremental analysis of solid material is that the material description used has an incremental strain potential energy density ${}^t_0\overline{W}$ such that

$$d\,{}^t_0\overline{W} = {}^t_0\overline{S}_{ij}\,d\,{}^t_0\varepsilon_{ij} \tag{2.9}$$

where ${}_0^t\bar{S}_{ij}$ are the components of the second Piola-Kirchhoff stress tensor and ${}_0^t\varepsilon_{ij}$ are the components of the Green-Lagrange strain tensor. The left subscript 'o' denotes the original configuration and the over bar is used to indicate that the quantities are computed from the displacement field.

For materials with an incremental potential concerning hyper-elasticity, the potential ${}_0^t\bar{W}$ physically represents the strain energy density due to displacement per unit of the original volume. A consequence of the material assumption described in Equation (2.9) is that the tensor

$${}_0\bar{C}_{ijrs} = \frac{\partial\, {}_0^t\bar{S}_{ij}}{\partial\, {}_0^t\varepsilon_{rs}} = \frac{\partial^2\, {}_0^t\bar{W}}{\partial\, {}_0^t\varepsilon_{ij}\, \partial\, {}_0^t\varepsilon_{rs}} \tag{2.10}$$

has the following symmetric property [163]:

$${}_0\bar{C}_{ijrs} = {}_0\bar{C}_{rsij} \tag{2.11}$$

For this reason, the displacement-based finite element method produces symmetric element tangent stiffness matrices and the potential based u/p formulation. The equations of motion derived on the basis of u/p formulation are described entirely by the form of the potential. The element force vector and the stiffness matrixes can be derived by the chain differentiation of the potential with respect to the displacement and pressure variables. The key step in the construction of the equations of motion is to properly modify the potential to include the pressure variable [164].

The application of the principle of virtual displacements to a typical element, yields the general governing equation in the variational form as described in [164]:

$$\delta\{ \int_{{}^0V} W d\,{}^0V \} = {}^tR \tag{2.12}$$

where ${}^tR$ describes the external virtual work at time t, ${}^0V$ is the reference volume at $t=0$ and W is the total potential energy per unit volume, which is composed of potential energy density attributed to displacement (denoted by ${}_0^t\overline{W}$), and that attributed to both the displacements and the pressures (denoted by ${}_0^tQ$), such that

$$W = {}_0^t\overline{W} + {}_0^tQ \tag{2.13}$$

In the above equation, ${}_0^tQ$ is related to hydrostatic pressures ${}^t\overline{p}$ due to displacements and due to separately-interpolated pressure variables ${}^t\tilde{p}$ in the following manner:

$${}_0^tQ = -\frac{1}{2\,{}_0P({}^t\overline{p})}({}^t\overline{p} - {}^t\tilde{p})^2 \tag{2.14}$$

In the above equation, the displacement and pressure are both treated as finite element field variables, which involve the corresponding interpolations on the basis of their respective nodal values. The operator ${}_0P(\cdot)$ is related to the deformation gradient tensor, the right Cauchy-Green deformation tensor and the Green-Lagrange strain tensor in the following manner:

$$ {}_0P(\cdot) = -\frac{1}{3\det({}_0^tX)}\,{}_0^tC_{mn}\,\frac{\partial(\cdot)}{\partial\,{}_0^t\varepsilon_{mn}} \tag{2.15} $$

where ${}_0^tX$ is the deformation gradient tensor, ${}_0^tC_{mn}$ is the right Cauchy-Green deformation tensor of dimension $m \times n$, and ${}_0^t\varepsilon_{mn}$ is the Green-Lagrange strain tensor.

Equation (2.12) indicates that the variation in the integrated ‘internal stress’ potential must equal the variation in the ‘external loading’ potential. The only admissible variations in the displacement-based finite element analysis are the displacement variations, which are controlled by the nodal point displacements. While in the u/p formulation, the unknown pressure variables are also subject to variations, which are used to generate the constraint equations.

Equation (2.12) and (2.13) yield the following form of the governing equation incorporating the variations in both the pressure and displacement variables:

$$ \delta\left(\int_{{}^0V}({}_0^t\overline{W}+{}_0^tQ)\,d\,{}^0V\right)={}^tR \tag{2.16} $$

2.3.2 Finite Element Matrices Based on TL Formulation

The matrix form of the governing incremental equations of motion for a typical rubber element, can be derived through linearization of the principle of virtual work with respect to the finite element variables as [164]:

$$\begin{bmatrix} {}^{t}KUU & {}^{t}KUP \\ {}^{t}KPU & {}^{t}KPP \end{bmatrix} \begin{bmatrix} \hat{u} \\ \hat{p} \end{bmatrix} = \begin{bmatrix} {}^{t+\Delta t}R \\ 0 \end{bmatrix} - \begin{bmatrix} {}^{t}FU \\ {}^{t}FP \end{bmatrix} \tag{2.17}$$

where ${}^{t+\Delta t}R$ consists of the nodal point forces corresponding to the external loading at time t + Δt, $\hat{u}$ and $\hat{p}$ are displacement and pressure vectors, respectively, which contain the increments in ${}^{t}\hat{u}_k$ and ${}^{t}\hat{p}_k$ (k=1,2,3). Further, the vectors, ${}^{t}FU$ and ${}^{t}FP$, contain the following entries:

$${}^{t}FU_i = \frac{\partial}{\partial {}^{t}\hat{u}_i}\left(\int_{{}^{0}V} {}^{t}_{0}W d^{0}V\right) = \frac{\partial}{\partial {}^{t}\hat{u}_i}\left(\int_{{}^{0}V} \left({}^{t}_{0}\overline{W} + {}^{t}_{0}Q\right) d^{0}V\right) = \frac{\partial}{\partial {}^{t}\hat{u}_i}\left[\int_{{}^{0}V}\left({}^{t}_{0}\overline{W} - \frac{1}{2\,{}_{0}P({}^{t}\overline{p})}\left({}^{t}\overline{p} - {}^{t}\tilde{p}\right)^{2} d^{0}V \right)\right]$$

$${}^{t}FP_i = \frac{\partial}{\partial {}^{t}\hat{p}_i}\left(\int_{{}^{0}V} {}^{t}_{0}W d^{0}V\right) = \frac{\partial}{\partial {}^{t}\hat{p}_i}\left(\int_{{}^{0}V} \left({}^{t}_{0}\overline{W} + {}^{t}_{0}Q\right) d^{0}V\right) = \frac{\partial}{\partial {}^{t}\hat{p}_i}\left[\int_{{}^{0}V}\left({}^{t}_{0}\overline{W} - \frac{1}{2\,{}_{0}P({}^{t}\overline{p})}\left({}^{t}\overline{p} - {}^{t}\tilde{p}\right)^{2} d^{0}V \right)\right]$$

2.18

The element of the stiffness matrix in Equation (2.17), ${}^{t}KUU$, ${}^{t}KUP$, ${}^{t}KPU$, ${}^{t}KPP$, can be determined from [164]:

$${}^{t}KUU_{ij} = \frac{\partial\, {}^{t}FU_i}{\partial\, \hat{u}_j}$$

$${}^{t}KUP_{ij} = \frac{\partial {}^{t}FU_i}{\partial {}^{t}\hat{p}_j} = \frac{\partial {}^{t}FP_j}{\partial {}^{t}\hat{u}_i} = {}^{t}KPU_{ji}$$

$${}^{t}KPP_{ij} = \frac{\partial {}^{t}FP_i}{\partial {}^{t}\hat{p}_j} \tag{2.19}$$

Equation (2.17) reveals that the force vector is partitioned into two parts, one part due to the displacement variations and the other part arising from the pressure variations. Similarly, the stiffness matrix is partitioned into four parts. Using chain differentiation, the components of force vector and stiffness matrix can be written as:

$$ {}^{t}FU_{i} = \frac{\partial}{\partial {}^{t}\hat{u}_{i}} \left(\int_{{}^{0}V} {}^{t}_{0}W d^{0}V \right) = \int_{{}^{0}V} \frac{\partial {}^{t}_{0}W}{\partial {}^{t}\hat{u}_{i}} d^{0}V = \int_{{}^{0}V} \frac{\partial {}^{t}_{0}W}{\partial {}^{t}_{0}\varepsilon_{kl}} \frac{\partial {}^{t}_{0}\varepsilon_{kl}}{\partial {}^{t}\hat{u}_{i}} d^{0}V = \int_{{}^{0}V} {}^{t}_{0}S_{kl} \frac{\partial {}^{t}_{0}\varepsilon_{kl}}{\partial {}^{t}\hat{u}_{i}} d^{0}V $$

$$ {}^{t}FP_{i} = \frac{\partial}{\partial {}^{t}\hat{p}_{i}} \left[\int_{{}^{0}V} \left(-\frac{1}{2\,{}_{0}P({}^{t}\overline{p})} \left({}^{t}\overline{p} - {}^{t}\widetilde{p} \right)^{2} d^{0}V \right) \right] = \int_{{}^{0}V} -{}_{0}CPP({}^{t}\overline{p} - {}^{t}\widetilde{p}) \frac{\partial {}^{t}\widetilde{p}}{\partial {}^{t}\hat{p}_{i}} d^{0}V \qquad (2.20) $$

where ${}_{0}CPP = -\frac{1}{{}_{0}P({}^{t}\overline{p})}$ and ${}_{0}P(\cdot)$ can be computed from Equation (2.15), and

$$ {}^{t}KUU_{ij} = \frac{\partial {}^{t}FU_{i}}{\partial {}^{t}\hat{u}_{j}} = \int_{{}^{0}V} \frac{\partial}{\partial {}^{t}\hat{u}_{j}} \left({}^{t}_{0}S_{kl} \frac{\partial {}^{t}_{0}\varepsilon_{kl}}{\partial {}^{t}\hat{u}_{i}} \right) d^{0}V $$

$$ = \int_{{}^{0}V} {}^{t}_{0}S_{kl} \frac{\partial^{2}\, {}^{t}_{0}\varepsilon_{kl}}{\partial {}^{t}\hat{u}_{i} \partial {}^{t}\hat{u}_{j}} d^{0}V + \int_{{}^{0}V} \frac{\partial {}^{t}_{0}S_{kl}}{\partial {}^{t}\hat{u}_{j}} \frac{\partial {}^{t}_{0}\varepsilon_{kl}}{\partial {}^{t}\hat{u}_{i}} d^{0}V $$

$$ = \int_{{}^{0}V} {}^{t}_{0}S_{kl} \frac{\partial^{2}\, {}^{t}_{0}\varepsilon_{kl}}{\partial {}^{t}\hat{u}_{i} \partial {}^{t}\hat{u}_{j}} d^{0}V + \int_{{}^{0}V} \frac{\partial}{\partial {}^{t}\hat{u}_{j}} \left[\frac{\partial {}^{t}_{0}W}{\partial {}^{t}_{0}\varepsilon_{kl}} \right] \frac{\partial {}^{t}_{0}\varepsilon_{kl}}{\partial {}^{t}\hat{u}_{i}} d^{0}V $$

$$= \int_{{}^0V} {}^{t}_{0}S_{kl} \frac{\partial^2\, {}^{t}_{0}\varepsilon_{kl}}{\partial {}^{t}\hat{u}_i \partial {}^{t}\hat{u}_j} d^0V + \int_{{}^0V} \frac{\partial^2\, {}^{t}_{0}W}{\partial {}^{t}_{0}\varepsilon_{kl} \partial {}^{t}_{0}\varepsilon_{rs}} \frac{\partial {}^{t}_{0}\varepsilon_{rs}}{\partial {}^{t}\hat{u}_j} \frac{\partial {}^{t}_{0}\varepsilon_{kl}}{\partial {}^{t}\hat{u}_i} d^0V$$

$$= \int_{{}^0V} {}^{t}_{0}S_{kl} \frac{\partial^2\, {}^{t}_{0}\varepsilon_{kl}}{\partial {}^{t}\hat{u}_i \partial {}^{t}\hat{u}_j} d^0V + \int_{{}^0V} {}_{0}CUU_{klrs} \frac{\partial {}^{t}_{0}\varepsilon_{rs}}{\partial {}^{t}\hat{u}_j} \frac{\partial {}^{t}_{0}\varepsilon_{kl}}{\partial {}^{t}\hat{u}_i} d^0V \tag{2.21}$$

where

$${}_{0}CUU_{klrs} = \frac{\partial^2\, {}^{t}_{0}W}{\partial {}^{t}_{0}\varepsilon_{kl} \partial {}^{t}_{0}\varepsilon_{rs}} = \frac{\partial^2}{\partial {}^{t}_{0}\varepsilon_{kl} \partial {}^{t}_{0}\varepsilon_{rs}} \left({}^{t}_{0}\overline{W} - \frac{1}{2\,{}_{0}P\left({}^{t}\overline{p}\right)} \left({}^{t}\overline{p} - {}^{t}\tilde{p}\right)^2 \right) \tag{2.22}$$

Note that ${}_{0}\overline{C}_{klrs} = \dfrac{\partial^2\, {}^{t}_{0}\overline{W}}{\partial {}^{t}_{0}\varepsilon_{kl} \partial {}^{t}_{0}\varepsilon_{rs}}$ and the second term in (2.22) can be expanded as:

$$\frac{\partial^2}{\partial {}^{t}_{0}\varepsilon_{kl} \partial {}^{t}_{0}\varepsilon_{rs}} \left(-\frac{1}{2\,{}_{0}P\left({}^{t}\overline{p}\right)} \left({}^{t}\overline{p} - {}^{t}\tilde{p}\right)^2 \right) = \frac{\partial}{\partial {}^{t}_{0}\varepsilon_{rs}} \left[-\frac{\partial}{\partial {}^{t}_{0}\varepsilon_{kl}} \left[\frac{1}{2\,{}_{0}P({}^{t}\overline{p})} ({}^{t}\overline{p} - {}^{t}\tilde{p})^2 \right] \right]$$

$$= \frac{\partial}{\partial {}^{t}_{0}\varepsilon_{rs}} \{ \frac{1}{2\left[{}_{0}P({}^{t}\overline{p})\right]^2} ({}^{t}\overline{p} - {}^{t}\tilde{p})^2 \frac{\partial\left[{}_{0}P({}^{t}\overline{p})\right]}{\partial {}^{t}_{0}\varepsilon_{kl}} - \frac{1}{{}_{0}P({}^{t}\overline{p})} ({}^{t}\overline{p} - {}^{t}\tilde{p}) \frac{\partial {}^{t}\overline{p}}{\partial {}^{t}_{0}\varepsilon_{kl}} \}$$

$$= -\frac{1}{\left[{}_{0}P({}^{t}\overline{p})\right]^3} \frac{\partial\left[{}_{0}P({}^{t}\overline{p})\right]}{\partial {}^{t}_{0}\varepsilon_{rs}} ({}^{t}\overline{p} - {}^{t}\tilde{p})^2 \frac{\partial\left[{}_{0}P({}^{t}\overline{p})\right]}{\partial {}^{t}_{0}\varepsilon_{kl}} + \frac{1}{\left[{}_{0}P({}^{t}\overline{p})\right]^2} ({}^{t}\overline{p} - {}^{t}\tilde{p}) \frac{\partial {}^{t}\overline{p}}{\partial {}^{t}_{0}\varepsilon_{rs}} \frac{\partial\left[{}_{0}P({}^{t}\overline{p})\right]}{\partial {}^{t}_{0}\varepsilon_{kl}}$$

$$+ \frac{1}{2\left[{}_{0}P({}^{t}\overline{p})\right]^2} ({}^{t}\overline{p} - {}^{t}\tilde{p})^2 \frac{\partial^2\left[{}_{0}P({}^{t}\overline{p})\right]}{\partial {}^{t}_{0}\varepsilon_{kl} \partial {}^{t}_{0}\varepsilon_{rs}} + \frac{1}{\left[{}_{0}P({}^{t}\overline{p})\right]^2} \frac{\partial\left[{}_{0}P({}^{t}\overline{p})\right]}{\partial {}^{t}_{0}\varepsilon_{rs}} ({}^{t}\overline{p} - {}^{t}\tilde{p}) \frac{\partial {}^{t}\overline{p}}{\partial {}^{t}_{0}\varepsilon_{kl}}$$

$$-\frac{1}{{}_0P({}^t\bar{p})}\frac{\partial {}^t\bar{p}}{\partial {}_0^t\varepsilon_{rs}}\frac{\partial {}^t\bar{p}}{\partial {}_0^t\varepsilon_{kl}}-\frac{1}{{}_0P({}^t\bar{p})}({}^t\bar{p}-{}^t\tilde{p})\frac{\partial^2\bar{p}}{\partial {}_0^t\varepsilon_{kl}\partial {}_0^t\varepsilon_{rs}}$$

$$={}_0CPP\frac{\partial {}^t\bar{p}}{\partial {}_0^t\varepsilon_{rs}}\frac{\partial {}^t\bar{p}}{\partial {}_0^t\varepsilon_{kl}}+{}_0CPP({}^t\bar{p}-{}^t\tilde{p})\frac{\partial^2\bar{p}}{\partial {}_0^t\varepsilon_{kl}\partial {}_0^t\varepsilon_{rs}}$$

$$+{}_0CPP^2({}^t\bar{p}-{}^t\tilde{p})\left\{\frac{\partial\left[{}_0P({}^t\bar{p})\right]}{\partial {}_0^t\varepsilon_{kl}}\frac{\partial {}^t\bar{p}}{\partial {}_0^t\varepsilon_{rs}}+\frac{\partial {}^t\bar{p}}{\partial {}_0^t\varepsilon_{kl}}\frac{\partial\left[{}_0P({}^t\bar{p})\right]}{\partial {}_0^t\varepsilon_{rs}}\right\}$$

$$+{}_0CPP^3({}^t\bar{p}-{}^t\tilde{p})^2\frac{\partial\left[{}_0P({}^t\bar{p})\right]}{\partial {}_0^t\varepsilon_{kls}}\frac{\partial\left[{}_0P({}^t\bar{p})\right]}{\partial {}_0^t\varepsilon_{rsl}}+\frac{1}{2}{}_0CPP^2({}^t\bar{p}-{}^t\tilde{p})^2\frac{\partial^2\left[{}_0P({}^t\bar{p})\right]}{\partial {}_0^t\varepsilon_{kl}\partial {}_0^t\varepsilon_{rs}}$$

(2.23)

and

$${}_0^tS_{kl}=\frac{\partial {}_0^tW}{\partial {}_0^t\varepsilon_{kl}}=\frac{\partial}{\partial {}_0^t\varepsilon_{kl}}\left({}_0^t\overline{W}-\frac{1}{2{}_0P({}^t\bar{p})}({}^t\bar{p}-{}^t\tilde{p})^2\right)={}_0^t\overline{S}_{kl}-\frac{\partial}{\partial {}_0^t\varepsilon_{kl}}\left[\frac{1}{2{}_0P({}^t\bar{p})}({}^t\bar{p}-{}^t\tilde{p})^2\right]$$

(2.24)

where ${}_0^t\overline{S}_{kl}=\dfrac{\partial {}_0^t\overline{W}}{\partial {}_0^t\varepsilon_{kl}}$ and

$$\frac{\partial}{\partial {}_0^t\varepsilon_{kl}}\left[\frac{-1}{2{}_0P({}^t\bar{p})}({}^t\bar{p}-{}^t\tilde{p})^2\right]=\frac{\partial\left[\frac{-1}{2{}_0P({}^t\bar{p})}({}^t\bar{p}-{}^t\tilde{p})^2\right]}{\partial\left[{}_0P({}^t\bar{p})\right]}\frac{\partial\left[{}_0P({}^t\bar{p})\right]}{\partial {}_0^t\varepsilon_{kl}}+\frac{\partial\left[\frac{-1}{2{}_0P({}^t\bar{p})}({}^t\bar{p}-{}^t\tilde{p})^2\right]}{\partial {}^t\bar{p}}\frac{\partial {}^t\bar{p}}{\partial {}_0^t\varepsilon_{kl}}$$

$$=\frac{1}{2\left[{}_0P({}^t\bar{p})\right]^2}({}^t\bar{p}-{}^t\tilde{p})^2\frac{\partial\left[{}_0P({}^t\bar{p})\right]}{\partial{}_0^t\varepsilon_{kl}}-\frac{1}{{}_0P({}^t\bar{p})}({}^t\bar{p}-{}^t\tilde{p})\frac{\partial{}^t\bar{p}}{\partial{}_0^t\varepsilon_{kl}}$$

$$=\frac{1}{2}{}_0CPP^2({}^t\bar{p}-{}^t\tilde{p})^2\frac{\partial\left[{}_0P({}^t\bar{p})\right]}{\partial{}_0^t\varepsilon_{kl}}+{}_0CPP({}^t\bar{p}-{}^t\tilde{p})\frac{\partial{}^t\bar{p}}{\partial{}_0^t\varepsilon_{kl}}$$

Hence

$${}_0^tS_{kl}={}_0^t\bar{S}_{kl}+{}_0CPP({}^t\bar{p}-{}^t\tilde{p})\frac{\partial{}^t\bar{p}}{\partial{}_0^t\varepsilon_{kl}}+\frac{1}{2}{}_0CPP^2({}^t\bar{p}-{}^t\tilde{p})^2\frac{\partial\left[{}_0P({}^t\bar{p})\right]}{\partial{}_0^t\varepsilon_{kl}} \tag{2.25}$$

$${}^tKUP_{ij}=\frac{\partial{}^tFU_i}{\partial\hat{p}_j}=\int_{{}^0V}\frac{\partial^2{}_0^tW}{\partial\hat{u}_i\partial\hat{p}_j}d^0V=\int_{{}^0V}\frac{\partial}{\partial\hat{p}_j}\left[\frac{\partial{}_0^tW}{\partial{}_0^t\varepsilon_{kl}}\frac{\partial{}_0^t\varepsilon_{kl}}{\partial\hat{u}_i}\right]d^0V$$

$$=\int_{{}^0V}\frac{\partial^2{}_0^tW}{\partial{}_0^t\varepsilon_{kl}\partial{}^t\tilde{p}}\frac{\partial{}^t\tilde{p}}{\partial\hat{p}_j}\frac{\partial{}_0^t\varepsilon_{kl}}{\partial\hat{u}_i}d^0V=\int_{{}^0V}{}_0CUP_{kl}\frac{\partial{}_0^t\varepsilon_{kl}}{\partial\hat{u}_i}\frac{\partial{}^t\tilde{p}}{\partial\hat{p}_j}d^0V \tag{2.26}$$

in which

$${}_0CUP_{kl}=\frac{\partial^2{}_0^tW}{\partial{}_0^t\varepsilon_{kl}\partial{}^t\tilde{p}}=\frac{\partial}{\partial{}_0^t\varepsilon_{kl}}\left\{\frac{\partial}{\partial{}^t\tilde{p}}\left[{}_0^t\bar{W}-\frac{1}{2{}_0P({}^t\bar{p})}({}^t\bar{p}-{}^t\tilde{p})^2\right]\right\}$$

$$=\frac{\partial}{\partial{}_0^t\varepsilon_{kl}}\left\{\frac{\partial}{\partial{}^t\tilde{p}}\left[-\frac{1}{2{}_0P({}^t\bar{p})}({}^t\bar{p}-{}^t\tilde{p})^2\right]\right\}$$

$$
=\frac{\partial}{\partial {}_0^{t}\varepsilon_{kl}}\left\{\frac{1}{{}_0P({}^{t}\overline{p})}({}^{t}\overline{p}-{}^{t}\widetilde{p})\right\}=\frac{\partial\left\{\frac{1}{{}_0P({}^{t}\overline{p})}({}^{t}\overline{p}-{}^{t}\widetilde{p})\right\}}{\partial\left[{}_0P({}^{t}\overline{p})\right]}\frac{\partial\left[{}_0P({}^{t}\overline{p})\right]}{\partial {}_0^{t}\varepsilon_{kl}}+\frac{\partial\left\{\frac{1}{{}_0P({}^{t}\overline{p})}({}^{t}\overline{p}-{}^{t}\widetilde{p})\right\}}{\partial {}^{t}\overline{p}}\frac{\partial {}^{t}\overline{p}}{\partial {}_0^{t}\varepsilon_{kl}}
$$

$$
=-\frac{1}{\left[{}_0P({}^{t}\overline{p})\right]^2}({}^{t}\overline{p}-{}^{t}\widetilde{p})\frac{\partial\left[{}_0P({}^{t}\overline{p})\right]}{\partial {}_0^{t}\varepsilon_{kl}}+\frac{1}{{}_0P({}^{t}\overline{p})}\frac{\partial {}^{t}\overline{p}}{\partial {}_0^{t}\varepsilon_{kl}}
$$

$$
=-{}_0CPP\frac{\partial {}^{t}\overline{p}}{\partial {}_0^{t}\varepsilon_{kl}}-{}_0CPP^2({}^{t}\overline{p}-{}^{t}\widetilde{p})\frac{\partial\left[{}_0P({}^{t}\overline{p})\right]}{\partial {}_0^{t}\varepsilon_{kl}} \tag{2.27}
$$

$$
{}^{t}KPP_{ij}=\frac{\partial {}^{t}FP_i}{\partial \hat{p}_j}=\frac{\partial}{\partial \hat{p}_j}\left\{\frac{\partial}{\partial \hat{p}_i}\left[\int_{{}^0V}{}_0^{t}W d^0V\right]\right\}=\int_{{}^0V}\frac{\partial}{\partial \hat{p}_i}\left[\frac{\partial {}_0^{t}W}{\partial \hat{p}_j}\right]d^0V
$$

$$
=\int_{{}^0V}\frac{\partial}{\partial \hat{p}_i}\left[\frac{\partial {}_0^{t}W}{\partial {}^{t}\widetilde{p}}\frac{\partial {}^{t}\widetilde{p}}{\partial \hat{p}_j}\right]d^0V=\int_{{}^0V}\frac{\partial^2 {}_0^{t}W}{\partial {}^{t}\widetilde{p}^2}\frac{\partial {}^{t}\widetilde{p}}{\partial \hat{p}_i}\frac{\partial {}^{t}\widetilde{p}}{\partial \hat{p}_j}d^0V=\int_{{}^0V}{}_0CPP\frac{\partial {}^{t}\widetilde{p}}{\partial \hat{p}_i}\frac{\partial {}^{t}\widetilde{p}}{\partial \hat{p}_j}d^0V \tag{2.28}
$$

in which

$$
\frac{\partial^2 {}_0^{t}W}{\partial {}^{t}\widetilde{p}^2}=\frac{\partial^2}{\partial {}^{t}\widetilde{p}^2}\left[{}_0^{t}\overline{W}-\frac{1}{2\,{}_0P({}^{t}\overline{p})}({}^{t}\overline{p}-{}^{t}\widetilde{p})^2\right]=-\frac{1}{{}_0P({}^{t}\overline{p})}={}_0CPP \tag{2.29}
$$

When ${}_0P({}^{t}\overline{p})$ is constant (as is the case for common material descriptions), several of the terms in the above equations are zero. The equilibrium is reached when for all the degrees of freedom [163],

$$ {}^{t}R_{i} - \int_{{}^{0}V} {}_{0}^{t}S_{kl} \frac{\partial {}_{0}^{t}\varepsilon_{kl}}{\partial \hat{u}_{i}} d^{0}V = 0 $$

and

$$ \int_{{}^{0}V} {}_{0}CPP({}^{t}\overline{p} - {}^{t}\tilde{p}) \frac{\partial {}^{t}\tilde{p}}{\partial \hat{p}_{i}} d^{0}V = 0 \tag{2.30} $$

2.3.3 Discretization of the Variables

For the purpose of evaluating the elements, ${}^{t}FU_{i}$, ${}^{t}FP_{i}$, ${}^{t}KUU_{ij}$, ${}^{t}KUP_{ij}$ (${}^{t}KPU_{ij}$), *and* ${}^{t}KPP_{ij}$, the change in the Green-Lagrange strain tensor ${}_{0}^{t}\varepsilon_{kl}$ and the interpolated pressure ${}^{t}\tilde{p}$ in terms of the incremental displacement and pressure variables need to be formulated. The displacement and pressure variables for a material point within an element are interpolated as:

$$ {}^{t}u_{i} = h_{L} {}^{t}u_{i}^{L} $$

$$ {}^{t}\tilde{p} = g_{i} {}^{t}\hat{p}_{i} \tag{2.31} $$

where ${}^{t}u_{i}^{L}$ is the displacement at node L of the element along the i^th^ direction and ${}^{t}\hat{p}_{i}$ is the corresponding nodal pressure. Further, h_{L} and g_{i} are the interpolation functions for displacements and pressure, respectively.

For the pressure, it can simply be written as:

$$\frac{\partial {}^t\tilde{p}}{\partial \hat{p}_i} = g_i \tag{2.32}$$

Using the Green-Lagrange strain tensor:

$${}_0^t\varepsilon_{kl} = \frac{1}{2}({}_0^t x_{b,k}\, {}_0^t x_{b,l} - \delta_{kl}) \tag{2.33}$$

where δ_{kl} is the Kronecker delta. The derivatives with respect to the nodal point displacements can be computed as:

$$\frac{\partial\, {}_0^t\varepsilon_{kl}}{\partial {}^t u_i^L} = \frac{1}{2}({}_0^t x_{i,k}\, {}_0 h_{L,l} + {}_0^t x_{i,l}\, {}_0 h_{L,k})$$

$$\frac{\partial^2\, {}_0^t\varepsilon_{kl}}{\partial {}^t u_i^L \partial {}^t u_j^M} = \frac{1}{2}({}_0 h_{L,k}\, {}_0 h_{M,l} + {}_0 h_{L,l}\, {}_0 h_{M,k})\delta_{ij} \tag{2.34}$$

Similarly, using ${}^t\overline{p} = {}_0 P({}_0^t\overline{W})$ with the Mooney-Rivlin material model, the pressure derivatives with respect to the Green-Lagrange strains can be obtained as:

$$\frac{\partial {}^t\overline{p}}{\partial\, {}_0^t\varepsilon_{kl}} = -\kappa\, {}_0^t J_3\, {}_t^0 C_{kl}$$

$$\frac{\partial^{2\,t}\overline{p}}{\partial\, {}_0^t\varepsilon_{kl}\, \partial\, {}_0^t\varepsilon_{rs}} = \kappa\, {}_0^t J_3\, {}_t^0 C_{kl}\, {}_0^t C_{rs} - \kappa({}_0^t J_3)^{-1}(\hat{\varepsilon}_{krc}\hat{\varepsilon}_{lsf} + \hat{\varepsilon}_{ksc}\hat{\varepsilon}_{lrf})\, {}_0^t C_{cf} \tag{2.35}$$

where $\hat{\varepsilon}_{ijk}$ is the permutation tensor and ${}_{t}^{0}C_{kl}$ is the inverse of the right Cauchy-Green deformation tensor ${}_{0}^{t}C_{kl}$. The κ represents the bulk modulus and J_3 is the reduced invariant, whose expression is to be derived in the next section.

2.3.4 Application of Mooney-Rivlin Material Model

The u/p formulations are considered to be well suited for the analysis of rubber materials due to their nearly incompressible response property. The basic ingredient in these formulations is the strain energy density ${}_{0}^{t}W$, which is defined by the specific material model used.

While various forms of the strain energy density function ${}_{0}^{t}W$ are available, one of the commonly used models is the Mooney-Rivlin material description model, which is used to characterize the tread rubber material undergoing large strains. The conventional Mooney-Rivlin material can be expanded as [164]:

$$ {}_{0}^{t}\tilde{W} = C_1({}_{0}^{t}I_1 - 3) + C_2({}_{0}^{t}I_2 - 3); \qquad {}_{0}^{t}I_3 = 1 \tag{2. 36}$$

where C_1 and C_2 are material constants and ${}_{0}^{t}I_i$ are the invariants given in terms of the components of the right Cauchy-Green deformation tensor:

$$ {}_{0}^{t}I_1 = {}_{0}^{t}C_{kk} $$

$$ {}_{0}^{t}I_2 = \frac{1}{2}[({}_{0}^{t}I_1)^2 - {}_{0}^{t}C_{ij}\,{}_{0}^{t}C_{ij}] $$

$$ {}_0^tI_3 = \det {}_0^tC \tag{2. 37} $$

In the above expressions of invariants, the following relations exist:

$$ {}_0^tC = {}_0^tX^T\,{}_0^tX $$

$$ {}_0^tX = {}_0^tR\,{}_0^tU $$

$$ {}_0^tC = {}_0^tX^T\,{}_0^tX = {}_0^tU^T\,{}_0^tR^T\,{}_0^tR\,{}_0^tU = {}_0^tU^T\,{}_0^tU = {}_0^tU\,{}_0^tU \tag{2. 38} $$

where ${}_0^tU$ is a symmetric stretch matrix and ${}_0^tR$ is an orthogonal (rotation) matrix.

In the Mooney-Rivlin model, $2(C_1 + C_2)$ represents the shear modulus and $6(C_1 + C_2)$ represents the Young's modulus when strains are small. In the above-described Mooney-Rivlin material description, it is assumed that the rubber is totally incompressible. A better assumption is that the bulk modulus is several thousand times as large as the shear modulus, which means that the material is almost or nearly incompressible. This assumption is realized by eliminating the restriction, ${}_0^tI_3 = 1$, and including a hydrostatic work term in the strain energy function to obtain:

$$ {}_0^t\tilde{\tilde{W}} = C_1({}_0^tI_1 - 3) + C_2({}_0^tI_2 - 3) + W_H({}_0^tI_3) \tag{2. 39} $$

The material description, however, cannot be applied directly, since all of the three terms in the above equation contribute to the pressure, such that:

$$'\overline{p} = C_{1\,0}P({}_0^tI_1) + C_{2\,0}P({}_0^tI_2) + {}_0P(W_H({}_0^tI_3)) \tag{2.40}$$

Particularly, the terms ${}_0P^2({}_0P({}_0^tI_1))$ and ${}_0P^2({}_0P({}_0^tI_2))$ are nonzero, since they are sensitive to the magnitude of the volume ratio. In order to obtain an appropriate expression to circumvent this problem, the reduced invariants are introduced:

$$\begin{aligned}
{}_0^tJ_1 &= {}_0^tI_1({}_0^tI_3)^{-1/3} \\
{}_0^tJ_2 &= {}_0^tI_2({}_0^tI_3)^{-2/3} \\
{}_0^tJ_3 &= ({}_0^tI_3)^{1/2} = (\det{}_0^tC)^{1/2} = \det{}_0^tX
\end{aligned} \tag{2.41}$$

The invariants ${}_0^tJ_1$ and ${}_0^tJ_2$ in Equation (2. 41) are insensitive to the magnitude of the volume ratio. The terms ${}_0P({}_0^tJ_1)$ and ${}_0P({}_0^tJ_2)$ are thus considered as zero. Using the $\det{}_0^tX$ than $\det{}_0^tC$, the strain energy density can be expanded as:

$${}_0^tW = C_1({}_0^tJ_1 - 3) + C_2({}_0^tJ_2 - 3) + W_H({}_0^tJ_3) \tag{2.42}$$

In the above expression, W_H has to satisfy the material restriction as in the following:

$${}_0P^2('\overline{p}) = \frac{d^{2\,\prime}\overline{p}}{d(\det{}_0^tX)} = 0 \quad or \quad \frac{d^3W_H({}_0^tJ_3)}{d(\det{}_0^tX)^3} = 0 \tag{2.43}$$

Equation (2.43) indicates that ${}^{t}\overline{p}$ depends only on ${}_{0}^{t}J_{3}$ and can be further derived as [163]:

$$ {}^{t}\overline{p} = -\kappa(\det{}_{0}^{t}X - 1) = -\kappa({}_{0}^{t}J_{3} - 1) \tag{2.44} $$

and

$$ {}_{0}P({}^{t}\overline{p}) = -\frac{d({}^{t}\overline{p})}{d(\det{}_{0}^{t}X)} = \kappa \tag{2.45} $$

Considering the potential energy attributed to the hydrostatic pressure $W_{H} = {}_{0}^{t}Q$ and the Equation (2.14), the differential form of the total strain energy density can be described as:

$$ d{}_{0}^{t}W = dW_{H} = -{}^{t}\overline{p}[d(\det{}_{0}^{t}X)] \tag{2.46} $$

$$ \begin{aligned} W_{H} &= -\int {}^{t}\overline{p}[d(\det{}_{0}^{t}X)] = -\int -\kappa[\det{}_{0}^{t}X - 1]d(\det{}_{0}^{t}X) \\ &= \frac{1}{2}\kappa(\det{}_{0}^{t}X - 1)^{2} = \frac{1}{2}\kappa({}_{0}^{t}J_{3} - 1)^{2} \end{aligned} \tag{2.47} $$

where κ represents the bulk modulus.

The stresses computed from displacements, corresponding to the strain energy density, are derived using the following equation:

$$ {}_0^t\overline{S}_{kl} = \frac{1}{2}\left(\frac{\partial_0^t W}{\partial_0^t \varepsilon_{kl}} + \frac{\partial_0^t W}{\partial_0^t \varepsilon_{lk}} \right) \tag{2.48} $$

Moreover, the constitutive tensor is computed using

$$ {}_0^t\overline{C}_{klrs} = \frac{1}{2}\left(\frac{\partial_0^t\overline{S}_{kl}}{\partial_0^t \varepsilon_{rs}} + \frac{\partial_0^t\overline{S}_{kl}}{\partial_0^t \varepsilon_{sr}} \right) \tag{2.49} $$

The use of the operator $\frac{1}{2}\left(\frac{\partial(\cdot)}{\partial_0^t \varepsilon_{ij}} + \frac{\partial(\cdot)}{\partial_0^t \varepsilon_{ji}} \right)$ instead of $\frac{\partial(\cdot)}{\partial_0^t \varepsilon_{ij}}$ is consistent with the fact that ${}_0^t\varepsilon_{ij}$ is a symmetric tensor and ensures that ${}_0^t\overline{S}_{ij}$ and ${}_0^t\overline{C}_{ijrs}$ have the correct symmetries. Since this operator is frequently used in the subsequent derivations, the following abbreviated notations are introduced:

$$ (\cdot)^{\bullet}_{ij} = \frac{1}{2}\left(\frac{\partial(\cdot)}{\partial_0^t \varepsilon_{ij}} + \frac{\partial(\cdot)}{\partial_0^t \varepsilon_{ji}} \right) \tag{2.50} $$

Using the relationship, ${}_0^t\varepsilon_{ij} = \frac{1}{2}({}_0^tC_{ij} - \delta_{ij})$, the above expression can also be rewritten as

$$ (\cdot)^{\bullet}_{ij} = \frac{\partial(\cdot)}{\partial_0^t C_{ij}} + \frac{\partial(\cdot)}{\partial_0^t C_{ji}} \tag{2.51} $$

It is noted that the operator $(\cdot)^{\bullet}_{ij}$ is a linear operator and may be manipulated using the rules of the chain differentiation.

Applying the operator (2. 51) to Equation (2. 42), yields following expression for the strain energy density:

$$ {}^{t}_{0}W = C_1({}^{t}_{0}J_1 - 3) + C_2({}^{t}_{0}J_2 - 3) + \frac{1}{2}k({}^{t}_{0}J_3 - 1)^2 \qquad (2.\ 52) $$

The above equation results in following expression for the stresses:

$$ {}^{t}_{0}\overline{S}_{ij} = ({}^{t}_{0}W)^{\bullet}_{ij} = C_1({}^{t}_{0}J_1)^{\bullet}_{ij} + C_2({}^{t}_{0}J_2)^{\bullet}_{ij} + k({}^{t}_{0}J_3 - 1)({}^{t}_{0}J_3)^{\bullet}_{ij} \qquad (2.\ 53) $$

where

$$ ({}^{t}_{0}J_1)^{\bullet}_{ij} = ({}^{t}_{0}I_3)^{-1/3}({}^{t}_{0}I_1)^{\bullet}_{ij} - \frac{1}{3}({}^{t}_{0}I_1)({}^{t}_{0}I_3)^{-4/3}({}^{t}_{0}I_3)^{\bullet}_{ij} $$

$$ ({}^{t}_{0}J_2)^{\bullet}_{ij} = ({}^{t}_{0}I_3)^{-2/3}({}^{t}_{0}I_2)^{\bullet}_{ij} - \frac{2}{3}({}^{t}_{0}I_2)({}^{t}_{0}I_3)^{-5/3}({}^{t}_{0}I_3)^{\bullet}_{ij} $$

$$ ({}^{t}_{0}J_3)^{\bullet}_{ij} = \frac{1}{2}({}^{t}_{0}I_3)^{-1/2}({}^{t}_{0}I_3)^{\bullet}_{ij} \qquad (2.\ 54) $$

Recalling the invariants described in Equation (2.37):

$$ {}^{t}_{0}I_1 = {}^{t}_{0}C_{kk}; \qquad {}^{t}_{0}I_2 = \frac{1}{2}[({}^{t}_{0}I_1)^2 - {}^{t}_{0}C_{ij}\,{}^{t}_{0}C_{ji}]; \qquad {}^{t}_{0}I_3 = \det{}^{t}_{0}C $$

The terms in right side of the Equations (2.54) can be expanded in the following manner:

$$({}^t_0 I_1)^{\bullet}_{ij} = 2\delta_{ij}$$

$$({}^t_0 I_2)^{\bullet}_{ij} = 2\,{}^t_0 I_1 \delta_{ij} - ({}^t_0 C_{ij} + {}^t_0 C_{ji})$$

$$({}^t_0 I_3)^{\bullet}_{ij} = [\det {}^t_0 C]^{\bullet}_{ij} = ({}^0_t C_{ij} + {}^0_t C_{ji}) \det {}^t_0 \tilde{C} \tag{2.55}$$

where

$${}^0_t C_{ij} = ({}^t_0 C_{ij})^{-1} \tag{2.56}$$

For the purpose of further consideration of ${}^t_0 C_{ij}$, the derivative law of a determinant is used. The derivative D' of a determinant D of order n whose entries are differentiable functions, can be written as [165]:

$$D' = D_{(1)} + D_{(2)} + \cdots + D_{(n)} \tag{2.57}$$

where $D_{(j)}$ is obtained from D by differentiating the entries in the j-th row.

For a third-order determinant C, it can be written that

$$\frac{\partial(\det C)}{\partial C_{ij}} = \frac{\partial}{\partial C_{ij}} \begin{vmatrix} C_{11} & C_{12} & C_{13} \\ C_{21} & C_{22} & C_{23} \\ C_{31} & C_{32} & C_{33} \end{vmatrix}$$

$$=\begin{vmatrix} \frac{\partial C_{11}}{\partial C_{ij}} & \frac{\partial C_{12}}{\partial C_{ij}} & \frac{\partial C_{13}}{\partial C_{ij}} \\ C_{21} & C_{22} & C_{23} \\ C_{31} & C_{32} & C_{33} \end{vmatrix} + \begin{vmatrix} C_{11} & C_{12} & C_{13} \\ \frac{\partial C_{21}}{\partial C_{ij}} & \frac{\partial C_{22}}{\partial C_{ij}} & \frac{\partial C_{23}}{\partial C_{ij}} \\ C_{31} & C_{32} & C_{33} \end{vmatrix} + \begin{vmatrix} C_{11} & C_{12} & C_{13} \\ C_{21} & C_{22} & C_{23} \\ \frac{\partial C_{31}}{\partial C_{ij}} & \frac{\partial C_{32}}{\partial C_{ij}} & \frac{\partial C_{33}}{\partial C_{ij}} \end{vmatrix} \qquad (2.58)$$

In the above expressions, two of the three determinants in the right hand side will be zero, and the remaining determinant consists of a row containing only one non-zero term, which is equal to 1. Introducing the notation $\tilde{C}$, which is defined as the matrix obtained from C with all its elements in the i$^{\text{th}}$ row except C_{ij} being zeros, it can be written as:

$$\frac{\partial(\det C)}{\partial C_{ij}} = \frac{1}{C_{ij}} \det \tilde{C} \qquad (2.59)$$

The above equation verifies the Equation (2.55) for the invariant $({}_0^tI_3)_{ij}^{\bullet}$.

The constitutive tensor is derived upon applying the operator in Equation (2.51), such that:

$$\begin{aligned} {}_0\overline{C}_{ijrs} &= ({}_0^t\overline{S}_{ij})_{rs}^{\bullet} = C_1(({}_0^tJ_1)_{ij}^{\bullet})_{rs}^{\bullet} + C_2(({}_0^tJ_2)_{ij}^{\bullet})_{rs}^{\bullet} + k[({}_0^tJ_3)_{rs}^{\bullet}({}_0^tJ_3)_{ij}^{\bullet} + ({}_0^tJ_3 - 1)(({}_0^tJ_3)_{ij}^{\bullet})_{rs}^{\bullet} \\ &= C_1({}_0^tJ_1)_{ijrs}^{\bullet\bullet} + C_2({}_0^tJ_2)_{ijrs}^{\bullet\bullet} + k[({}_0^tJ_3)_{rs}^{\bullet}({}_0^tJ_3)_{ij}^{\bullet} + ({}_0^tJ_3 - 1)({}_0^tJ_3)_{ijrs}^{\bullet\bullet} \end{aligned} \qquad (2.60)$$

where

$$({}_0^tJ_1)^{**}_{ijrs} = ({}_0^tI_3)^{-1/3}({}_0^tI_1)^{**}_{ijrs} - \frac{1}{3}({}_0^tI_3)^{-4/3}[({}_0^tI_1)^{*}_{ij}({}_0^tI_3)^{*}_{rs} + ({}_0^tI_1)^{*}_{rs}({}_0^tI_3)^{*}_{ij} + ({}_0^tI_1)({}_0^tI_3)^{**}_{ijrs}]$$
$$+\frac{4}{9}({}_0^tI_1)({}_0^tI_3)^{-7/3}({}_0^tI_3)^{*}_{ij}({}_0^tI_3)^{*}_{rs}$$

$$({}_0^tJ_2)^{**}_{ijrs} = ({}_0^tI_3)^{-2/3}({}_0^tI_2)^{**}_{ijrs} - \frac{2}{3}({}_0^tI_3)^{-5/3}[({}_0^tI_2)^{*}_{ij}({}_0^tI_3)^{*}_{rs} + ({}_0^tI_2)^{*}_{rs}({}_0^tI_3)^{*}_{ij} + ({}_0^tI_2)({}_0^tI_3)^{**}_{ijrs}]$$
$$+\frac{10}{9}({}_0^tI_2)({}_0^tI_3)^{-8/3}({}_0^tI_3)^{*}_{ij}({}_0^tI_3)^{*}_{rs}$$
$$({}_0^tJ_3)^{**}_{ijrs} = -\frac{1}{4}({}_0^tI_3)^{-3/2}({}_0^tI_3)^{*}_{ij}({}_0^tI_3)^{*}_{rs} + \frac{1}{2}({}_0^tI_3)^{-1/2}({}_0^tI_3)^{**}_{ijrs} \tag{2.61}$$

and

$$({}_0^tI_1)^{**}_{ijrs} = 0$$
$$({}_0^tI_2)^{**}_{ijrs} = 4\delta_{ij}\delta_{rs} - 2(\delta_{ir}\delta_{js} + \delta_{is}\delta_{jr})$$
$$({}_0^tI_3)^{**}_{ijrs} = [\hat{\varepsilon}_{irc}\hat{\varepsilon}_{jsf} + \hat{\varepsilon}_{isc}\hat{\varepsilon}_{jrf} + \hat{\varepsilon}_{jrc}\hat{\varepsilon}_{isf} + \hat{\varepsilon}_{jsc}\hat{\varepsilon}_{irf}]\,{}_0^t\overline{C}_{cf} \tag{2.62}$$

The pressure derivatives required in the u/p formulation are derived through chain differentiation:

$$\frac{\partial^t\overline{p}}{\partial_0^t\varepsilon_{kl}} = -k\,{}_0^tJ_3\,{}_t^0C_{kl}$$
$$\frac{\partial^{2\,t}\overline{p}}{\partial_0^t\varepsilon_{kl}\partial_0^t\varepsilon_{rs}} = k\,{}_0^tJ_3\,{}_t^0C_{kl}\,{}_0^tC_{rs} - k({}_0^tJ_3)^{-1}(\hat{\varepsilon}_{krc}\hat{\varepsilon}_{lsf} + \hat{\varepsilon}_{ksc}\hat{\varepsilon}_{lrf})\,{}_0^tC_{cf} \tag{2.63}$$

where $\hat{\varepsilon}_{ijk}$ is the permutation tensor and ${}_{t}^{0}C_{kl}$ is the inverse of the right Cauchy-Green deformation tensor ${}_{0}^{t}C_{kl}$.

2.3.5 Solutions for the Incremental Analysis

The objective of the analysis is to obtain displacement and pressure variables, such that the right-hand-side of Equation (2.17) is identically zero. The Newton-Raphson scheme can be employed in an iterative manner to solve the global Equation (2.17). Assuming continuous pressure between elements and omitting the left subscripts for simplicity, Equation (2.17) can be rewritten as:

$$\begin{aligned}[KUU]\hat{u}+[KUP]\hat{p}&=R-FU\\ [KUP]^{T}\hat{u}+[KPP]\hat{p}&=0-FP\end{aligned} \tag{2.64}$$

The solution of the above equation yields:

$$\begin{aligned}\hat{p}&=[KPP]^{-1}(-FP-[KUP]^{T}\hat{u})\\ [K]\hat{u}&=R-F\end{aligned} \tag{2.65}$$

where

$$\begin{aligned}[K]&=[KUU]-[KUP][KPP]^{-1}[KUP]^{T}\\ F&=FU-[KUP][KPP]^{-1}FP\end{aligned} \tag{2.66}$$

The Equations (2.65) and (2.66) can be solved using the Gauss elimination method to derive the element stiffness matrix [K] and the force vector **F**, which can then be assembled into the global stiffness matrix and force vector. Once the global set of equations has been solved, the displacement incremental field $\hat{u}$ is known and the pressure incremental field $\hat{p}$ can be obtained at the element level using Equation (2.65).

2.4 SUMMARY

The fundamental concepts and governing equations for the linear isotropic materials are presented to form a theoretical basis for the subsequent nonlinear incremental analysis. A general formulation for the nearly incompressible rubber material is derived based on the mixed interpolation of the displacement and pressure variables. The finite element matrices composing the global equations for a rubber element, and the required incremental form of the interpolated displacement and pressure variables are then derived using the Total Lagrangian formulation. A detailed u/p nonlinear formulation, using the Mooney-Rivlin material model, is further derived for the implementation of the nonlinear incremental analysis. Finally, the procedure for obtaining the iterative solutions from the global equations is described. The u/p formulations derived on the basis of the Mooney-Rivlin material model in this chapter are used to generate the finite element matrices for the hyper-elastic element, used to represent the rubber tread block and the rubber layers in the subsequent development of the nonlinear finite element tire model.

CHAPTER 3 MODELING AND INCREMENTAL ANALYSIS OF A TRUCK TIRE

3.1 INTRODUCTION

The ride, handling, braking and directional performance characteristics of road vehicles are directly related to the tire-road interactions, and the static and dynamic response of the tires. The early tire models generally involved either the membrane analysis or considered the tread as a pressed string, while the sidewalls were considered as elastic foundation supporting the tread [8]. Other studies modeled the tire as a ring so as to incorporate the tread bending [3]. More elaborate models were developed by considering the tire as a sandwich structure whose core resisted the deformations in shear, while the outer layers resisted the deformation in bending [5]. Wang *et al.* [127] introduced the Moire method to carry out an in-plane strain and displacement analysis from the experimental stress-strain data obtained for the tread and the belt regions.

A large number of FE based tire models have been proposed during the past few years to study various structural aspects of the tires, which include interlayer deformations and stresses, fiber forces, interlayer shear forces, etc. [4]. The majority of the reported FE tire models, however, are mainly based on linear analysis of the multi-layered system, assuming small deformations of the layers and negligible shear interactions between the anisotropic layers. Only a limited number of nonlinear FE tire models, reported in the literature, consider the thickness of the individual rubber layers, while the fiber layers are considered only as membranes to facilitate the large nonlinear deformation analysis of the nearly incompressible rubber layers [126]. Such studies thus do not consider the interactions between the individual anisotropic fiber layers. Nemeth *et al.* [126] described the use of a software package comprising FE models for design purposes, which incorporated volume element modeling of the rubber layers and membrane element modeling of the fiber layers. The large shear deformations of the fiber layers thus could not be considered. The analysis of the shear stresses developed between the fiber layers necessitates the consideration of nonlinear analysis of such layers of finite thickness. Moreover, the reported studies are mostly concerned with car tires and very few of them are related to heavy duty truck tires. The dimensional geometry, material properties of each layer, and especially, the loading conditions of truck tires, are quite different from those of the car tires.

In this chapter, a detailed and efficient nonlinear FE model of a truck tire is developed to predict the three-dimensional (3-D) stress, strain and deformation fields as functions of the inflation pressure and the normal loads acting on the tire. The tire model is developed considering the nearly incompressible property of the tread rubber block, and large magnitude and nonlinear deformations of the multi-layered system under the tread. The model thus permits the analysis of shear interactions between the belts and the carcass layers.

3.2 DEVELOPMENT OF THE FINITE ELEMENT TIRE MODEL

A tire structure comprises of composite layers of different materials and exhibits strongly nonlinear deformation characteristics. The development of an effective and reliable tire model thus essentially involves consideration of the nearly incompressible material property of the tread rubber block and the anisotrpic material properties of each layer. The model should also consider the orientation and geometry of the high modulus cords in the individual layers, stacking sequence of different layers and nonlinear analysis of the multiple layers in order to predict the inter-ply interactions.

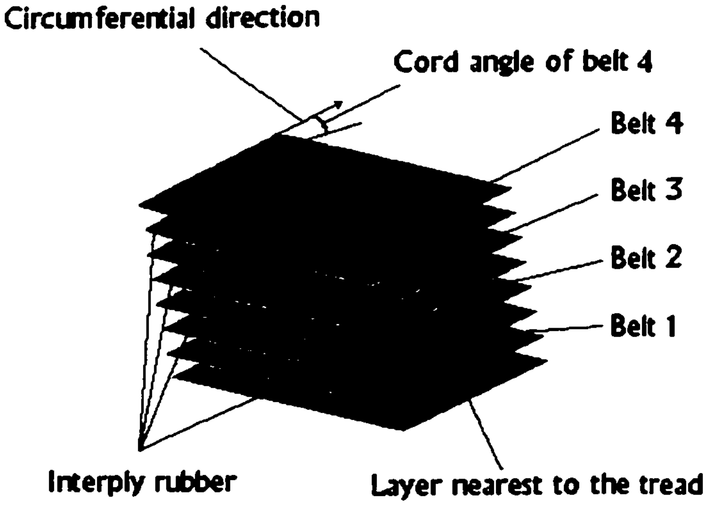

(a)

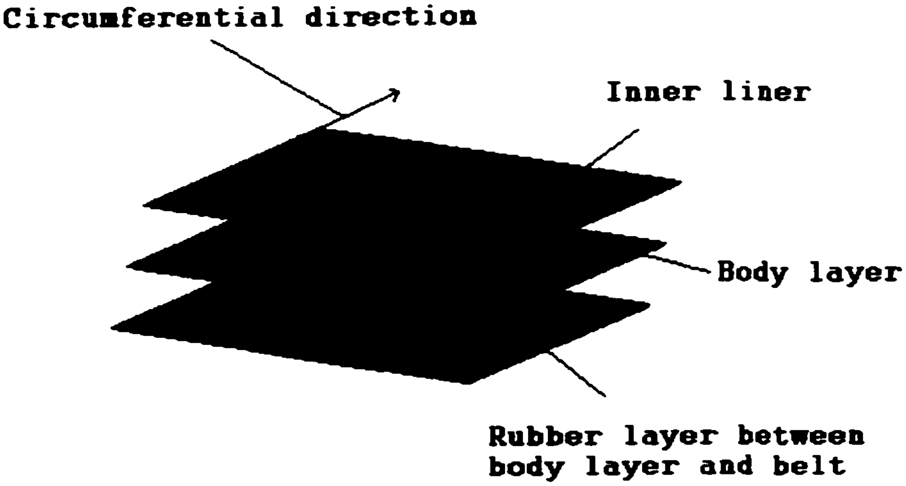

(b)

Figure 3.1: The stacking sequence of the layers in (a) the belts, and (b) the carcass.

A radial truck tire with four circumferential ribs, one steel cord carcass layer and four steel belts in the crown area, is considered for the model development. Figure 3.1 illustrates a schematic of the stacking sequence of the belts and the carcass layers. The cord angles relative to the circumferential direction in the belts beginning from the one nearest to the body ply are assumed as –22°, +22°, –22°, +22° respectively. The thickness of the belt is considered to be approximately two times the steel cord diameter. The inter-ply rubber layers represent the isotropic rubber medium between the different belts, and between the belt and the body layer. The tire model is developed using essential features of the tire structure and cross section geometry, such as the number of belts and carcass layers, tread geometry, section height and width, thickness of the layers, number of cords and cord angles. The bead and end effects of the belts are neglected in order to derive a more efficient model with reasonable demand on the computer run time.

The finite element model of the entire tire structure is developed by performing the meshing of the tire cross-section, as shown in Figure 3.2(a). The finite element representation of the rubber and the layer elements in the tire cross-section is illustrated in Figure 3.2(b). Figure 3.2(c) illustrates the isometric view of the finite element model of the tire developed using ANSYS®. The isometric view of the layered elements, and the amplified rubber element and the layers in the layer elements representing the belts and carcass used in the development of the finite element tire model, are shown in Figure 3.3.

The belts and carcass layers are composed of different orthotropic materials and further, the principal directions of each layer may be oriented differently. Such layers of different materials can be conveniently modeled using the layered elements, SOLID46, as illustrated in Figure 3.3, which is readily available within the ANSYS® element library [166].

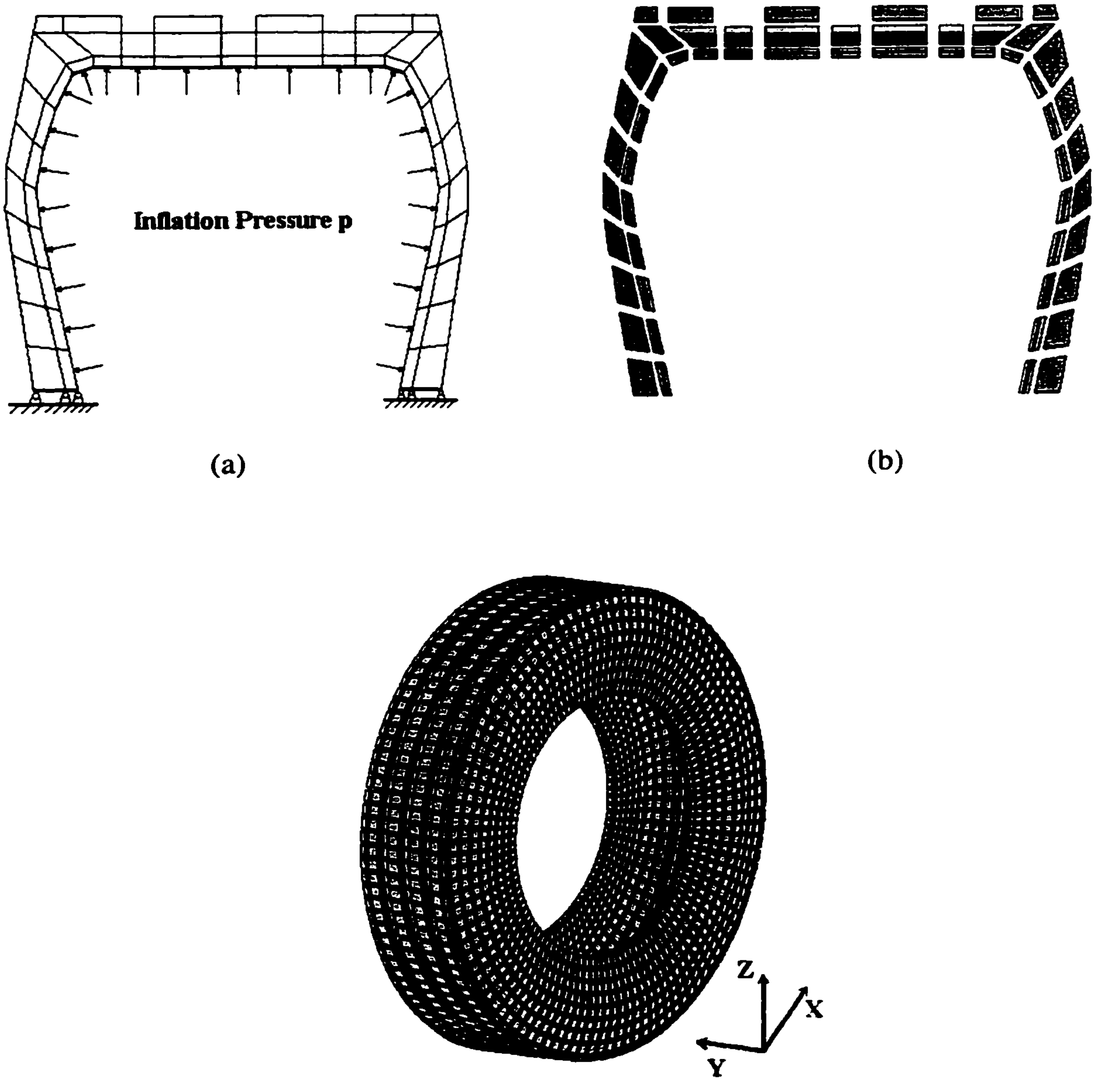

(a) (b)

(c)

Figure 3.2: (a) Meshing of the cross section; (b) finite element representation of the cross section by the rubber elements and the layer elements; and (c) isometric view of the finite element model of the tire using ANSYS®.

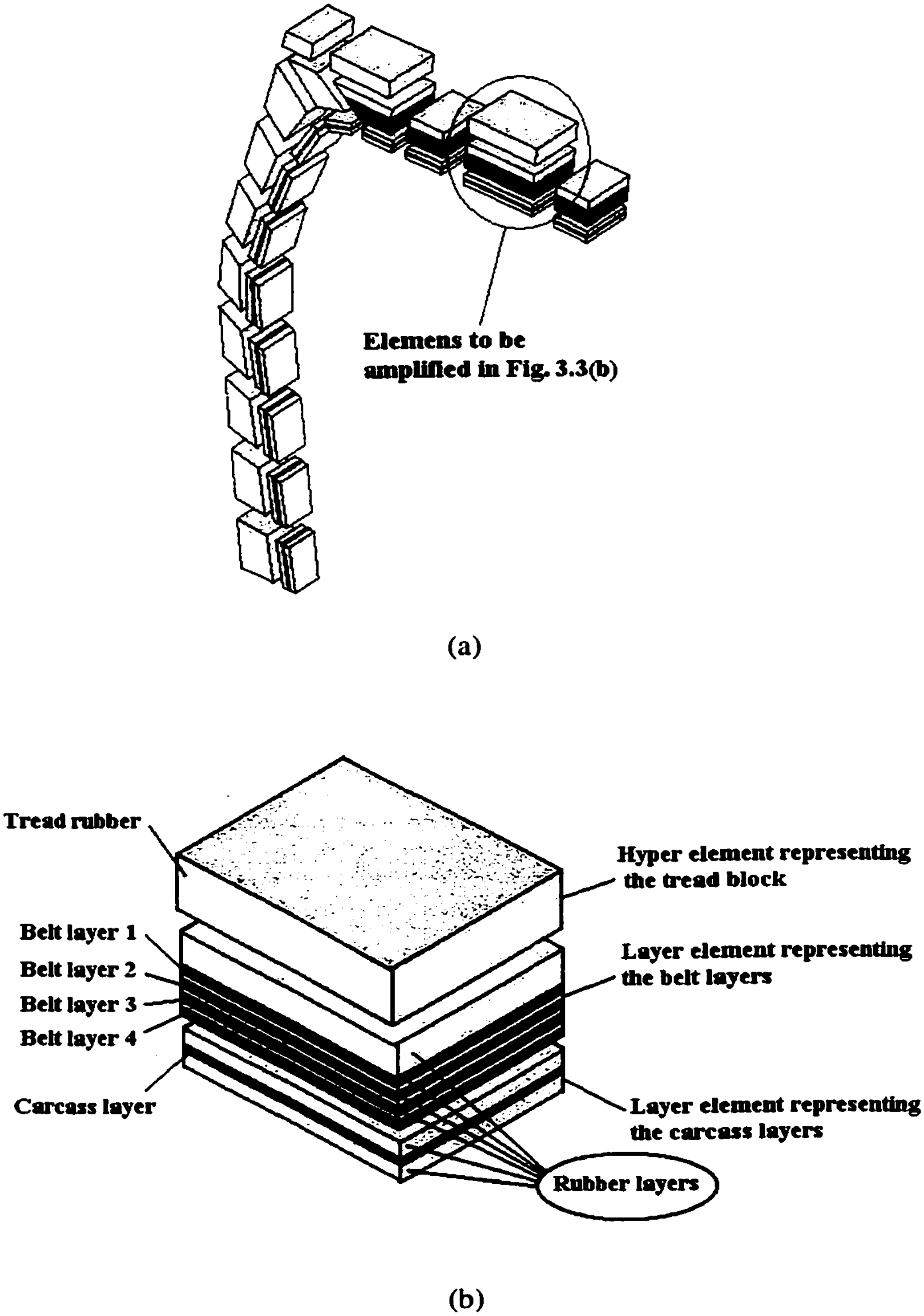

Figure 3.3: (a) Finite element representation of the rubber and layered elements; and (b) an amplified rubber element and the layer elements in the crown area through thickness direction.

The SOLID46 element is designed to model layered thickness shells or solids and is thus employed to model the multi-layered belt and the sidewalls. The element can appropriately model the nonlinearities, such as large deflections and stress stiffening effects. Moreover, the element allows up to 250 different material layers through the element thickness and hence plays an important role in reducing the total number of elements employed in the development of the tire model. The use of the layered elements, however, necessitates the identification of the material properties, fiber layer (cord) orientation, layer thickness, etc. The choice of this element further allows for the analysis of inter-ply shear stresses through the thickness direction of the layers.

The element SOLID46, illustrated in Figure 3.4, is defined by eight nodes, layer thickness, layer material direction angles, and orthotropic material properties. The element possesses three-degree-of-freedoms at each node: translations along the nodal x, y and z directions. The element has an effective stiffness in the transverse direction such that the non-zero inter-laminar shear stresses, strains and displacements in the transverse direction can be incorporated.

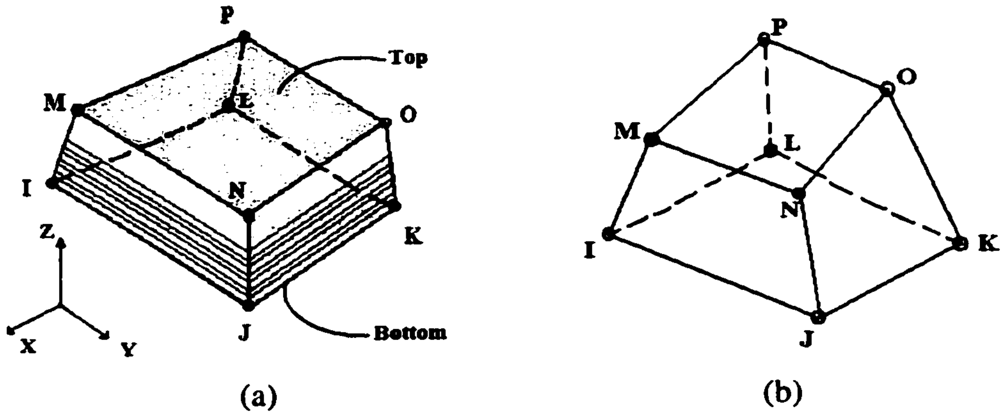

(a) (b)

Figure 3.4: Schematic representations of the 3-D 8-Node elements: (a) layered element; and (b) hyper-elastic element.

The input of the SOLID46 element may be in matrix form or layer form. In the matrix form, the matrices must be computed outside of the ANSYS analysis. The thermal strains, the majority of the stresses and the failure criteria, however, are not available with the matrix input. For layered (non-matrix) input, the layer thicknesses are computed by scaling the specified constant thickness inputs to ensure consistent thicknesses between the nodes. Although the failure criteria are defined with the layered input, the node locations may imply that layers are tilted or warped. The SOLID46 element, however, does not permit zero volumes and zero thickness layers or layers tapering down to zero thickness.

To analyze the rubber material that undergoes large strains and displacements with small volume changes in a tire structure, the eight-node hyper-elastic element HYPER58, also available in the ANSYS® element library [166] and shown in Figure 3.4, are used in conjunction with the two-term Moony-Rivlin material model. The HYPER58 element is defined by eight nodes with three degree-of-freedom (d.o.f.) at each node: translations along the nodal x, y and z directions. The element is applicable for nearly incompressible rubber-like materials with arbitrarily large displacements and strains. The hyper-elastic formulation is nonlinear and requires an iterative solution. The finite element stiffness matrices and force vectors relating to the element are formulated using the mixed u/p (displacement/pressure) formulation, as described in Chapter 2. This allows for the formulation of the element matrices to be formed by mixed variational principles with the pressure introduced to enforce the incompressibility constraint. The element input data include eight nodes, the isotropic material properties, and the constants defining the Mooney-Rivlin strain energy function, which is valid for a wide range of nearly incompressible rubber and rubber-like materials, as described in Chapter 2. The temperatures may also be defined as inputs to describe the body loads at the nodes. The thermal effects may also be incorporated by defining the material properties as functions of the temperature. As in the case of the SOLID46 layered element, the zero volume elements are not permitted.

3.3 METHOD OF ANALYSIS

The tire model is developed assuming that the inflated tire is connected or fixed to the rigid rim through common nodes, as shown in Figure 3.5, which is widely adopted in the reported studies on structural modeling of tires [126-127, 167-168]. The tire model is subjected to loading in two sequential steps. The initial loading is caused by the tire inflation pressure, which is assumed to be uniform within the tire. The inflated static tire is then subjected to normal loading through the application of a specified normal deflection at the contact region. Figure 3.5 further illustrates the loading and boundary conditions of the tire model in the vertical-axle plane crossing the center of the contact patch. The friction in the contact patch is considered to be very low, assuming smooth and uniform contacting surface to facilitate the solution process. This assumption is considered to be adequate in the investigation of the stress fields generated in the individual layers of a tire as functions of the loads and structural parameters.

ANSYS® supports both the rigid to flexible and flexible to flexible surface to surface contact elements to solve a contact problem. These contact elements use a "target surface" and a "contact surface" to form a contact pair. The target element TARGE170, a 3-node triangular or 4-node quadrilateral element for the rigid target surface, is designed and used to represent the target surface for the associated contact elements. The contact elements CONTA173, 4-node element available in the ANSYS® element library, are created on the surface of the solid elements, the HYPER58 elements representing the tread of the tire. The target surface is discretized by a set of target segments (TARGE170), which are coupled with their associated contact elements CONTA173. An iterative algorithm is employed to determine the contact surface and elements corresponding to given loading condition.

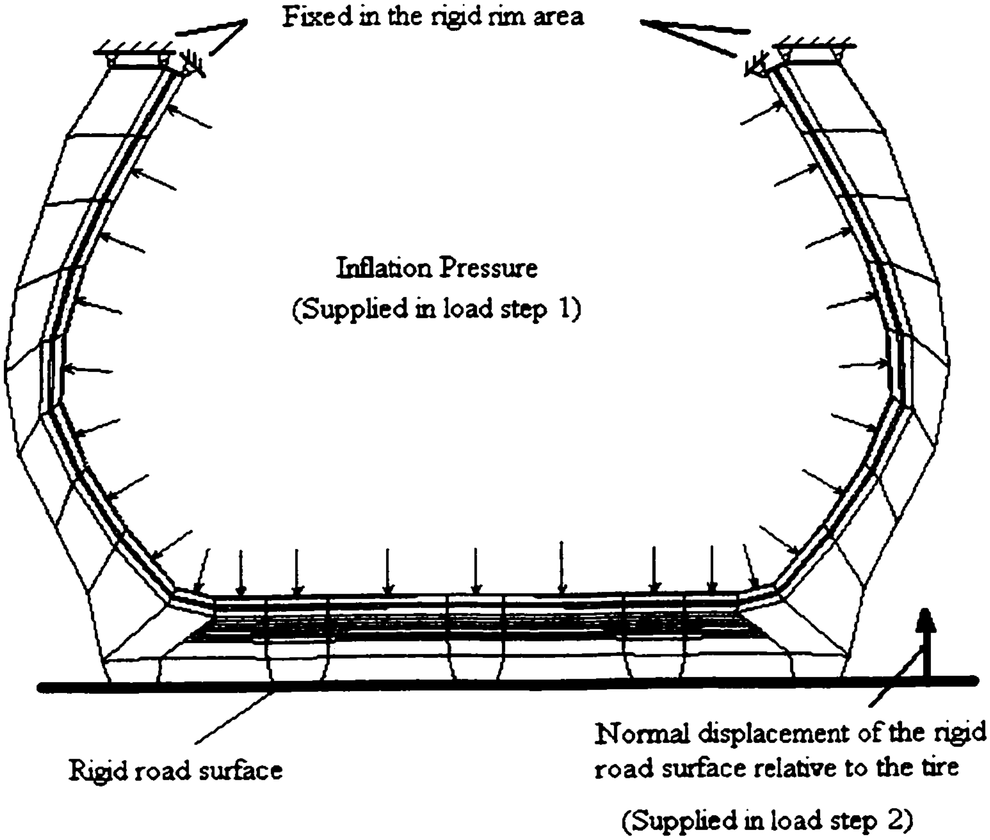

Figure 3.5: Loading and boundary conditions of the finite element tire model in the vertical axle plane crossing the center of the contact patch.

These surface-to-surface elements are well suited for the tire-road contact problem and support large deformations with the various friction models. Moreover, they can be created using the ANSYS® meshing tools on the target and contact surfaces with the TARGE170 and CONTA173 elements, respectively. The finite element model recognizes the possible contact pairs through the presence of the specific contact elements. The node ordering of the target segment elements is a critical task for detection of the contact and defining the target surface. The nodes must be ordered so that the outward normal to the target surface is defined by the right hand rule, pointing to the contact surface. The normal deflection of the tire against the road can be realized and controlled by adjusting the translational displacements of the target surface along the vertical direction, while the rim of the tire is fixed. The material properties of the underlying elements are used to compute an appropriate contact stiffness, while the augmented Lagrangian method is employed to solve the nonlinear contact problem.

3.4 IDENTIFICATION OF MODEL PARAMETERS

The nonlinear finite element tire model is analyzed to study the deformation field, footprint geometry, contact pressure distribution, principal stress field and inter-ply shear stresses. The data related to the tread rubber material properties are estimated from the data reported in the published study [170]. Figure 3.6 illustrates the estimated properties for a single cube element of the tread rubber. The figure describes the estimated experimental stress-strain data for three different deformation modes: (a) uniaxial tension; (b) equibiaxial tension; and (c) pure shear (planar tension), as illustrated in Figure 3.7. The reported properties are considered to calculate the Mooney-Rivlin

constants to formulate the strain energy density for the hyper-elastic element in the finite element tire model.

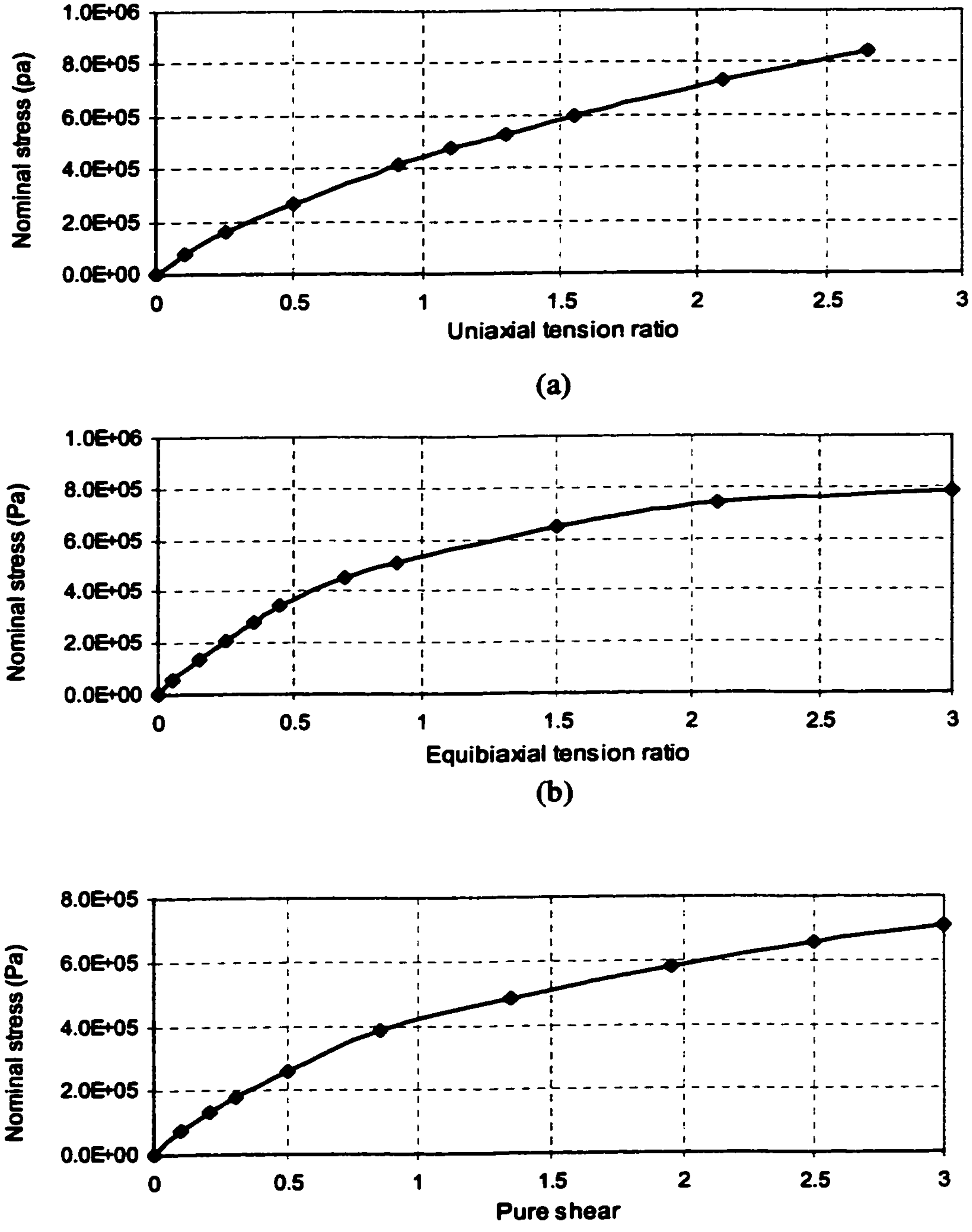

(a)

(b)

(c)

Figure 3.6: Estimated rubber properties based on the reported data: (a) Uniaxial tension, (b) Equibiaxial tension and (c) Pure shear.

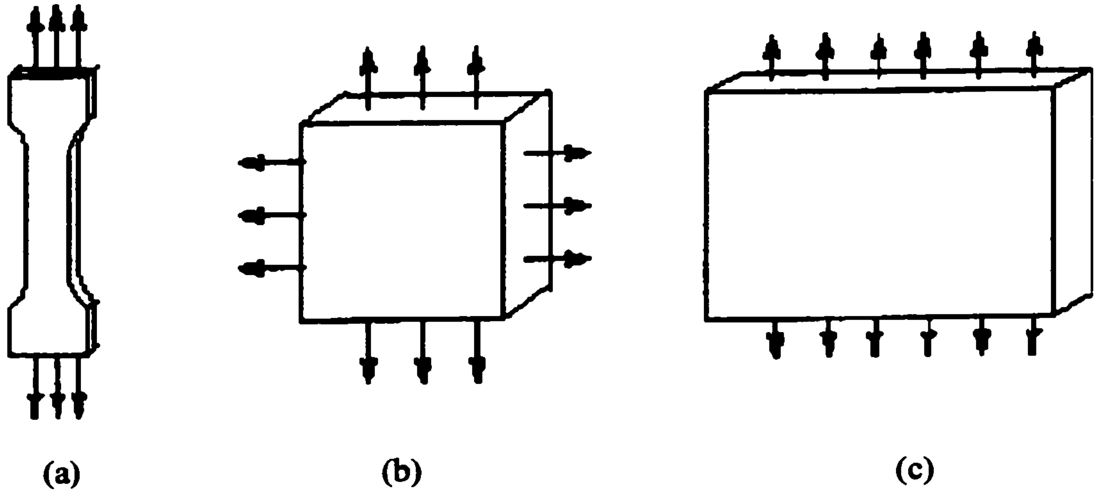

Figure 3.7: Illustration of deformation modes: (a) Uniaxial tension, (b) Equibiaxial tension and (c) Planar tension (Pure shear).

The geometric configuration of the tire was selected from the measurements performed on a 12.5R22.5 truck tire, such as section height and tread depth. The detailed data concerning the geometry of cords in each individual layer are estimated primarily from the reported data [130, 169]. The material properties and constants for the belt and carcass plies are illustrated in Table 3.1 to 3.4. In table 3.1 and 3.2, the layer 1 represents the rubber medium between the belt layer 1 and the tread. The layer 1 in Tables 3.3 and 3.4 refers to the rubber layer between the carcass layer and the belt. The values of Young's modulus, shear modulus and Poison's ratios in principal directions for each individual layers, are estimated using the Halpin-Tsai equations in conjunction with the constants provided in Table 3.5 to 3.7 [130]. The constants describing the composite layers and elastic properties for the rubber and the cords in the layers are derived from the reported data for car tires [129-130, 171]. In view of the estimated material properties, the results derived from the model are considered to describe the tire response in a qualitative manner. The application of the model based on adequately measured material properties of layers in belts and carcass casing are expected to yield a quantitative analysis of a specific tire.

Table 3.1: Estimated material properties and constants for the belt plies

Layer No.	Anisotropic Or Isotropic	Longitudinal Young's modulus E_1 (MPa)	Transverse Young's modulus E_2 (MPa)	Degree of Anisortropy E_1/E_2
1	Isotropic	13.8	13.8	1
2	Anisotropic	13,884	20.2	687
3	Isotropic	13.8	13.8	1
4	Anisotropic	13,884	20.2	687
5	Isotropic	13.8	13.8	1
6	Anisotropic	13,884	20.2	687
7	Isotropic	13.8	13.8	1
8	Anisotropic	13,884	20.2	687

Table 3.2: Estimated material properties and constants for the belt plies

Layer No.	Cords Angle θ (degree)	Shear Modulus G or G_1, G_2, G_3 (MPa)	Poisson's ratio ν or ν_1,ν_2,ν_3	Layer thickness (mm)
1	-	G=4.63	0.49	6
2	22	$G_1=6.03$ $G_2=0.76G_1$ $G_3=G_1$	$\nu_1=0.4645$ $\nu_2=0.42$ $\nu_3=0.4645=\nu_1$	1.5
3	-	G=4.63	0.49	1
4	-22	$G_1=6.03$ $G_2=0.76G_1$ $G_3=G_1$	$\nu_1=0.4645$ $\nu_2=0.42$ $\nu_3=0.4645=\nu_1$	1.5
5	-	G=4.63	0.49	1
6	22	$G_1=6.03$ $G_2=0.76G_1$ $G_3=G_1$	$\nu_1=0.4645$ $\nu_2=0.42$ $\nu_3=0.4645=\nu_1$	1.5
7	-	G=4.63	0.49	1
8	-22	$G_1=6.03$ $G_2=0.76G_1$ $G_3=G_1$	$\nu_1=0.4645$ $\nu_2=0.42$ $\nu_3=0.4645=\nu_1$	1.5

Note: G_1, G_2 and G_3 represent the shear modulus in the belt plane, and transverse planes normal to the cords and along the cords direction, respectively. Similarly, ν_1,ν_2 and ν_3 are the Poison's ratios associated with these planes.

Table 3.3: Estimated material properties and constants for the carcass plies

Layer No.	Anisotropic or isotropic	Longitudinal young's modulus E_1 (MPa)	Transverse Young's modulus E_2 (MPa)	Degree of Anisortropy E_1/ E_2
1	Isotropic	11.04	11.04	1
2	Anisotropic	11,714	15.3	767
3	Isotropic	11.04	11.04	1

Table 3.4: Estimated material properties and constants for the carcass plies

Layer No.	Cords angle (degree)	Shear Modulus G or G_1, G_2, G_3 (MPa)	Poisson's ratio ν or ν_1,ν_2,ν_3	Layer thickness (mm)
1	-	G=3.68	0.49	3
2	90	G_1=4.62 G_2=0.77G_1, G_3=G_1	ν_1=0.4685 ν_2=0.43, ν_3=ν_1	1
3	-	G=3.68	0.49	3

Note: G_1, G_2 and G3 represent the shear moduli in the belt plane, and transverse planes normal to the cords and along the cords direction, respectively. Similarly, ν_1,ν_2 and ν_3 are the Poison's ratios associated with these planes.

Table 3.5: Estimated constants describing the composite layers

	Volume fraction for cords (%)	Radius of Twisted cords (mm)	Cord end count (Ends per centimeter)
Belt Ply	13.4	0.4	4
Body Ply	11.3	0.3	4

Table 3.6: Estimated elastic constants for the rubber in the plies

	Young's Modulus E (MPa)	Shear Modulus G (MPa)	Poisson's Ratio ν	Density ρ (kg/m^3)
Belt Ply	13.8	4.60	0.49	1190
Body Ply	11.04	3.68	0.49	1190

Note: Density of the tread rubber is assumed as 1164 kg/m^3 [172]. The derived densities for the belt and carcass layer are 1910 and 1810 kg/m^3, respectively, which are estimated based on the volume ratios occupied by each component of the individual layers. The Mooney-Rivlin constants for the tread rubber and the outer rubber layer of carcass are assumed as C_1 = 1203786.67 Pa and C_2=2361.69 Pa.

Table 3.7: Estimated elastic constants for the twisted cords in the plies

	Young's Modulus E (MPa)	Shear Modulus G (MPa)	Poisson's Ratio ν
Belt Ply	$1.06*10^5$	$7.59*10^4$	0.30
Body Ply	$1.06*10^5$	$7.59*10^4$	0.30

3.5 DISCUSSION OF MODEL RESULTS

The finite element tire model is analyzed using the ANSYS® software and the results, expressed in terms of deformation, stress and strain fields, and contact pressure distribution, are discussed in the following sections.

3.5.1 Deformation Field and Contact Pressure Distribution

The traction, braking, ride quality and pavement loading characteristics of a vehicle are directly related to the tire deformation and pressure distribution at the tire-road interface. These properties, however, are further related to inflation pressure and various structural properties of the tire. The tire model is thus analyzed to derive the radial deformation field, contact patch geometry and pressure distributions under different inflation pressures, while the normal load is varied by varying the normal static deflection of the non-rolling tire.

Figure 3.8 illustrates the isometric and front views of the deformed tire under an inflation pressure of 621.3 kPa (90 psi) and a normal load that corresponds to the tire deflection, ΔZ=60 mm. Figure 3.9 illustrates the radial deformation fields derived from the model under two different normal loads: F_z=6.1 kN and F_z=17.4 kN. While the maximum radial deformation occurs, as expected, in the lateral centerline of the contact patch, the radial deflection field reveals nonlinear response of the tire with the normal load. The labels 'SMN' and 'SMX' describe the minimum and maximum values of the plotted items, respectively. It should be mentioned here that the coordinate system shown in Figure 3.8 is valid only for the contact patch, in which the Z-axis is vertical to the road surface. The normal deflection and thus the normal load are thus conveniently represented by ΔZ and F_z, respectively.

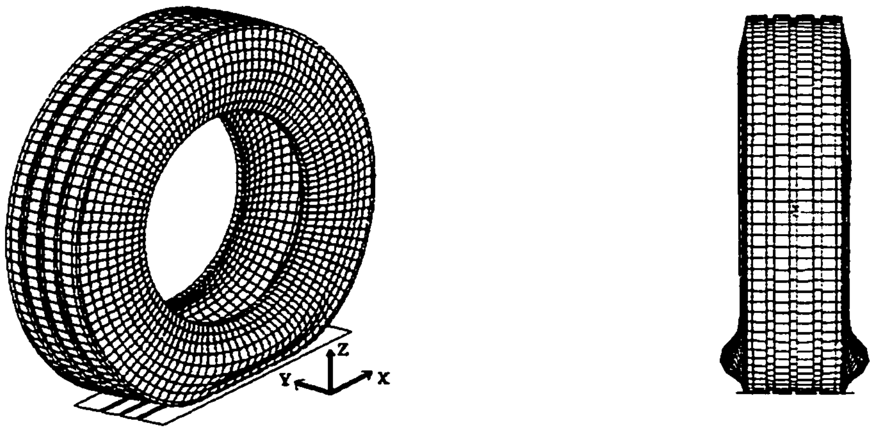

Figure 3.8: Isometric and front views of the statically loaded non-rolling tire. ($\Delta Z = 60$ mm; $p_i = 621.3$ kPa)

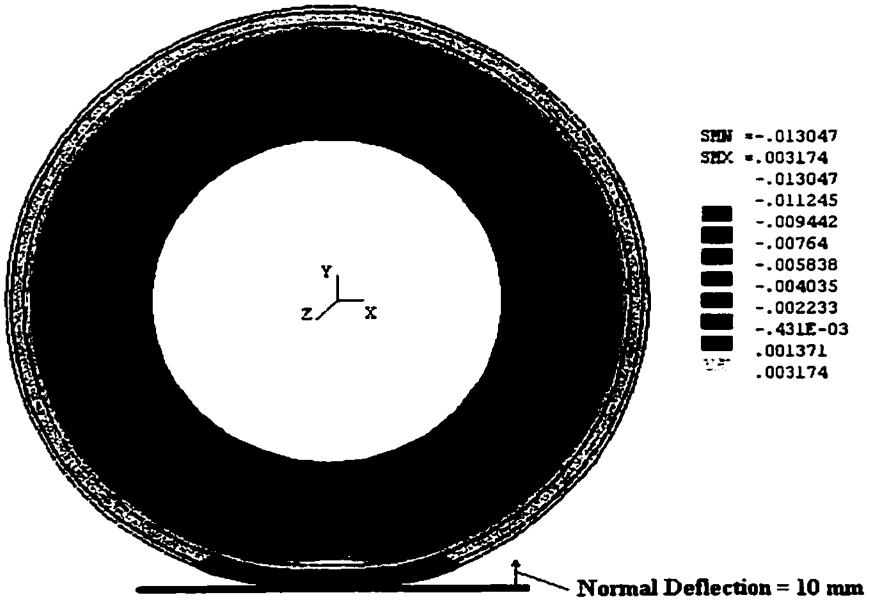

$\Delta Z = 10$ mm; $F_z = 6.1$ kN

*Figure 3.9(a): Radial deformation fields under small normal load. ($p_i = 621.3$ kPa)

**Note: SMN is the minimum value of the plotted item; SMX is the maximum bounded value of the plotted item. The unit of the deformation shown in the legend is m.*

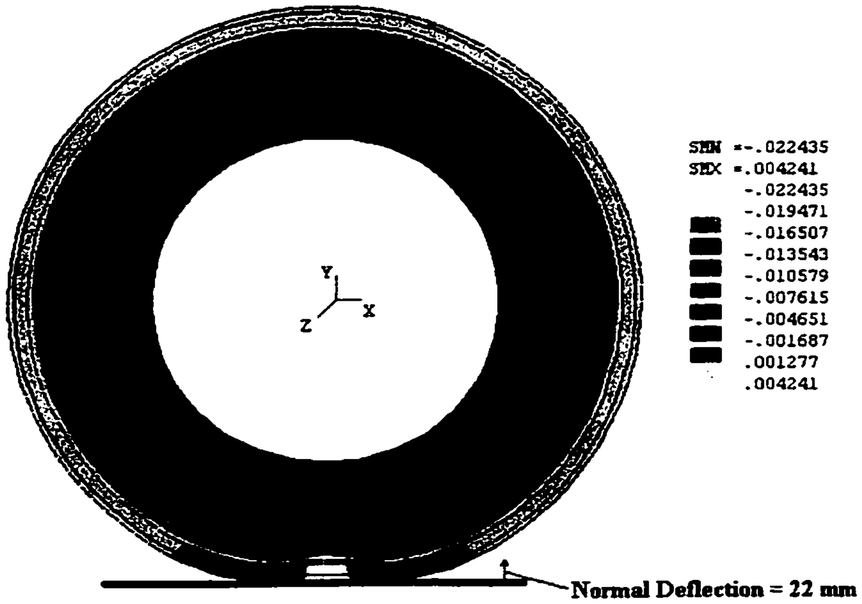

$\Delta Z = 22$ mm; $F_z = 17$ kN

*Figure 3.9(b): Radial deformation fields under regular normal load. ($p_I = 621.3$ kPa)

**Note: SMN is the minimum value of the plotted item; SMX is the maximum bounded value of the plotted item. The unit of the deformation shown in the legend is m.*

The analysis of the FE tire model followed by the post-processing can provide two- and three-dimensional contact pressure fields under different inflation pressures and normal loads. The resulting pressure fields are further analyzed to derive the contact patch geometry and contact pressure distribution, as a function of normal load. Figures 3.10 to 3.12 illustrate the contact pressure distributions in the contact patch and the footprint shapes of the tire under different inflation pressures, ranging from 545.3 to 821 kPa (79 to119 psi), and normal loads, ranging from 17.7 to 31 kN. The figures also summarize the lengths and widths of the contact patch obtained under different inflation pressures and normal loads. The legends in the figures show the color map representing the different ranges of the averaged values of the nodal contact pressures in Pascal.

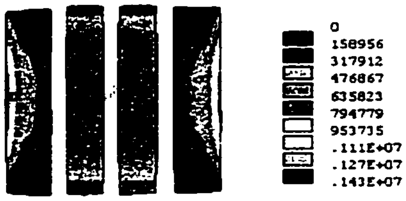

Pressure: 545.3 kPa
Load: 17.79 kN
Length: 20.93 cm
Width: 22.12 cm

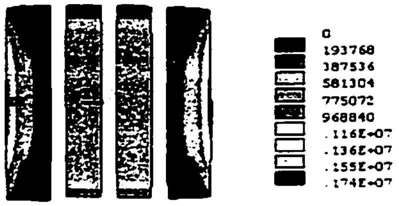

Pressure: 545.3 kPa
Load: 22.66 kN
Length: 23.12 cm
Width: 22.16 cm

Pressure: 545.3 kPa
Load: 26.68 kN
Length: 25.07 cm
Width: 22.31 cm

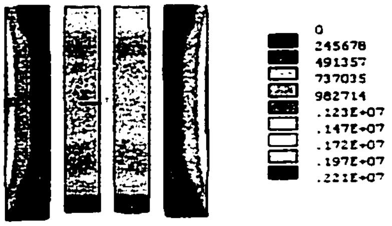

Pressure: 545.3 kPa
Load: 31.08 kN
Length: 28.17 cm
Width: 22.53 cm

Figure 3.10: The footprints and the contact pressure distributions derived from the FE model, under different normal loads. (p_i = 545.3 kPa)

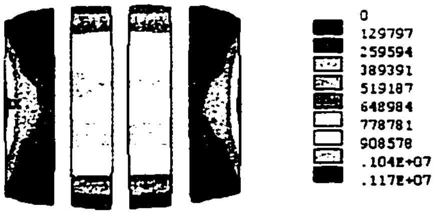

Pressure: 683.4 kPa
Load: 17.677 kN
Length: 18.89 cm
Width: 22.06 cm

Pressure: 683.4 kPa
Load: 26.54 kN
Length: 22.73 cm
Width: 22.18 cm

Pressure: 683.4 kPa
Load: 31.078 kN
Length: 24.67 cm
Width: 22.28 cm

Figure 3.11: The footprints and the contact pressure distributions derived from the FE model, under different normal loads. (p_i = 683.4 kPa)

Pressure: 821 kPa
Load: 17.91 kN
Length: 18.74 cm
Width: 22.18 cm

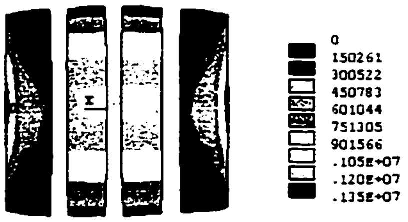

Pressure: 821 kPa
Load: 22.57 kN
Length: 19.8 cm
Width: 22.28 cm

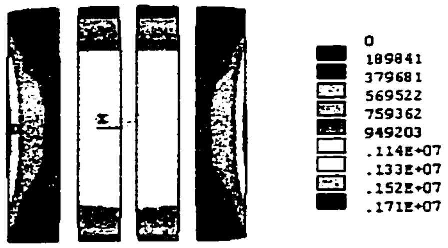

Pressure: 821 kPa
Load: 26.97 kN
Length: 21.46 cm
Width: 22.31 cm

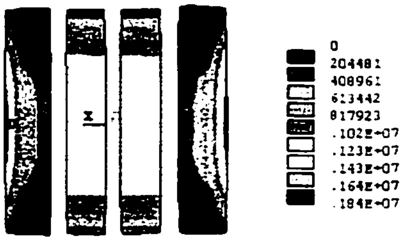

Pressure: 821 kPa
Load: 31.11 kN
Length: 23.08 cm
Width: 22.47 cm

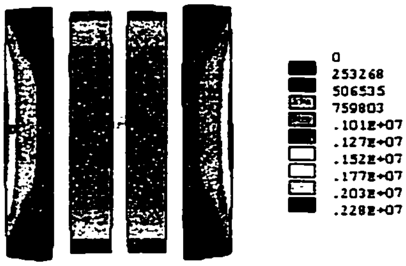

Pressure: 821 kPa
Load: 38.31 kN
Length: 25.93 cm
Width: 22.56 cm

*Figure 3.12: The footprints and the contact pressure distributions derived from the FE model, under different normal loads. (p_i = 821 kPa).

**Note:* The legends in the figures show the color map representing the different ranges of the averaged values of the nodal contact pressures in Pascal.

The results show that the contact length and thus the net contact area increases with increase in the normal load for a specific inflation pressure and decrease with increase in the inflation pressure for a specific normal load. The influence of the inflation pressure and the normal load on the width of the contact area, however, is not significant.

The three-dimensional contact pressure fields, generated from the average values of the pressures acting at centers of each contact element, are shown in Figure 3.13, for different inflation pressures, p_l = 621.3 kPa (90 psi), 759.3 kPa (110 psi) and 828.4 kPa (120 psi), and normal deflections, ΔZ=15mm, 22mm, 30mm and 36mm.

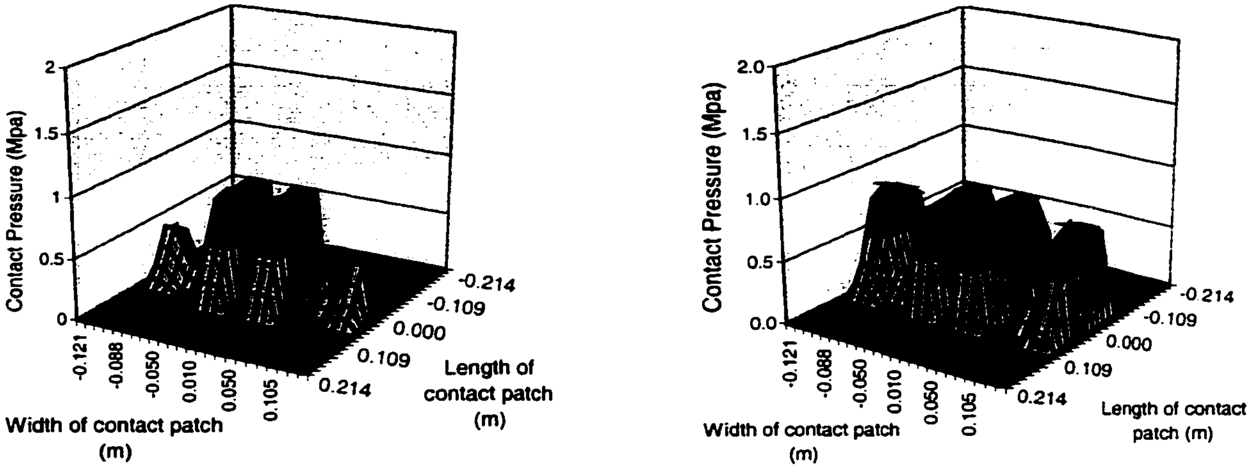

ΔZ=15 mm; F_Z=11.2 kN

ΔZ=22 mm; F_Z=17.4 kN

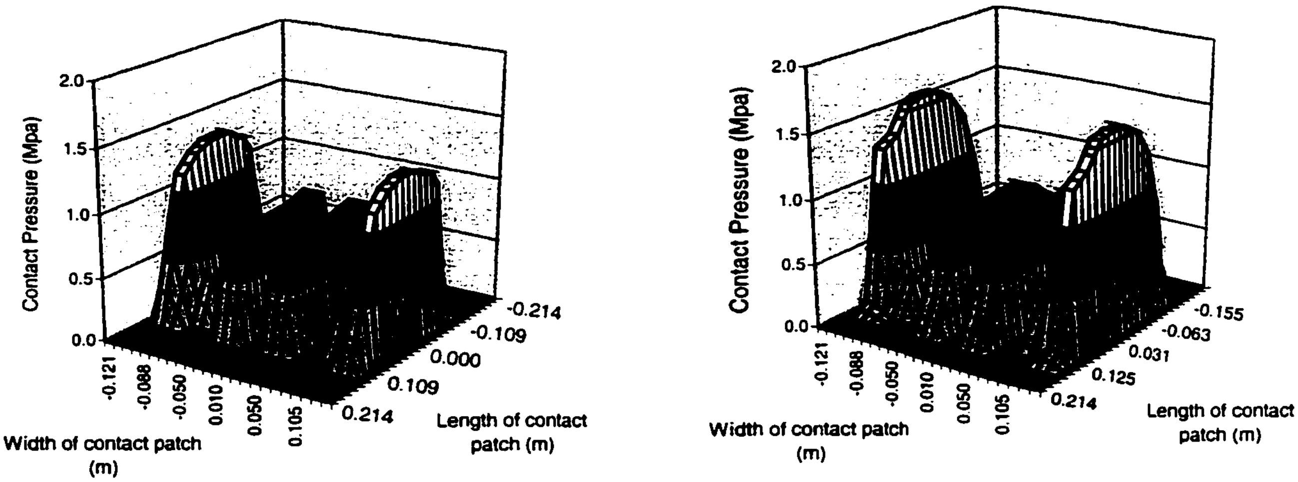

ΔZ=30 mm; F_Z=24.3 kN

ΔZ=36 mm; F_Z=31.5 kN

Figure 3.13(a): The computed three-dimensional contact pressure distribution fields under different normal loads, p_l = 621.3 kPa (90 psi).

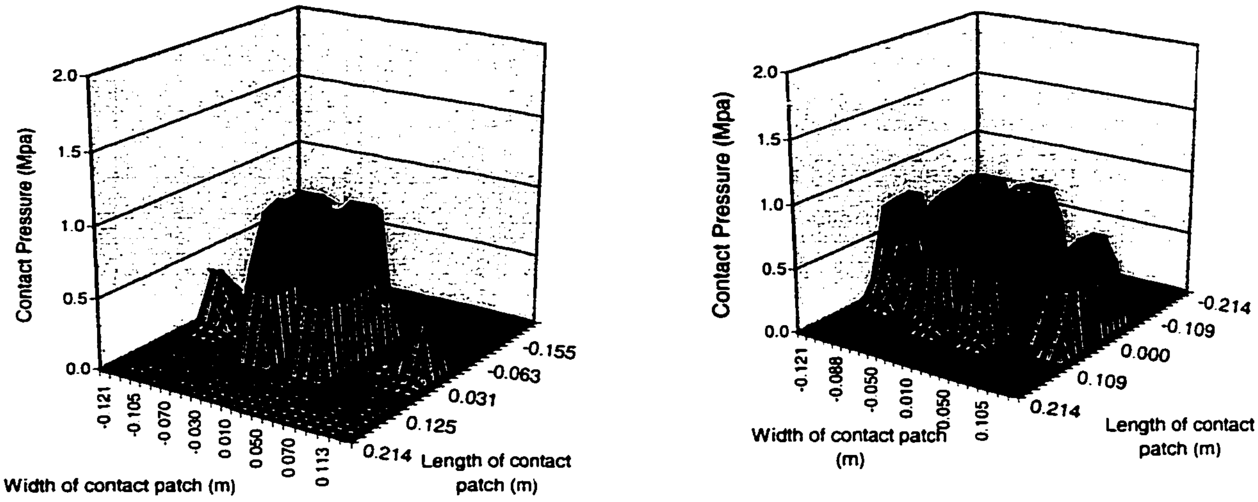

ΔZ =15 mm; F_Z=11.6 kN

ΔZ=22 mm; F_Z=19.6 kN

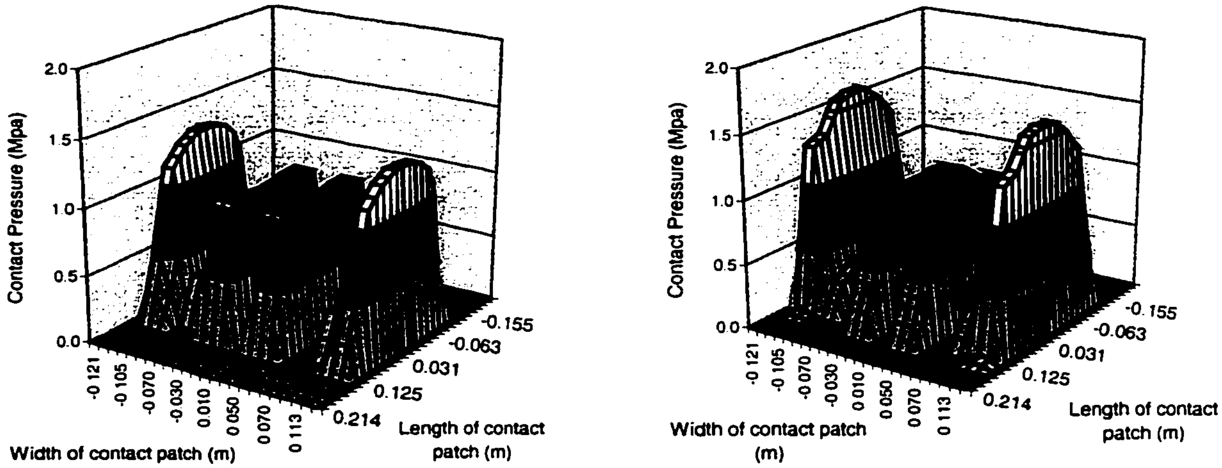

ΔZ=30 mm; F_Z=27.6 kN

ΔZ=36 mm; F_Z=34.7 kN

Figure 3.13(b): The computed three-dimensional contact pressure distribution fields under different normal loads, p_i = 759.3 kPa (110 psi).

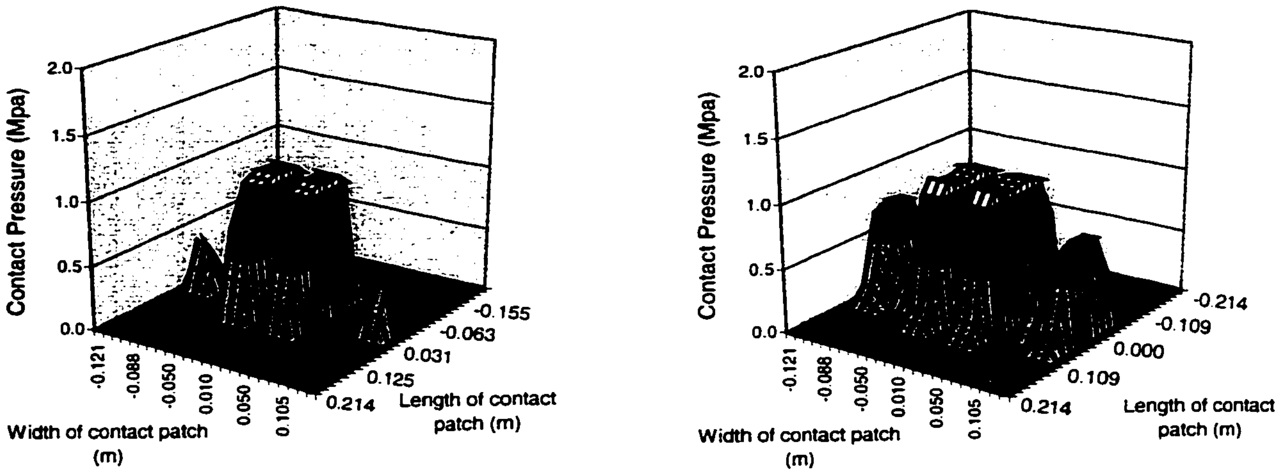

ΔZ=15 mm; F_Z=12.1 kN

ΔZ =22 mm; F_Z=21.7 kN

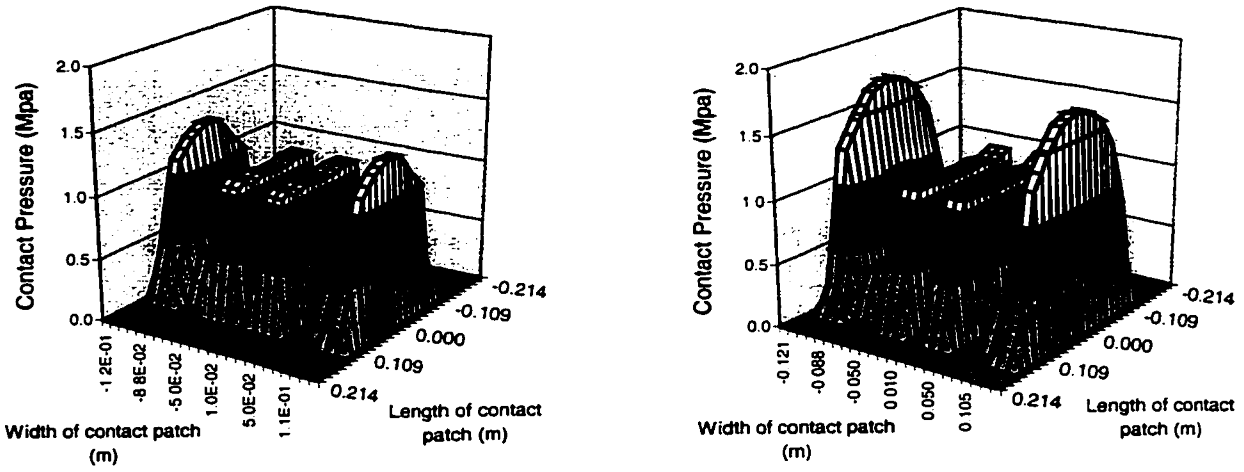

ΔZ=30 mm; F_Z=28.6 kN

ΔZ=36 mm; F_Z=36.5 kN

Figure 3.13(c): The computed three-dimensional contact pressure distribution fields under different normal loads, p_i = 828.4 kPa (120 psi).

The analysis of the contact pressure distributions derived under different normal loads, shown in figures 3.10 to 3.13, indicate that the high contact pressure peaks occur at inner side of the inner ribs (near the central circumferential line), when the normal load is lower than a critical value around 15 kN. The pressure peaks tend to shift towards the outer ribs, as shown in the figures, when normal load is increased beyond 20 kN. The ratio of the peak pressure values occurring in the outer ribs to the peak pressure in the inner ribs tends to increase considerably with increase in the normal load. Such trends in pressure distribution have also been observed in reported experimental studies on car tires [131, 141].

3.5.2 Stress Fields in the Principal Directions

The FE tire model is further analyzed to derive stress fields along the principal directions corresponding to 621.3 kPa (90 psi) inflation pressure and $F_z = 17$ kN. Figure 3.14 illustrates the first, second and third principal-direction stress fields together with the capped hidden side and front views of the loaded tire. The principal-direction stress fields reflect the energy dissipation trends in the tire and, to some degree, affect the tire fatigue life. These stress fields are often considered in the structure design optimization and optimization studies. Since the exact stress-state of a point within the tire body is determined by the corresponding stress tensor, complete description of the stress state of a point involves the analysis of all the stress components in the stress tensor. The following analysis of the specific stress component fields reflects some aspects of the stress states of the tire subjected to inflation pressure of 621.3 kPa (90 psi) and normal load of 17 kN.

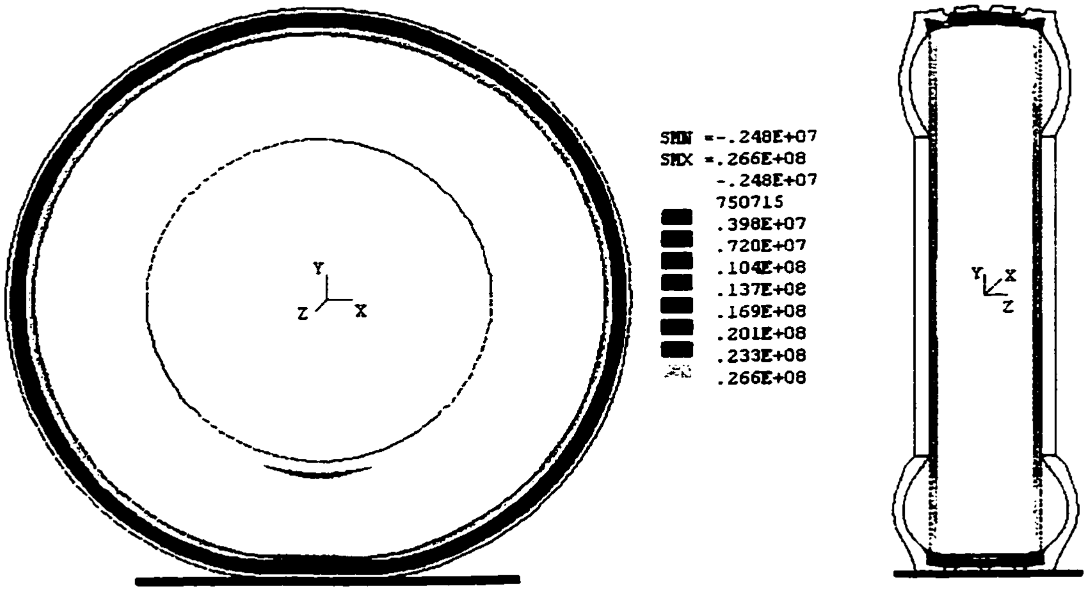

First principal-direction stress field

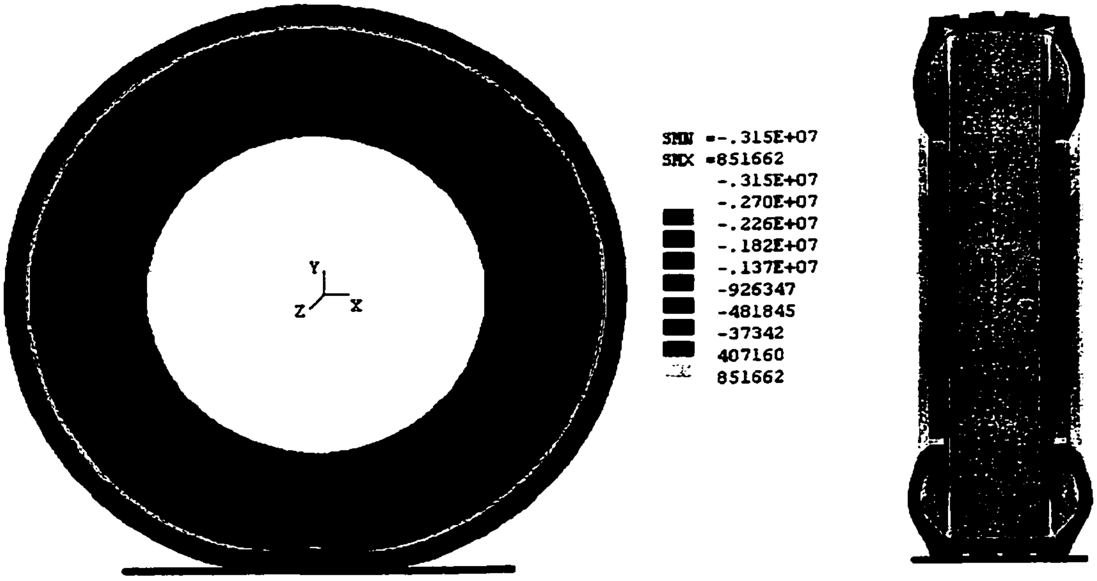

Second principal-direction stress field

*Figure 3.14: The stress fields in the principal directions for the deformed tire (capped-hidden side and front views), $p_I = 621.3$ kPa, $F_z = 17$kN.

**Note: SMN is the minimum value of the plotted item; SMX is the maximum bounded value of the plotted item. The unit of the stress value shown in the legend is Pascal (Pa).*

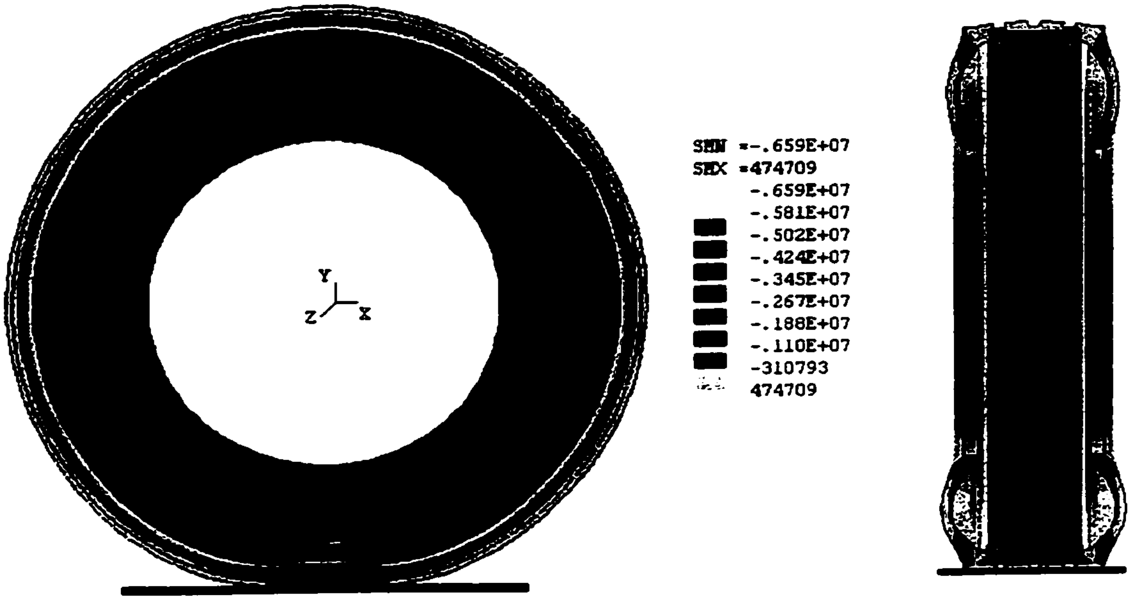

Third principal-direction stress field

*Figure 3.14: The stress fields in the principal directions for the deformed tire (capped-hidden side and front views), p_l = 621.3 kPa, F_z = 17kN. (Continued)

**Note: SMN is the minimum value of the plotted item; SMX is the maximum bounded value of the plotted item. The unit of the stress value shown in the legend is Pascal (Pa).*

The results show higher values of the first principal-direction stress in each case, which occurs along the circumferential line in the carcass layers and the belts. The highest values of the first principal-direction stress occur in the vicinity of the center of the contact patch. The second and third principal-direction stresses exhibit their maximum values in the shoulder regions, which is most likely attributed to the abrupt changes in the geometry of the carcass layer, and the discontinuities in the material properties associated with the carcass and the belts. It should be noted that the computed stress fields include the effects of both the inflation pressure and the normal loading.

3.5.3 Fiber Stresses and Inter-ply Shear Stresses

Fiber stresses in a rolling tire relate to the cornering and traction properties of a tire. The shear stresses developed between different belt layers, belt and carcass, and belt and tread interfaces directly affect the stability and integrity of the tire structure. Too high an inter-ply shear stress in the belts may cause delamination damage. Only a few reported studies in the field, however, have attempted to analyze the inter-ply shear stresses and distribution of fiber forces in the tires [57, 126-127]. The proposed nonlinear FE tire model incorporating multi-layered elements permits the analysis of fiber forces and inter-ply shear stresses in the tires.

Figure 3.15 illustrates the distribution of the tensile stresses in the circumferential direction in the belts and the carcass layers caused by both the inflation pressure and the normal load. The tensile stress fields of the belt layers and the corresponding displacements are asymmetric about the circumferential axis, which is most likely attributed to the asymmetric stacking sequence of the belt layers, although the geometry and loading are symmetric. This asymmetric behavior is also attributed to the coupling effects, which are inherent in the composites, such as the coupling between the bending and the twisting, and that between the extension and bending movements. It can be seen that the circumferential tensile stress values in the belt layers are much higher than the stresses in the carcass layers near the contact patch. The distribution of the circumferential tensile stresses in the carcass layers and the belt layers along the lateral axis of the tire are evaluated corresponding to three different normal loads (6.1 kN, 11.2 kN and 17 kN) to examine the peak stresses.

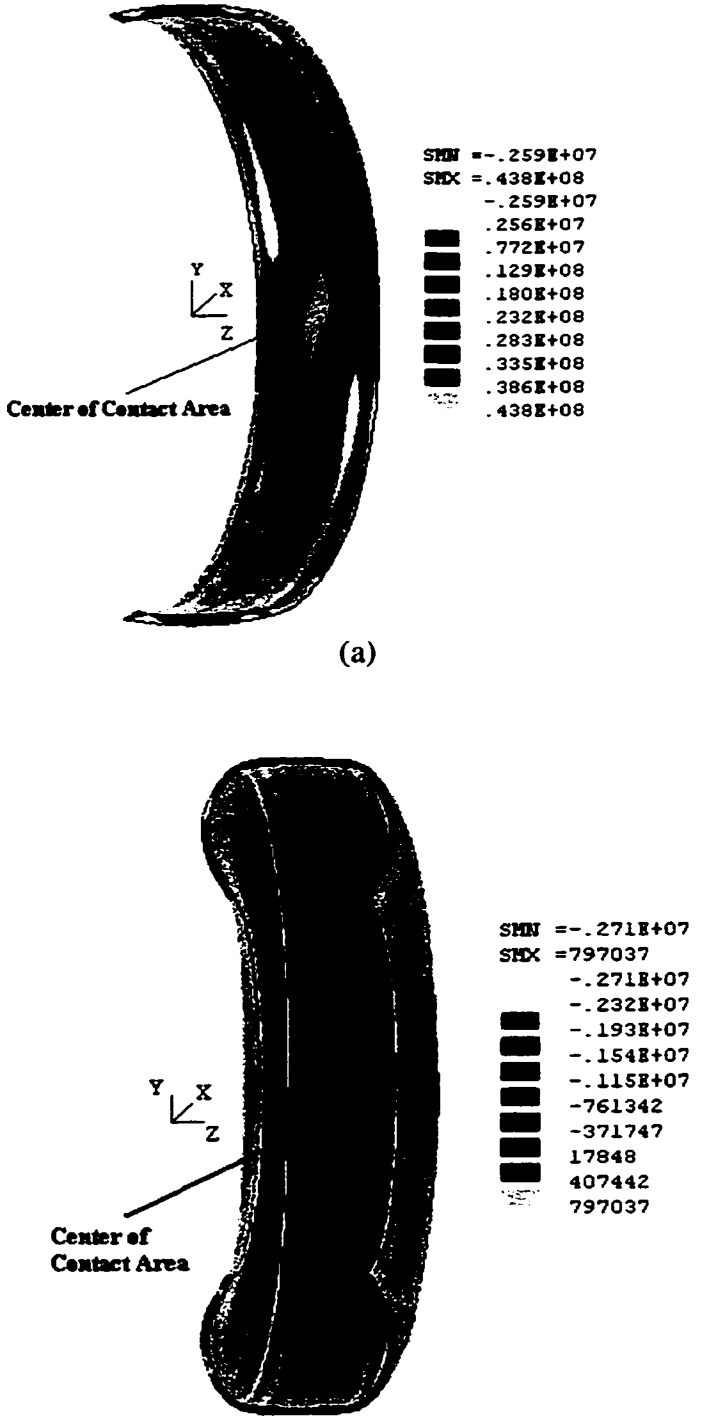

(a)

(b)

*Figure 3.15: Tensile stress fields in (a) the belts; and (b) the carcass layers. (p_I = 621.3 kPa, F_z = 17kN)

**Note: SMN is the minimum value of the plotted item; SMX is the maximum bounded value of the plotted item. The unit of the stress value shown in the legend is Pascal (Pa).*

Figure 3.16 illustrates the distribution of the circumferential tensile stresses in the carcass layer, along the lateral direction of the tire at the lateral centerline of the contact patch for different normal loading conditions. The results show that the tensile stresses are distributed nearly symmetrically about the contact patch centerline. An increase in the normal load and thus the normal deflection causes higher circumferential tensile stresses in the centerline elements of the carcass layer. Light loading of the tire results in peak stress in the vicinity of the center of the contact patch. An increase in the normal load tends to increase the stresses considerably in the elements in the vicinity of the outer periphery.

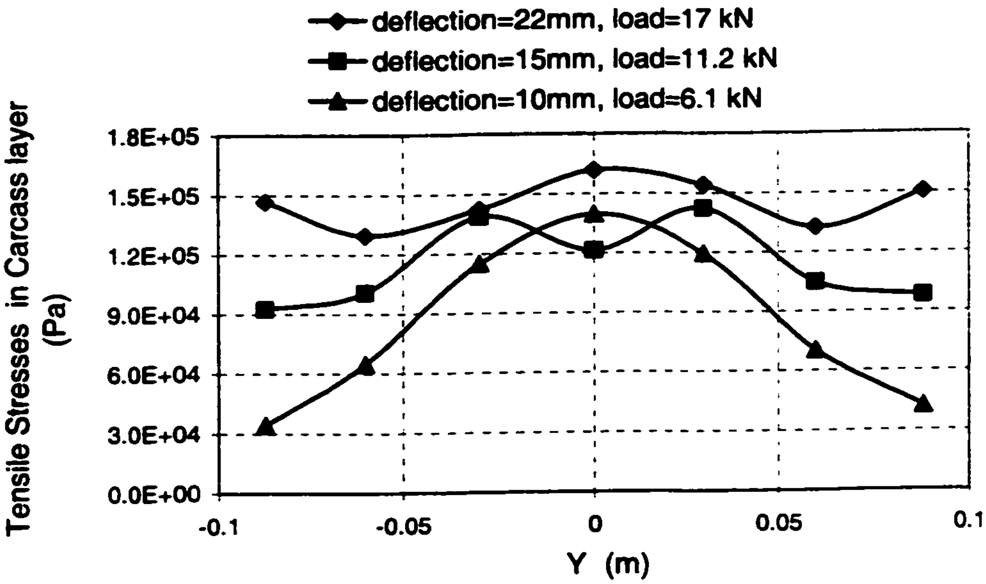

Figure 3.16 Tensile stresses in carcass layer for different normal loads; $p_i = 621.3$ kPa.

The distribution of circumferential tensile stresses in different belt layers for different normal loads are presented in Figure 3.17. The results show that the belt 3 experiences the highest stresses over most of the tire width, while belt 4 is subjected to higher stresses near the periphery. The tensile stresses in the belts 4 and 3, located near

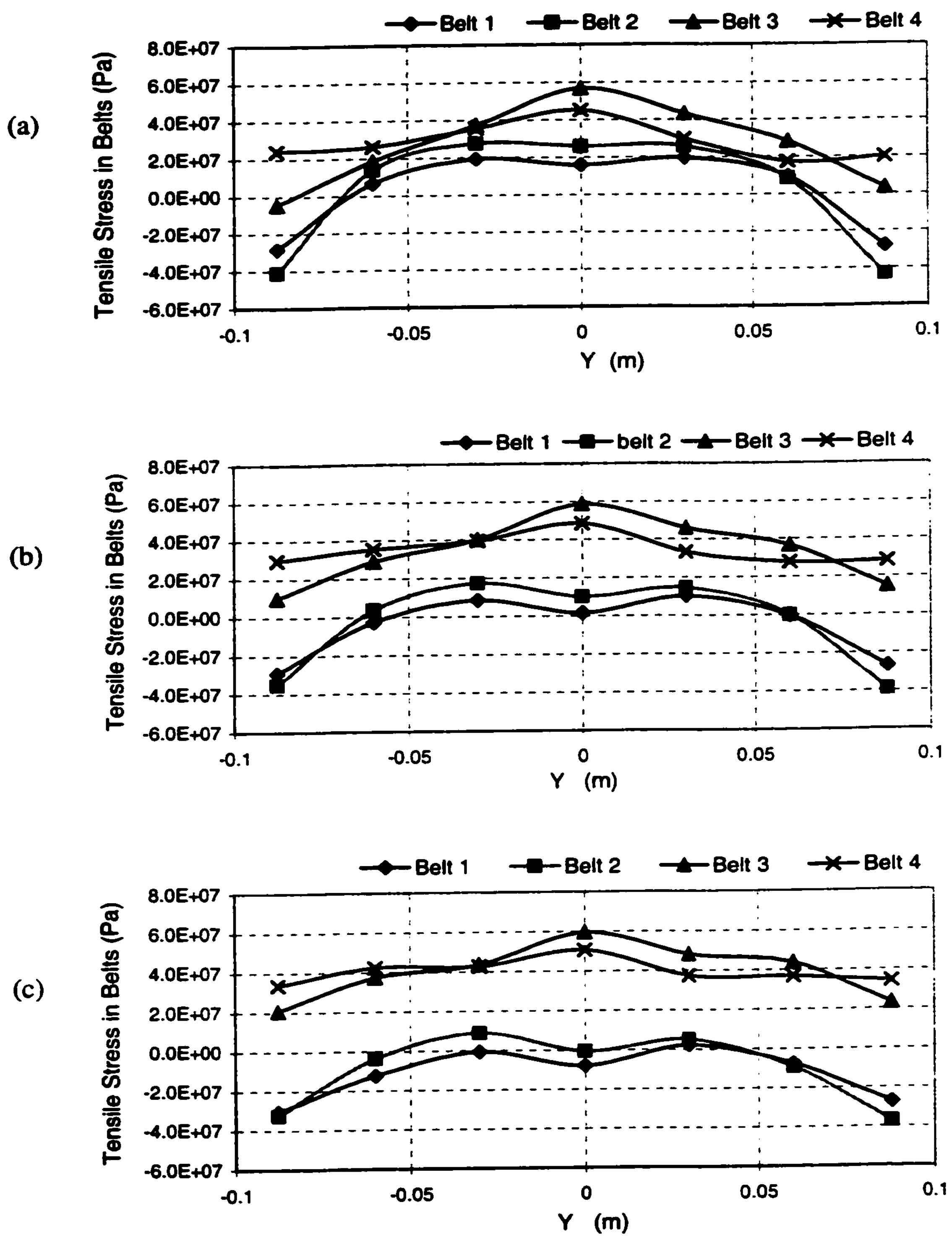

Figure 3.17: Tensile stresses in different belts for different loads; $p_I = 621.3$ kPa: (a) $F_z = 6.1$ kN; (b) $F_z = 11.2$ kN; (b) $F_z = 17$ kN.

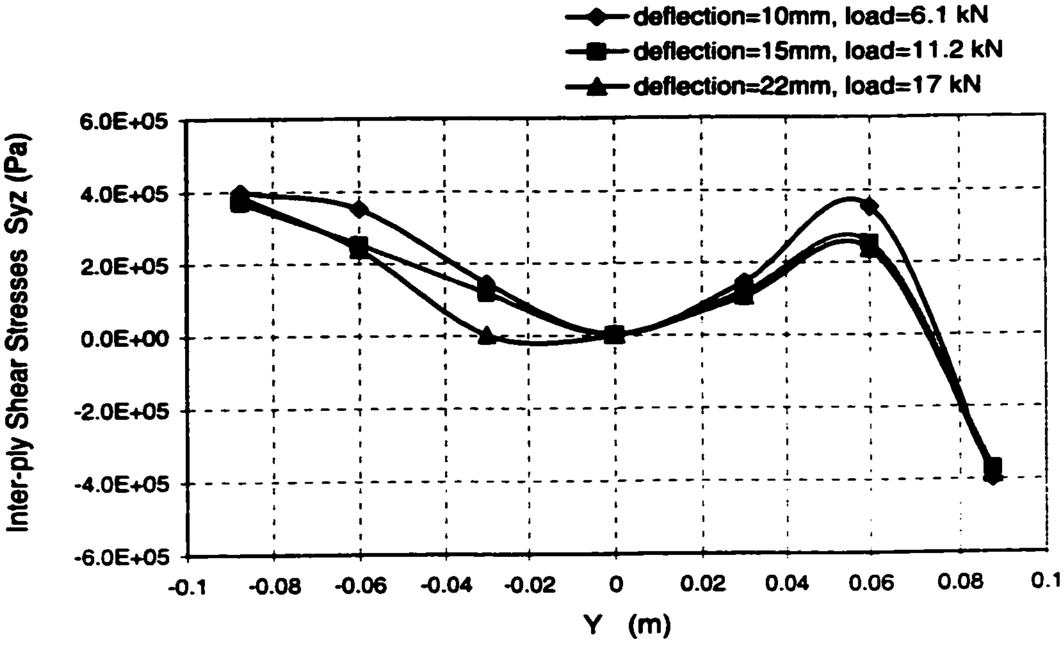

(a)

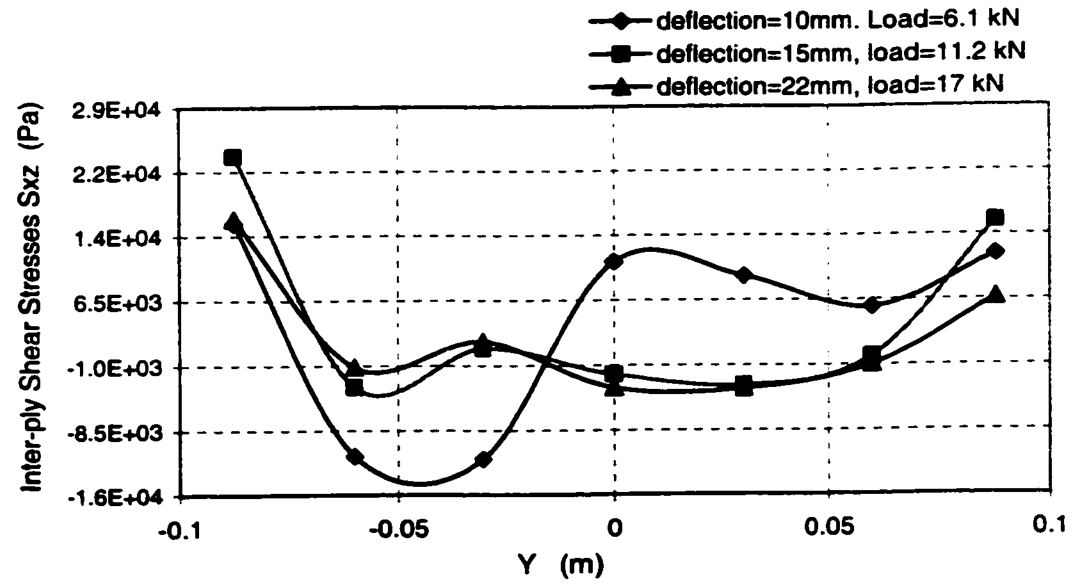

(b)

Figure 3.18: Inter-ply shear stresses between the belt 4 and the carcass layer under different loads: (a) Out-of-tire plane shear stress, S_{yz}; (b) In-tire plane shear stress, S_{xz}.

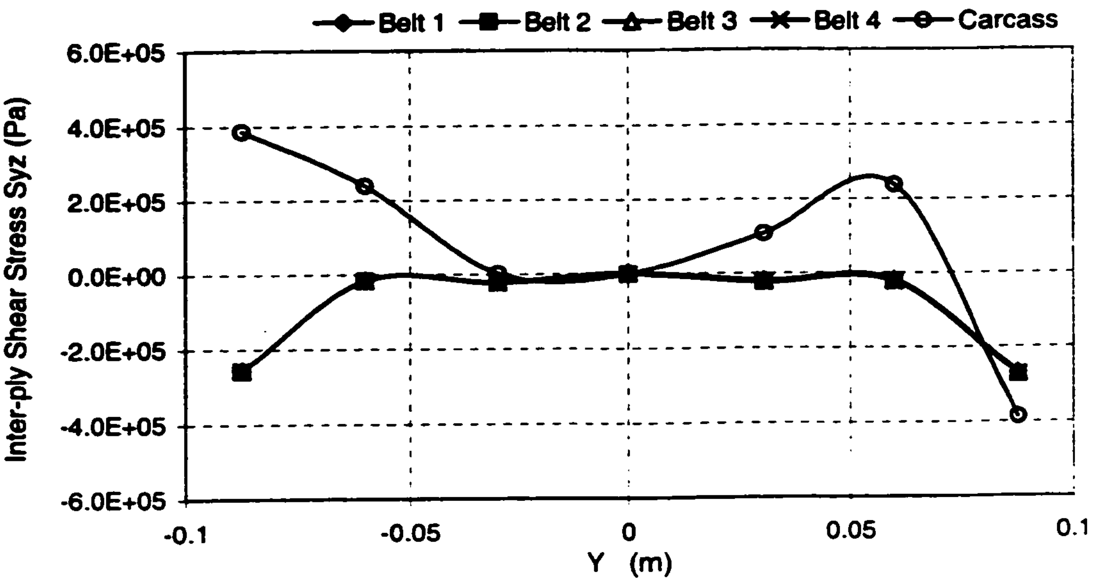

(a)

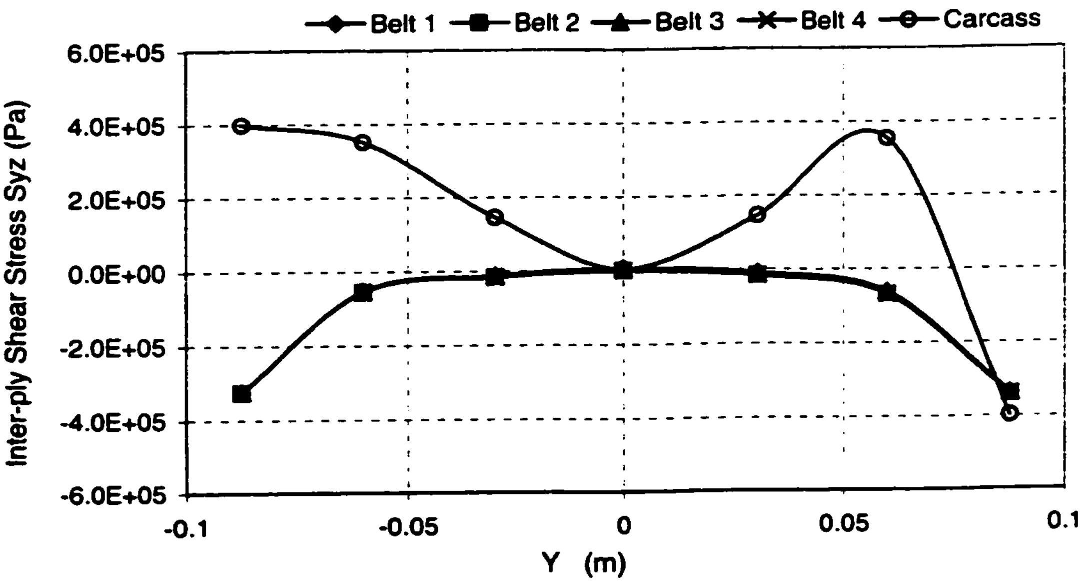

(b)

Figure 3.19: Out-of-tire-plane shear stress S_{yz} between belts, and belt and carcass layers under different loads: (a) $\Delta Z = 22$ mm; $F_z = 17$ kN; (b) $\Delta Z = 10$ mm; $F_z = 6.1$ kN.

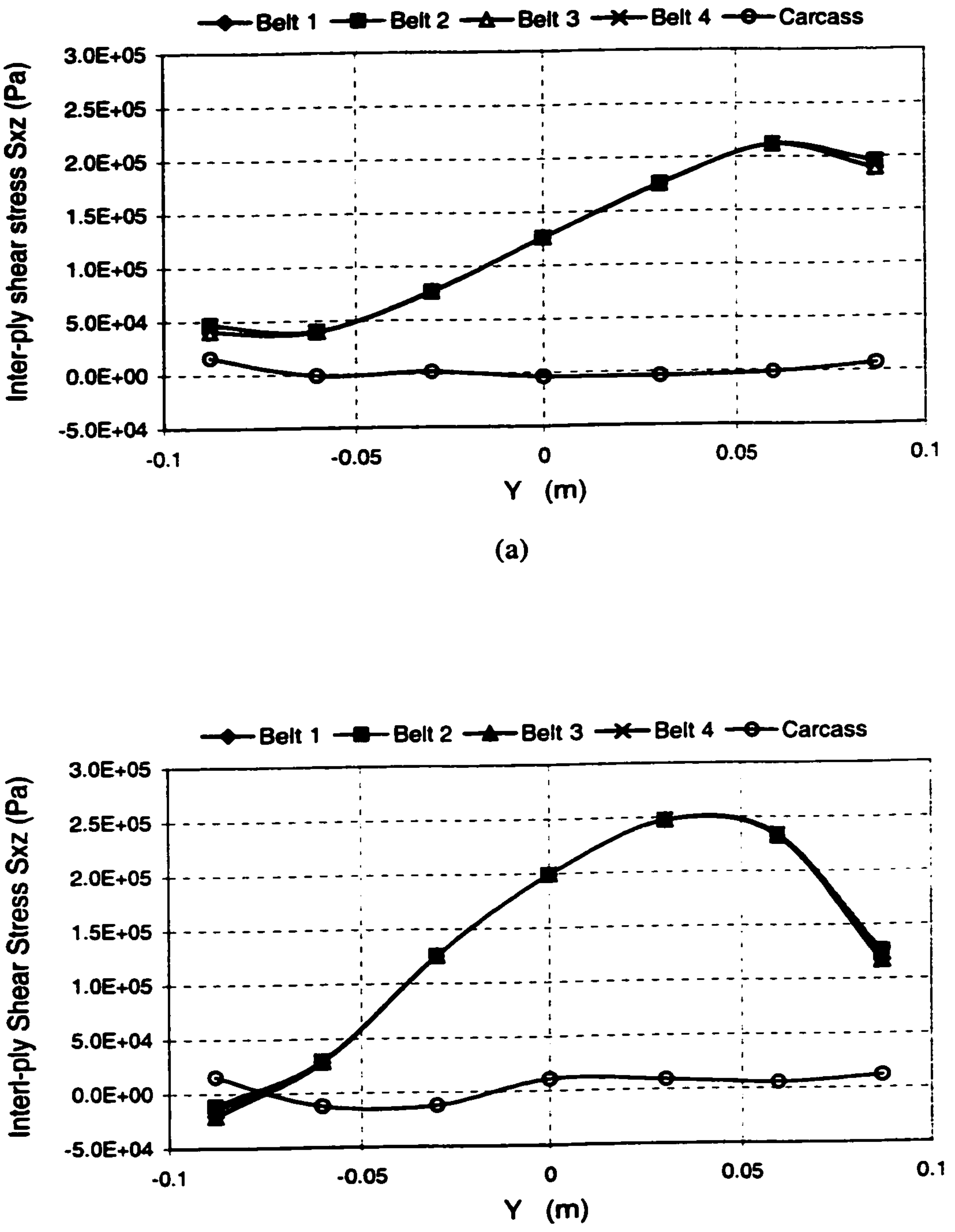

(a)

(b)

Figure 3.20: In-tire-plane shear stress S_{xz} between belts, and belt and carcass layers under different loads: (a) $\Delta Z = 22$ mm; $F_z = 17$ kN; (b) $\Delta Z = 10$ mm; $F_z = 6.1$ kN.

the carcass layers, are considerably larger than those observed in the belts located near the tread layer. As the normal load increases, the tensile stresses in belts 4 and 3 tend to increase, while the variations in the peak values occurring near the center of the selected element strip are insignificant. The peak values of the tensile stresses in belts 2 and 1, however, decrease with increase in the normal load.

Figure 3.18 illustrates the inter-ply shear stress distribution between the belt 4 and the carcass layers in- and out-of- the tire plane. The results represent the shear stresses derived for elements in the lateral centerline of the contact patch. The out-of-tire-plane shear stresses S_{yz} represent the stresses in the transverse plane of the tire, while the in-tire-plane shear stresses S_{xz} describe the stresses along the longitudinal direction. The result shows that the out-of-tire-plane inter-ply shear stresses S_{yz} are over ten times higher than the in-tire-plane stresses S_{xz} developed between the belt 4 and the carcass layer. It can be further observed that variations in the normal load yield significant changes in S_{yz} between the belt 4 and the carcass layer, while the influence of normal load on the S_{xz} is also considerable. It should be noted that these computed stress values represent only one averaged component of the stress tensor associated with each of the considered element. A more elaborate stress analysis on the interactions between different layers should involve all the stress components related to the considered elements.

The inter-ply shear stresses, S_{yz} and S_{xz}, developed between different belt layers and the belt and carcass layers are presented in Figure 3.19 and 3.20, respectively, under two different normal loads: 6.1 kN and 17 kN. The out-of-tire-plane shear stresses S_{yz} developed between the carcass layer and the belt 4, which is on the top surface of the carcass layer, are significantly higher than the corresponding shear stresses generated between the belt layers near the shoulder area, as shown in Figure 3.19. The stresses S_{yz} developed between every two adjacent layers approach zero value at the center location of the contact patch. The in-tire-plane shear stresses S_{xz} generated between any two adjacent belt layers are generally larger than the corresponding S_{xz} values developed between the belt 4 and the carcass layer, as shown in Figure 3.20. The in-tire-plane shear stresses S_{xz} generated between belt layers, located in the strip of elements transversely arranged through the contact center, appear to be anti-symmetric about the center of the contact patch, as can be seen from Figure 3.20. The peak values of S_{xz} generated between the belt layers tend to move further away from the center of the contact patch to the outer periphery in the cross-section of the tire when normal load increases. No significant differences are observed in the shear stresses S_{yz} and S_{xz} generated between belt layers for different loading conditions. The peak values of S_{yz} and S_{xz} occurring near the shoulder area may result in the onset of delamination damage in the tire.

3.6 EXPERIMENTAL WORK AND MODEL VALIDATION

The static force-deflection characteristics of tires are strongly related to the tire structural parameters, static load and inflation pressure. As in practical operating conditions, a tire usually encounters considerable variations in the static load due to changes in the number of passengers in service or in the weight of the goods in transportation. Further more, the inflation pressure of tires may also vary considerably. It is thus essential to characterize the tire properties over a wide range of pre-loads and inflation pressures.

A test stand, comprising an electro-hydraulic actuator and an instrumented tire platform was developed to measure the static force deflection characteristics of a candidate truck tire (12.5R22.5) under different pre-loads, ranging from 17.8 kN to 40 kN, and inflation pressures, ranging from 545.3 kPa to 828.4 kPa. Figure 3.21 illustrates a pictorial view of the test stand and measured force-deflection properties of the tire. The tire was initially charged at a desired inflation pressure and was preloaded to a specified pre-load value. The inflation pressure was then adjusted to achieve the desired pressure under the pre-load.

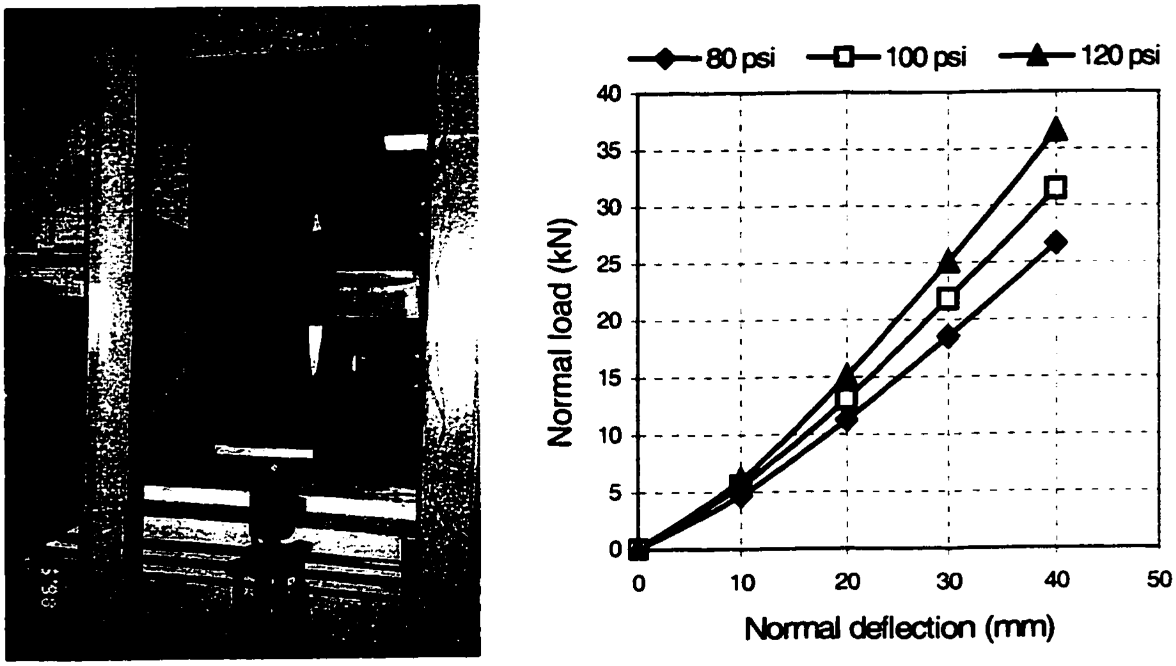

Figure 3.21: A pictorial view of the test stand and the measured normal load-deflection characteristics of a 12.5R22.5 tire.

The tire was supported between a fixed inertial reference and an electro-hydraulic actuator. A force transducer was installed between the tire support and the actuator piston to measure the tire force. The signal from the linear variable differential transformer (LVDT) position sensor, integrated within the actuator, was considered for the measurement of the tire deformation. A series of experiments were performed to measure the force-deflection characteristics of the tire over a wide range of inflation pressures. The geometry of the contact patch of the tire was also acquired in the laboratory over a range of normal loads and inflation pressures. In the experiment, the actuator was positioned to ensure clear access to the tire tread in the vicinity of the contact region. A sheet of paper was placed on the support plate and the dark color paint was applied on the tire tread. The actuator piston was then positioned to achieve a specified normal load corresponding to a preset inflation pressure. The resulting imprint of the painted tread was scanned to determine the contact patch geometry.

The measured force and deflection data are used to examine the validity of the FE model in a limited manner. The computed force-deflection characteristics are compared with the measured data, as shown in Figure 3.22. The results show comparable nonlinear normal force-deflection characteristics of the FE model and the measured data. The results further show that the static vertical stiffness increases with increase in the inflation pressure. Both the measured data and the model results show similar trends in load-deflection characteristics, and considerable deviation corresponding to large deflection. The magnitude of errors between the computed and measured data also increases with the increase in the normal load for a specific inflation pressure. The deviation between the model results and the measured data are most likely caused by the lack of precise material properties and the errors generated in the geometric measurements.

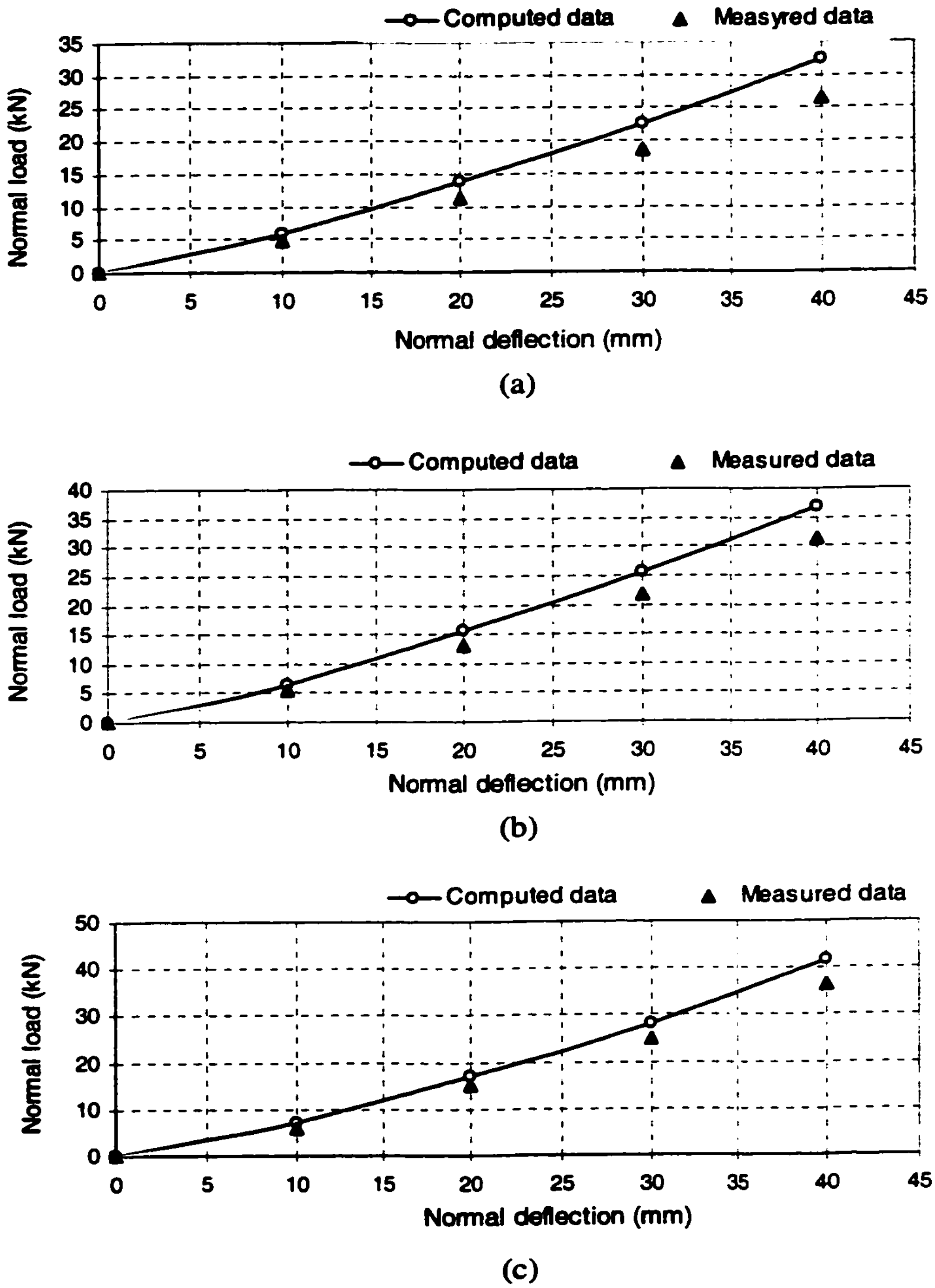

Figure 3.22: Comparison of the computed normal load-deflection characteristics with the measured data: (a) 545.3 kPa; (b) 683.4 kPa; and (c) 821.4 kPa.

The validity of the analysis is further examined by comparing the computed contact patch geometry from the FE model with the data obtained from the experiments performed in the laboratory, as shown in Figure 3.23. The tire inflated with different inflation pressures, ranging from 545.3 to 821.45 kPa (79 to 119 psi), was deflected to achieve different normal loads ranging from 17.68 to 40 kN. The comparisons show reasonably good agreements between the computed and measured footprints. The variations in the footprint length and width due to increasing normal load for different inflation pressures, as derived from the model, are also illustrated in Figure 3.24 and Figure 3.25, respectively. The results show reasonably good agreement with the measured data.

Pressure 545 3 kPa (79 psi)
Load 17 785 kN
Length 21 29 cm
Width 22 02 cm

Pressure: 545.3 kPa
Load: 17 79 kN
Length: 20.93 cm
Width: 22.12 cm

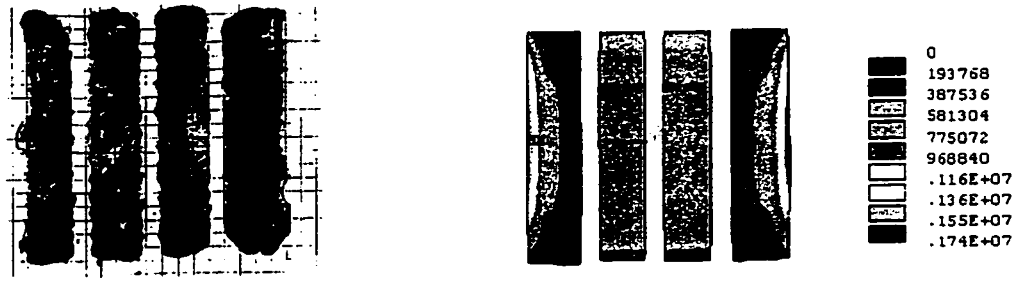

Pressure 545 3 kPa (79 psi)
Load 22.68 kN
Length 23 42 cm
Width 22 10 cm

Pressure: 545.3 kPa
Load: 22.66 kN
Length: 23.12 cm
Width: 22.16 cm

Figure 3.23(a): Computed and measured footprint shapes for different loads and inflation pressures, $p_i = 545.3$ kPa.

Pressure: 545.3 kPa (79 psi)
Load 26.68 kN
Length 25.22 cm
Width 22.28 cm

Pressure 545.3 kPa
Load 26.68 kN
Length: 25.07 cm
Width: 22.31 cm

Pressure 545.3 kPa (79 psi)
Load 31.08 kN
Length 29.11 cm
Width 22.05 cm

Pressure 545.3 kPa
Load: 31.08 kN
Length: 28.17 cm
Width: 22.53 cm

Figure 3.23(a): Computed and measured footprint shapes for different loads and inflation pressures, p_I = 545.3 kPa. (Continued)

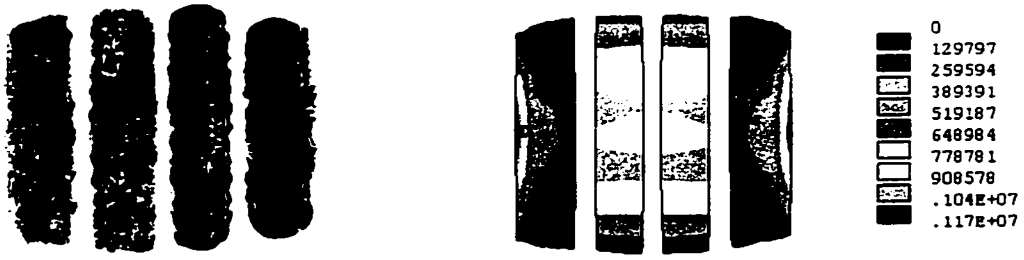

Pressure: 683.4 kPa (99 psi)
Load: 17.68 kN
Length: 19.3 cm
Width 21.94 cm

Pressure 683.4 kPa
Load: 17.677 kN
Length 18.89 cm
Width: 22.06 cm

Figure 3.23(b): Computed and measured footprint shapes for different loads and inflation pressures, p_I = 683.4 kPa.

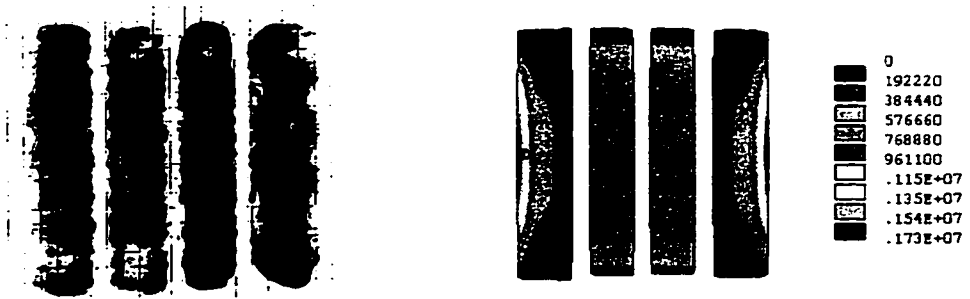

Pressure 683 4 kPa (99 psi)
Load 26 54 kN
Length 23 42 cm
Width 22 25 cm

Pressure 683.4 kPa
Load 26.54 kN
Length. 22 73 cm
Width. 22.18 cm

Pressure 683 4 kPa (99 psi)
Load 31 08 kN
Length 25 20 cm
22.35 cm

Pressure 683.4 kPa
Load 31 078 kN
Length 24.67 cm
Width 22.28 cm

Figure 3.23(b): Computed and measured footprint shapes for different loads and inflation pressures, p_i = 683.4 kPa. (Continued)

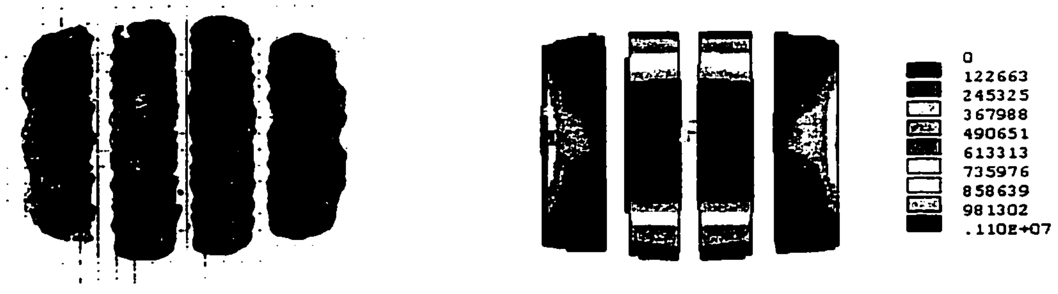

Pressure 821 kPa (119 psi)
Load 17 88 kN
Length 19 03 cm
Width 22 53 cm

Pressure: 821 kPa
Load: 17 91 kN
Length 18.74 cm
Width 22 18 cm

Figure 3.23(c): Computed and measured footprint shapes for different loads and inflation pressures, p_i = 821 kPa.

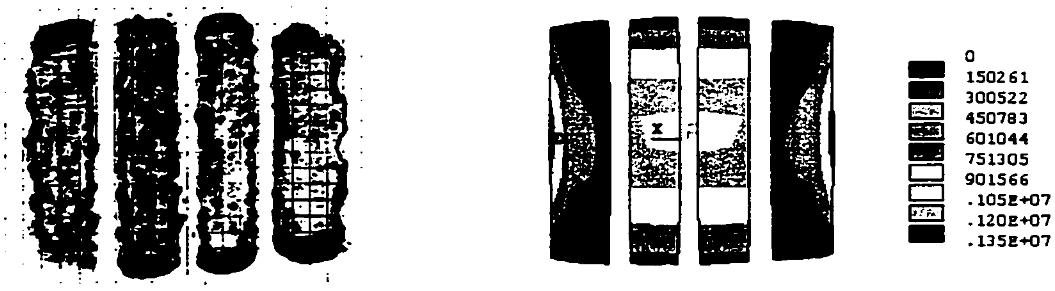

Pressure 821 kPa (119 psi)
Load 22.56 kN
Length 20.50 cm
Width 22.27 cm

Pressure 821 kPa
Load: 22.57 kN
Length: 19 8 cm
Width 22.28 cm

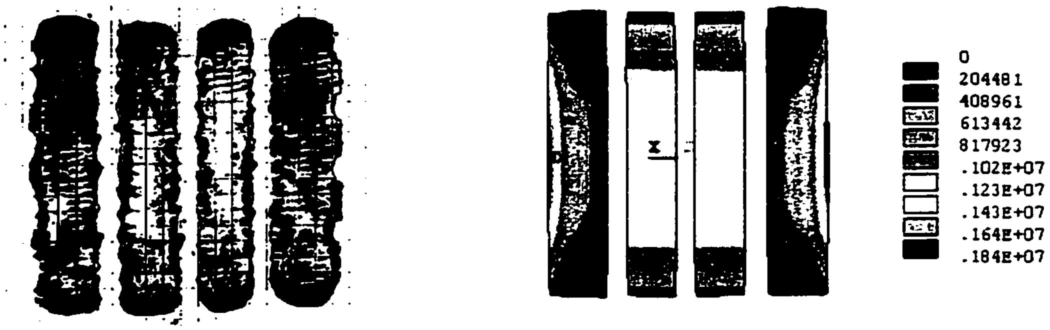

Pressure 821 kPa (119 psi)
Load 31.08 kN
Length 24.00 cm
Width 22.58 cm

Pressure 821 kPa
Load: 31.11 kN
Length 23.08 cm
Width: 22.47 cm

Pressure 821 kPa (119 psi)
Load 38.28 kN
Length 27.10 cm
Width 22.17 cm

Pressure 821 kPa
Load: 38 31 kN
Length: 25.93 cm
Width: 22.56 cm

Figure 3.23(c): Computed and measured footprint shapes for different loads and inflation pressures, p_i = 821 kPa. (Continued)

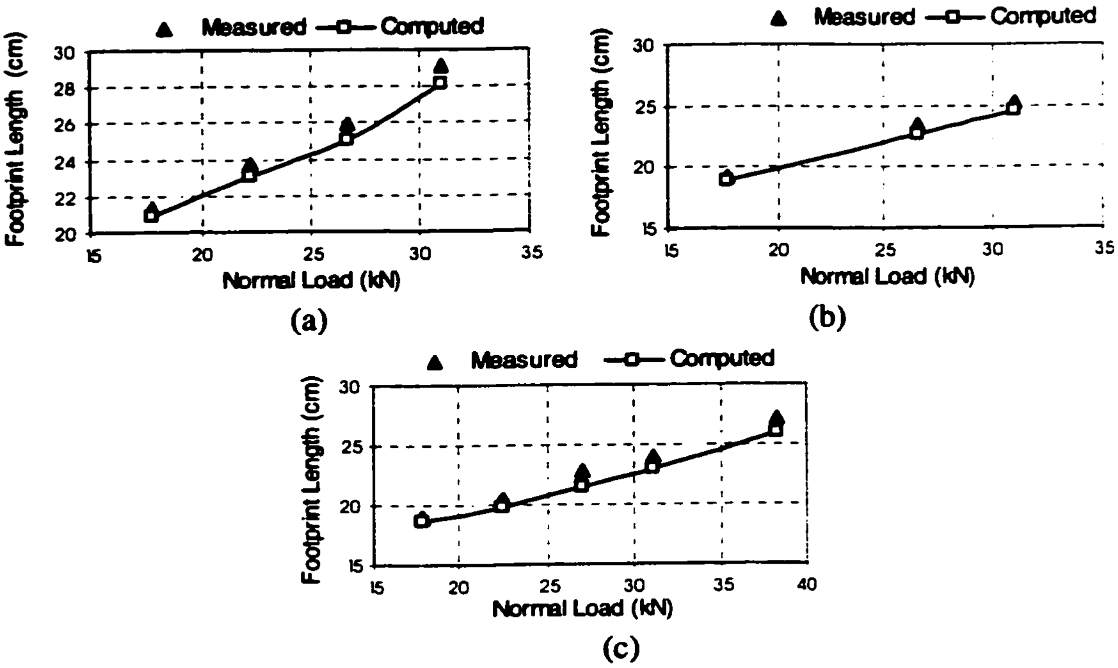

(a)

(b)

(c)

Figure 3.24: Comparison of the computed and measured footprint lengths as function of the normal load: (a) 545.3 kPa; (b) 683.4 kPa; and (c) 821.4 kPa.

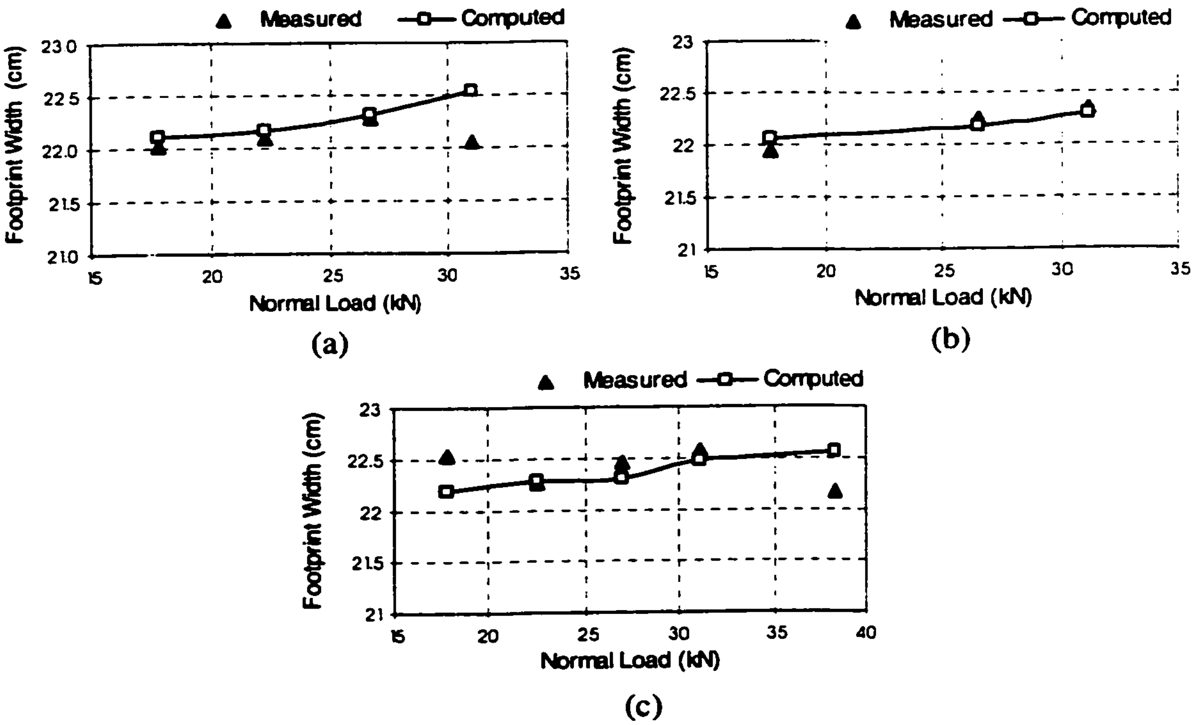

(a)

(b)

(c)

Figure 3.25: Comparison of the computed and measured footprint widths as function of the normal load: (a) 545.3 kPa; (b) 683.4 kPa; and (c) 821.4 kPa.

As discussed above, the computed and measured normal force-deflection characteristics and especially, the contact patch geometry (shapes and lengths), show reasonably good agreement over a wide range of normal loads and inflation pressures. The differences between the measured and computed normal force-deflection characteristics are considered to be resulting from the errors associated with the estimated material properties for the rubber block and individual layers of the candidate tire. It can be concluded that the results derived from the FE tire model can be used for qualitative analysis of a truck tire. The FE tire model can thus be further used to perform a parametric study to derive a more desirable set of structural parameters so as to minimize the maximum stresses within the tire body.

3.7 SUMMARY

A nonlinear FE model of a truck tire is developed to study the three-dimensional stress, strain and deformation fields of a truck tire subjected to normal load and inflation pressure loading conditions. The proposed model is capable of predicting the inter-ply shear stresses between the layers, and can be employed to analyze the shear interactions between the layers and the fiber forces in individual layers, which are related to the traction/braking and cornering properties of tires. The occurrence of too high a shear stress has been related to delamination damage in the multi-layered tire system. The contact patch geometry and pressure distributions derived from the FE model suggest that high contact pressure peaks occur at inner side of the inner ribs under light to medium loading. The pressure peaks, however, tend to shift outward along the lateral direction under high normal loads. The ratio of the peak pressures occurring in the outer ribs to those in the inner ribs tends to increase considerably with increase in the normal load.

From the model results, it is concluded that the highest values of the first principal-direction stress occur in the vicinity of the center of the contact patch. The second and third principal stresses exhibit their maximum values in the shoulder areas, which is considered to be resulting from the abrupt changes in the geometry of the carcass layer and the discontinuities in the material properties associated with the carcass and the belts. The tensile stress fields of the belt layers and the corresponding displacements are asymmetric about the circumferential axis, which is attributed to the asymmetric stacking sequence of the layers. The tensile stresses in the carcass layer are distributed nearly symmetrically about the contact patch centerline. An increase in the normal load tends to increase the stresses considerably in the elements in the vicinity of the shoulder area. The tensile stresses in belts 4 and 3, located near the carcass layers, are considerably larger than those observed in belts 2 and 1 located near the tread layer.

The shear stresses derived from the elements in the lateral center-line of the contact patch show that the out-of-tire-plane inter-ply shear stresses S_{yz} are over ten times higher than the in-tire-plane stresses S_{xz} developed between the belt 4 and the carcass layer. The influence of normal load on the S_{xz}, however, is more significant than that on S_{yz}. The out-of-tire-plane shear stresses S_{yz} developed between the carcass layer and belt 4, are significantly higher than the corresponding shear stresses generated between the belt layers near the shoulder area. The peak values of S_{xz} generated between the belt layers tend to move further away from the center of the contact patch to the outer periphery in the cross-section of the tire when normal load increases. The peak values of

S_{yz} and S_{xz} occurring near the shoulder area may be considered as the main factors causing the delamination damage in the tire.

The contact geometry and the normal force-deflection characteristics of the tire model are compared with the laboratory-measured data over a wide range of normal loads and inflation pressures to examine the model validity. The comparisons revealed reasonably good agreements between the model results and the measured data in a qualitative sense.

The validated tire model is employed in the following chapter to perform the parametric study to investigate the influence of variations in the structural and geometric parameters on the maximum inter-ply shear stresses in the belt layers. The parametric study aims to derive a more desirable structural configuration that may lead to lower magnitudes of the maximum shear stresses in the belt layers under a range of normal loading conditions.

CHAPTER 4 PARAMETRIC STUDY ON SHEAR INTERACTIONS IN A TRUCK TIRE

4.1 INTRODUCTION

A radial tire structure can be described as a non-rigid inflated torus composed of a flexible carcass of high-tensile cords restricted by stiff belts and fastened to steel beads. The belts stabilize the tire casing in radial direction, provide rigidity to the tread region and enhance the structural integrity to realize desired tire behavior. The tire response characteristics to an applied load, expressed in terms of stresses, strains and deformations of different layers, are inherently dependent on various tire structural parameters, such as angle of cords in each layer, number of layers used in the belts and material properties of different layers [5, 129]. The tire behavior under specific inflation pressure and normal load may further be influenced by its geometric features described by aspect ratio, rim radius, tread depth, etc. [171].

While fiber stresses in a rolling tire relate to cornering and traction properties of the tire, the shear stresses developed in different belt layers, and at the belt and the carcass interface directly affect the stability and integrity of the tire structure. Most of the reported models do not reflect the complexity of a real tire and thus could not incorporate the concerned shear interactions, since they are primarily based on linear analysis of the multi-layered system, assuming small deformations of anisotropic layers and negligible shear interactions between the layers [4, 5]. Too high a magnitude of inter-ply shear stress in the belts may cause delamination damage. The analysis of the structural integrity and stability characteristics of tires thus necessitates the analyses of the inter-ply shear stresses in a multi-layered loaded tire. Only limited efforts, however, have been made to analyze the inter-ply shear stress fields and distribution of fiber forces in individual layers of tires [57, 126-127]. The majority of the reported studies focus on the car tires, where the variations in operating loads and inflation pressure are considered to be small. The heavy vehicle tires differ considerably from the car tires in geometry, material properties of the layers, and especially the loading conditions. The structural analysis of truck or bus tires have been addressed in only few studies [129], specifically the influence of variations in the operating and design parameters on the fiber forces and inter-ply shear stresses in a loaded truck tire have not been investigated.

In this chapter, the nonlinear finite element tire model developed in Chapter 3 is employed to conduct a parametric study on the shear stresses developed in the belt layers in a truck tire. The effects of variations in the geometric and anisotropic material properties of the individual layers in the multi-layered system, and the orientations of the cords in different layers on the maximum inter-ply shear stresses are investigated. The parameters considered concerning the geometry of the tire include the aspect ratio, rim radius and tread depth. The parameters related to structural features and material properties of individual layers in the belts, such as the cord angle, total number of belt layers under the crown and number of twisted cords per unit width of an individual layer, are further considered. The influences of these parameters on the maximum shear stresses developed in individual belt layers are investigated for a non-rolling radial truck tire with 690.3 kPa (100 psi) inflation pressure, and 20 and 30 mm normal deflections. The results are analyzed to derive a more desirable set of geometric and structural parameters in order to reduce the maximum shear stresses in the belt layers of a loaded tire. The maximum inter-ply shear stresses computed using the proposed set of parameters are compared with the stresses derived corresponding to the nominal tire parameters to demonstrate the potential benefits of the selected parameters.

4.2 PERFORMANCE MEASURES AND PARAMETERS SELECTION

The peak shear stresses developed between the individual layers due to inflation and normal load, which are considered to be one of the main cause of delamination failure of a tire, can be investigated in the belt plane (S_{yz}), the tire plane (S_{xy}) and the axle plane normal to the tire plane (S_{xz}). Since a radial truck tire comprises of multiple belt layers, the first step in investigating the influence of the various structural parameters on the maximum shear interactions between belt layers is to determine the stress fields developed in the above mentioned planes for each belt layer under certain loading conditions. The magnitudes of the shear stress fields in each plane are then compared to identify the plane that encounters the maximum value of the peak shear stresses. The subsequent parametric study can then be focused on the influence of the individual parameters on the maximum values of stresses in the concerned plane. The parameters involved in the investigation are selected based upon their effectiveness concerning the anisotropy of the individual layers, the structural components and the geometry of the tire in order to derive a more desirable structural configuration that can lead to lower maximum shear stresses in a loaded tire.

The cord angles in belt layers, total number of cord-reinforced layers in the belt and number of cord ends per unit of width of each layer are among the most important structural parameters of a tire. Since the belt layers containing different cord angles are essential in stabilizing the tire casing in radial direction and are in a highly stressed state, these anisotropic-property-related parameters directly affect the stress response of a loaded tire. The primary geometric parameters affecting the configuration of a tire may include the aspect ratio, rim radius and tread depth. The effects of these geometric parameters on the inter-ply shear stress field of a truck tire have not been reported.

The variations in a single structural/geometric parameter, however, may yield variations in the tire's normal load and load-deflection characteristics. The selected parameters are thus varied within a relatively small range, such that the resulting influence on the load-deflection characteristics is minimal, as illustrated in Figure 4.1 to 4.6, where a single parameter is varied, while the remaining parameters are held at their nominal values. The results show that the variations in the structural and geometric parameters within the considered ranges affect the load-deflection characteristics in an

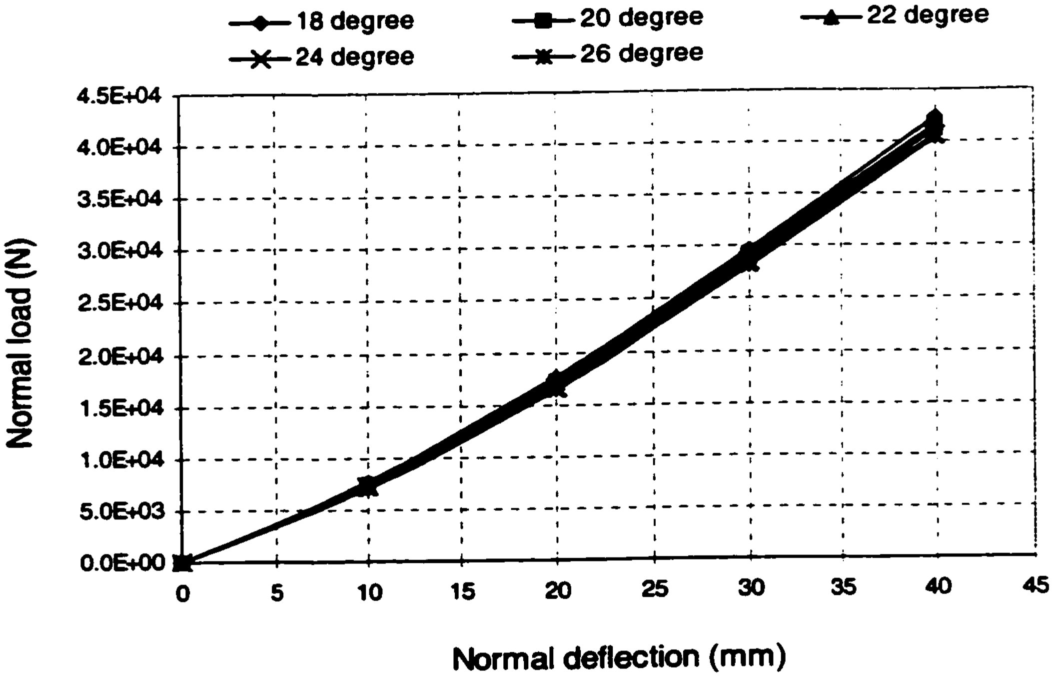

Figure 4.1: Effect of variations in the cord angle in the individual layers on the tire load-deflection characteristics, p_i = 828.4 kPa (120 psi).

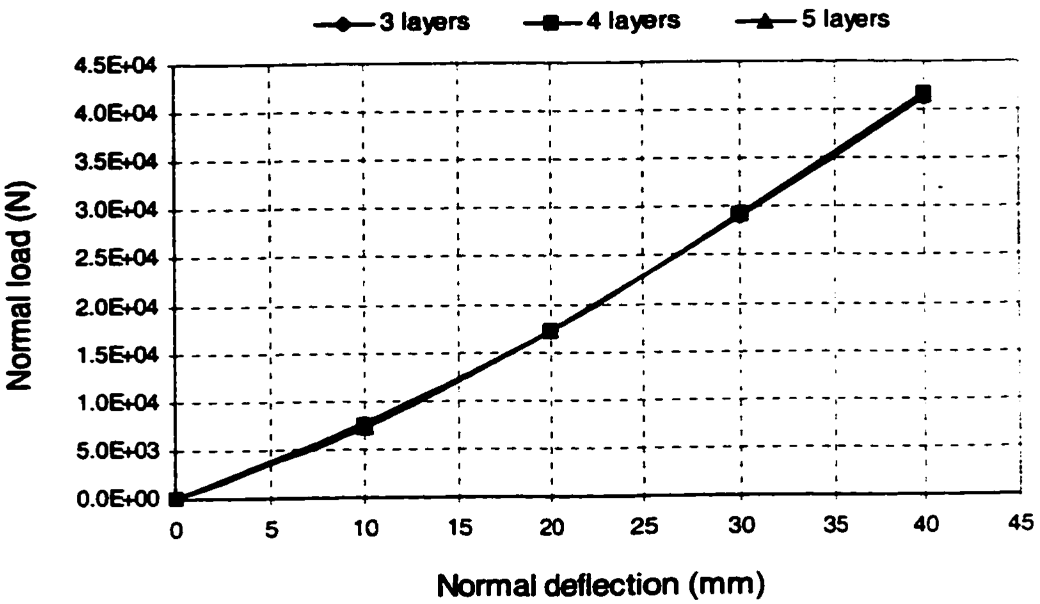

Figure 4.2: Effect of variations in the number of layers in the belt on the tire load-deflection characteristics, p_i = 828.4 kPa (120 psi).

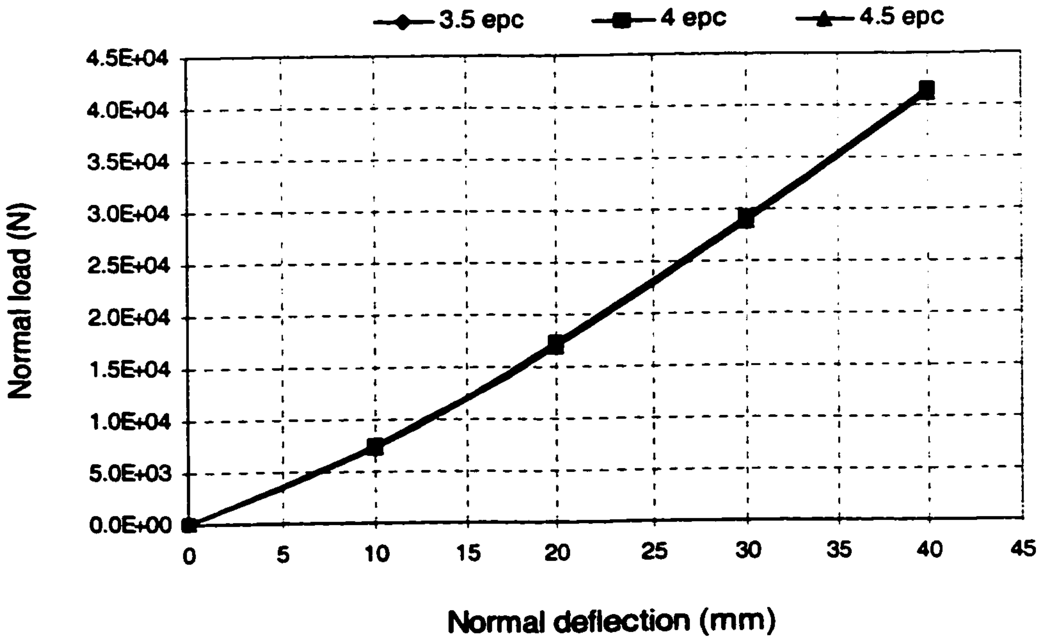

Figure 4.3: Effect of variations in the amount of twisted cord ends per centimeter (*epc*) in each layer on the tire load-deflection characteristics, p_i = 828.4 kPa (120 psi).

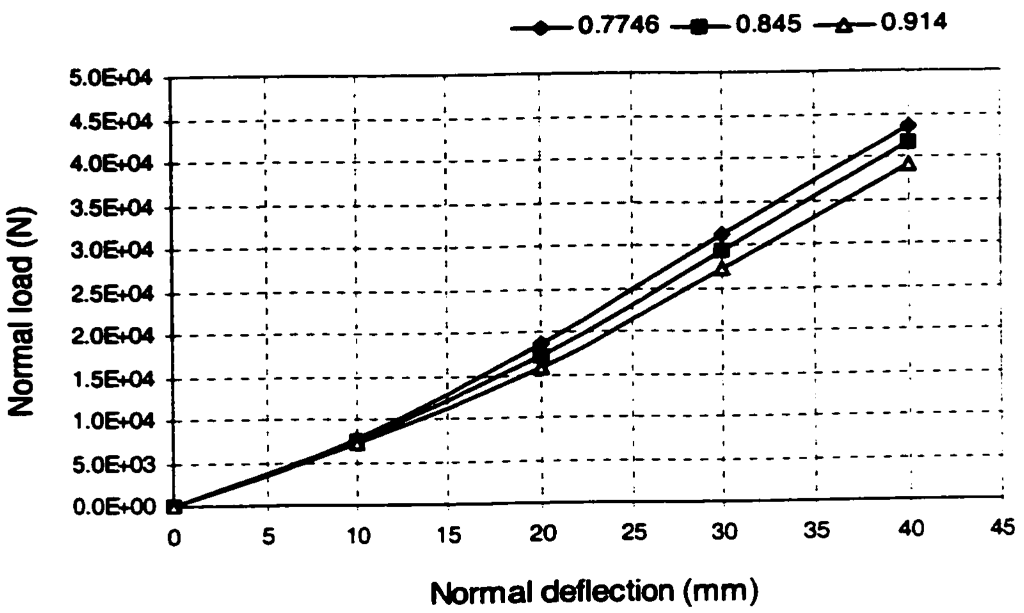

Figure 4.4: Effect of variations in aspect ratio on the tire load-deflection characteristics, p_i = 828.4 kPa (120 psi).

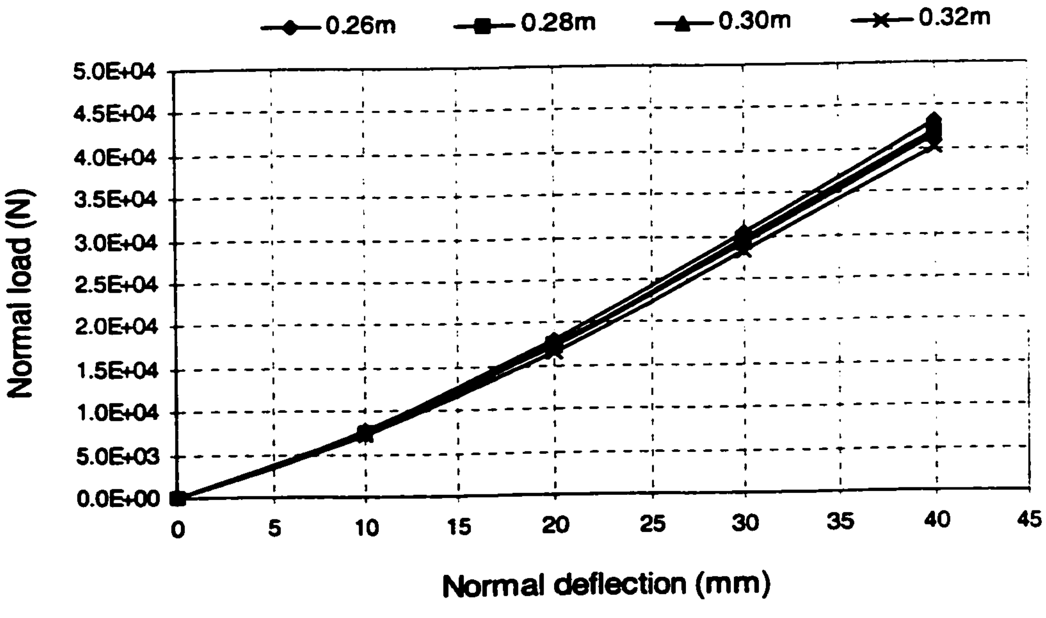

Figure 4.5: Effect of variations in rim radius on the tire load-deflection characteristics, p_i = 828.4 kPa (120 psi).

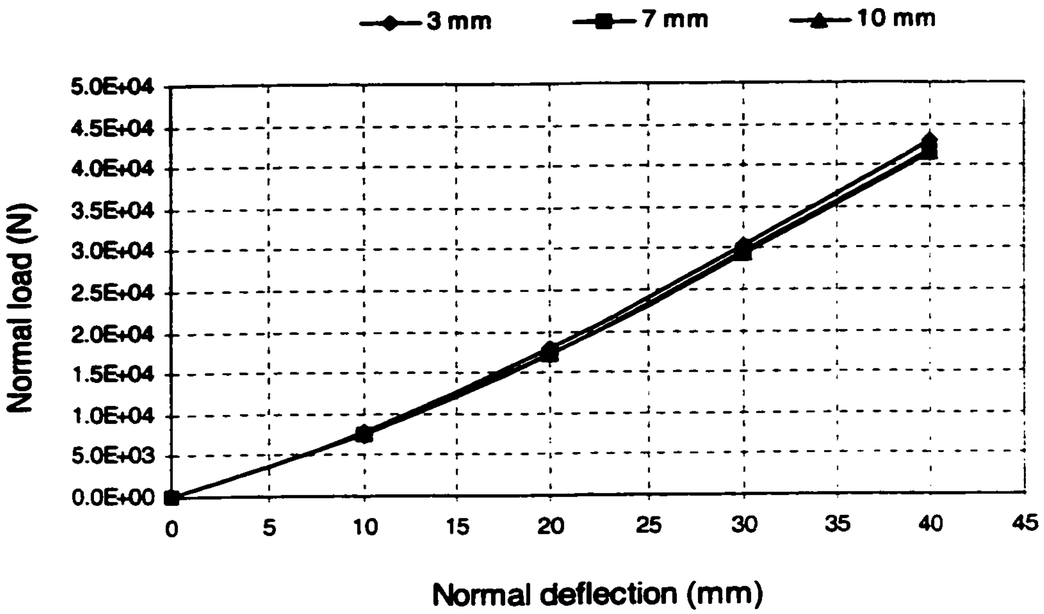

Figure 4.6: Effect of variations in tread depth on the tire load-deflection characteristics, p_i = 828.4 kPa (120 psi).

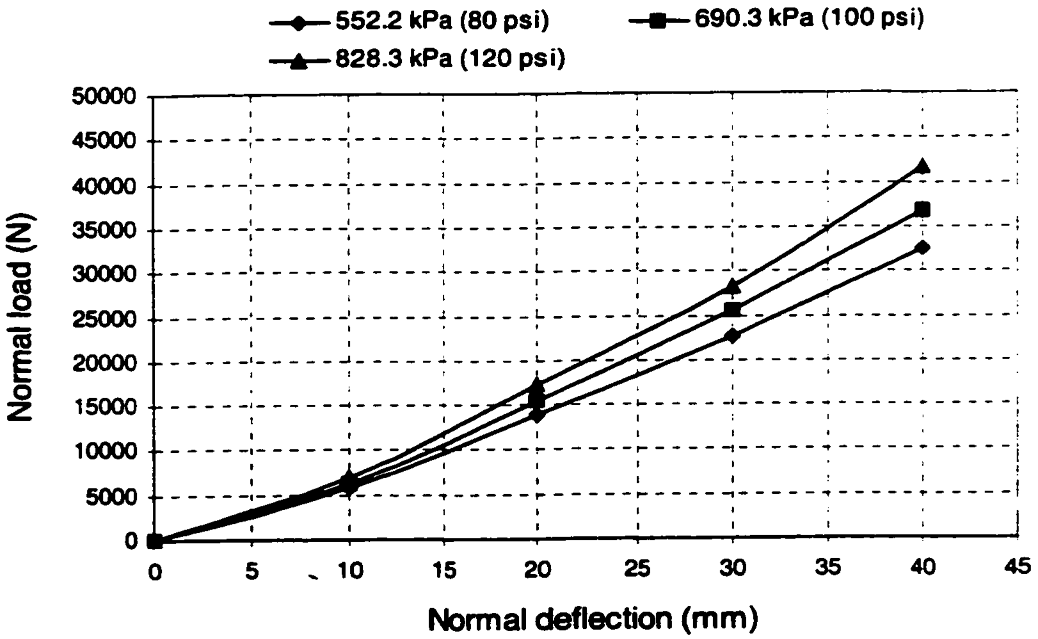

Figure 4.7: Effect of variations in inflation pressure on the tire load-deflection characteristics, p_i = 828.4 kPa (120 psi).

insignificant manner. The variations in the selected parameters, however, are considered to be sufficiently large to illustrate their effects on the maximum shear stresses in the layers for given normal load and inflation pressure. The variations in the inflation pressure, however, significantly influence the tire load-deflection characteristics, as illustrated in Figure 4.7. An increase in the inflation pressure yields higher tire stiffness.

Based on the above observations and consideration of the limitation of the software concerning the load application in the involved contact problem, constant deflection condition was chosen to conveniently perform the parametric analysis. The results of the parametric study are considered to be valid for nearly constant load condition, which is considered to be representative of the loading conditions for an in-service tire. It should be mentioned here that material properties employed in the model are estimated from the data reported in various published studies as described in Chapter 3. The geometric configuration of the tire was selected from the measurements performed on a 12.5R22.5 truck tire. In view of the estimated material properties, the results derived from the model are considered to describe the tire response in a qualitative manner. The application of the proposed methodology and model in conjunction with adequately measured material properties of the layers in belts and carcass casing, however, are expected to yield a quantitative analysis of a specific tire. In the following analysis, the inflation pressure, the normal deflection and thus the normal load are considered as the primary operating parameters that affect the maximum shear interaction in the belt layers of the loaded tire.

Figure 4.8(a) illustrates an isometric view of the inflated tire subject to a static normal deflection as represented in the ANSYS® software. In Figure 4.8(b), the deflected

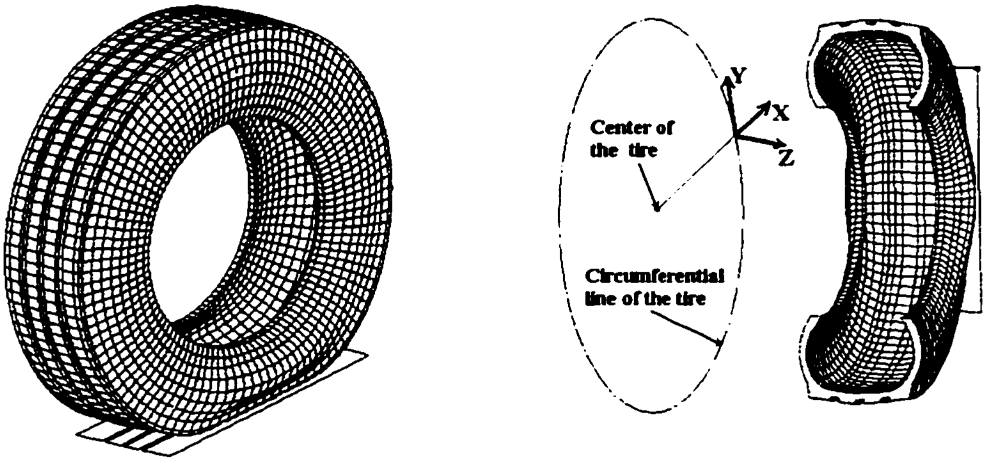

(a) (b)

Figure 4.8: Isometric view of the deflected tire: (a) deflected tire (b) capped view of the rotated deflected tire and the coordinate system.

tire is rotated by approximately 90 degrees for convenient viewing of the maximum shear stress field in each belt layer. The figure also shows the cylindrical coordinate system used in the subsequent parametric study, where x-axis represents the radial direction, y-axis represents the tangential direction along the circumferential line of the tire and z-axis represents a direction parallel to the axle. Figure 4.9 to 4.11 illustrate the shear stress fields (S_{yz}, S_{xy} and S_{xz}) for each individual belt layers as a function of the inflation pressure. The stress fields are estimated under a constant normal deflection: $\Delta Z = 30$mm, using the pre-estimated nominal structural parameters. The nominal simulation parameters used in the analyses are: tread depth = 10 mm, total number of belts = 4, *epc* (amount of cord ends per centimeter) for each layer = 4, cord angle = ±22 degrees, rim radius = 0.3m, and aspect ratio = 0.845. In the above figures, S_{xy} and S_{xz} represent the shear stresses in the wheel plane and in the transverse plane of the tire, respectively, while the S_{yz} represents the shear stresses in the belt plane.

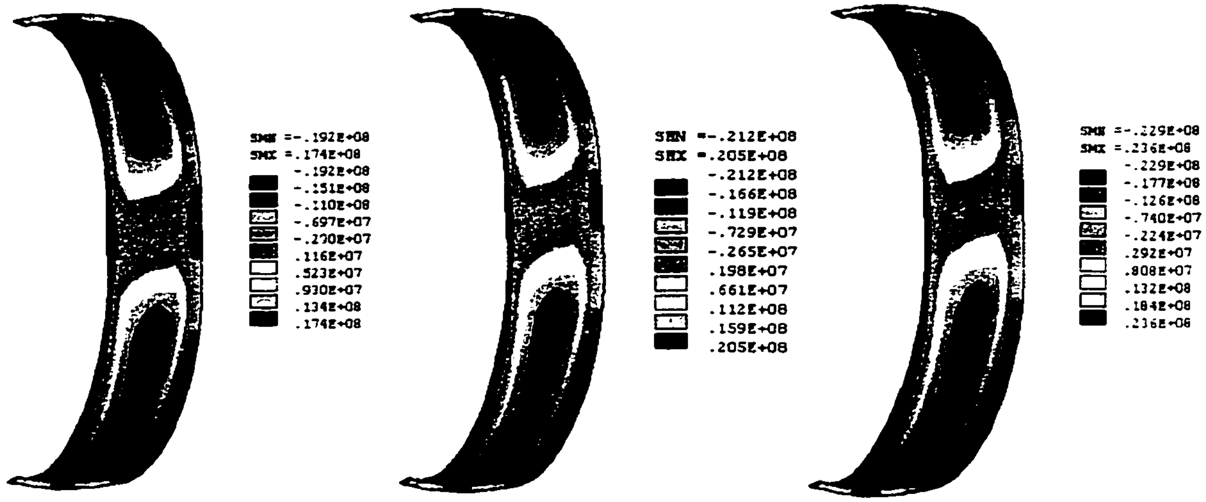

552.2 kPa (80 psi) 690.3 kPa (100 psi) 828.4 kPa (120 psi)

(a)

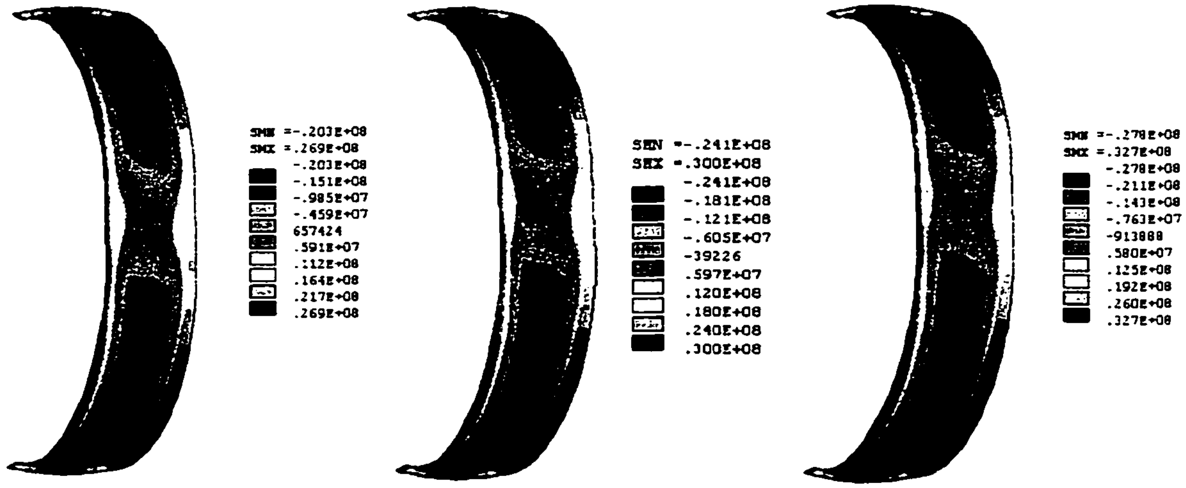

552.2 kPa (80 psi) 690.3 kPa (100 psi) 828.4 kPa (120 psi)

(b)

*Figure 4.9: Shear stress S_{yz} fields in the different belt layers, ΔZ = 30mm: (a) layer 1; (b) layer 2; (c) layer 3; and (d) layer 4.

**Note: SMN is the minimum value of the plotted item; SMX is the maximum bounded value of the plotted item. The unit of the stress value shown in the legend is Pascal (Pa).*

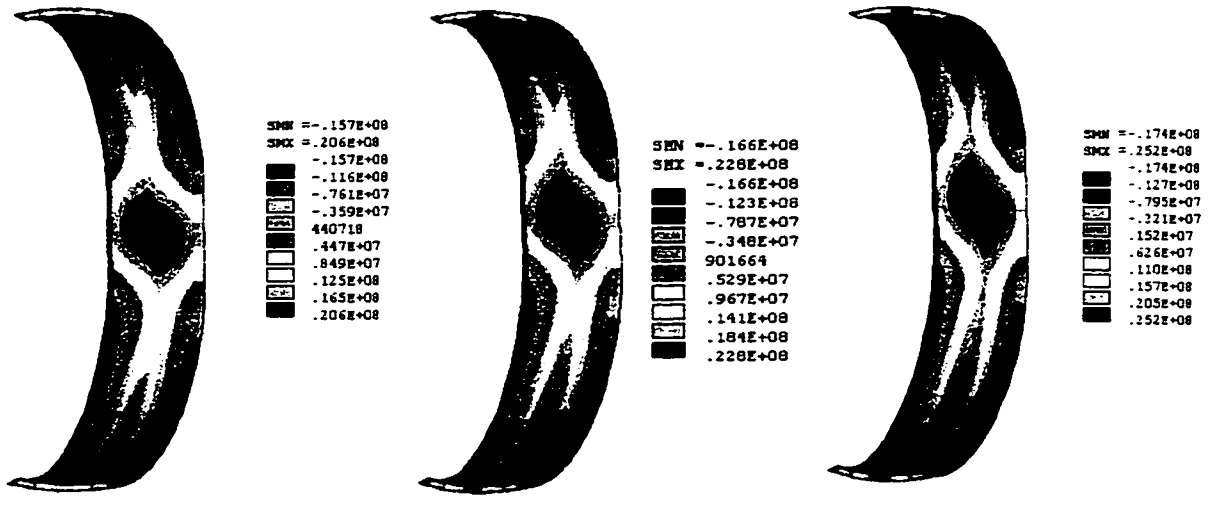

552.2 kPa (80 psi) 690.3 kPa (100 psi) 828.4 kPa (120 psi)

(c)

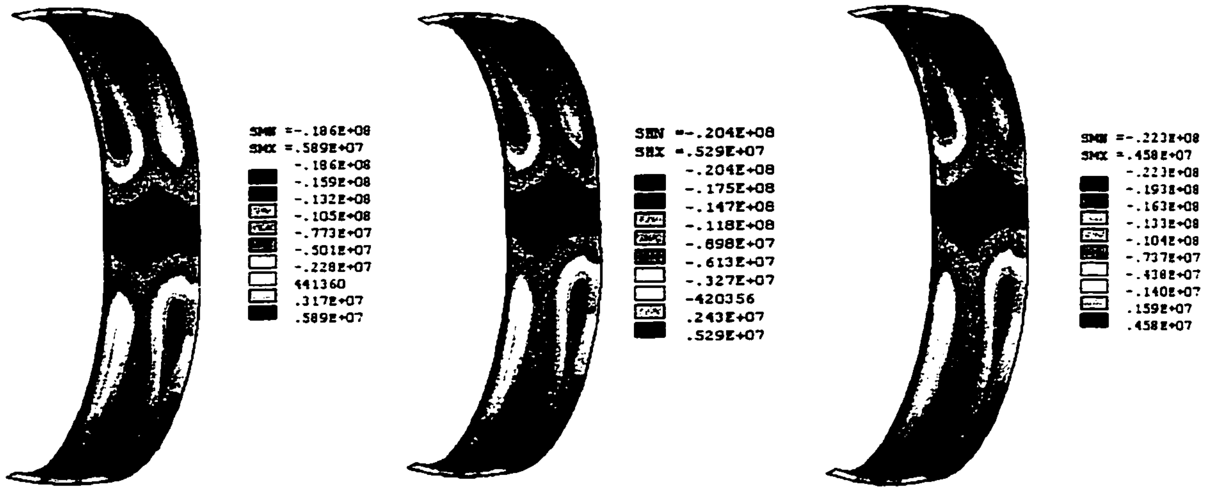

552.2 kPa (80 psi) 690.3 kPa (100 psi) 828.4 kPa (120 psi)

(d)

*Figure 4.9: Shear stress S_{yz} fields in the different belt layers, ΔZ = 30mm: (a) layer 1; (b) layer 2; (c) layer 3; and (d) layer 4. (Continued)

**Note: SMN is the minimum value of the plotted item; SMX is the maximum bounded value of the plotted item. The unit of the stress value shown in the legend is Pascal (Pa).*

552.2 kPa (80 psi) 690.3 kPa (100 psi) 828.4 kPa (120 psi)

(a)

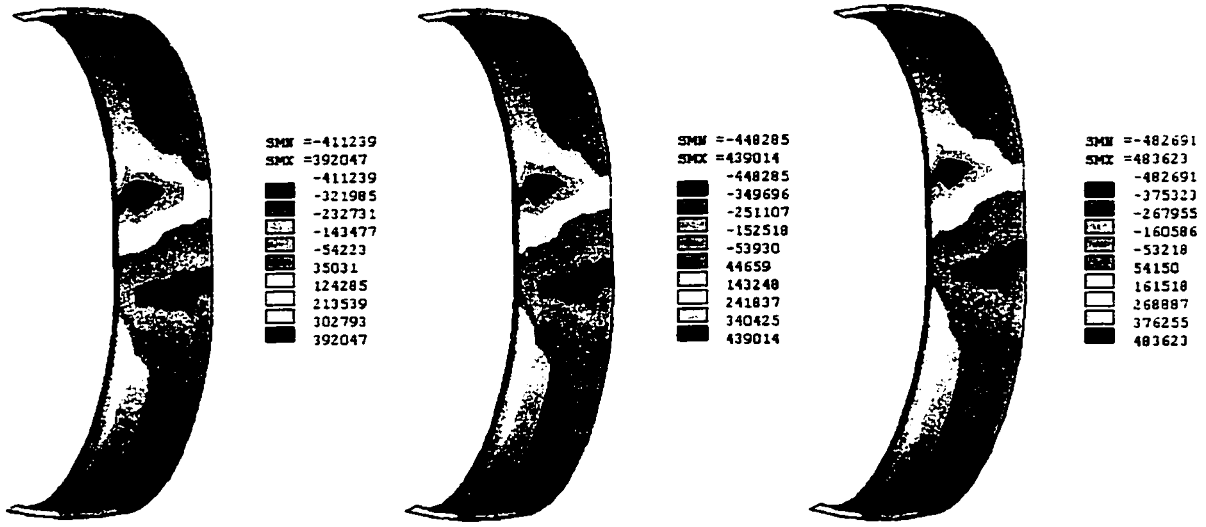

552.2 kPa (80 psi) 690.3 kPa (100 psi) 828.4 kPa (120 psi)

(b)

*Figure 4.10: Shear stress S_{xy} fields in the different belt layers, ΔZ = 30mm: (a) layer 1; (b) layer 2; (c) layer 3; and (d) layer 4.

**Note: SMN is the minimum value of the plotted item; SMX is the maximum bounded value of the plotted item. The unit of the stress value shown in the legend is Pascal (Pa).*

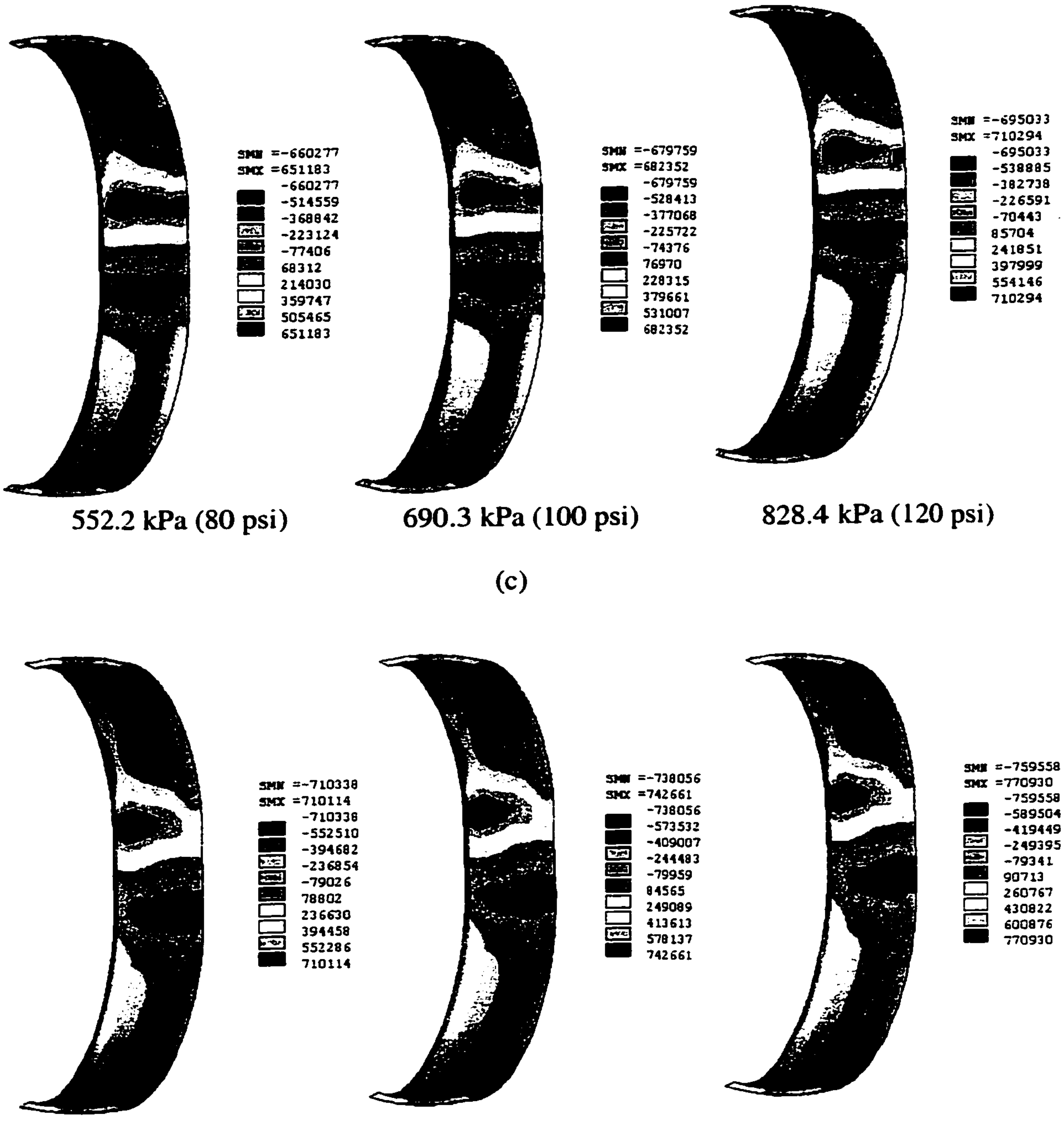

552.2 kPa (80 psi) 690.3 kPa (100 psi) 828.4 kPa (120 psi)

(c)

552.2 kPa (80 psi) 690.3 kPa (100 psi) 828.4 kPa (120 psi)

(d)

*Figure 4.10: Shear stress S_{xy} fields in the different belt layers, ΔZ = 30mm: (a) layer 1; (b) layer 2; (c) layer 3; and (d) layer 4. (Continued)

**Note: SMN is the minimum value of the plotted item; SMX is the maximum bounded value of the plotted item. The unit of the stress value shown in the legend is Pascal (Pa).*

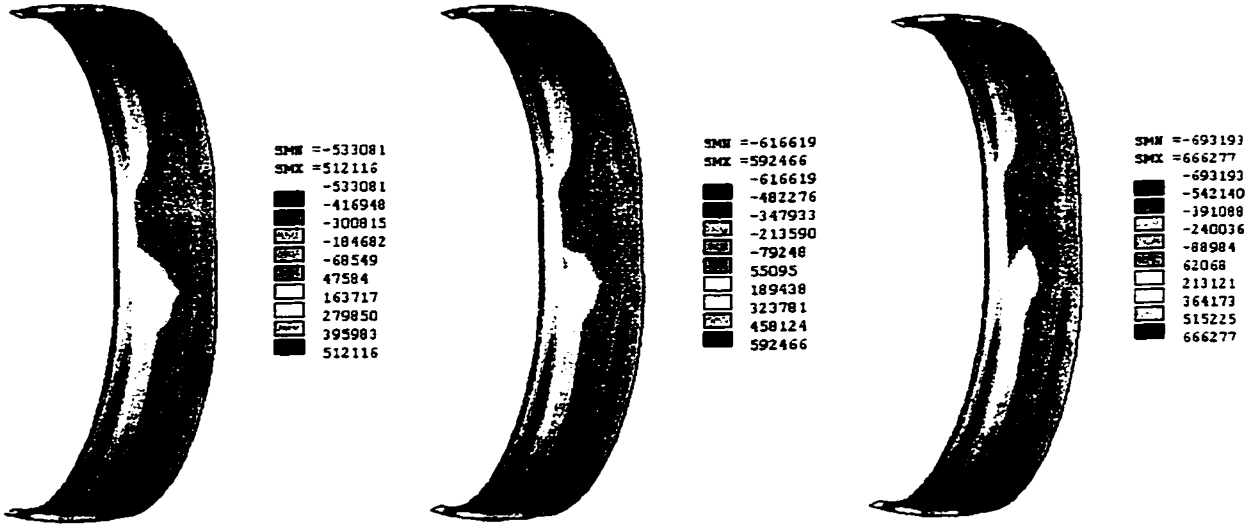

552.2 kPa (80 psi) 690.3 kPa (100 psi) 828.4 kPa (120 psi)

(a)

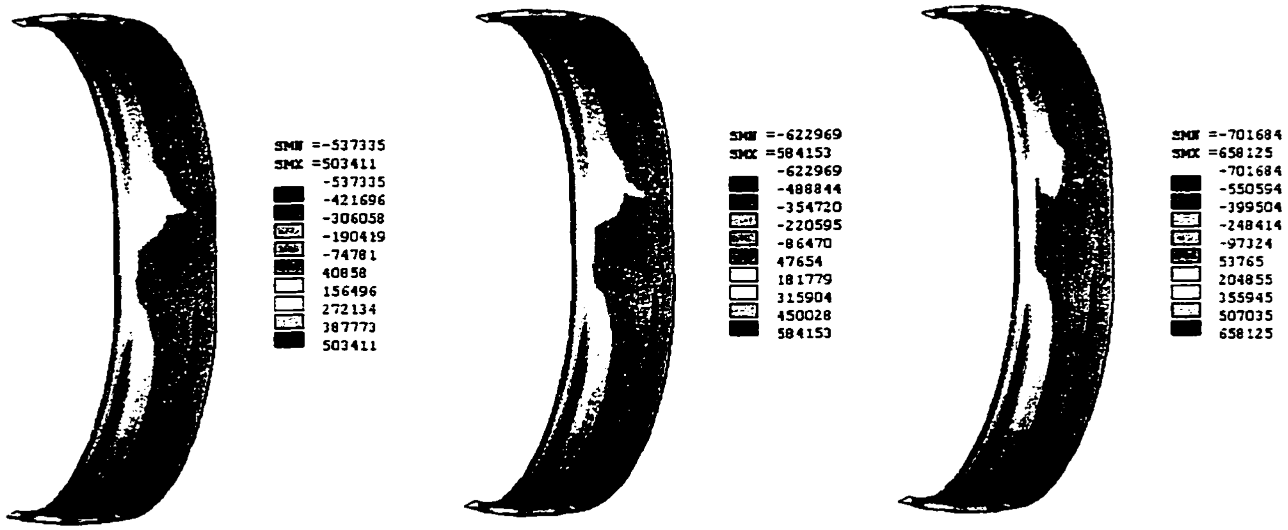

552.2 kPa (80 psi) 690.3 kPa (100 psi) 828.4 kPa (120 psi)

(b)

*Figure 4.11: Shear stress S_{xz} fields in the different belt layers, $\Delta Z = 30$mm: (a) layer 1; (b) layer 2; (c) layer 3; and (d) layer 4.

**Note: SMN is the minimum value of the plotted item; SMX is the maximum bounded value of the plotted item. The unit of the stress value shown in the legend is Pascal (Pa).*

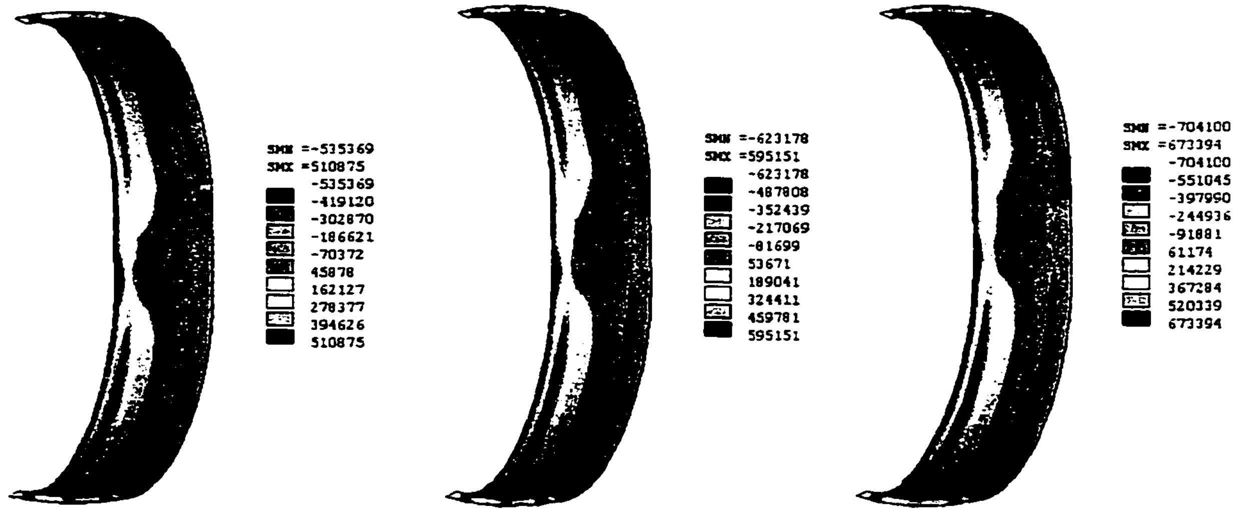

552.2 kPa (80 psi) 690.3 kPa (100 psi) 828.4 kPa (120 psi)

(c)

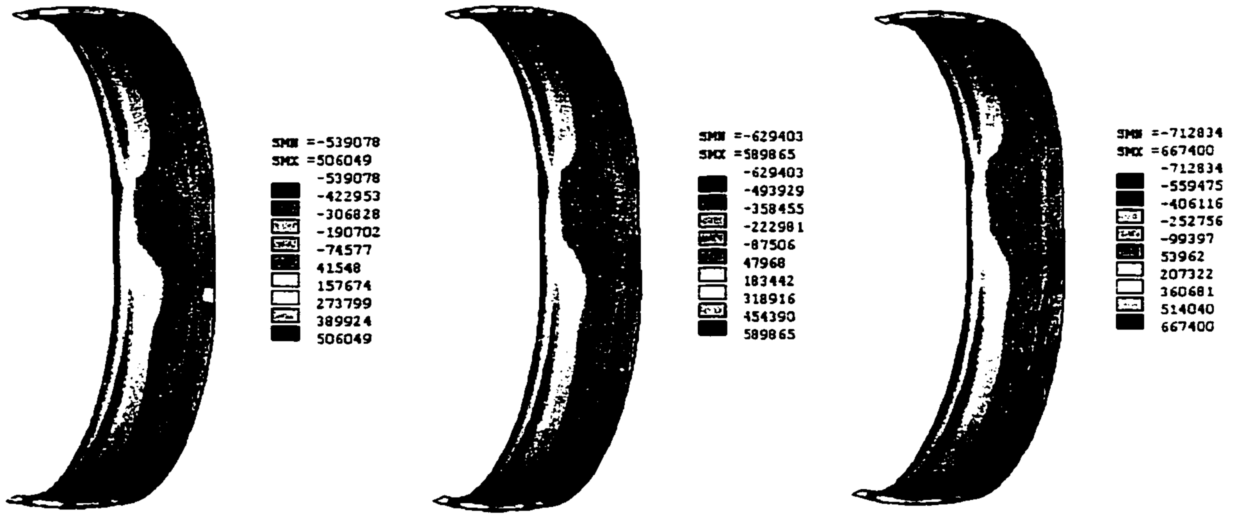

552.2 kPa (80 psi) 690.3 kPa (100 psi) 828.4 kPa (120 psi)

(d)

*Figure 4.11: Shear stress S_{xz} fields in the different belt layers, $\Delta Z = 30\text{mm}$: (a) layer 1; (b) layer 2; (c) layer 3; and (d) layer 4. (Continued)

**Note: SMN is the minimum value of the plotted item; SMX is the maximum bounded value of the plotted item. The unit of the stress value shown in the legend is Pascal (Pa).*

The layers 1 and 2, closer to the tread, reveal concentration of high shear stresses S_{yz} in the central portions of the belt near the edges and extremities of the contact patch, as illustrated in Figure 4.9. Moreover, both layers also reveal high stresses in the central regions on both sides out of the contact patch. The layers 3 and 4, located closer to the carcass, however, yield concentration of S_{yz} near the center of the contact patch. The layer 4 further yields high magnitude of S_{yz} on the two opposite edges of the belt, farther from the contact patch center. The layer 3 also reveals high values of S_{yz} in its central portion along the circumferential line of the tire farther away from the contact patch, when the inflation pressure is higher than 690.3 kPa.

The Figure 4.10 and 4.11 illustrate the S_{xy} and S_{xz} fields in different belt layers for different inflation pressure loading conditions and constant normal deflection (ΔZ = 30mm), respectively. The results show relatively high values of the shear stresses S_{xy} in layers 1, 2 and 4, which occur near the edges of the contact patch. The peak stresses S_{xy} in layers 2 and 4 tend to shift towards the edges of the belt when the inflation pressure increase from 552.2 to 828.4 kPa. The distributions and locations of the peak stresses in layers 1 and 4, however, are only slightly affected by the increase in the inflation pressure. The high stresses S_{xy} in layer 3 appear to be concentrated in the opposite sides of the contact patch, near the edges of the contact region. The magnitudes and concentration of S_{xy} increase considerably with increase in the inflation pressure. The peak values of S_{xz} developed in each layer, however, tend to concentrate near the edges of the individual belt away from the contact patch. The variation in the inflation pressure yields almost negligible influence on the distribution of the S_{xz}. The magnitudes of S_{xz} in the individual layers, however, increase with increase in the inflation pressure. The results clearly show that the magnitudes of the shear stresses S_{xz} and S_{xz} are considerably lower than those of the S_{yz} developed in the belt layers. The effects of variations in the selected parameters on the peak shear stresses are presented in the following section.

4.3 PARAMETRIC STUDY

The distributions of the fiber forces along the circumferential line of a pneumatic tire have been investigated in many studies [5, 15, 57 and 126]. The distributions of shear stress fields within each belt as function of the loading conditions, however, have been attempted in only few studies [127]. This may be partly attributed to the complexities associated with the identification of material and geometric properties of individual layers in a multi-layered system.

The parametric study is initially performed to study the effects of variations in the operating parameters, such as normal load and inflation pressure, on the maximum shear stresses developed in the belt layers. The effects of variations in the structural and geometric parameters on the maximum shear stresses developed in the belt layers are then investigated for the truck tire with 100 psi (690.3 kPa) inflation pressure and constant normal deflections of 20 mm and 30 mm. These selected values of normal deflections represent normal loads in the order of 17 kN and 30 kN, respectively.

4.3.1 Influence of the Inflation Pressure and the Normal Load

The tire inflation pressure and normal load directly affect its radial stiffness characteristics, contact patch geometry and the contact pressure distributions in the tire-road interface. Moreover, the pressure and normal loads strongly influence the tire deformation and the stress fields developed in the cord-reinforced layers in the loaded tire. The influences of the variations in the inflation pressure and the normal load on the shear stress fields, especially the maximum shear stresses in different individual cord-reinforced layers have not been reported. The finite element model of the truck tire developed in this dissertation is used to study the trends in the peak shear stresses (S_{xy}, S_{xz} and S_{yz}) as functions of the inflation pressure and the normal deflection.

Figure 4.12 and 4.13 illustrate the maximum shear stresses (S_{xy}, S_{xz} and S_{yz}) in different belt layers as functions of the inflation pressure for specific normal deflection condition. The results show that all of the shear stresses in the wheel plane, the transverse plane and in the belt plane increase, with increase in the inflation pressure. This increase in the peak stresses is mostly attributed to the increased radial stiffness of the tire under a high inflation pressure that intensifies the stresses developed in the belt layers. The results reveal that increasing the inflation pressure from 690.3 kPa (100 psi) to 828.4 kPa (120 psi) results in significant increase in the maximum shear stresses S_{yz} in layer 2, and a relatively small increase in the maximum shear stresses S_{yz} in the other layers. The results further show nearly identical trends for both the normal deflections considered, while the magnitude of peak S_{yz} tends to be higher under 30mm normal deflection. The peak shear stresses in the transverse plane (S_{xz}) increase considerably with increase in the inflation pressure, while the corresponding increases in the peak shear stresses in the wheel plane (S_{xy}) are relatively small. A comparison of Figures 4.12 and 4.13 further reveals that peak magnitudes of S_{yz} are considerably larger than those of S_{xy} and S_{xz}.

Figure 4.14 illustrates the peak shear stresses in different belt layers as functions of normal deflection of the tire inflated at a pressure, $p_I = 100$ psi, and with the nominal

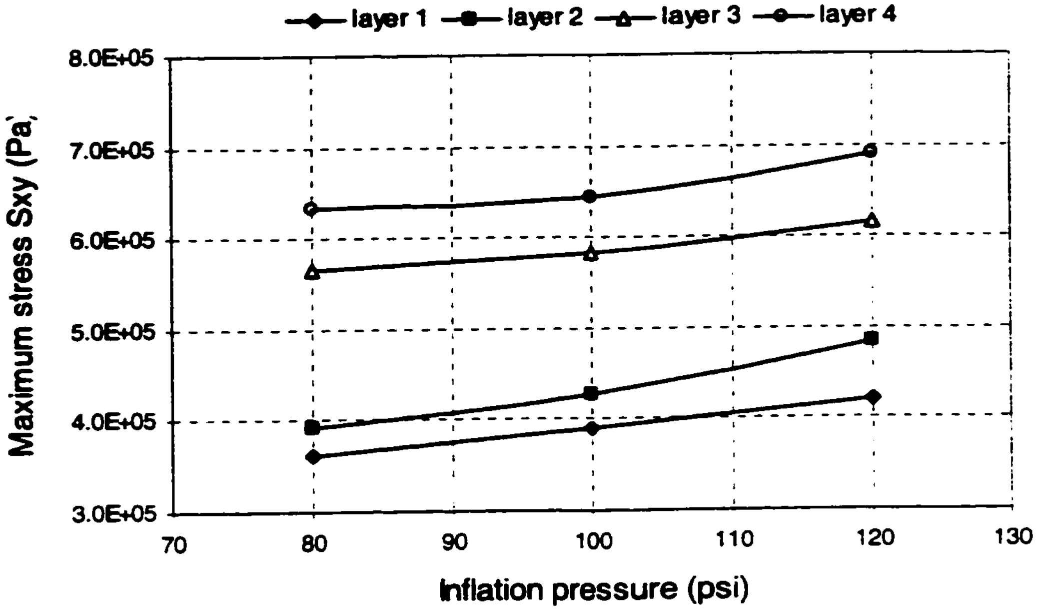

(a)

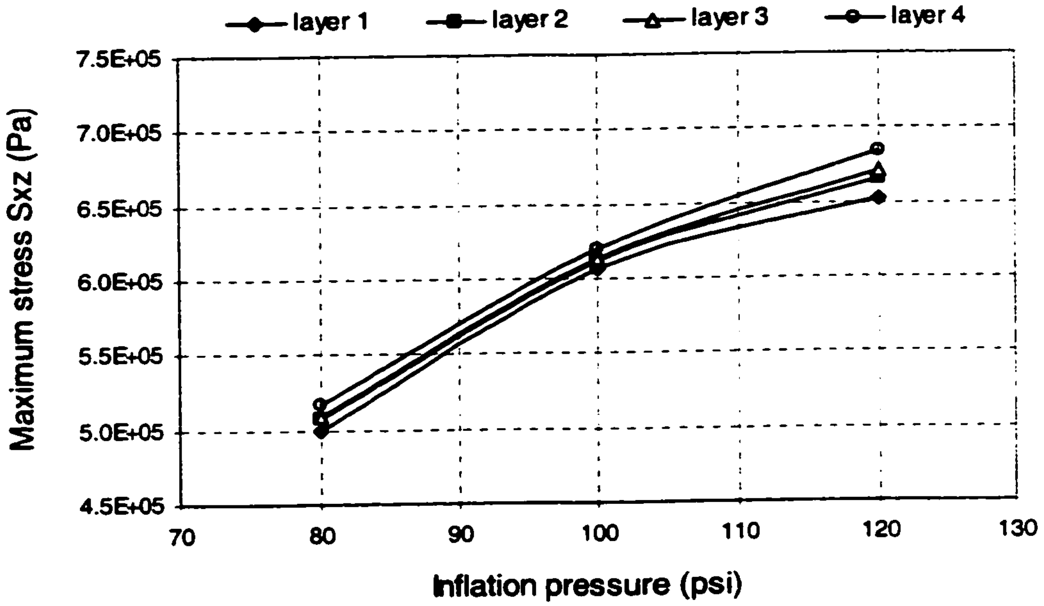

(b)

Figure 4.12: Influence of inflation pressure on the maximum shear stresses in different belt layer; $\Delta Z = 20$mm: (a) S_{xy} in the wheel plane; and (b) S_{xz} in the transverse plane.

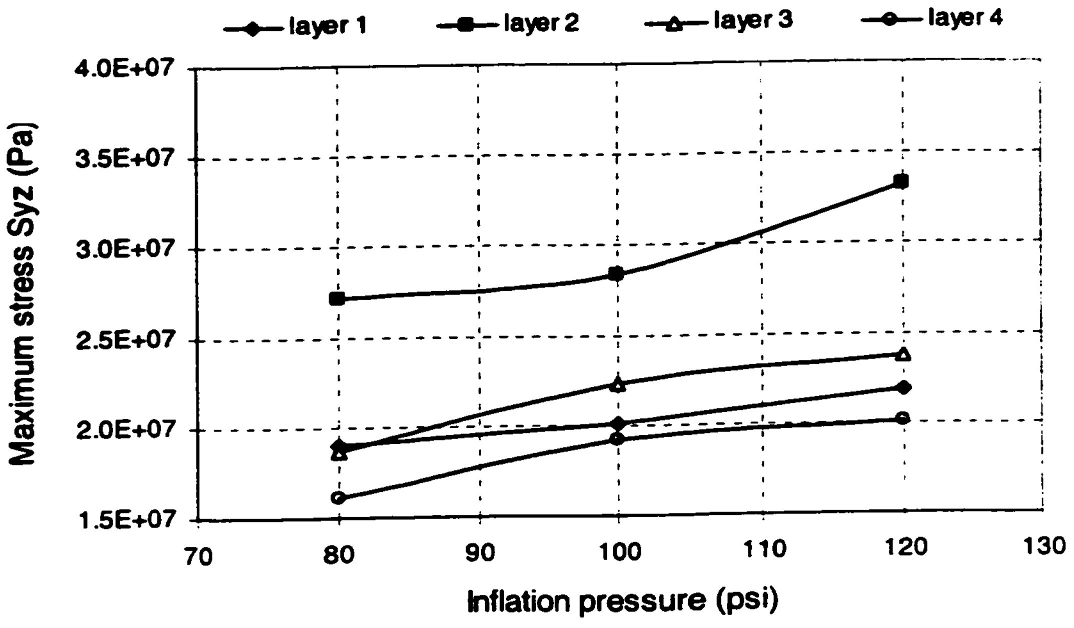

(a)

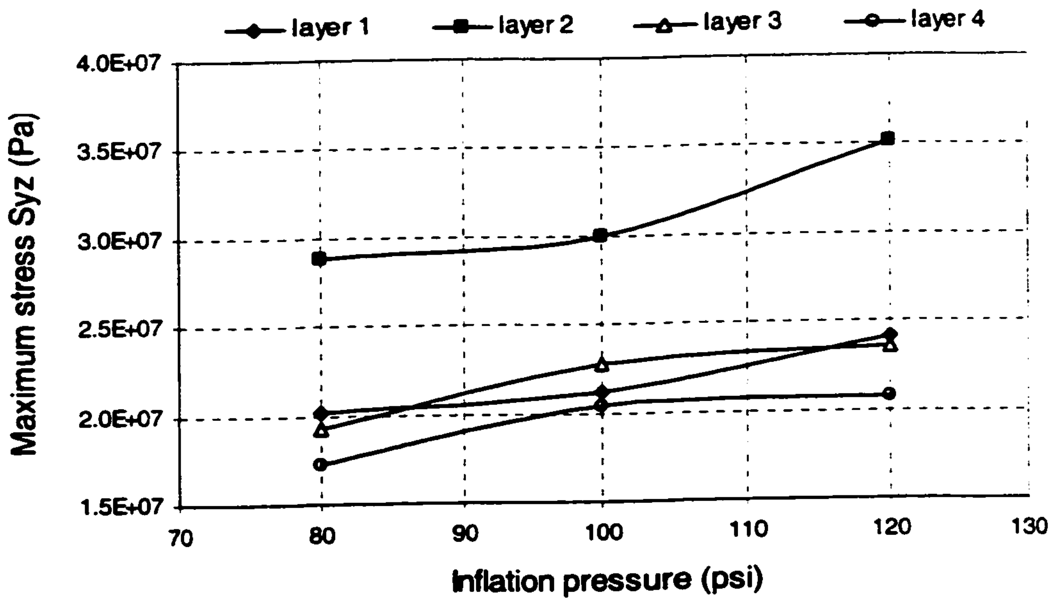

(b)

Figure 4.13: Maximum shear stresses (S_{yz}) in different belt layers as a function of the inflation pressure: (a) $\Delta Z = 20$mm; and (b) $\Delta Z = 30$mm.

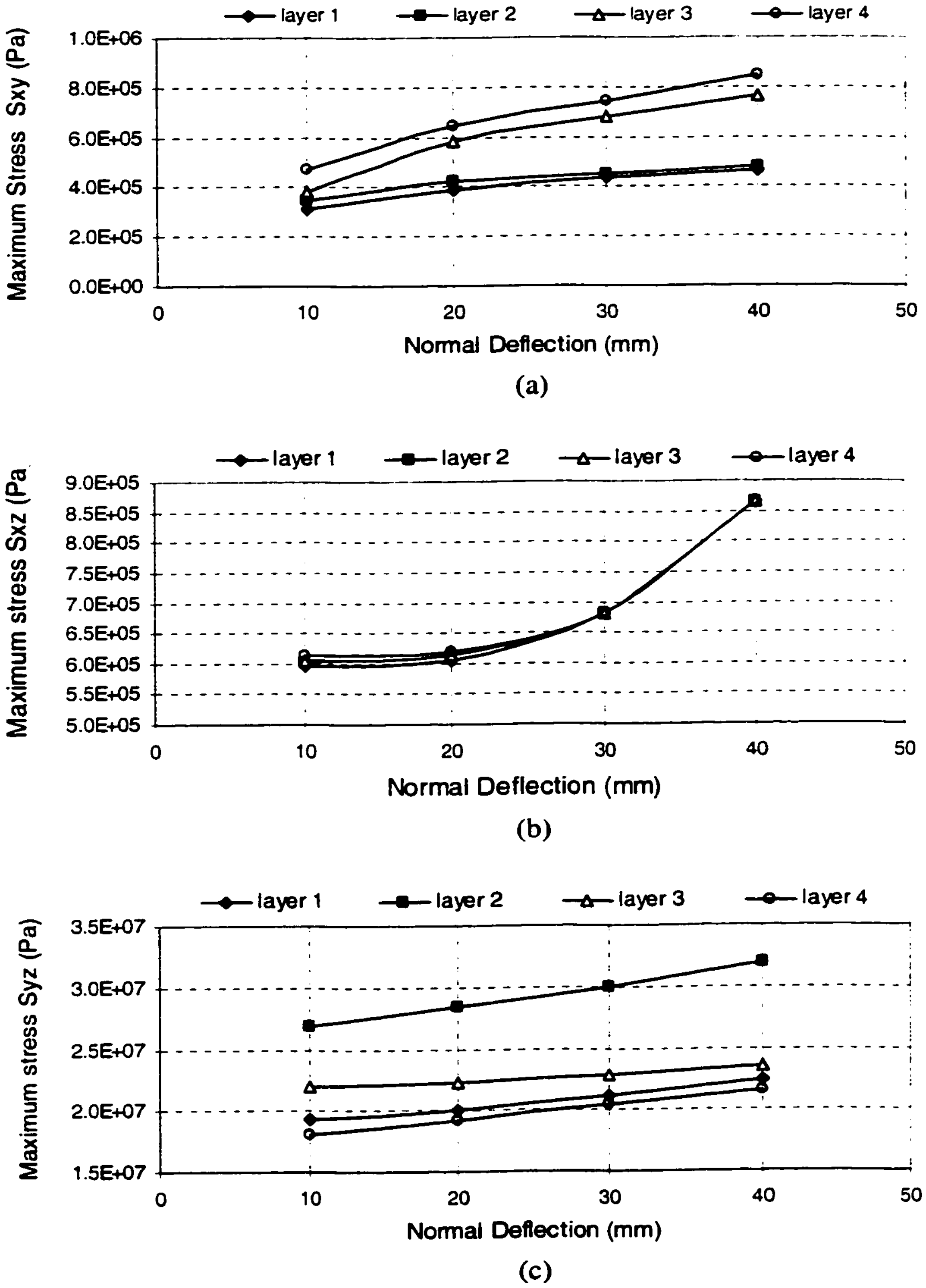

Figure 4.14: Maximum shear stresses in different belt layers as a function of the normal deflection; $p_l = 690.3$ kPa: (a) S_{xy} in the wheel plane; (b) S_{xz} in the transverse plane; and (c) S_{yz} in the belt plane.

structural and geometric parameters. The results show that the maximum shear stresses S_{xy} and S_{xz} increase significantly, in a nonlinear manner, with increase in the normal deflection and thus the normal load, while the S_{yz} increases almost linearly. The maximum shear stresses S_{xy} developed in layer 4 are the highest followed by those developed in layers 3, 2 and 1. An increase in the normal deflection yields only slight variations in the peak stresses S_{xz} in all the different layers. The maximum shear stress S_{yz} develops in layer 2, which tends to increase nearly linearly with the normal deflection. The lowest value of maximum shear stress S_{yz} occurs in layer 4, adjacent to the carcass layer. The results also show that the maximum value of the shear stresses (S_{yz}) in different layers are around 30 to 50 times higher than the corresponding shear stresses S_{xy} and S_{xz}, when normal deflection ΔZ is within the range of 20 to 30 mm for the considered loading condition. The subsequent parametric study is thus focused on the influence of various structural parameters on the maximum shear stress S_{yz}, with the loading conditions of 690.3 kPa (100 psi) inflation pressure, and 20 and 30 mm normal deflections. The maximum value of S_{yz} is considered as the main cause that could result in the delamination failure of tires. In the analysis, the layer 1 refers to the layer nearest to the tread and layer 4 lies adjacent to the carcass layers.

4.3.2 Influence of the Aspect Ratio

The aspect ratio of a tire affects its outline configuration and the dimensions of the cross section, and thus may influence the stress distribution properties of different layers. The aspect ratio of the selected tire is varied from 0.77 to 0.91 by varying only the radial coordinates of the element nodes at the rim edges. The section width and overall diameter of the tire thus remain unchanged, while the section height alone is varied to achieve different aspect ratios. Figure 4.15 illustrates the influence of variations in the aspect ratio on the maximum shear stresses, S_{yz}, developed between different belt layers of the tire subjected to an inflation pressure of 100 psi and normal deflections of 20 and 30 mm, respectively. The results show that increasing the aspect ratio yields a large increase in the maximum shear stress S_{yz} in layer 2, and relatively small increase in the layer 1, irrespective of the normal load considered. This may be due to the fact that increasing the aspect ratio enlarges the coupling effects between the bending and twisting movements of the cord reinforced belt layer 2 relative to its adjacent layers 1 and 3. The influence of variations in the aspect ratio on the maximum shear stresses S_{yz} in layer 1 is considerably less than that observed for layer 2. This may be attributed to its adjacent rubber layer connecting with the tread, which considerably alleviates the shear stress concentration on the top surface of the layer 1. The peak values of S_{yz} in layer 3 and 4, however, decrease with increase in the aspect ratio. The layer 4 has a radially arranged cord reinforced carcass layer as its adjacent layer, while the layer 3 is located in the core of the multi-layered system. The effects of variations in the aspect ratio on the stresses in both the layers are therefore relatively small, when the tire is deformed. The results suggest that peak shear stresses developed in the belt layers could be reduced with lower aspect ratio tire design.

It is further observed that a larger normal deflection and thus the higher normal load yields higher maximum shear stresses S_{yz} in all the layers for different aspect ratios. Table 4.1 summarizes the percent increase in S_{yz}, when tire deflection is increased from 20 mm to 30 mm, for different aspect ratios.

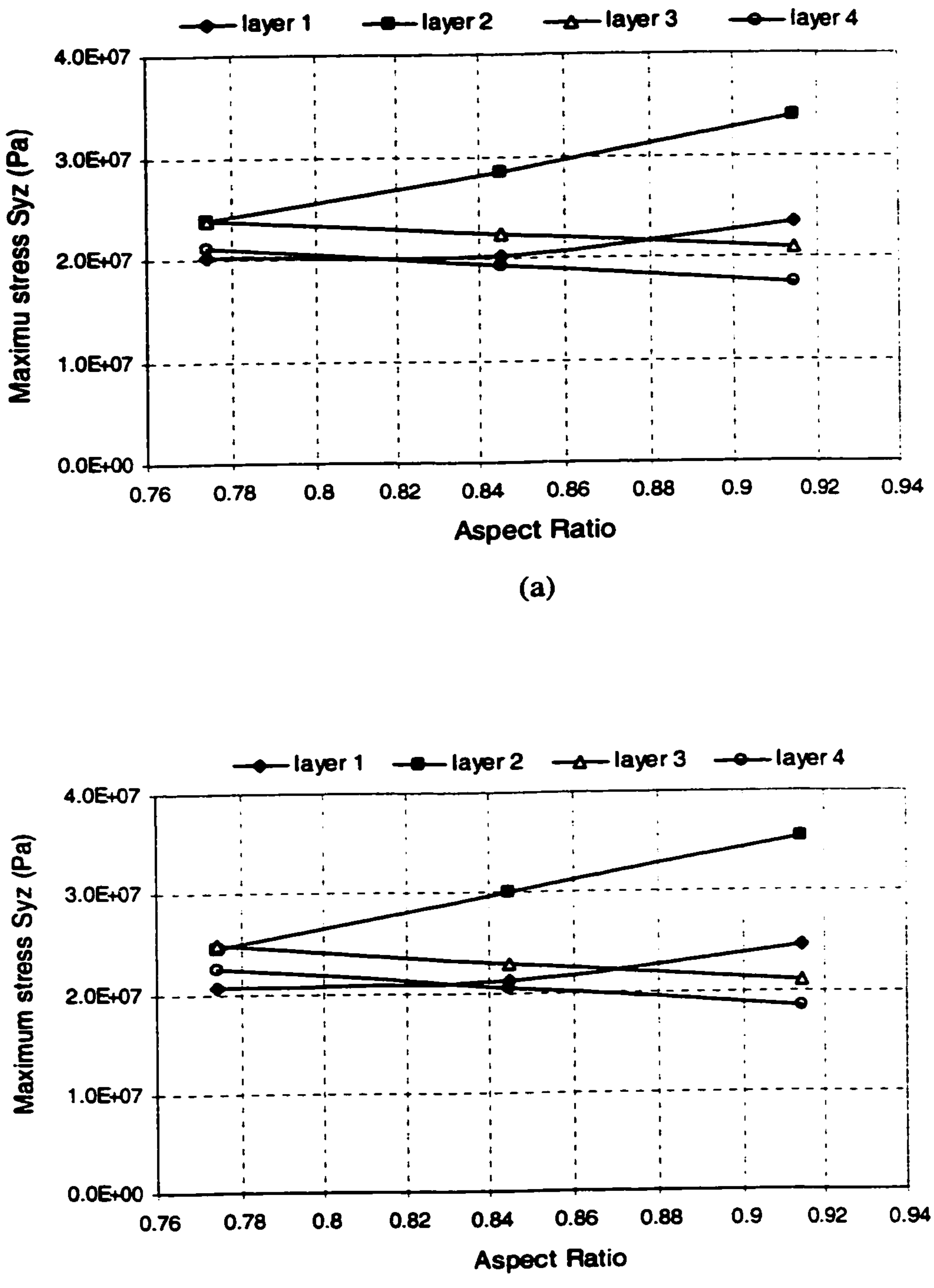

(a)

(b)

Figure 4.15: Peak values of S_{yz} of different belt layers as a function of the aspect ratio, $p_i = 690.3$ kPa (100 psi): (a) $\Delta Z = 20$ mm; and (b) $\Delta Z = 30$ mm.

Table 4.1 Percent variations in the peak stresses S_{yz} for different aspect ratios.

Aspect Ratio	Percent increase in maximum S_{yz} when ΔZ increased from 20 to 30 mm			
	Layer 1	Layer 2	Layer 3	Layer 4
0.7746	2%	2.9%	4.2%	7.1%
0.845	5.5%	5.6%	2.2%	6.3%
0.914	4.7%	4.4%	1%	5%

4.3.3 Influence of the Cord Angle

Among the various design parameters, the cord angle plays a significant role in determining the behavior of a radial tire and the stress fields in each belt layer. The influence of variations in the cord angle (θ) on the maximum shear stresses S_{yz} for different belt layers, is shown in Figure 4.16. The cord angles are varied from 18 to 26 degrees, and are designated as $+\theta$, $-\theta$, $+\theta$ and $-\theta$, respectively, beginning from layer 1, which is nearest to the tread rubber block.

The results show that increasing the cord angle within the considered range yields considerably lower peak values of S_{yz} in belt 2, while the peak values in belt 3 and 4 increase. The peak shear stress in the outer belt (layer 1) decreases with increase in the value of cord angle from 18 to 22 degree, and then increases slightly with further increase in cord angle from 22 to 26 degree. The increasing trend for peak shear stress in layer 3 and 4 as function of the cord angle may be attributed to the complex bending and twisting coupling behavior of the composite layers. The observation that the maximum shear stresses S_{yz} in belt 2 decrease with increase in the cord angle, however, remains to be investigated further to be fully understood. The results further show nearly identical trends for both loading conditions considered in the study.

The effects of variations in normal deflection on the maximum inter-ply shear stresses S_{yz} corresponding to different cord angles are summarized in Table 4.2 in terms

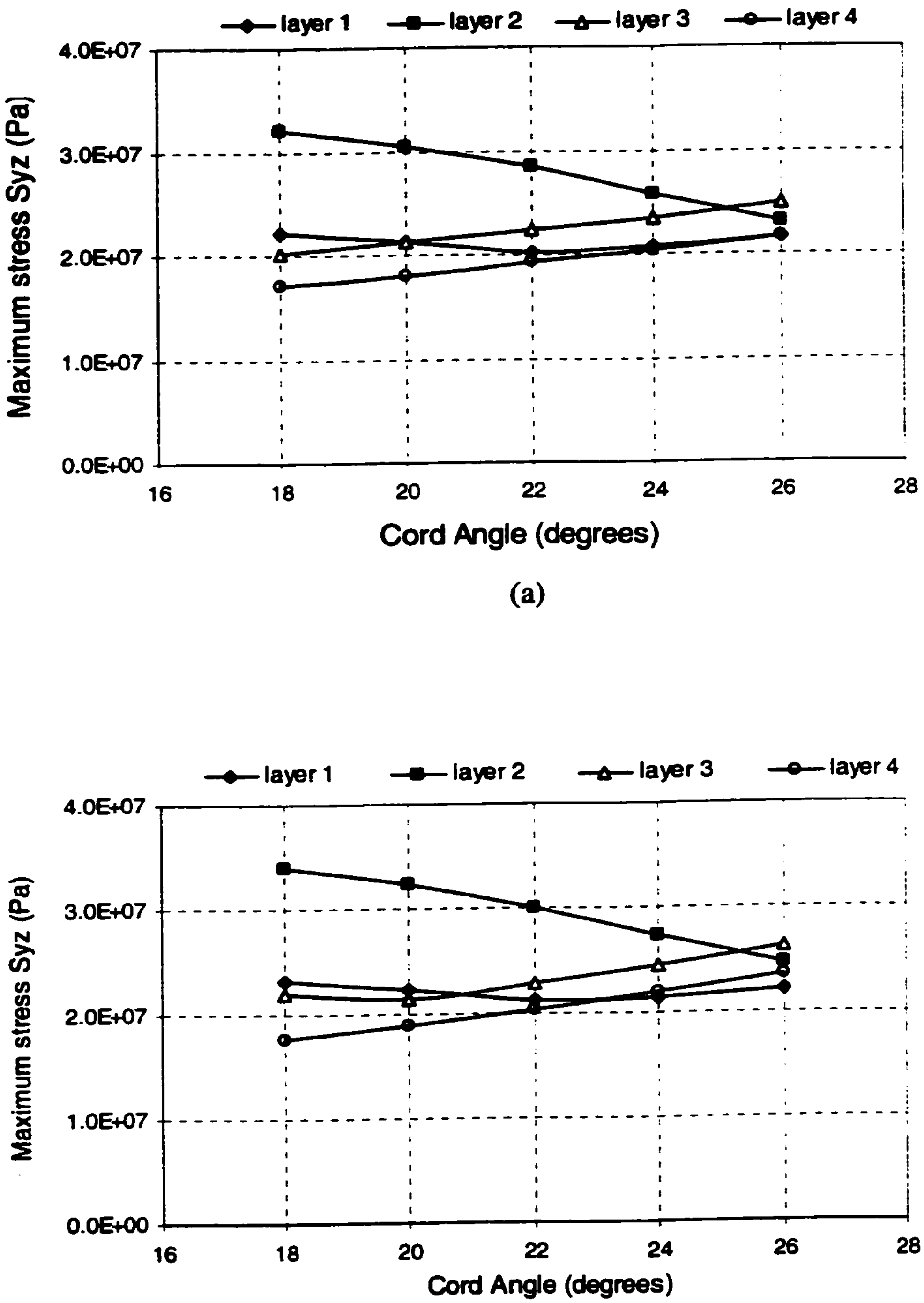

(a)

(b)

Figure 4.16: Peak values of S_{yz} developed in belt layers as a function of cord angle; $p_l = 690.3$ kPa: (a) $\Delta Z = 20$ mm; and (b) $\Delta Z = 30$ mm.

Table 4.2 Percent variations in the peak stresses S_{yz} for different cord angles

Cord angle (degree)	Percent increase in maximum S_{yz} when ΔZ increased from 20 to 30 mm			
	Layer 1	Layer 2	Layer 3	Layer 4
18	5%	5.6%	12%	3.5%
20	5.2%	5.9%	1%	5%
22	5.5%	5.6%	2.2%	6.3%
24	2.9%	6.2%	3.8%	7.8%
26	2.8%	6.5%	5.6%	9.3%

of percent increase. It is observed that increasing the normal deflection from 20 mm to 30 mm yields considerable increases in the maximum shear stress S_{yz} in layers 2 and 4 for cord angles ranging from 22 to 26 degrees. The maximum shear stresses S_{yz} in layer 4, however, always remain lower than the peak stresses in layer 2 and 3 in the considered range of cord angles. The maximum shear stresses S_{yz} in layer 3 are considerably less affected by the variation in the normal load, when compared with the stresses in the other layers for 20 and 22 degree cord angles. The maximum shear stress S_{yz} in layer 3, however, is significantly affected by the load variation when the cord angle assumes a value of 18 degrees. Based on the above results, it is suggested that a cord angle of approximately 25 degrees could be used to achieve a good compromise in the values of maximum shear stresses developed in all the layers under the conditions considered in this study. Cord angles smaller than 25 degrees result in higher values of the maximum shear stress in layer 2, while a larger cord angle yields higher maximum shear stress in layer 3.

4.3.4 Influence of the Number of Belt Layers

The number of belts used in a radial tire affects its rigidity and shear stress fields in a considerable manner. The belt layers provide high rigidity to the tread against distortion, and affect the rate of tread wear and the tire rolling resistance. Assuming identical geometry and material properties of each individual layer, the use of fewer belts could adversely influence the tire stability. The use of too many belts, on the other hand. directly affects the weight and the cost. The influence of the variations in the total number of cord reinforced layers in the belt has not been reported thus far. In the following analysis, the peak shear stresses developed within individual layers of the tire are computed by varying the total number of belt layers embedded in the crown area from 3 to 5. The thickness of each layer and the total thickness of the tire in the thickness direction are kept unchanged. The change in the number of belt layers may yield different shear stress fields in the different belt layers, when compared with those attained for the four-layer-belt case. This necessitates the determination of the various shear stress fields S_{xy}, S_{xz} and S_{yz} in the different belt layers for the loading conditions considered.

The shear stress fields S_{xy}, S_{xz} and S_{yz} in the different belt layers of the tire with 3 and 5 belt layers are illustrated in Figures 4.17 and 4.18, respectively. The results are derived under 690.3 kPa inflation pressure and 30 mm normal deflection. Figure 4.17 shows that the high values of the stress S_{xy} in each belt layers occur in the contact patch near the opposite edges of the belt. Moreover, similar to the results obtained for the four-layer-belt tire (Figure 4.10), the high values of the stress S_{xz} derived for the three-layer-belt concentrate within the narrow portion near the shoulder areas along both the edges of the belt, farther away from the contact region. The computed values of the shear stress S_{yz} fields for three-layer-belt are quite similar to those derived for layers 1, 2 and 3 of the four-layer-belt system, shown in Figure 4.9. In the case of the five-layer-belt (Figure 4.18), the shear stress fields of S_{yz} in layers 1, 2, 4 and 5 are also similar to those in the

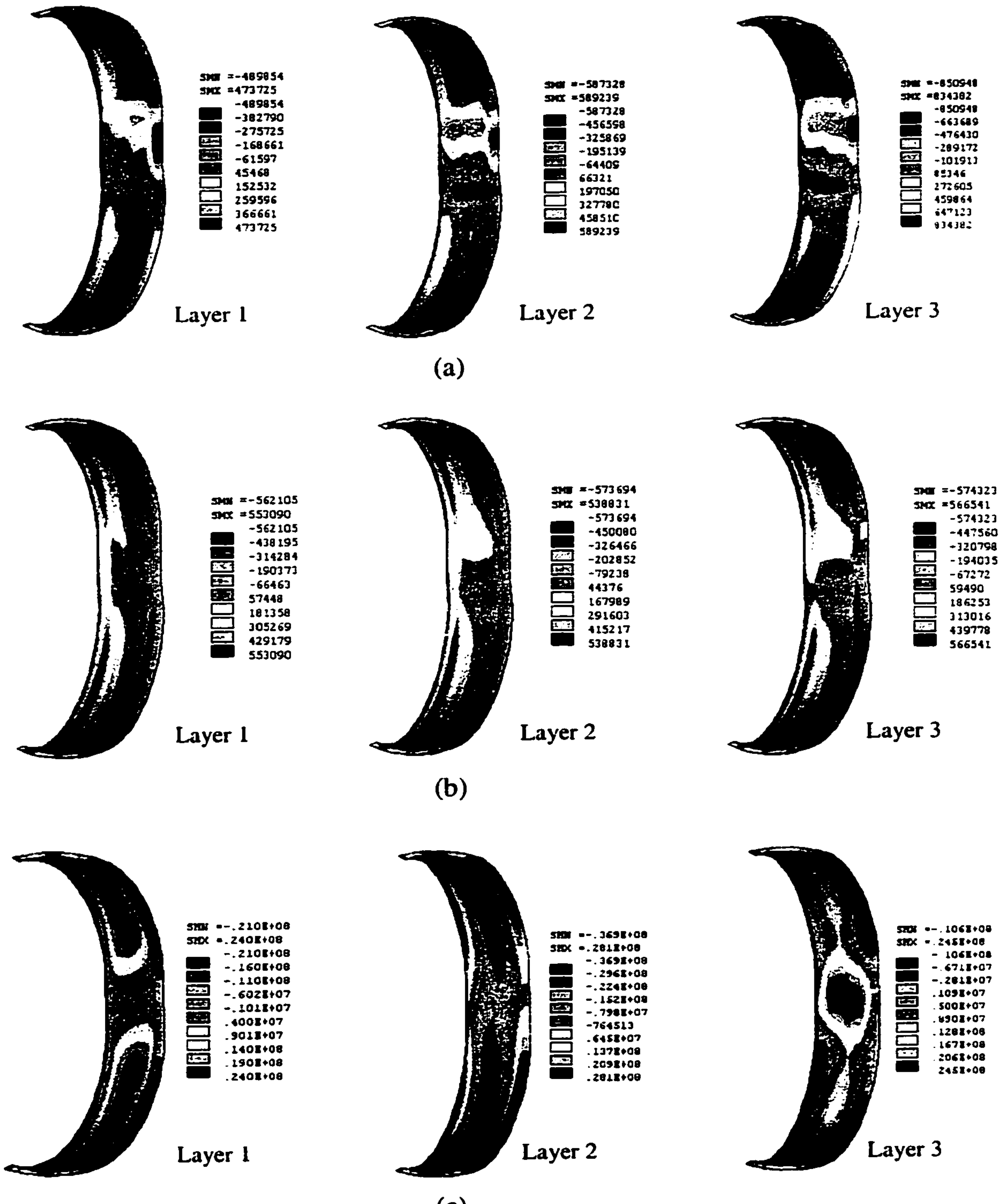

(a) (b) (c)

*Figure 4.17: Shear stress fields in different belt layers; $p_I = 690.3$ kPa (100 psi), $\Delta Z = 30$ mm; Total number of layers in belt = 3. (a) S_{xy} (b) S_{xz} and (c) S_{yz}.

**Note: SMN is the minimum value of the plotted item; SMX is the maximum bounded value of the plotted item. The unit of the stress value shown in the legend is Pascal (Pa).*

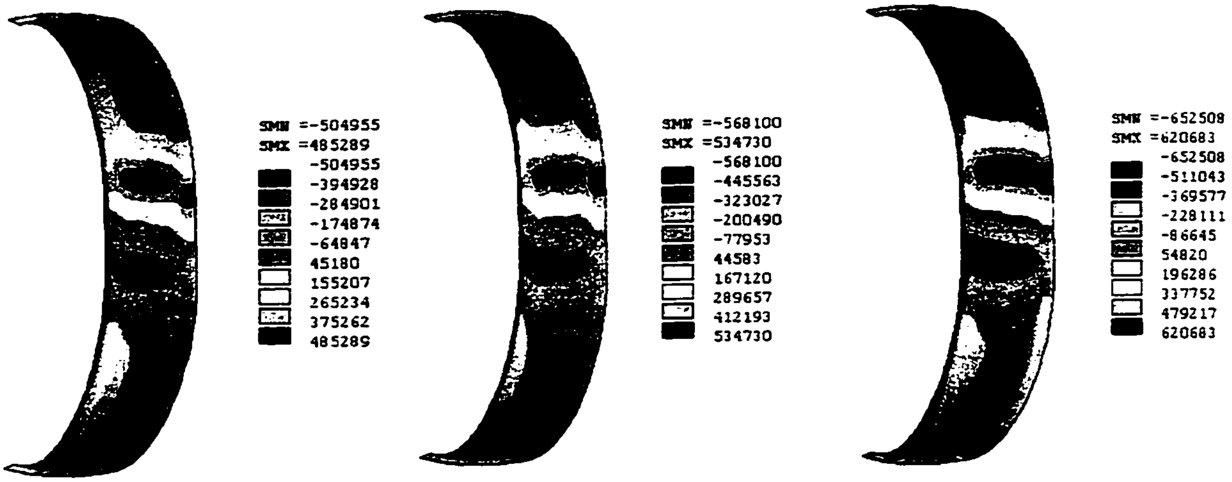

Layer 1 Layer 2 Layer 3

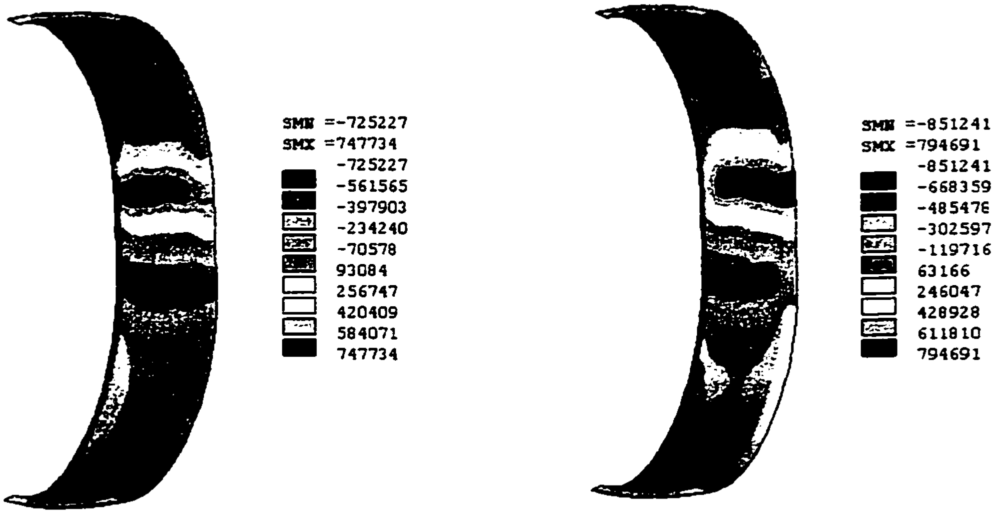

Layer 4 Layer 5

*Figure 4.18(a): Shear stress fields S_{xy} in different belt layers; $p_l = 690.3$ kPa (100 psi), $\Delta Z = 30$ mm; Total number of layers in belt = 5.

**Note: SMN is the minimum value of the plotted item; SMX is the maximum bounded value of the plotted item. The unit of the stress value shown in the legend is Pascal (Pa).*

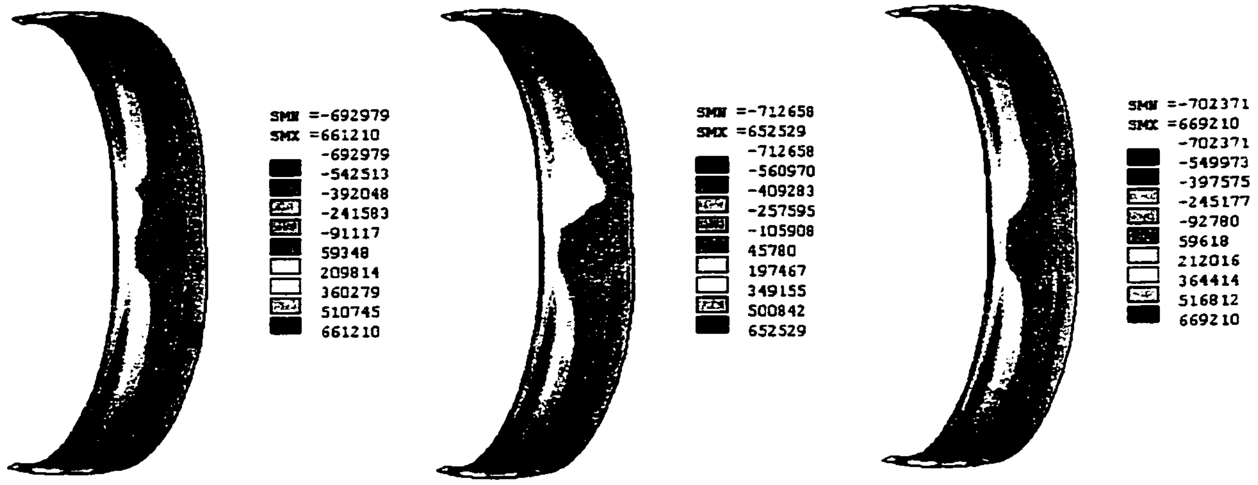

Layer 1 Layer 2 Layer 3

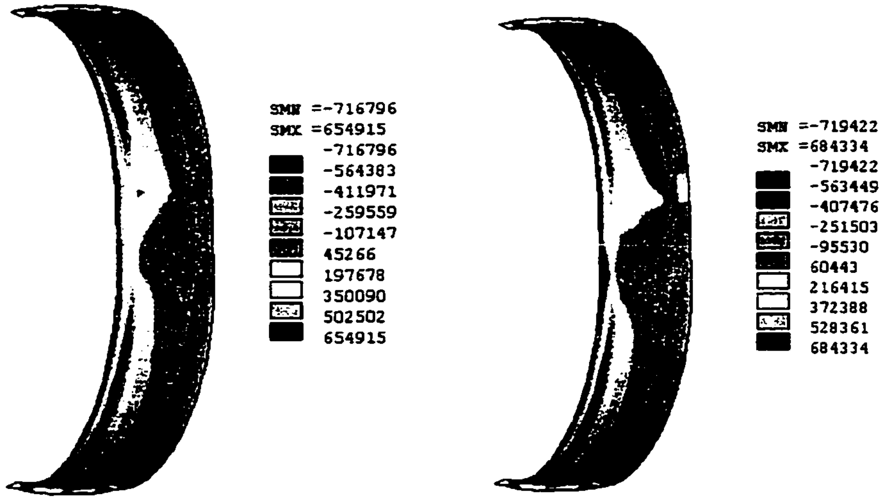

Layer 4 Layer 5

*Figure 4.18(b): Shear stress fields S_{xz} in different belt layers; $p_I = 690.3$ kPa (100 psi), $\Delta Z = 30$ mm; Total number of layers in belt = 5.

**Note: SMN is the minimum value of the plotted item; SMX is the maximum bounded value of the plotted item. The unit of the stress value shown in the legend is Pascal (Pa).*

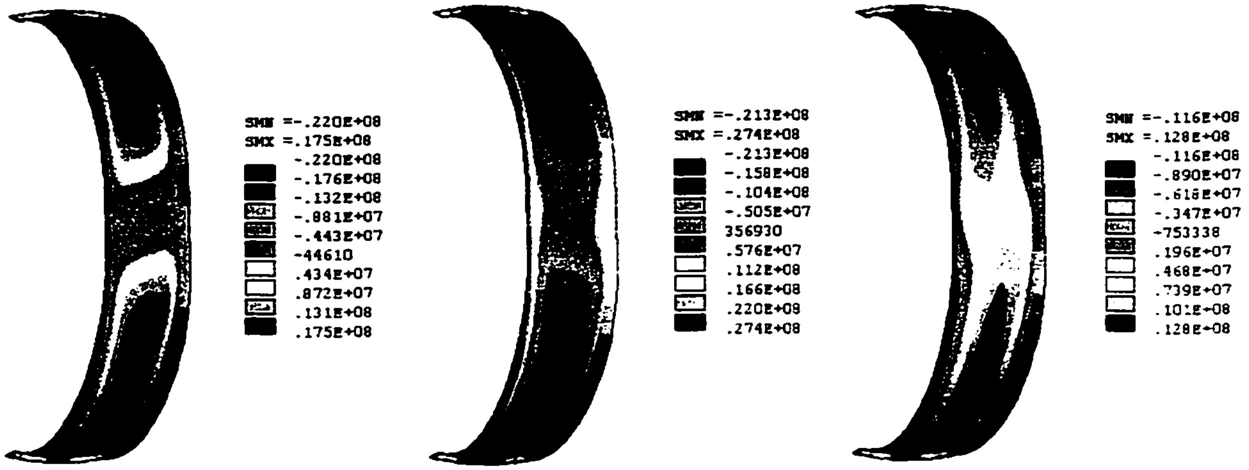

Layer 1 Layer 2 Layer 3

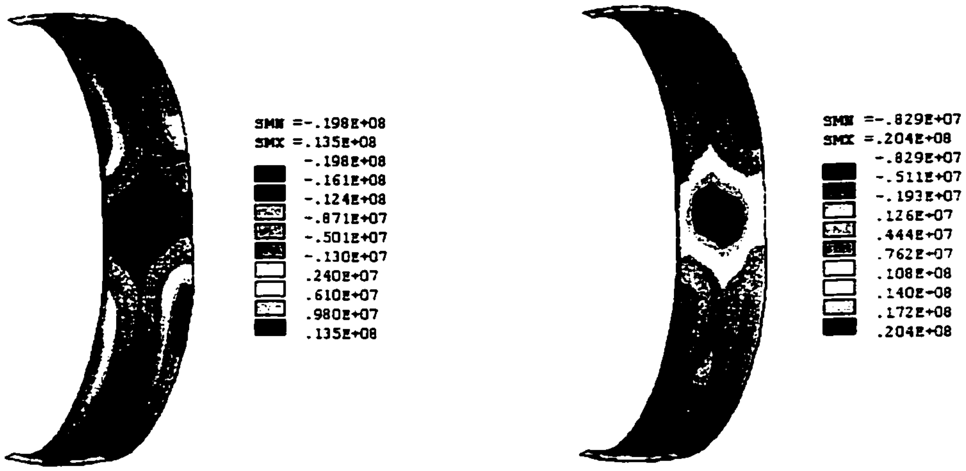

Layer 4 Layer 5

*Figure 4.18(c): Shear stress fields S_{yz} in different belt layers; $p_i = 690.3$ kPa (100 psi), $\Delta Z = 30$ mm; Total number of layers in belt = 5.

**Note: SMN is the minimum value of the plotted item; SMX is the maximum bounded value of the plotted item. The unit of the stress value shown in the legend is Pascal (Pa).*

layers 1, 2, 4 and 3, respectively, of four-layer-belt system. The layer 3, in the five-layer-belt case, however, reveals concentration of high shear stresses S_{yz} in the relatively narrow central portions of the belt near the edges and extremities of the contact patch. The shear stress S_{xy} fields in the individual layers in five-layer-belt case exhibit trends similar to those observed for four-belt-layer case, namely, the concentration of high magnitudes of S_{xy} occurs within two small regions, near the edges of the contact patch but in the opposite side. Similar to the three-layer-belt and four-layer-belt cases, the high stresses (S_{xz}) for the five-layer-belt case concentrate near both edges of the individual belts away from the contact patch for all the layers.

Figure 4.19 illustrates the peak values of shear stresses S_{yz} developed in individual layers for two different normal loads when the number of belt layers is varied from 3 to 5. Each curve in the figure represents the maximum value of shear stress S_{yz} in a specific layer but corresponds to different total number of belts. For example, the curve for layer 2 represents its peak shear stress response for total number of belts of 3, 4 and 5. As the number of belt layers increases from 3 to 5, the peak shear stresses S_{yz} in layers 2 and 3 decrease significantly, irrespective of the normal load. The peak value of stress S_{yz} in layer 1 tends to decrease slightly when the total number of belt layers is increased from 3 to 4 and increase slightly with further increase in the number of belt layers. The peak value of the stress S_{yz} in layer 4 increases slightly when one more layer is added. The addition of the fifth belt layer tends to lower the maximum shear stresses in the layers 1 to 3 and has negligible effect on the peak value of the stress S_{yz} of layer 4. The maximum of the peak shear stress S_{yz} among all the layers are developed in layer 2 and are significantly reduced with the increase in the number of belt layers, irrespective of the applied load.

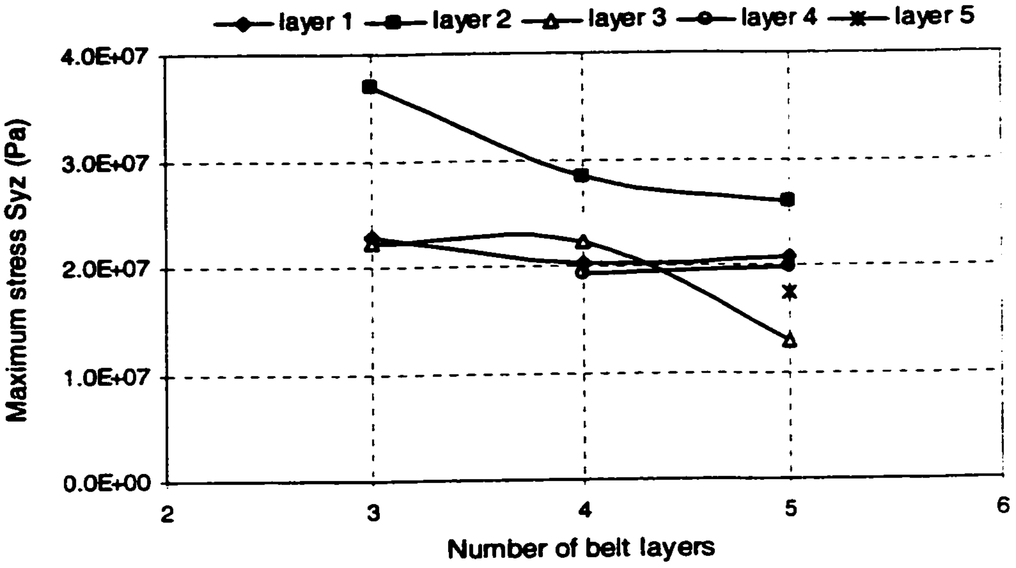

(a)

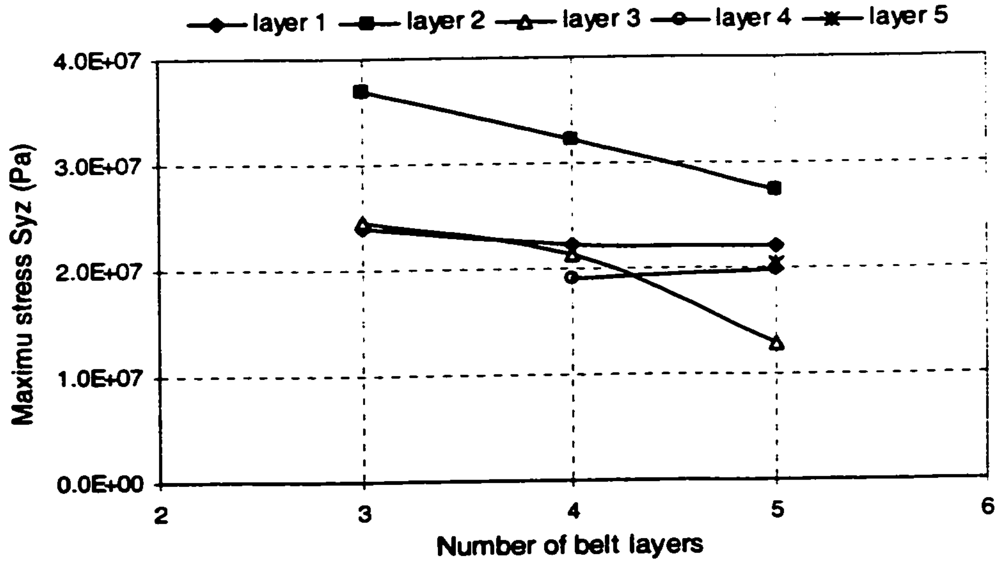

(b)

Figure 4.19: Peak values of shear stress S_{yz} of individual belt layers as a function of the total number of belt layers; p_l = 690.3 kPa: (a) ΔZ = 20 mm; and (b) ΔZ = 30 mm.

An increase in the normal deflection yields higher maximum shear stresses S_{yz} in almost all the layers, specifically in layers 1 and 5, irrespective of the number of layers in the belt. The percent increases in S_{yz} in different individual layers corresponding to different number of belt layers, when ΔZ is increased from 20 mm to 30 mm, are illustrated in Table 4.3. The results also show that addition of the fifth belt layer leads to a more even distribution of peak shear stresses in different belt layers. This suggests that a tire design with 5 layers is more desirable for the conditions considered in the study.

Table 4.3 Percent variations in peak stresses S_{yz} for different total number of belt layers

Total number of layers	Percent increase in maximum S_{yz} when ΔZ increased from 20 to 30 mm				
	Layer 1	Layer 2	Layer 3	Layer 4	Layer 5
3	5.3%	-0.5%	10.4%		
4	5.5%	5.6%	2.2%	6.3%	
5	5.8%	5.4%	-0.8%	0%	18%

Figure 4.20 and 4.21 further illustrate the peak values of shear stresses S_{xy} and S_{xz} of individual belt layers as a function of the total number of belt layers, respectively, for the loading condition: p_i = 100 psi and ΔZ = 20 and 30 mm. The results show that the peak values of shear stresses S_{xy} in layer 3 decrease significantly with the increase in the number of belt layers, irrespective of the normal loads, while the peak shear stresses S_{xz} in each layer increase with the increase in the number of belt layers. The magnitudes of the peak S_{xy} and S_{xz}, however, are over 40 times lower than the peak S_{yz} in the layers. The peak shear stresses S_{yz} developed in individual layers in the belt plane, are thus considered more important in the shear interaction analysis of the layers of a tire than those in wheel plane and transverse plane (S_{xy} and S_{xz}), irrespective of the total number of layers in the belt.

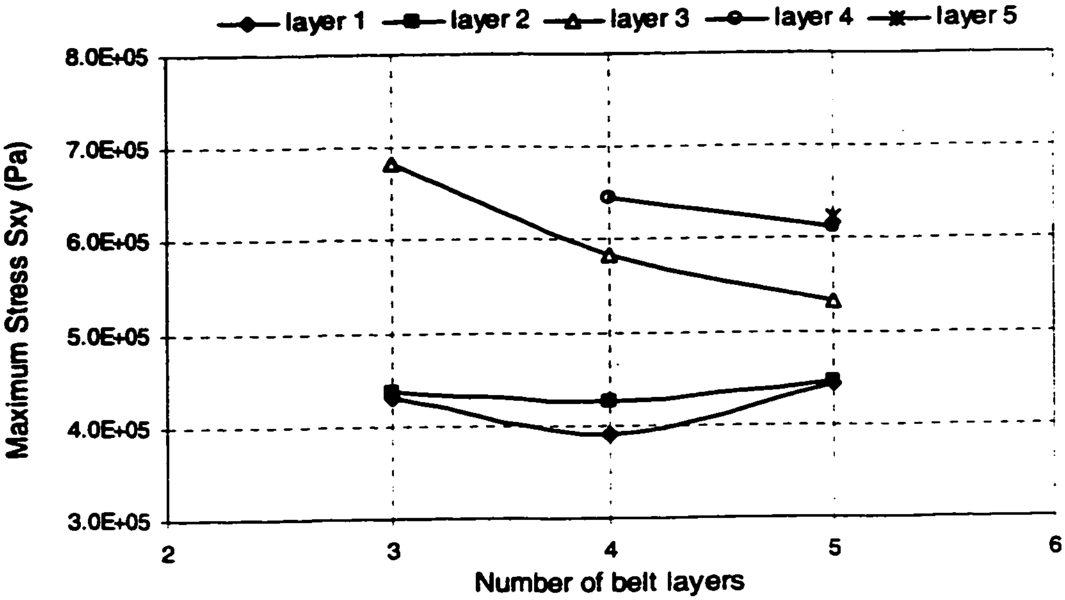

(a)

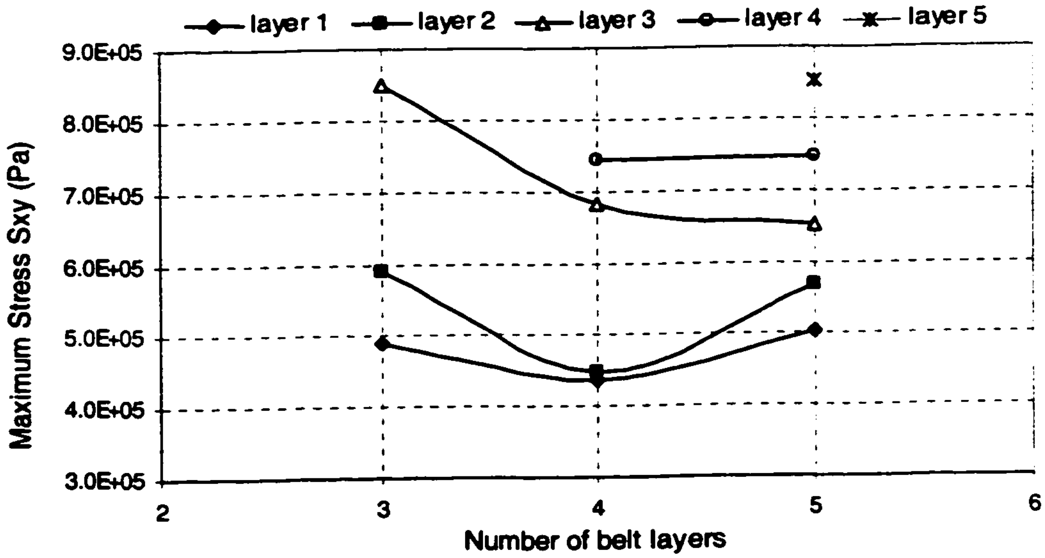

(b)

Figure 4.20: Peak values of shear stress S_{xy} of individual belt layers as a function of the total number of belt layers; $p_i = 690.3$ kPa: (a) $\Delta Z = 20$ mm and (b) $\Delta Z = 30$ mm.

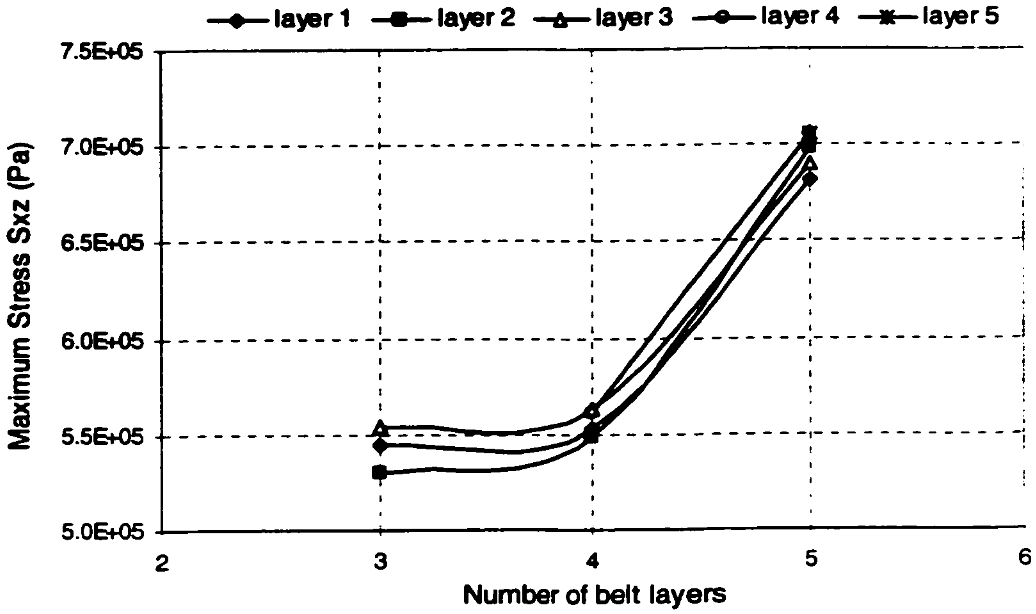

(a)

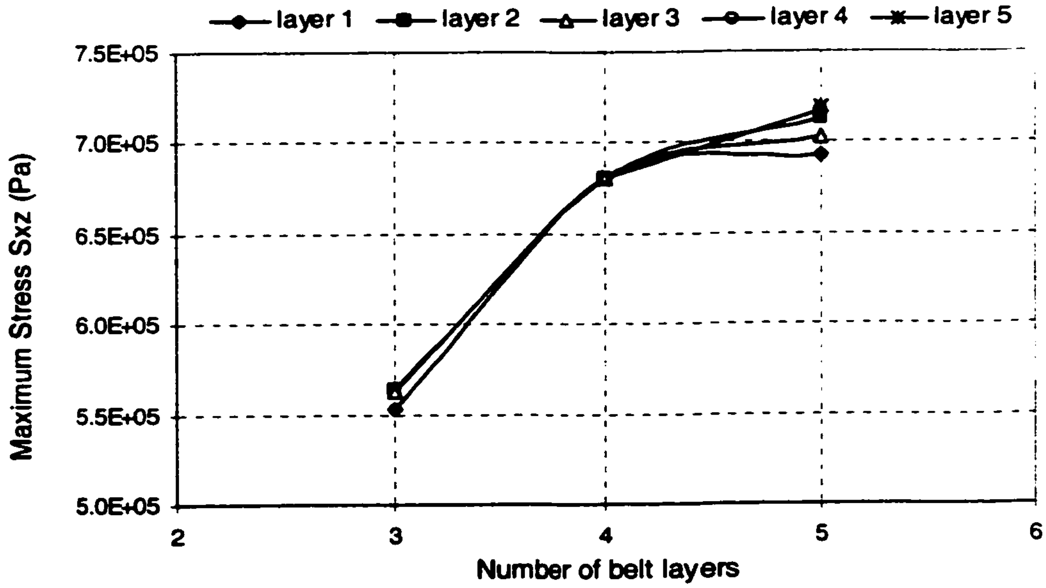

(b)

Figure 4.21: Peak values of shear stress S_{xz} of individual belt layers as a function of the total number of belt layers; p_l = 690.3 kPa: (a) ΔZ = 20 mm and (b) ΔZ = 30 mm.

4.3.5 Influence of the Rim Radius

The rim radius determines the tire size and may also affect the stress fields in different belt layers. The variations in the rim radius are realized by changing the radial coordinates of element nodes in the cross section. While the cross section area of the tire remains unchanged, the outer diameter alone is varied. The peak values of S_{yz} in individual layers are computed for different values of rim radius, ranging from 0.26 m to 0.32 m, and normal deflection of 20 mm and 30 mm.

The results presented in Figure 4.22 show negligible effect of the rim radius on peak values of S_{yz} in different belt layers for both normal deflections: $\Delta Z = 20$ and 30 mm. Varying the rim radius, however, affects both the peak values of shear stresses S_{xy} and S_{xz} significantly, as shown in Figure 4.23, although the peak values of S_{xy} and S_{xz} in the layers are much lower than the corresponding peak value of S_{yz}. Both S_{xy} and S_{xz} take their minimum values when the rim radius takes the value of 0.30m. The above observations are considered to be attributed to the curvature changes in the belt associated with the variation in the rim radius and need to be further investigated with more elaborate theoretical and experimental analysis. The percent variations in the peak shear stresses S_{yz} in the layers corresponding to different rim radii due to the normal load are illustrated in Table 4.4. It is observed that an increase in the normal load yields considerable increases in the peak shear stresses S_{yz} in all the layers, especially large increases in the magnitudes in layers 1, 2 and 4. Based on the above observations, it is suggested that a rim radius of 0.3 m, which results in the lowest magnitudes of S_{xy} and S_{xz} in different belt layers, is to be desirable for the conditions considered in the study.

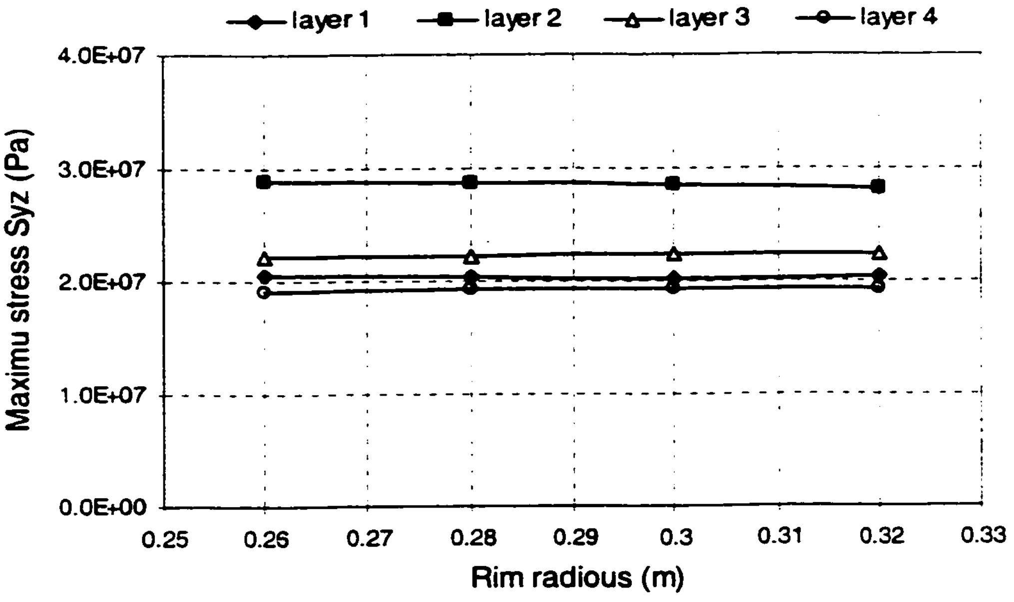

(a)

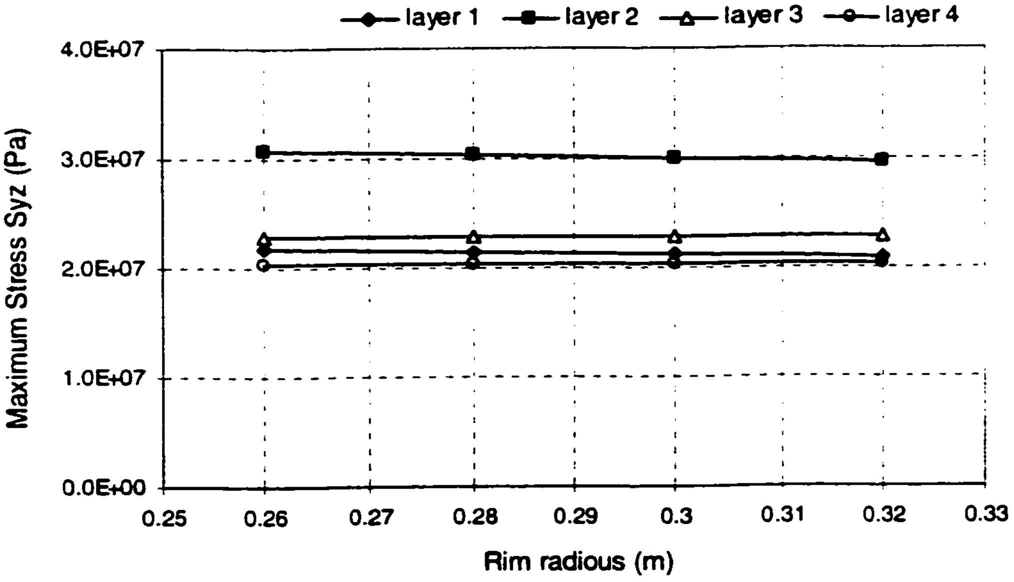

(b)

Figure 4.22: Peak values of shear stresses S_{yz} as a function of rim radius; $p_l = 690.3$ kPa: (a) $\Delta Z = 20$ mm; and (b) $\Delta Z = 30$ mm.

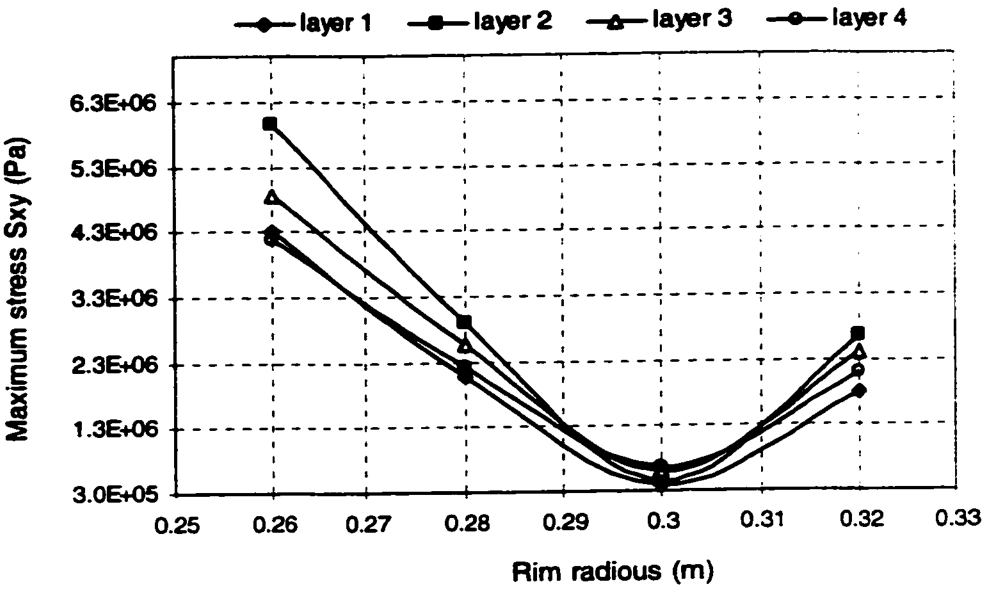

(a)

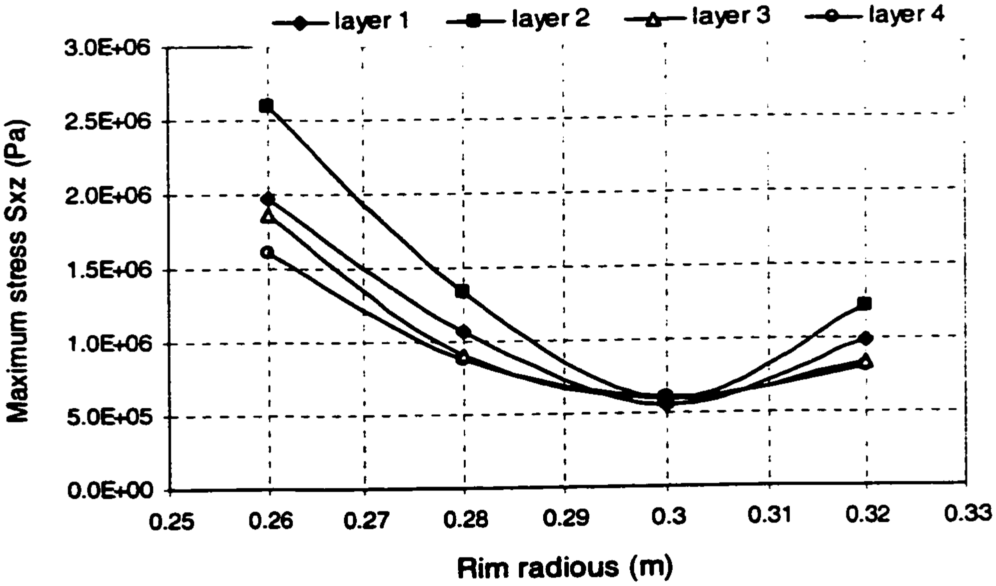

(b)

Figure 4.23: Peak values of shear stresses as a function of rim radius; $p_l = 690.3$ kPa and $\Delta Z = 20$ mm: (a) S_{xy}; and (b) S_{xz}.

Table 4.4 Percent variations in peak stresses S_{yz} for different rim radii

Rim radius (m)	Percent increase in maximum S_{yz} when ΔZ increased from 20 to 30 mm			
	Layer 1	Layer 2	Layer 3	Layer 4
0.26	5.8%	6.2%	3.2%	6.8%
0.28	5.4%	6.3%	2.7%	6.3%
0.30	5.5%	5.6%	2.2%	6.3%
0.32	3.0%	5.7%	2.2%	6.3%

4.3.6 Influence of the Tread Depth

Heavy truck tires with high loads at the tire-road interface employ tread compounds with high resistance to abrasion, tearing, and crack growth, and with low hysteresis to reduce internal heat generation and rolling resistance [9]. While the effects of the tread and the tread pattern on the tire-road interaction have been investigated [129], the influence of variations in the tread depth on the stress fields of a loaded tire have not been addressed in the reported studies. The variations in the tread depth from 3 mm to 10 mm yield almost insignificant effects on the peak values of S_{yz} and S_{xy} of individual layers, as illustrated in Figure 4.24. The variations in the tread depth, however, yield complex changes in S_{xz} under different normal deflections as can be seen in Fig. 4.25. An increase in the tread depth tends to lower the peak shear stresses S_{xz} in belt layers under normal deflection of 20 mm, and yields considerably higher values under normal deflection of 30 mm. It should be mentioned that varying the tread depth itself, with the other portions of the cross-section area unchanged, would cause variations in the aspect ratio of the tire. The effect of variations in the aspect ratio due to the variations in the tread depth, however, is considered to be negligible. The effect of varying the normal load on the percent change in the peak shear stress values of S_{yz} in the layers for the considered tread depths are illustrated in Table 4.5. It can be seen that increasing the

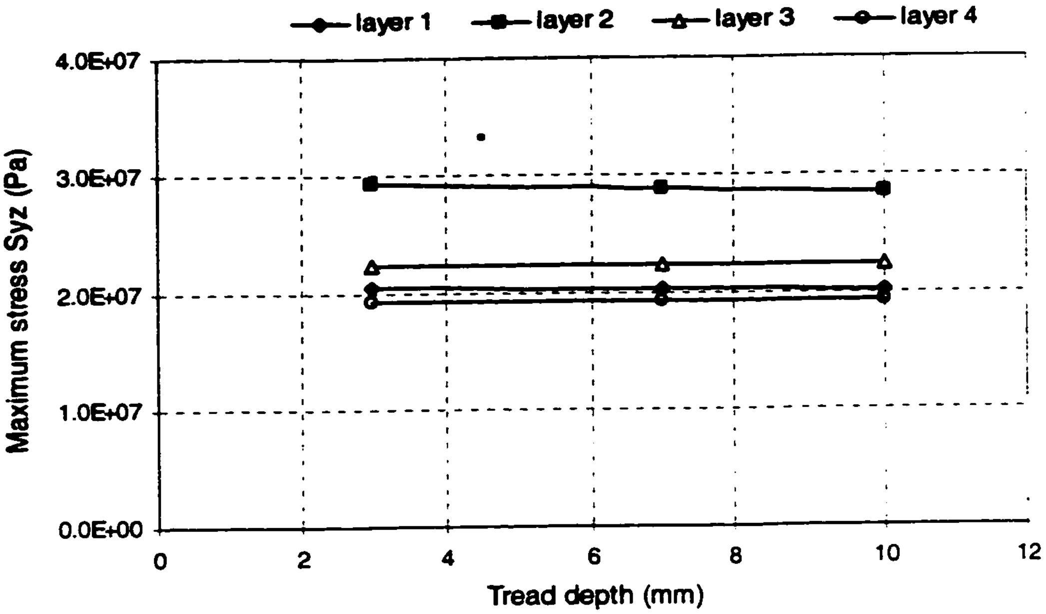

(a)

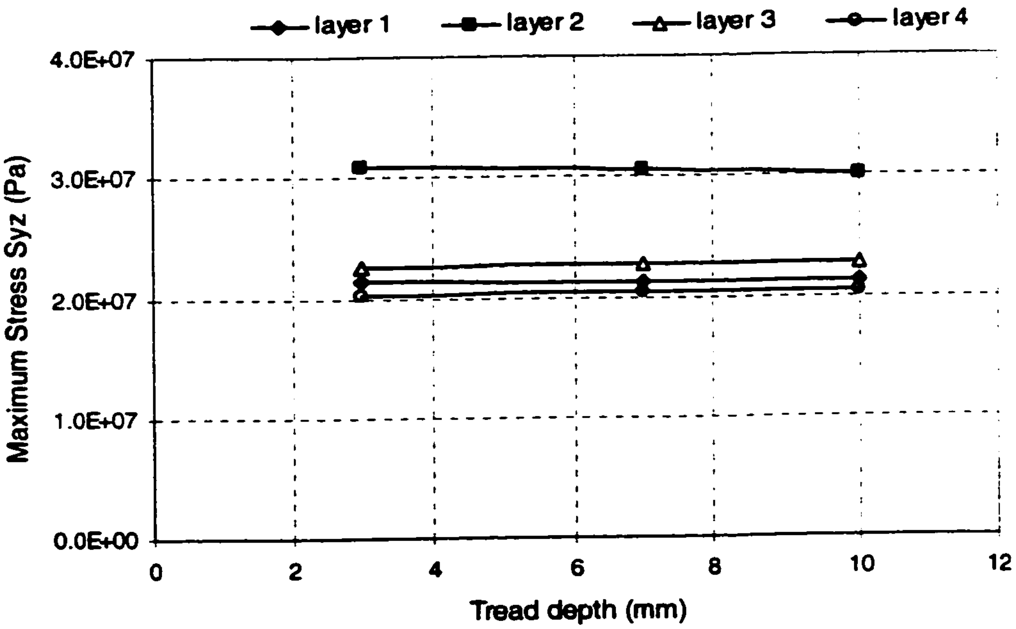

(b)

Figure 4.24: Peak values of S_{yz} of layers as a function of the tread depth; p_i = 690.3 kPa (100 psi): (a) ΔZ = 20 mm and (b) ΔZ = 30 mm.

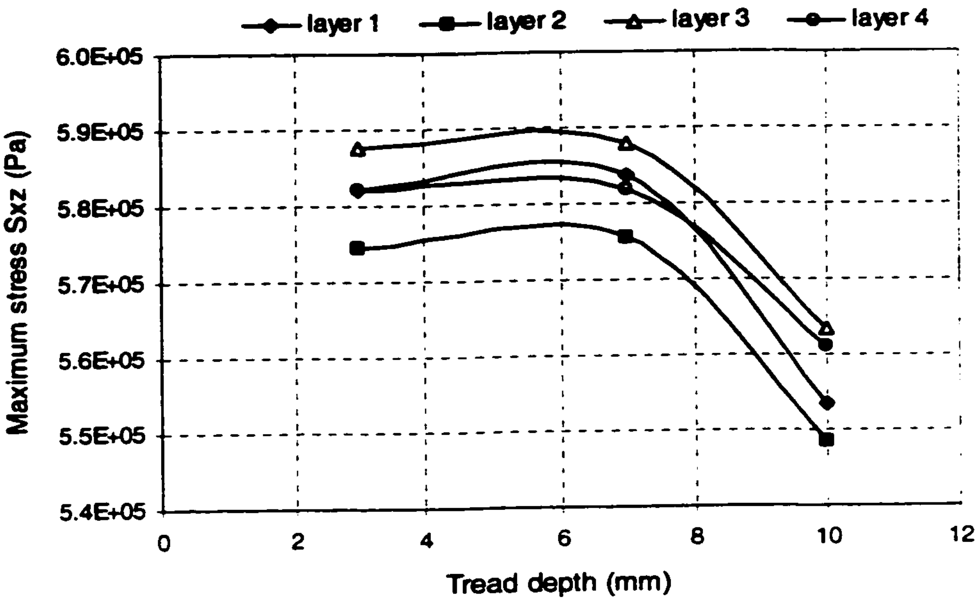

(a)

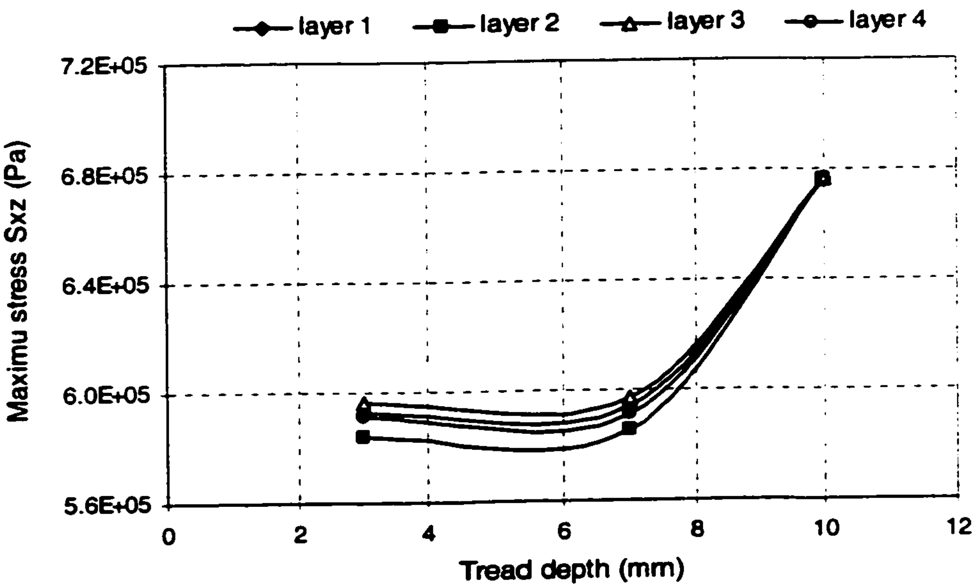

(b)

Figure 4.25: Peak values of S_{xz} of layers as a function of the tread depth; p_i = 690.3 kPa (100 psi): (a) ΔZ = 20 mm and (b) ΔZ = 30 mm.

normal load yields significant increases in the peak stress S_{yz} in layers 1, 2 and 4, but relative small increase in the peak stress in layer 3 for all the values of the tread depths considered. There are no clear trends in the observed variations in the peak shear stresses as function of the tread depth. It is considered that the design of the tread depth relies on factors other than the shear stresses developed in the multi-layered system, such as heat resistance and wear resistance.

Table 4.5 Percent variations in peak stresses S_{yz} for different tread depths

Tread depth (mm)	Percent increase in maximum S_{yz} when ΔZ increased from 20 to 30 mm			
	Layer 1	Layer 2	Layer 3	Layer 4
10	5.5%	5.6%	2.2%	6.3%
7	4.9%	5.9%	2.2%	5.7%
3	4.9%	5.5%	1%	5.2%

4.3.7 Influence of the Cord Ends per Centimeter (*epc*)

The number of cord ends per centimeter (*epc*) along the width of each individual layer determines the longitudinal and transverse Young's modulus of the layer, when the thickness of the layer is considered to be a constant. The Young's modulus of each layer can be estimated from the volume ratio of the cords to that of the rubber matrix, and the material properties of the cords in the composite layers. The effect of varying *epc* on the material properties, such as the Young's modulus and Poison's ratio, can be estimated from the Halpin-Tsai equations [130], when volume ratio of the cords and the rubber matrix in the belt, and their individual material properties are known. The effect of variations in the material properties of the layers on the stress fields can thus be investigated by varying the value of the *epc*.

Figure 4.26 illustrates the effect of varying the value of *epc* on the maximum shear stresses S_{yz} in the belt layers. Three distinct values of *epc* (3.5, 4 and 4.5) are considered for the analysis. It should be noted that a higher value of *epc* yields stiffer belts. The results show that increasing the values of the cords per centimeter in the width of each belt yields considerable increase in the maximum value of shear stresses S_{yz} in layer 2, and relatively slight increases in the peak shear stresses in all the other layers, irrespective of the normal load. The results also reveal nearly linear trends in variations of the maximum shear stresses (S_{yz}) in each belt layer with the *epc*. For the simulation conditions considered, a lower value of *epc* (3.5) yields lower peak values of S_{yz} in all the layers, as shown in Figs. 4.26. This is attributed to the fact that a lower *epc* value yields a soft layer that can experience large deformations and thus relatively small potential stress concentration. The effects of varying the normal loads on the peak shear stress values of S_{yz} in the layers for the considered values of *epc* are illustrated in Table 4.6. While increasing the normal load and thus the deflection yield increases in all the belt layers, varying the normal load has relatively small effect on the maximum shear stress in layer 3 but relative large influence on the magnitude of the peak shear stress in layer 4. The above results thus suggest that a lower value of *epc* (3.5) may be desirable with twisted cords that have a diameter of 0.8 mm and belt thickness of 1.5 mm for the considered truck tire.

Table 4.6 Percent variations in peak stresses S_{yz} for different values of *epc*

Value of *epc* (Ends/cm)	Percent increase in maximum S_{yz} when ΔZ increased from 20 to 30 mm			
	Layer 1	Layer 2	Layer 3	Layer 4
3.5	2.6%	6%	1.4%	4.8%
4	5.5%	5.6%	2.2%	6.3%
4.5	5.2%	6.1%	3.5%	7.1%

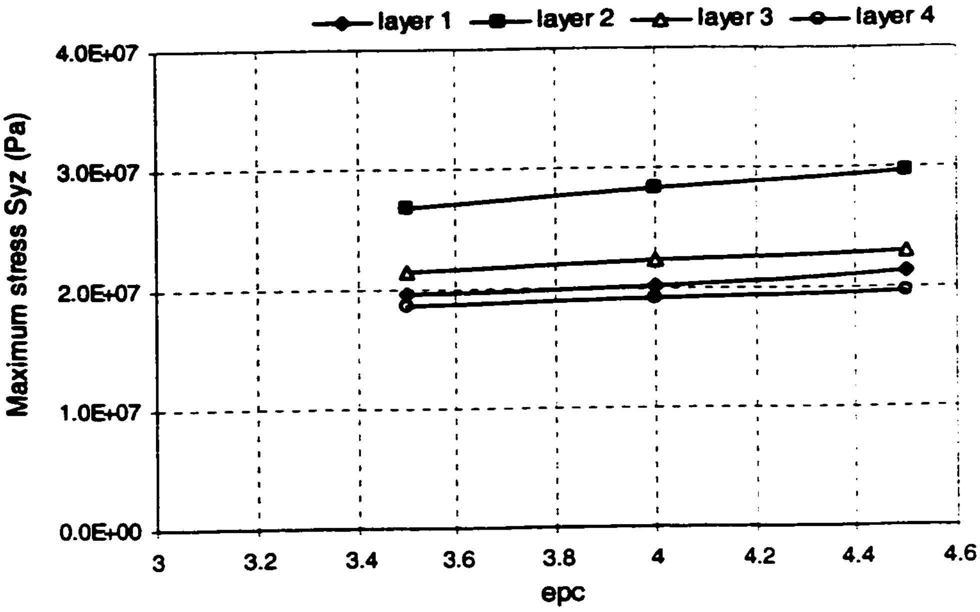

(a)

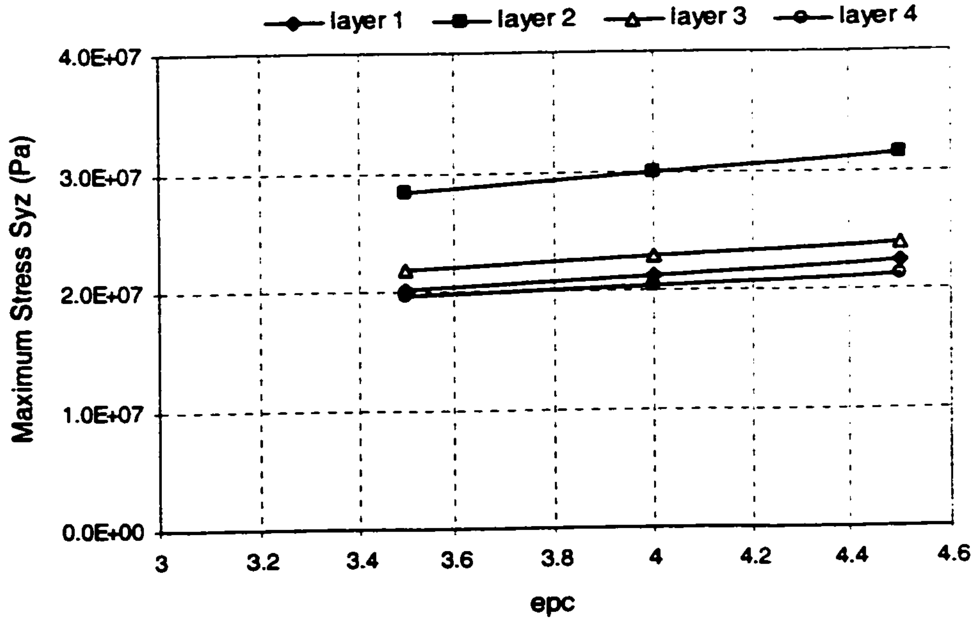

(b)

Figure 4.26: Peak values of S_{yz} of layers as a function of the value of epc; p_l = 690.3 kPa (100 psi): (a) ΔZ = 20 mm and (b) ΔZ = 30 mm.

4.3.8 Discussions on the Desirable Set of Parameters

The results presented in **Figure 4.15** through **Figure 4.26** could be used to derive a set of desirable geometric and structural parameters to achieve lower values of the maximum shear stresses in the belt layers under the loading conditions considered. The analyses were performed using the pre-estimated nominal simulation parameters. The results suggest that peak shear stresses could be reduced significantly using the selected parameters. The selected structural, geometric and operating parameters are compared with the estimated nominal parameters in Table 4.7.

Table 4.7(a) Nominal and desirable structural, geometric and operating parameters

Parameters	Aspect ratio	Cord angle Degree	Number of layers	Rim radius m
Nominal	0.845	±22	4	0.30
Desirable	0.777	±25	5	0.30

Table 4.7(b) Nominal and desirable structural, geometric and operating parameters

Parameters	Tread depth mm	*epc*	Inflation pressure kPa	Normal deflection mm
Nominal	10	4	-	
Desirable	10	3.5	<690.3	20-30

The tire model is further analyzed using these simulation parameters to study their potential performance benefits in terms of peak shear stresses, S_{yz}, S_{xy} and S_{xz} in the belt layers, as a function of the normal deflection or normal load. Figure 4.27 illustrates the peak shear stresses (S_{yz}, S_{xy} and S_{xz}) developed in the individual layers as function of the normal deflection in the 10-40 mm range, when the inflation pressure is 690.3 kPa, as derived from the tire model with the selected set of parameters. The results are compared with those obtained using nominal parameters shown in Figure 4. 14.

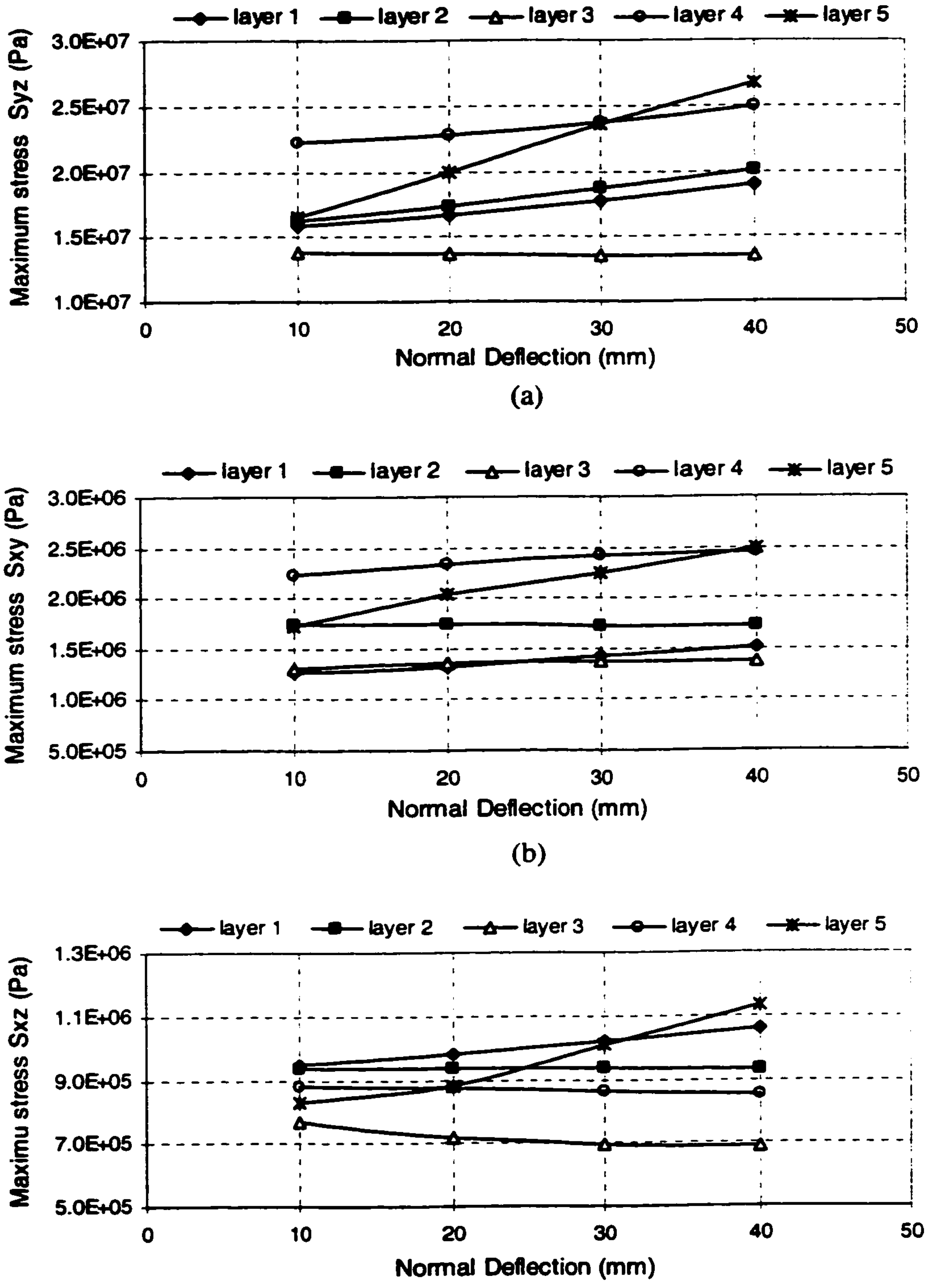

(a)

(b)

(c)

Figure 4.27: Peak values of shear stresses in belt layers of tire model based upon selected values of the parameters, as a function of normal deflection; p_I = 690.3 kPa (100 psi): (a) S_{yz}; (b) S_{xy} and (c) S_{xz}

The comparisons clearly show that the maximum shear stresses S_{yz} in all the layers, especially in layer 2 are significantly reduced. The maximum shear stresses S_{xy} and S_{xz} developed in the belt layers with the proposed parameters, however, increase. The magnitudes of S_{xy} and S_{xz}, however, are less than one tenth and one twentieth of the peak values S_{yz} values in the layers, respectively. Considering that the peak values of S_{yz} are significantly larger than those of S_{xy} and S_{xz}, the S_{yz} values obtained using the selected set of parameters are compared with those obtained using the nominal parameters. The relative percentage changes in the peak values are illustrated in Figure 4.28. A positive value of percent change represents reduction in the peak value of S_{yz} due to selected set of parameters, while the negative values refer to an increase in the peak value of S_{yz}.

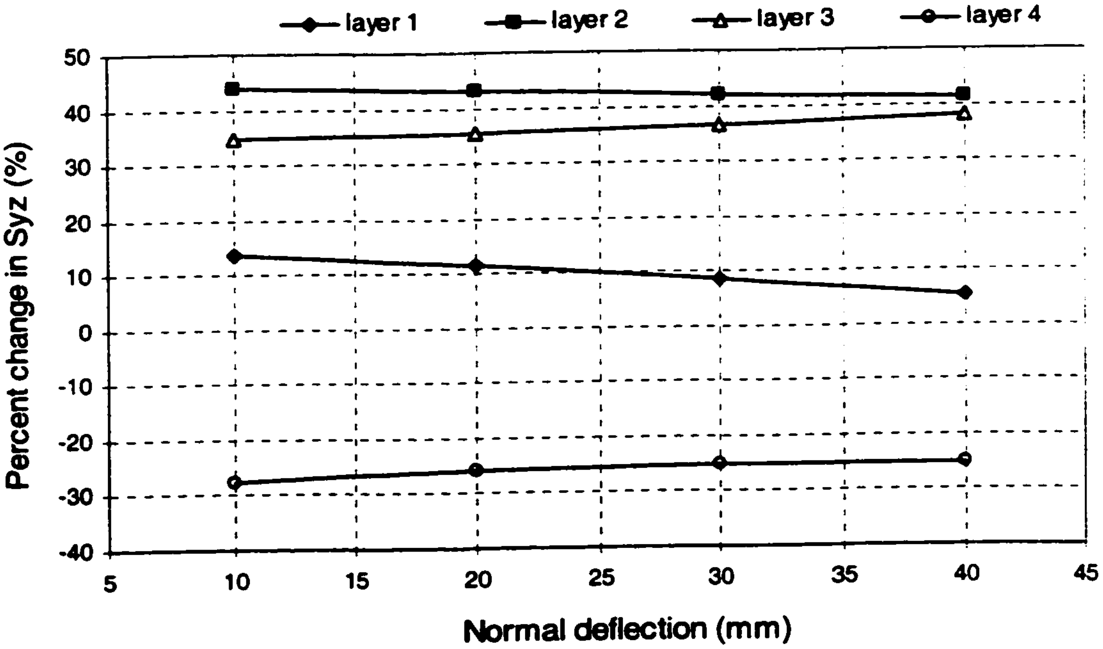

Figure 4.28: The percent changes in peak values of S_{yz} of different belt layers of tire models based upon the selected and nominal parameters, as a function of normal deflection; p_i = 690.3 kPa.

The results show that the tire model with the selected set of parameters yields considerably lower peak values of shear stress S_{yz} of all the layers, with the exception of the layer 4, irrespective of the normal load/deflection. The use of the selected set of parameters, yields 35-45% lower values of S_{yz} in belts 2 and 3, and 6-13% lower values of S_{yz} in belt 1, depending upon the normal load. The peak shear stress S_{yz} developed in layer 4, however, increases considerably (≈ 26%) in the considered range of normal deflections (10 to 40 mm). The proposed design parameters yield highest peak stress S_{yz} in the layer 4.

Figure 4.29 further illustrates the percentage reduction in the highest peak values of the shear stresses S_{yz} developed in the belt layers as a function of the normal deflection for different inflation pressures. The comparison reveals that the highest peak stress S_{yz} in the belt layers, attained using the selected parameters is 21.6-23.4%, 18.3-27.9% and 18.6-25.8% lower than that computed from the nominal parameters, for the inflation pressure of 690.3, 552.2 and 828.4 kPa, respectively. For an inflation pressure of 690.3 kPa, the highest peak stresses (corresponding to the maximum normal deflection of 40 mm) occur in layer 2 and in layer 5, with the nominal and proposed set of parameters, respectively. The magnitudes of these peak stresses corresponding to the nominal and selected parameters are 31.9 MPa and 26.8 MPa, respectively, as shown in Figure 4.14(c) and Figure 4.27(a). The relative reductions in the highest peak stress in the belt layers decrease with increase in the normal deflection for a lower inflation pressure (552.2 kPa) and increase under a higher inflation pressure (882.4 kPa), as illustrated in Figure 4.29. The reductions in the highest peak stress S_{yz} of different belt layers, however, are obtained at the expense of higher peak shear stresses S_{xy} and S_{xz}. This may be acceptable considering that the peak shear stresses S_{yz} in different layers are approximately over 10 and 20 times higher than the corresponding S_{xy} and S_{xz} values.

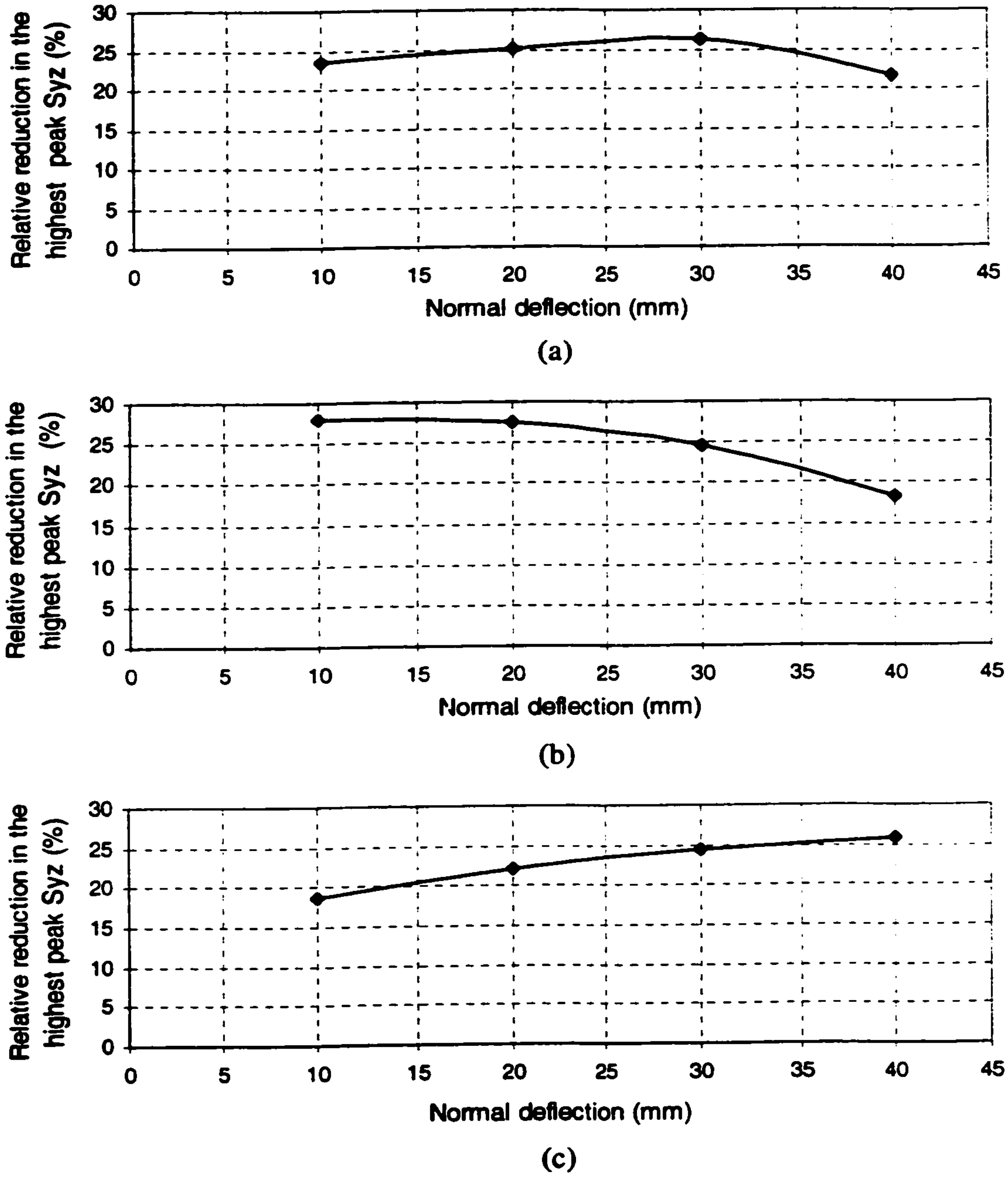

(a)

(b)

(c)

Figure 4.29: The reduction of the highest peak shear stress S_{yz} in the belt layers as a function of the normal deflection: (a) p_i = 690.3 kPa (b) p_i = 552.2 kPa; and (c) p_i = 828.4 kPa.

4.4 SUMMARY

A qualitative study of the effects of structural and geometric parameters on the maximum shear stresses developed in different layers of a truck tire is performed using the finite element tire model developed in Chapter 3. The maximum values of the shear stresses developed in individual layers and their locations are evaluated for a radial truck tire under an inflation pressure of 690.3 kPa and specified normal load/deflections. The influence of the parameters including the inflation pressure and the normal deflection, the cord angle and number of cord ends per centimeter (*epc*) for each layer, rim radius, tread depth, aspect ratio and the total number of layers, on the maximum shear stress developed in different layers of a loaded tire are investigated. A desirable set of these parameters is identified to achieve lower value of maximum shear stresses in the belt layers over a range of inflation pressure and normal load conditions. The results show that the use of the proposed set of parameters can significantly reduce the maximum shear stresses in the multi-layered system for a tire with inflation pressure ranging from 552.2 to 828.4 kPa and the normal deflection ranging from 10-40mm. The highest maximum shear stress developed in the belt layers is reduced by 18.3 to 27.9% and the reductions in S_{yz} in layers 2 and 3 occur in the 35 to 45% range, depending on the tire deformation and the inflation pressure. The reductions in the maximum shear stresses S_{yz} are achieved at the expense of increasing the maximum shear stresses S_{xy} and S_{xz}. The magnitudes of the peak S_{xy} and S_{xz}, however, are considerably smaller than that of the S_{yz}.

The validated tire model is further used in the following chapter to analyze the contact pressure distribution in the tire-road interface. The contact pressure fields derived from the finite element model are analyzed to propose a function for estimating the tire-road contact pressure distribution. The three-dimensional pressure fields are used to derive a two-dimensional contact pressure distribution using the equivalent work as the basis. The curve fitting techniques are applied to derive a polynomial function to describe the contact pressure distribution as a function of the inflation pressure, normal load and the coordinate along the contact patch.

CHAPTER 5 ESTIMATION OF TIRE-ROAD CONTACT PRESSURE DISTRIBUTION

5.1 INTRODUCTION

The distribution of normal load in the contact patch between a tire and the road surface affects the operating properties of the tires, since they are closely related to the tire's performance in terms of cornering characteristics, road damage potentials, noise generation and wear. The distribution of the tire load in the plane of the road surface is an important factor, since it can provide considerable insight into the structural design of the tire and its effects on the vehicle performance and the potential road damage.

The contact pressure field developed in the tire-road interface is strongly related to the tire inflation pressure, vertical load and structural properties. While a number of pressure sensing systems have been used to measure the tire-road contact pressure distribution [131], analytical techniques do not yet exist for effective estimation of the contact pressure distribution as a function of the inflation pressure and the normal load. A large number of analytical tire models, however, have been developed to study the structural behavior of the tires [4, 5]. Many studies on the tire-road contact pressure distribution and the contact patch geometry of statically loaded tires have been undertaken during the last three decades, using either experimental techniques or analytical models of varying complexities [131-133]. The majority of the reported models, however, are based on rather insufficient experimental data or relatively simple theoretical basis to establish the contact conditions. These models, such as the models reported in [139, 141], are normally based on the membrane or thin shell theory with membrane or thin shell elements representing the inflated tire. These models are thus considered adequate for linear analysis. Many other studies have also derived the contact pressure distributions from finite element tire models of varying complexities [135-138]. Very few studies, however, have derived an effective formulation to estimate the 2D contact pressure distribution that could be applied for the studies on ride properties and road damaging potential of heavy vehicle tires.

Studies on pavement damage potentials due to tire loads and ride dynamics of vehicles mostly consider the tire as an elastic element with a point contact with the road surface. Such a methodology can not predict the distribution of tire loads and thus may provide an overestimation of the pavement damage potentials of tires. In these studies, the 3-D contact pressure field, due to its complexities, is simplified and replaced by a nominal force acting at a point within the contact patch beneath the center of the tire. Some of the reported studies have considered the contributions due to variations in normal load and inflation pressures through the development of equivalent spring rate of the point-contact tire spring [152-154]. The contributions due to geometry of the tire enveloping the road surface, however, are ignored.

An estimate of the tire load distribution at the contact surface may be derived from the known 3-D contact pressure field computed from an effective finite element tire model and the resultant tire force generated from an equivalent point-contact spring. The simplicity of the vehicle ride or pavement loading models could thus be retained through the use of the equivalent point-contact tire models. This necessitates the derivation of analytical formulations of 2D contact pressure distributions as a function of the normal load, inflation pressure and the coordinate along the contact patch length.

In this chapter, an analytical procedure to estimate the tire-road contact pressure distribution, along the length direction of the contact patch, as a function of the inflation pressure and normal load for a truck tire is proposed. The modeling process is based on the 3-D pressure fields computed from the developed nonlinear finite element tire model, which considers the structural geometry, the anisotropic material properties of the multiple layers and the nearly incompressible property of the tread rubber block. The 3-D pressure fields are analyzed to derive a 2-D contact pressure distribution using the equivalent work as the basis. Curve fitting techniques are applied to derive a polynomial function to describe the contact pressure distribution as a function of the normal load, inflation pressure and coordinate along the contact patch.

5.2 ANALYSIS OF 3-D CONTACT PRESSURE FIELDS

The traction, braking, ride and pavement loading characteristics of a vehicle are directly related to the pressure distribution that is developed in the tire-road interface. These properties, however, are further related to inflation pressure, normal load and various structure properties of the tire [6]. The finite element tire model developed in Chapter 3 is used to derive the contact patch geometry and pressure distribution of the tire at various loading conditions. The tire model is validated by comparing the normal force-deflection characteristics and the contact patch geometry (footprint shapes and footprint length) computed from the finite element model with the experimental measurements obtained in the laboratory over a wide range of normal loads and inflation pressures. The comparisons revealed reasonably good agreements between the model results and the measured data, the results derived from the finite element tire model are thus considered valid in a qualitative sense.

The finite element tire model is analyzed to determine the 3-D contact pressure fields for different inflation pressures ranging from 552.4 to 828.36 kPa (80 to 120 psi), while the normal load acting on the tire is varied by varying the maximum normal deflection of the tire. The typical computed 3-D contact pressure distributions for the selected radial truck tire subjected to 15 and 30 mm normal deflections and inflation pressures of 552.4, 621.3 and 828.4 kPa, are illustrated in Figure 5.1 to 5.3. The analyses are performed by applying a known pressure load, which are followed by application of a normal load by varying the normal deflection. The results reveal that for a constant inflation pressure the highest contact pressure peak initiates in the inner ribs and then tends to swift to the outer ribs with the increase in the normal deflection. Increasing the inflation pressure coupled with light normal load, however, yields concentration of high peak of contact pressure in the inner rib areas.

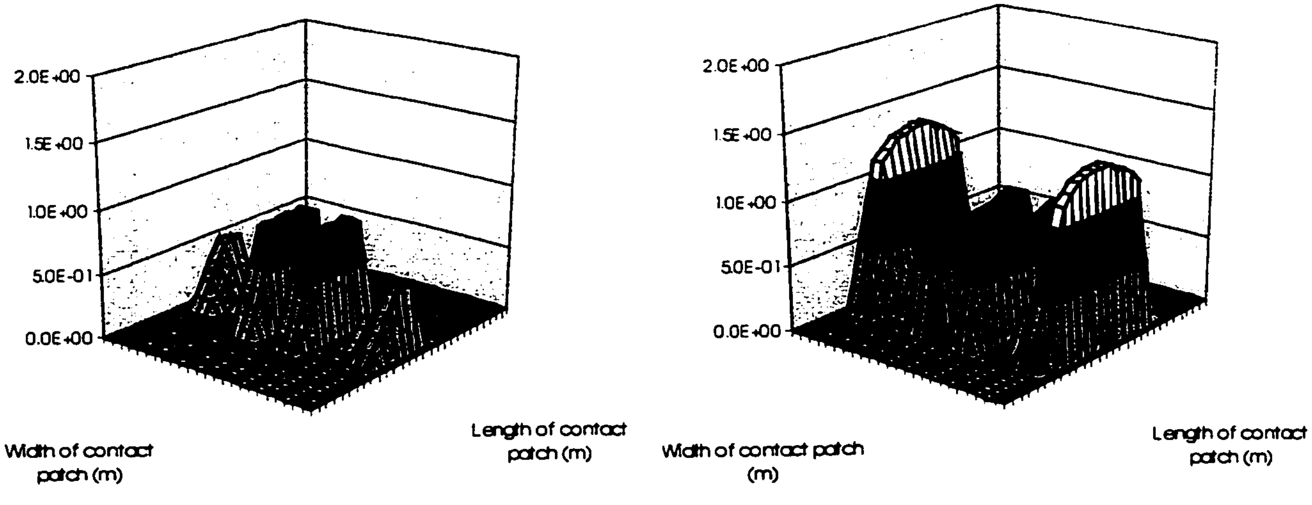

F_z = 10.5 KN

F_z = 22.9 KN

Figure 5.1: 3-D contact pressure fields under different normal loads; p_i = 552.2 kPa.

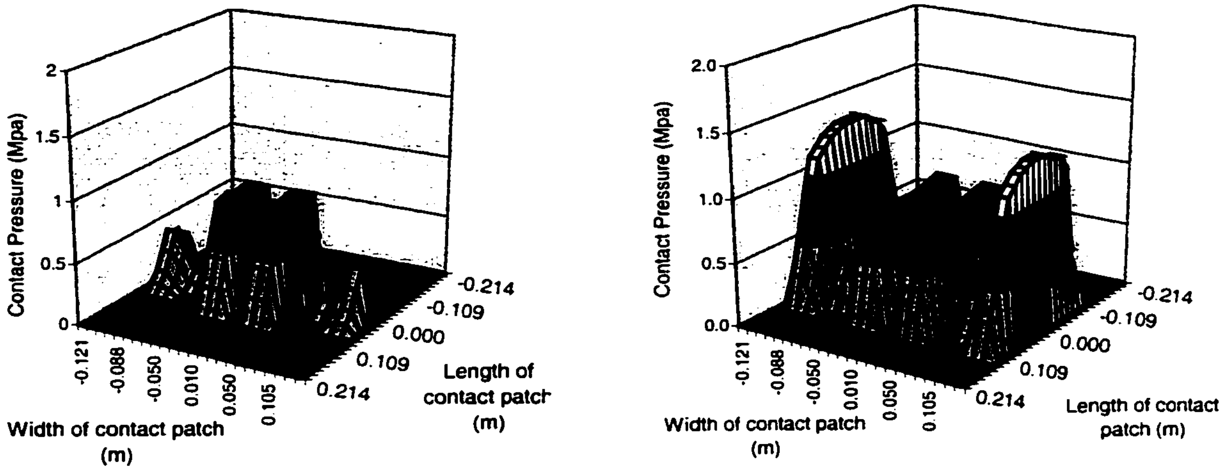

Fz = 11.2 KN

Fz = 24.3 KN

Figure 5.2: 3-D contact pressure fields under different normal loads; p_i = 621.3 kPa.

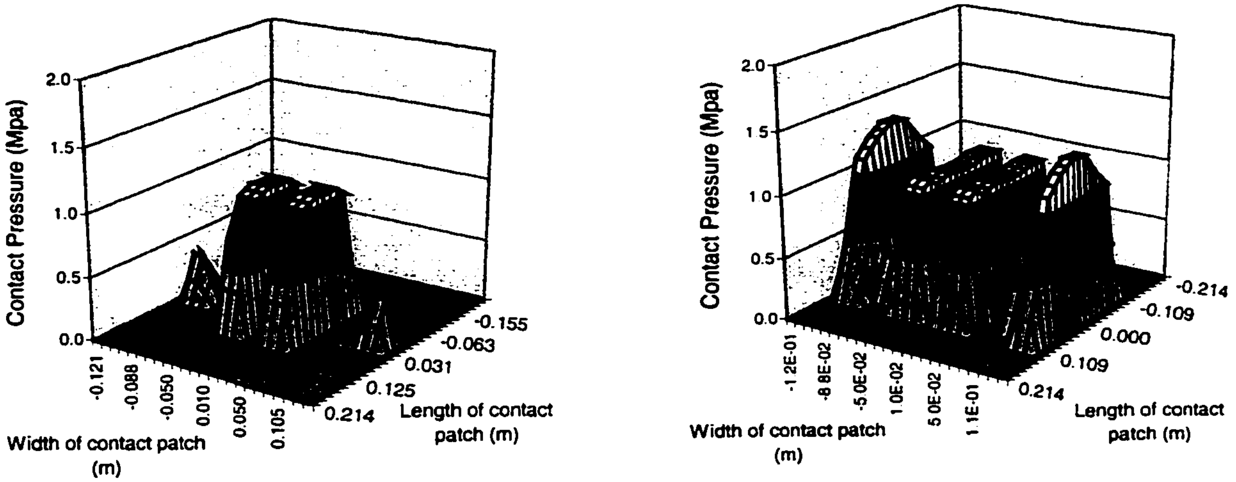

Fz = 12.1 KN

Fz = 28.6 KN

Figure 5.3: 3-D contact pressure fields under different normal loads; p_i = 828.4 kPa.

The critical values of the normal load, beyond which the pressure peaks tend to shift from inner ribs to the outer ribs, depend upon the tire inflation pressure. The results further reveal that the ratio of the peak pressure values occurring in the outer ribs to the peak pressure in the inner ribs tends to increase considerably with increase in the normal load for a given inflation pressure. Figure 5.4 illustrates the peak contact pressures observed within the inner and outer ribs of the tire as a function of the normal deflection and the inflation pressure.

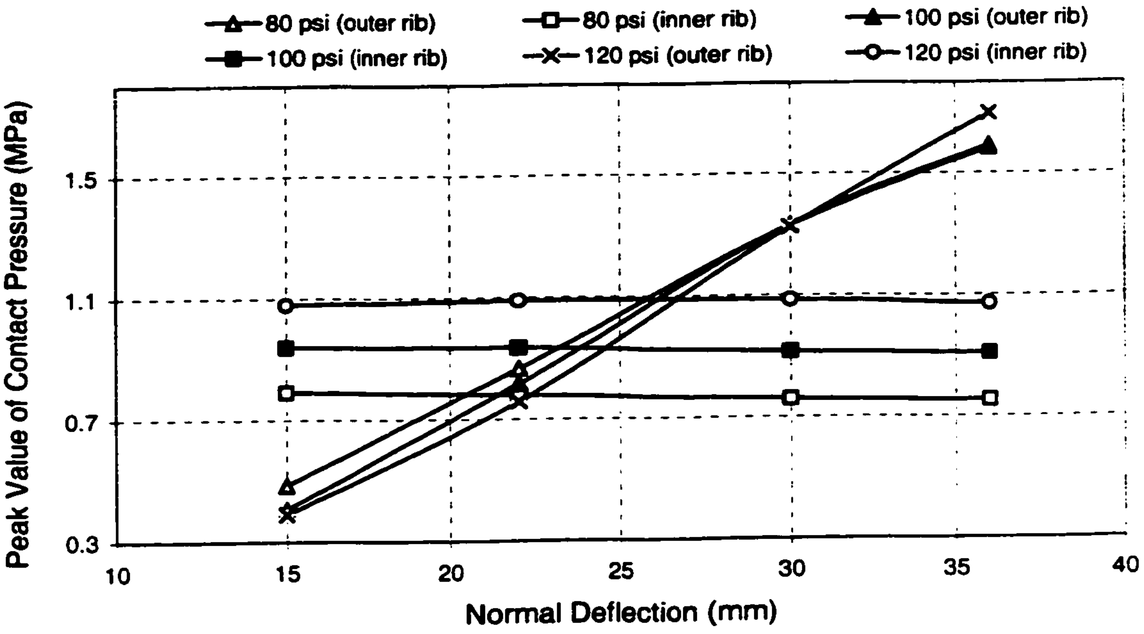

Figure 5.4: Peak contact pressure as a function of the normal deflection.

The results reveal that the peak pressures occurring within a rib are strongly related to the normal deflection. An increase in the normal deflection from 15 to 36 mm yields negligible effect on the peak values occurring in the inner ribs, but significant effect on the peak values of the contact pressure in the outer ribs. The peak contact pressure increases with the increase in the normal deflection and thus the normal load, for a given inflation pressure. The peak value corresponding to lower inflation pressure is higher than the peak value corresponding to a higher inflation pressure, when the normal deflection is below 30 mm. For a given normal deflection, increasing the inflation pressure results in higher contact pressure peaks in the outer rib areas. The intersection of the peak pressure curves for inner and outer ribs for a specific inflation pressure can be used to define the critical normal load. The results show that higher contact pressure peaks occur in the vicinity of inner ribs near the central circumferential line, when the normal load is lower than a critical value. The critical value of the normal load, however, increases with the increase in the inflation pressure.

The pressure peaks tend to shift towards the outer ribs, when the normal load is increased beyond the critical value. The ratio of the peak pressure occurring in the outer ribs to that in the inner ribs tends to increase most significantly when the normal load is increased beyond the critical value, specifically for the lower inflation pressures. Under lower inflation pressures, the contact pressure peaks shift to the outer ribs very rapidly, with increase in the normal load. Such characteristics of the contact pressure distributions are attributed to the upward deflection of the crown center in the contact patch and the deep downward deflections of the edges of the belts near the shoulder areas. Such trends in the contact pressure distribution have also been observed in reported experimental studies [131, 141].

5.3 ESTIMATION OF 2-D CONTACT PRESSURE DISTRIBUTION

Studies on ride dynamics and pavement damage potentials of heavy vehicle tires mostly consider in-plane models of the vehicle, where the tire-road interactions are modeled as a point-contact spring. The spring rate of the equivalent tire spring, invariably derived from the measured force-deflection data, is known to vary considerably with the inflation pressure as described earlier in Chapter 3. The point-contact approach, although quite simple and convenient, yields the resultant tire force acting at a point on the road surface. This contact force can cause an overestimate of the road damaging potentials of the dynamic loads and is known to exaggerate the wheel-hop tendency [152]. Analysis of the tire force transmitted to the pavement necessitates the development of adequate tire models to describe the contact patch geometry and the distribution of the contact forces on the road surface. Development of such a model, however, is quite complex due to complex tire geometry, structure and material properties. Alternately, the proposed finite element based tire model may be applied to derive the contact pressure distribution in the longitudinal-vertical plane of the contacting tire. The resultant contact force may be related to the force developed by the equivalent point-contact spring model of the tire [153-154]. A polynomial function may then be formulated to express the resultant force by its distribution on the road surface as a function of the normal load and inflation pressure.

5.3.1 Method of Analysis

Let the tire contact patch be represented by l rows and k columns of elements, where each element within the contact patch is subjected to a centralized force, P_{nm} (n = 1,..., l; m = 1,..., k) acting at the geometric center of the element, as shown in Figure 5.5(a). The magnitude of this point force (P_{nm}) can be computed from the element geometry and the average contact pressure p_{nm}:

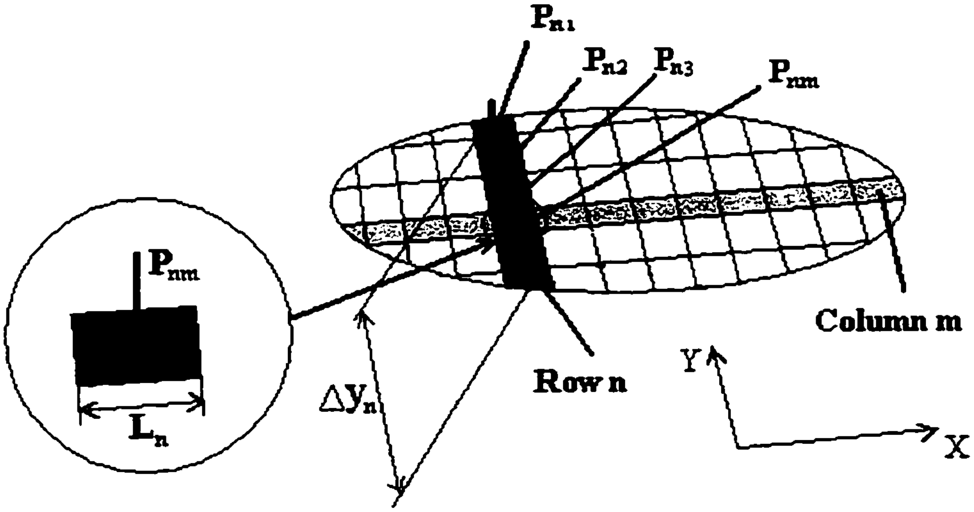

Figure 5.5(a): Schematic representation of the contact area.

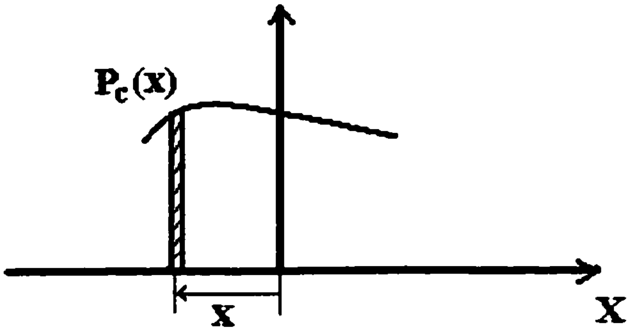

Figure 5.5: (b): Illustration of contact pressure as a function of coordinate x.

$$P_{nm} = p_{nm} s_{nm} \tag{5.1}$$

where s_{nm} is the area of the element, located in row n and column m of the contact patch. The work done by the centralized force can be computed from the average normal deflection of the element dz_{nm}, in the following manner:

$$W_{nm} = P_{nm} \cdot dz_{nm} \quad . \tag{5.2}$$

The equivalent 2-D contact pressure due to elements in row n can then be computed as:

$$p_n = \frac{\sum_{m=1}^{k} W_{nm}}{dz_n \cdot L_n \cdot (\Delta y_n)}; \qquad n = 1, \ldots, l \tag{5.3}$$

where L_n and Δy_n are the length and the total width of elements in row n, respectively, as illustrated in Figure 5.5(a). The normal deflection dz_n represents the average vertical deflection of the elements in row n. p_n (n = 1, ..., l) describes the 2-D equivalent contact pressure acting on the road surface in the longitudinal-vertical (X-Z) plane. The distributed tire-road contact force acting on the road surface, F_{zn} (n = 1, ...,l), can then be estimated from:

$$F_{zn} = p_n L_n (\Delta y_n); \qquad \text{n} = 1, \ldots, l \tag{5.4}$$

The equivalent contact pressure along the longitudinal direction, derived from Equation (5.4), is considered to act along the circumferential centerline of the tire and can be expressed as a polynomial function of the longitudinal coordinate of the contact patch corresponding to a given inflation pressure and normal load. The origin of the longitudinal axis is placed at the intersection of the vertical centerline of the tire with the road surface. The normalized contact pressure could be expressed as a function of the value of the equivalent point-contact force or the normalized equivalent normal load:

$$\left(\frac{p_c(x)}{1(Pa)}\right)=\sum_{i=1}^{q}a_i\left(\frac{F_z}{1(N)}\right)\cdot\left(\frac{x}{1(m)}\right)^{q-i} \qquad (5.5)$$

where $p_c(x)$ is the contact pressure in Pascal (Pa) and x is the longitudinal coordinate from the contact center in meter (m), as shown in Figure 5.5(b), while F_z is the resultant normal load in Newton (N), q describes the order of the polynomial function and $a_i\left(\frac{F_z}{1(N)}\right)$ are the coeficients described as functions of normalized F_z.

5.4 IDENTIFICATION OF POLYNOMIAL FUNCTIONS

From the above analyses on the 3-D contact pressure fields and the contact geometry analysis performed in Chapter 3, it is apparent that the magnitude of the contact pressure peak and the length of the contact area, are strongly influenced by the inflation pressure and the normal load in a nonlinear manner. The 2-D contact pressure fields are thus expected to be strongly dependent upon the normal load F_z and the inflation pressure p_l in a highly complex manner. Figures 5.6 and 5.7 illustrate the 2-D contact pressure distribution of the truck tire under 621.3 kPa (90 psi) and 759.3 kPa (110 psi) inflation pressures, respectively, as estimated from Equation (5.3). The figures also show the corresponding curves fitting the pressure distribution data for different normal loads. The pressure distribution identified from the finite element model shows slight asymmetry about the vertical centerline of the tire, which is considered to be mostly attributed to the asymmetric stacking sequence of the belts and the carcass layers. The corresponding curves, derived from the polynomial function of Equation (5.3), however, appear to be less asymmetric about the contact center.

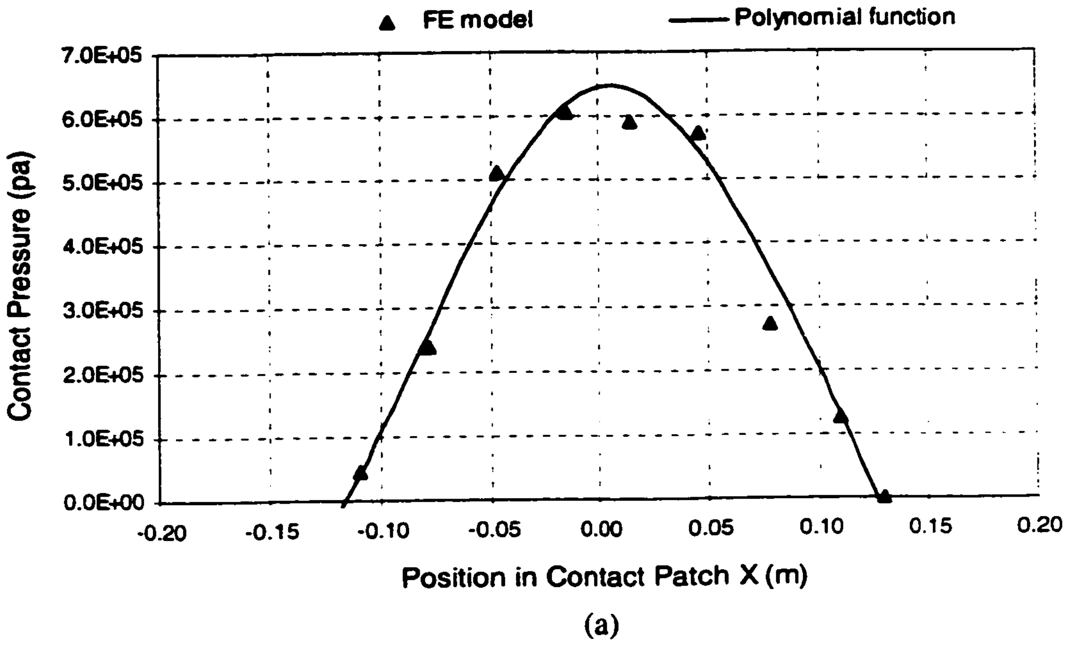

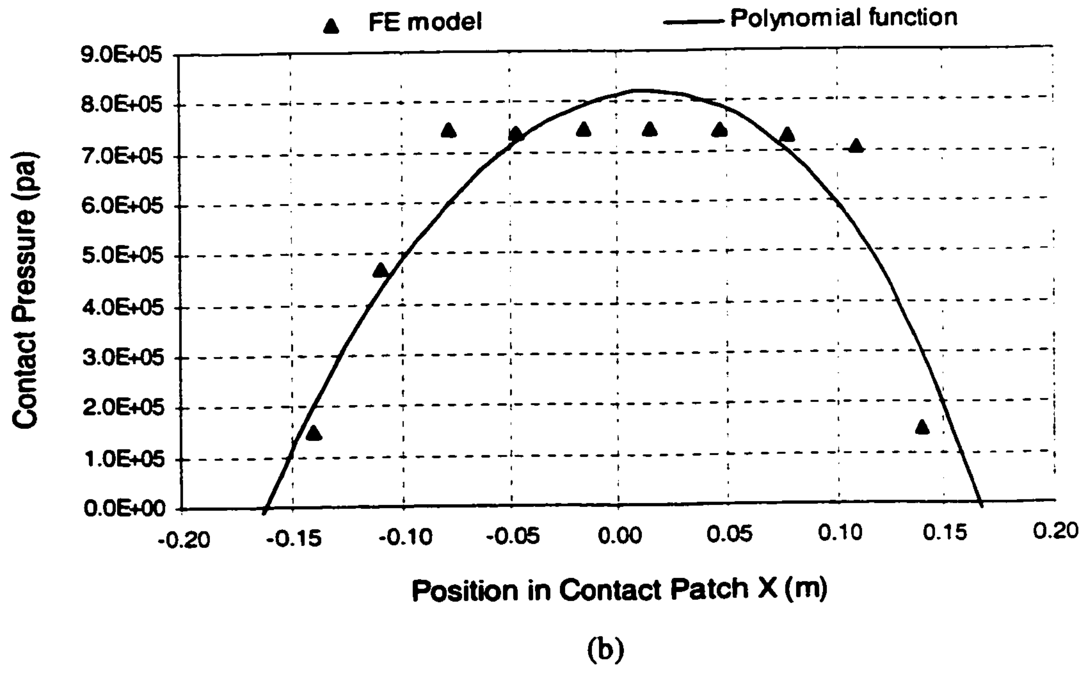

Figure 5.6: 2-D contact pressure distributions for different normal loads; p_l = 621.3 kPa: (a) F_z= 17.1 kN; and (b) F_z= 31.1 kN.

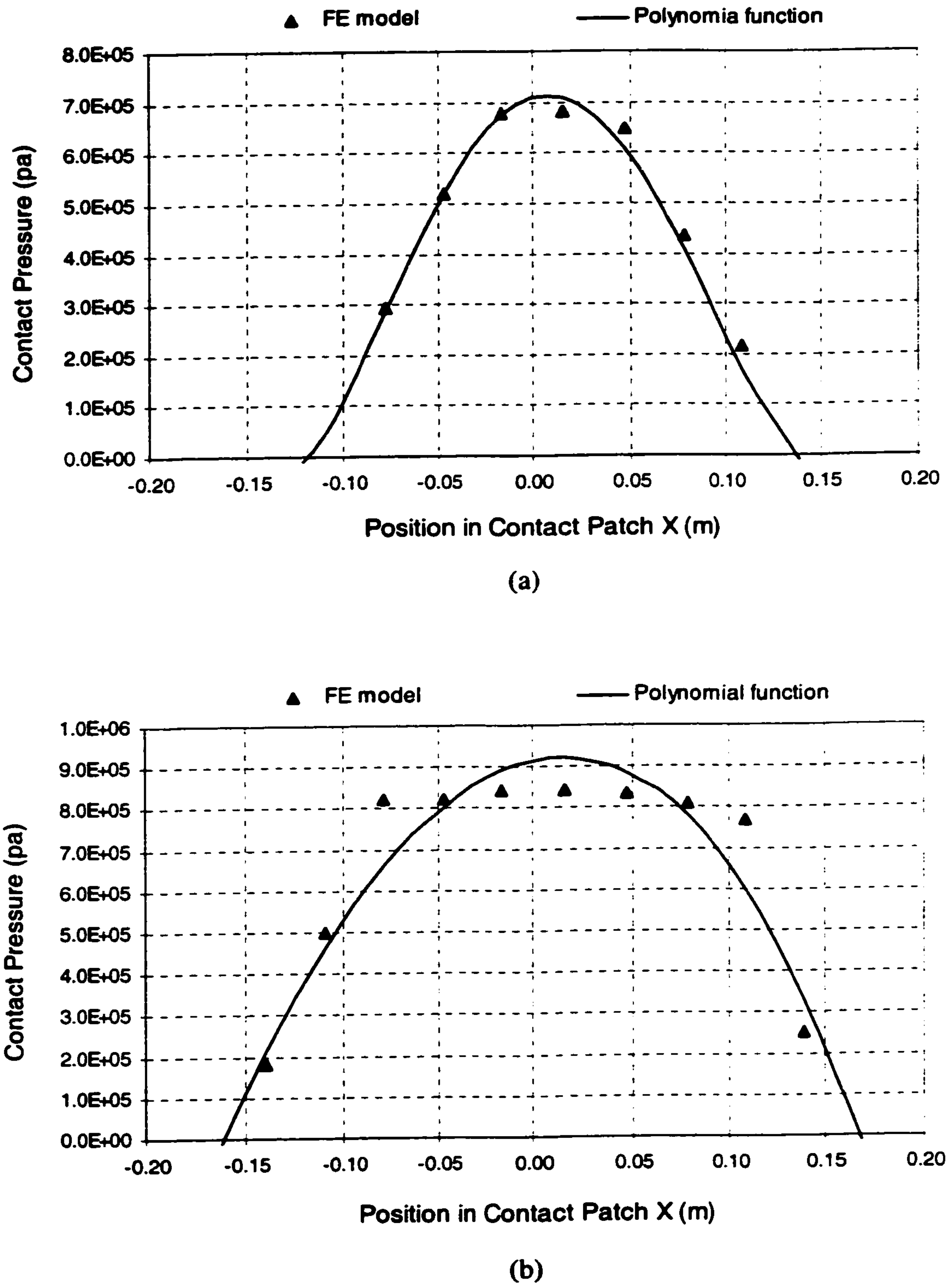

(a)

(b)

Figure 5.7: 2-D contact pressure distributions for different normal loads; p_I = 759.3 kPa: (a) F_z = 19.4 kN; and (b); F_z = 34.7 kN.

The results reveal that the contact pressure distribution is strongly dependent on both the inflation pressure and the normal load, and that the length of the contact patch varies nonlinearly with the normal load and inflation pressure. The 2-D contact pressure distribution (p_c) along the length direction of the contact patch in the tire-road interface is thus considered to be a function of the inflation pressure (p_l), the normal load (F_z) and the coordinate (x) along the longitudinal direction. A polynomial function is thus formulated to describe these dependencies. The detailed form of the function is derived through analysis of the dependency of the contact pressure distribution on each individual variable, while the remaining variables are held as constants. The derived formulation is validated by comparing the estimated contact pressure distribution with the data obtained from the finite element model.

5.4.1 Identification of the Polynomial Coefficients

The identification of the polynomial coefficients is initiated by analyzing the 2-D contact pressure distributions derived from the computed 3-D contact pressure fields as a function of the longitudinal coordinate (x), where the normal load (F_z) and the inflation pressure (p_l) are treated as constant parameters. The coefficients (a_i) of the derived formulation of the contact pressure distribution $p_c(x)$, are then used to define a polynomial function in the normal load (F_z), while the inflation pressure (p_l) is still treated as a fixed parameter. The identified coefficients (k_{ij}) of the derived polynomial function (a_i), can be further estimated as functions of the inflation pressure (p_l). Finally, the polynomial formulation describing the contact pressure distribution as a function of the inflation pressure, normal load and longitudinal coordinate can be achieved.

In view of the nonlinear characteristics of the contact pressure distribution as function of the inflation pressure, normal load and the longitudinal coordinate, the coefficients (a_i) of the polynomial are identified as functions of both F_z and p_l. The curve fitting is initially performed for a constant value of p_l. The analysis is performed for given values of p_l ranging from 80-120 psi (552.2-828.4 kPa). The results reveal that the contact pressure distribution can be accurately described by a fourth-order polynomial in x, which is equivalent to $q = 5$ in Equation (5.5), while the inflation pressure and the normal load are kept constants. Figures 5.8 and 5.9 illustrate the variations in the coefficients a_i, ($i = 1, 2, 3, 4, 5$) as functions of the normal load for $p_l = 621.3$ kPa (90 psi) and 828.4 kPa (120 psi), respectively. The coefficient values derived from equations (5.3) and (5.5) are indicated by symbols (▲), while the corresponding curve-fit is indicated by a continuous line. While the coefficients a_i (i = 1, 4, 5) increase with increase in the normal load until certain value of the normal load, a_1 and a_4 decrease significantly, and a_5 approaches to a nearly steady value, when normal load increases further. On the contrary, a_2 and a_3 reduce at first and then increase with further increase in the normal load. The results show that the coefficients a_i, (i = 1, ..., 5) are strongly related to variations in the normal load in a nonlinear manner. Moreover, increasing the inflation pressure yields significant increases in a_1, a_4 and a_5 and considerable reductions in a_2 and a_3 for the same normal load values. The results reveal that the the

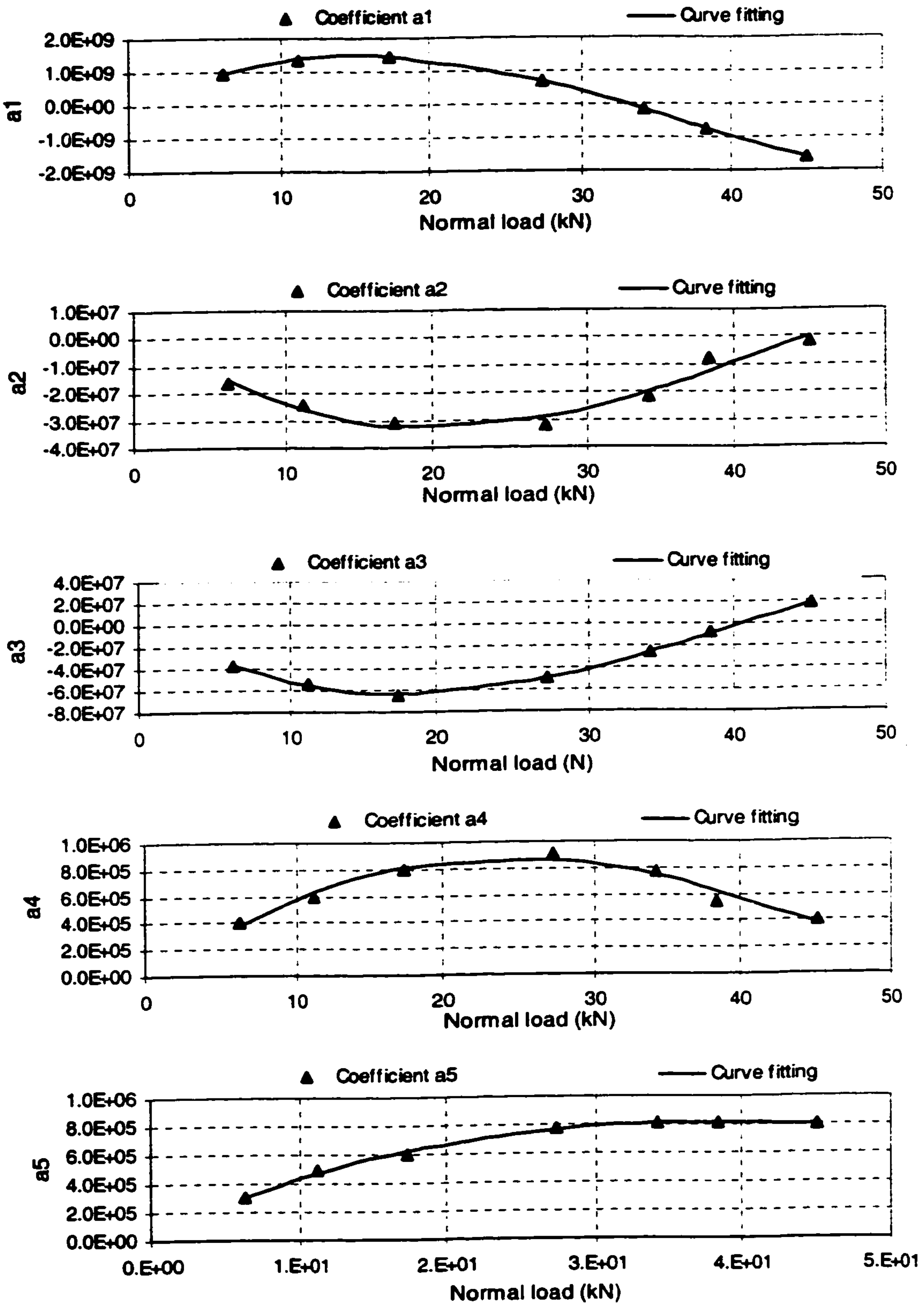

Figure 5.8: Variations in coefficients a_i (i = 1, 2, 3, 4, 5) with the normal load F_z; p_i = 621.3 kPa (90 psi).

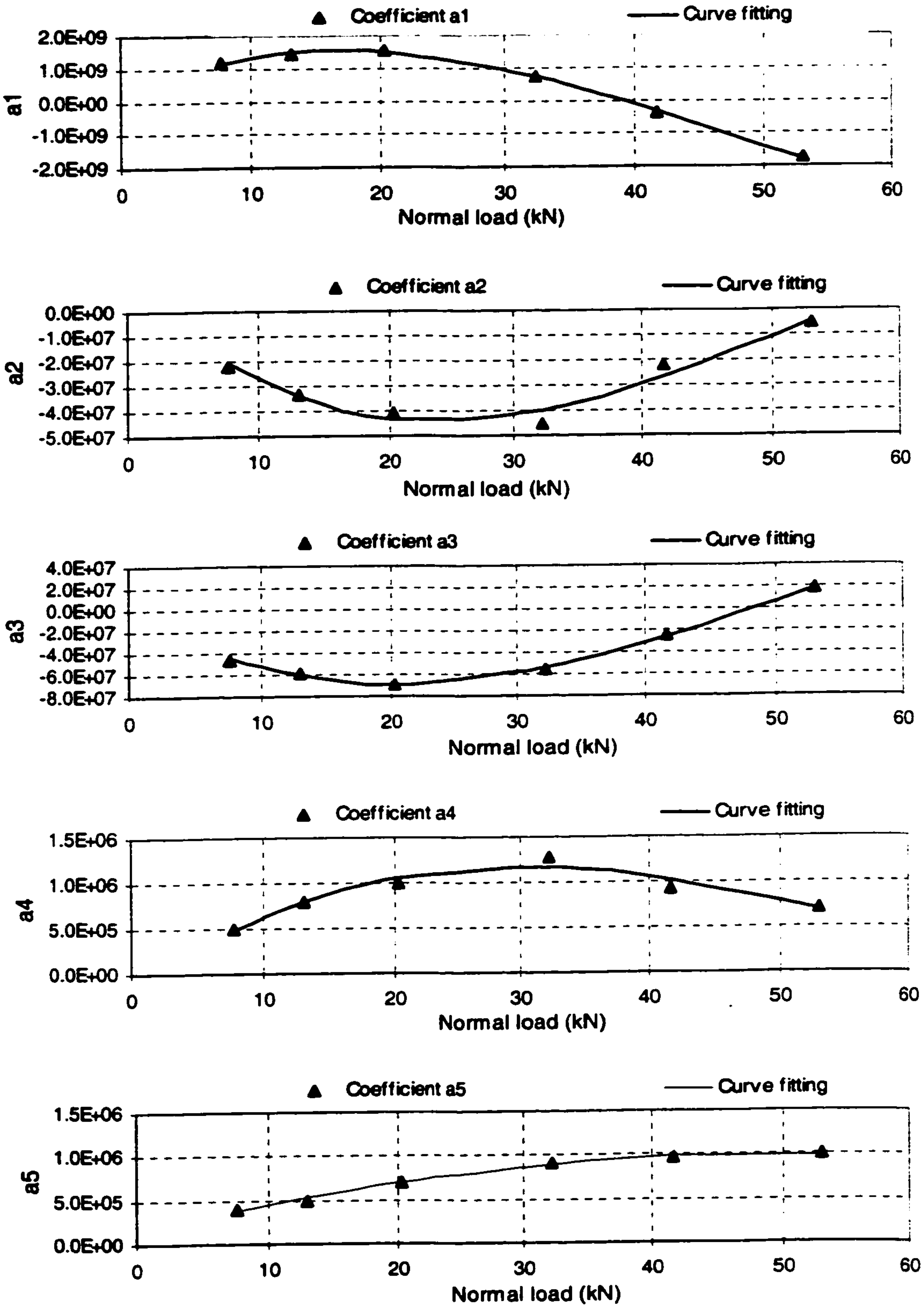

Figure 5.9: Variations in coefficients a_i (i = 1, 2, 3, 4, 5) with the normal load F_z; p_I = 828.4 kPa (120 psi).

variations in the normal load and in the inflation pressure have strong effects on the values of a_i, (i = 1, ..., 5) in a nonlinear manner.

The dependency of a_i on the inflation pressure can be incorporated by expressing them as polynomial functions in normal load F_z for a range of p_l. The analyses performed for a given inflation pressure revealed that each of the coeffiecients a_i can be accurately desribed by a third-order polynomial in normal load F_z in Newton (N), such that

$$a_i = \sum_{j=1}^{r} k_{ij} \left(\frac{p_l}{1(psi)} \right) \cdot \left(\frac{F_z}{1(N)} \right)^{r-j} \qquad (i = 1, 2, 3, 4, 5) \qquad (5.6)$$

where $r = 4$ and k_{ij} (j = 1, 2, 3, 4) are the interpolation coefficients corresponding to a_i, which are dependent on the inflation pressure p_l and can further be expressed as third-order polynomial functions in normalized p_l:

$$k_{ij} = \sum_{l=1}^{s} w_l \left(\frac{p_l}{1(psi)} \right)^{s-l} ; \qquad (j = 1, 2, 3, 4;\ i = 1, 2, \ldots, 5) \qquad (5.7)$$

where w_l (l = 1, 2, 3, 4) are the coefficients of the polynomial and $s = 4$.

Curve-fitting is further performed to identify the constant coefficients w_l (l = 1, 2, 3, 4). Equations (5.6) and (5.7) are solved to derive the coefficients k_{ij} (j = 1, 2, 3, 4) as functions of p_l that correspond to each a_i and F_z. The relationships between k_{ij} (j = 1, 2, 3, 4; i=1, 2, 3, 4, 5) and p_l corresponding to each a_i are shown in Figure 5.10(a-e). It can be seen that the coefficients k_{ij} corresponding to coefficients a_1 and a_3 are nearly linearly related to the inflation pressure, while the coefficients of k_{ij} corresponding to a_2, a_4 and a_5 appear highly nonlinear functions of the inflation pressure.

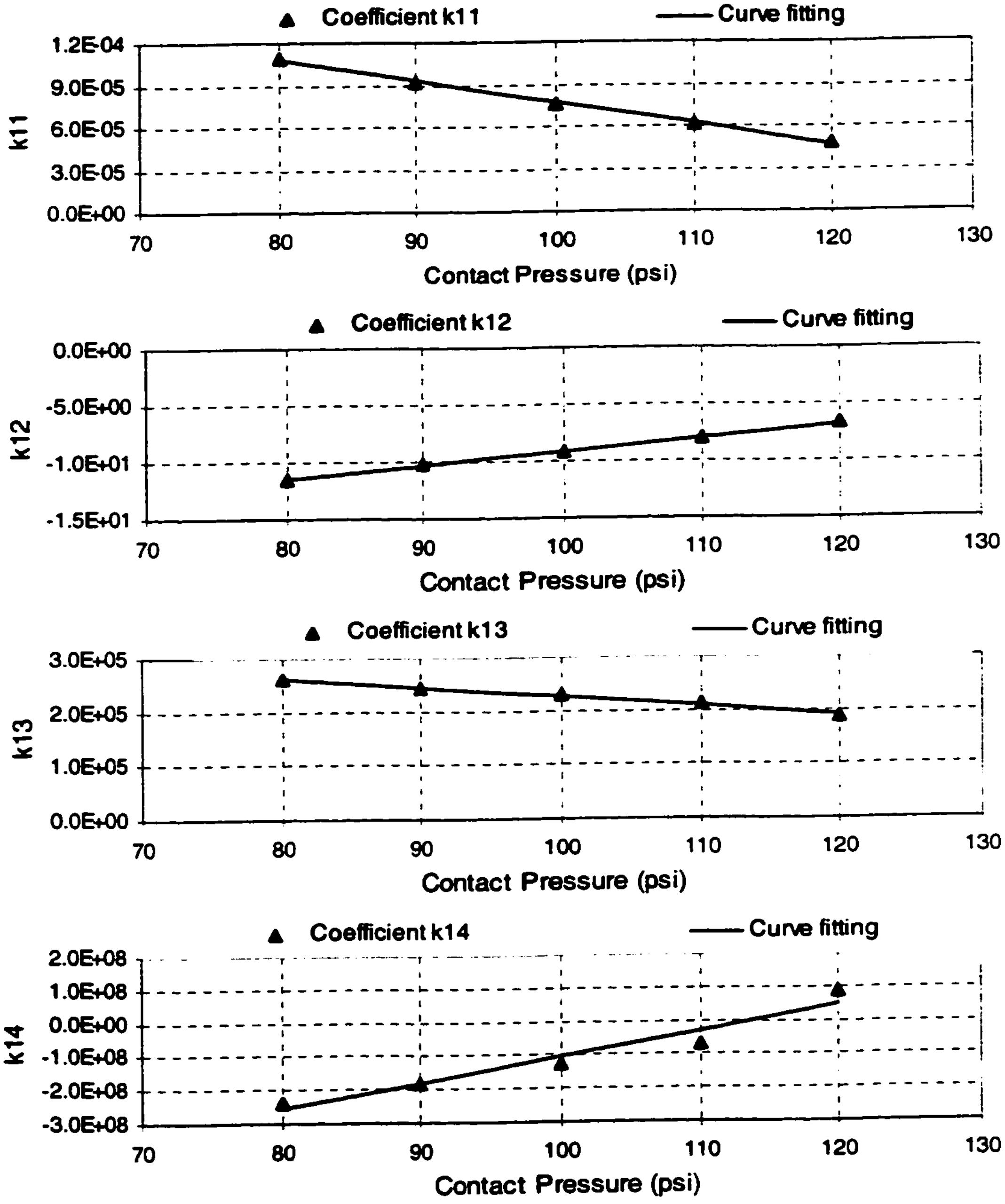

Figure 5.10(a): Variations in coefficients k_{1j} (j = 1, 2, 3, 4) with inflation pressure (corresponding to coefficient: a_1).

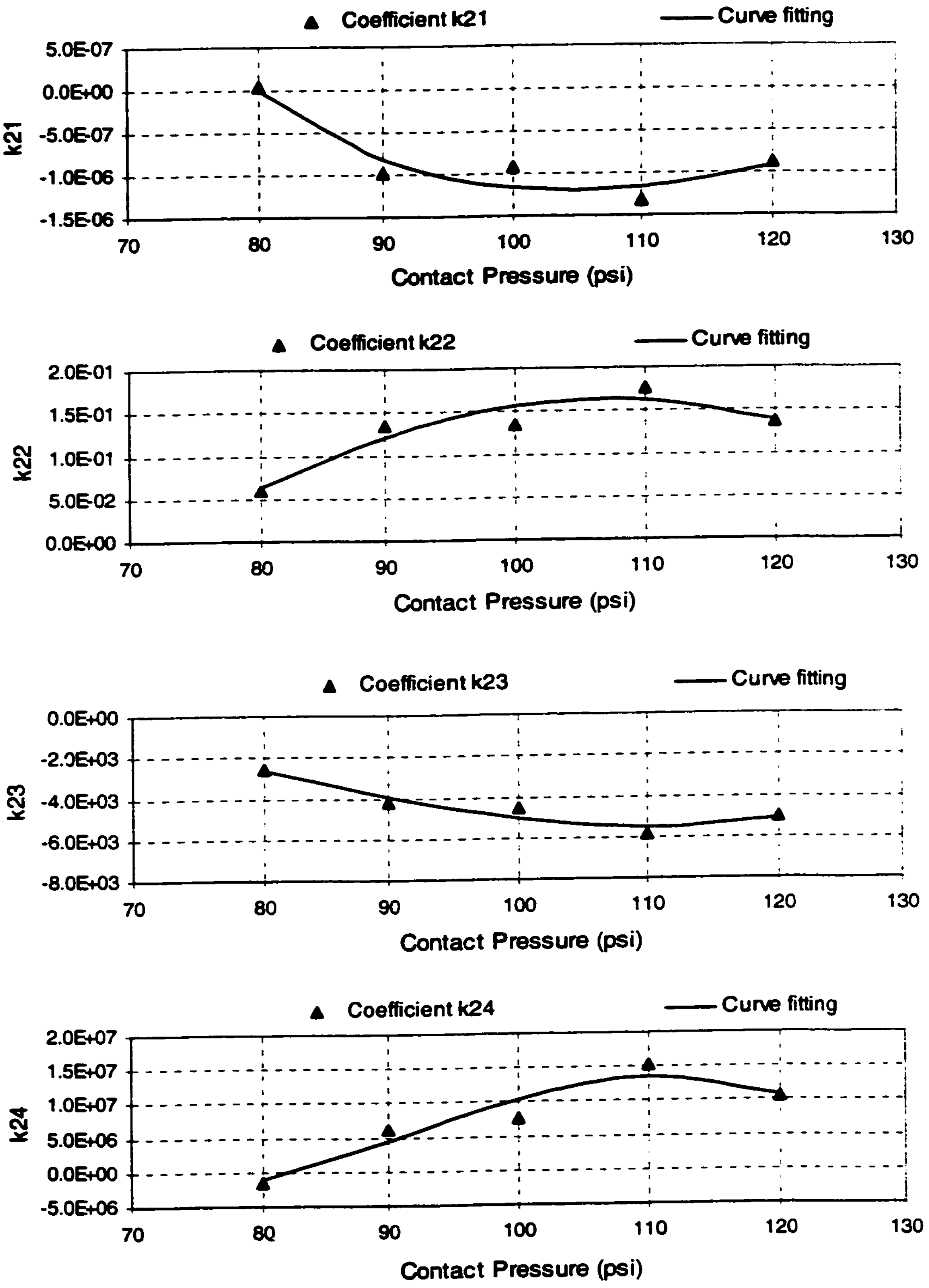

Figure 5.10(b): Variations in coefficients k_{2j} (j = 1, 2, 3, 4) with inflation pressure (corresponding to coefficient: a_2).

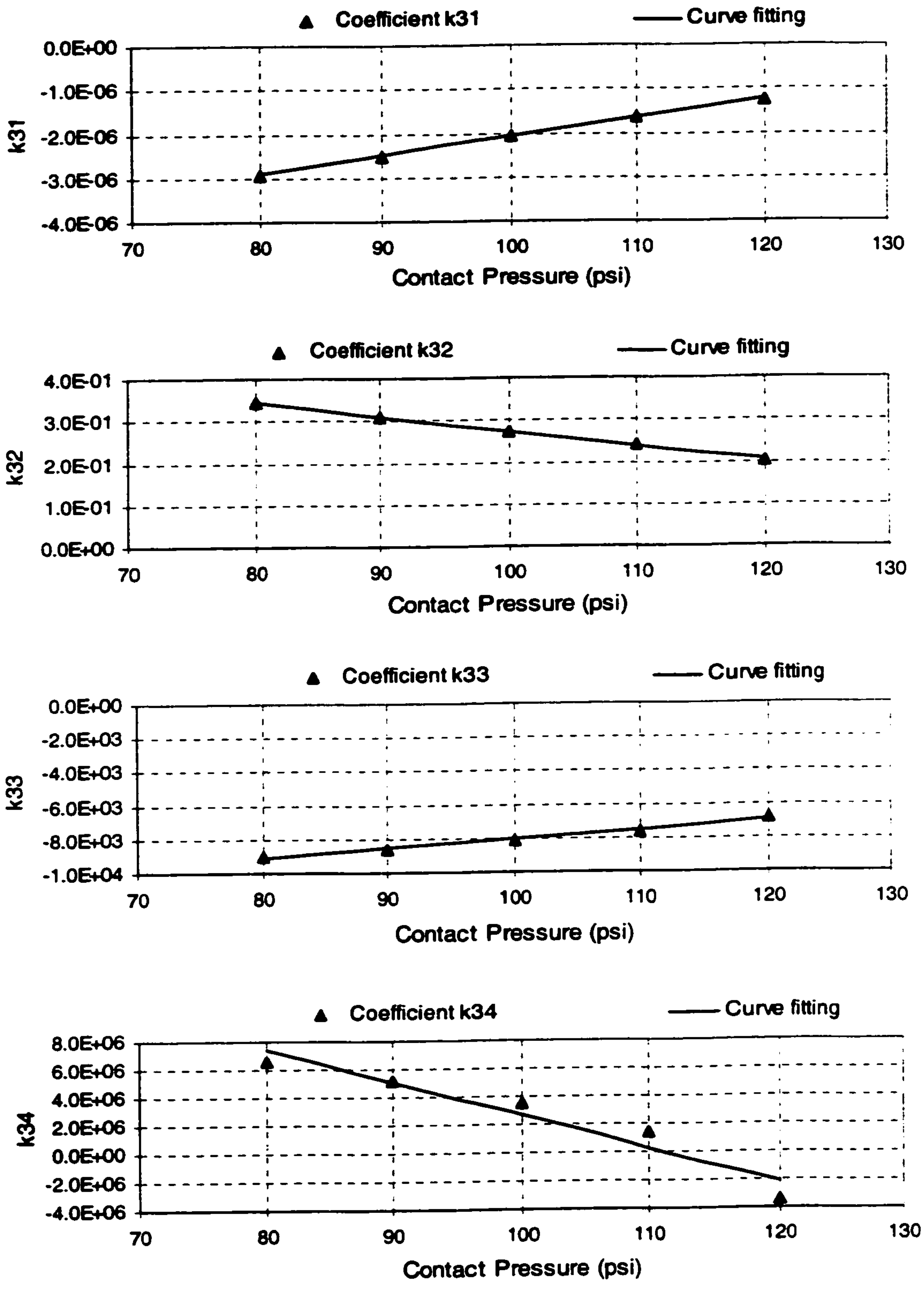

Figure 5.10(c): Variations in coefficients k_{3j} (j = 1, 2, 3, 4) with inflation pressure (corresponding to coefficient: a_3).

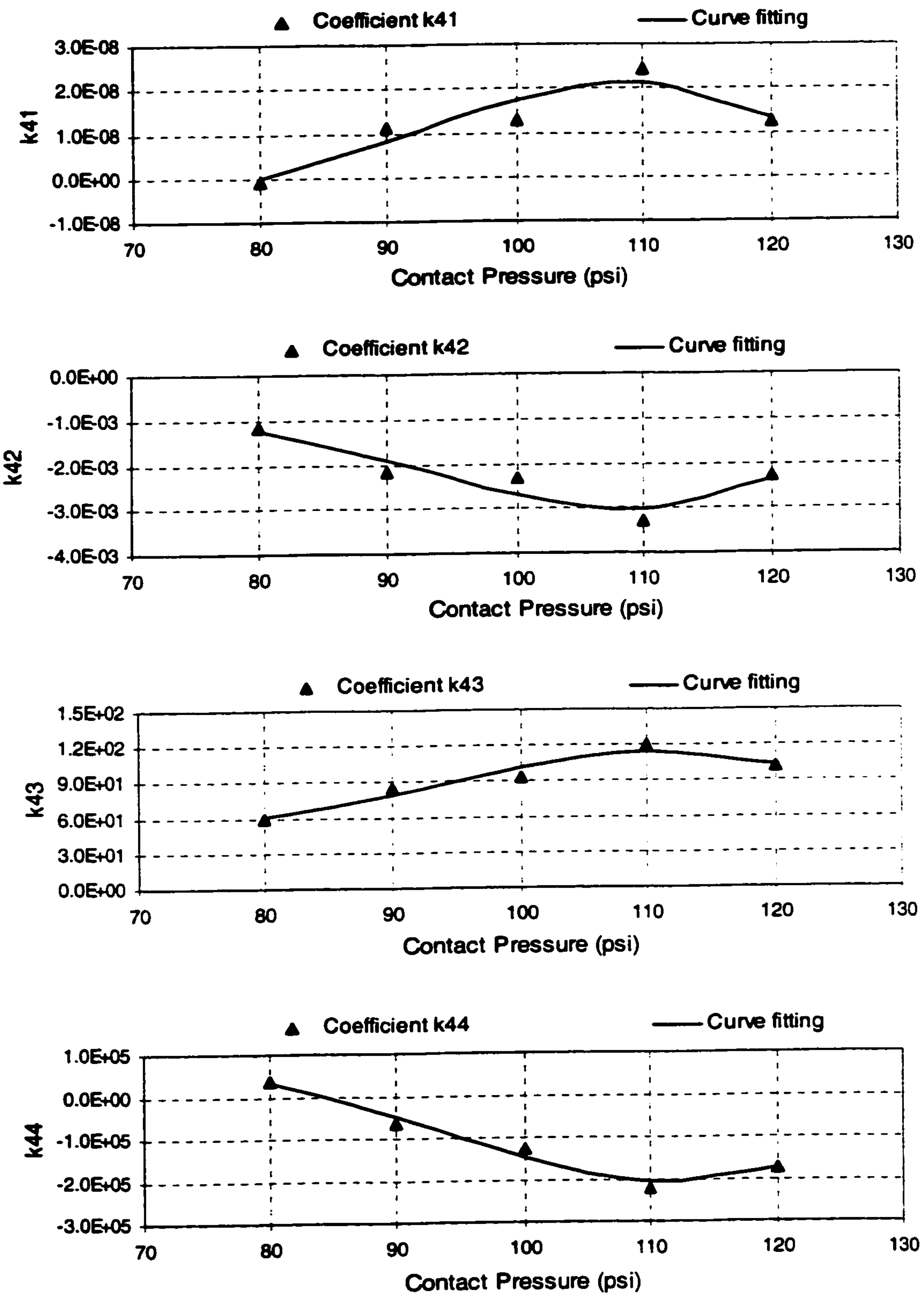

Figure 5.10(d): Variations in coefficients k_{4j} (j = 1, 2, 3, 4) with inflation pressure (corresponding to coefficient: a_4).

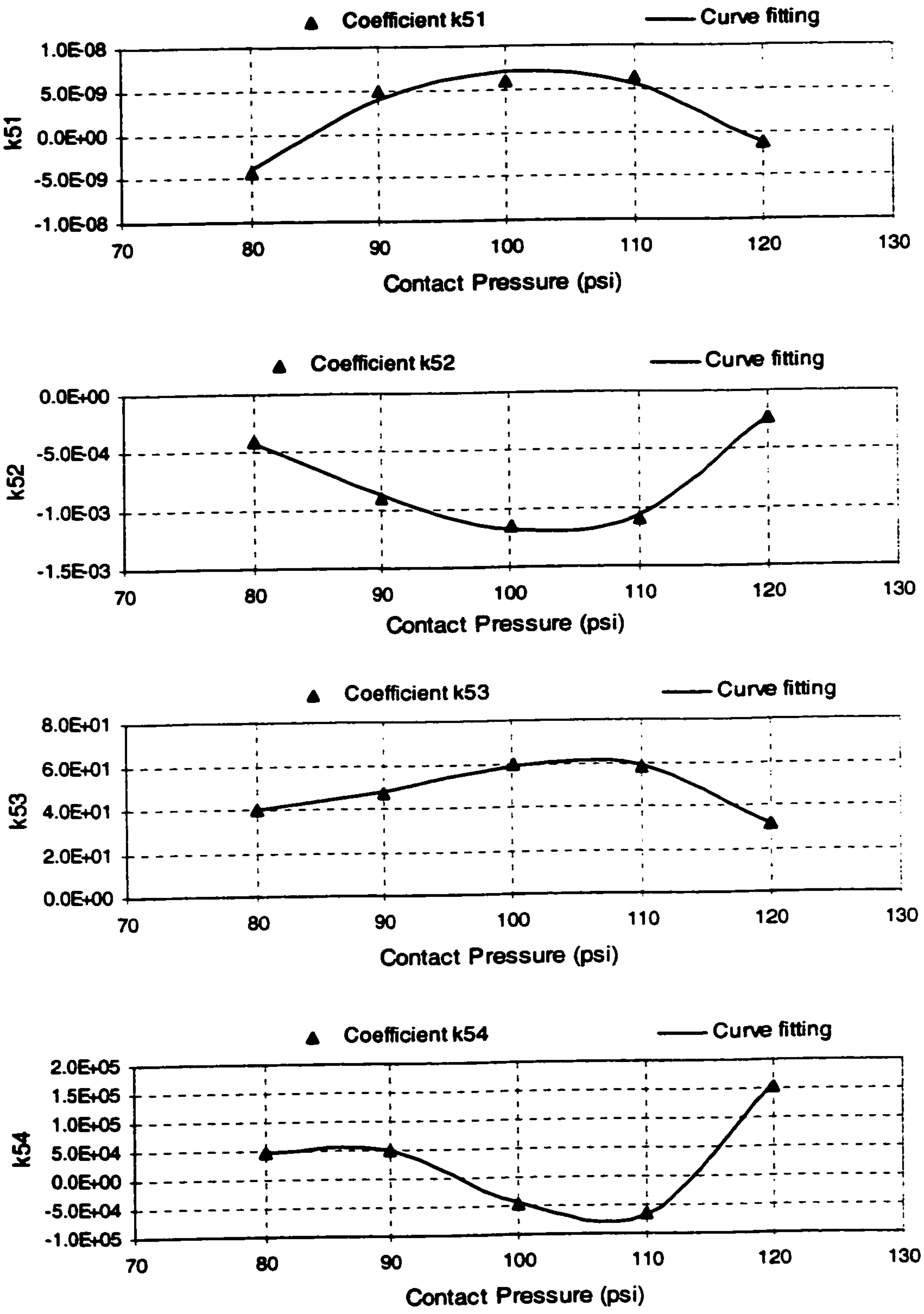

Figure 5.10(e): Variations in coefficients k_{5j} (j = 1, 2, 3, 4) with inflation pressure (corresponding to coefficient: a_5).

Once the values of w_l for each k_{ij} (j = 1, 2, 3, 4), which are derived for each a_i (i=1, 2, 3, 4, 5), are known, the matrix W_i (i = 1, ..., 5) can be established and used to derive the series of coefficients a_i in order to obtain the pressure distribution polynomial function. Based on the assumption that the contact pressure distribution for given values of inflation pressure and normal load can be expressed as a polynomial function in coordinate x and that the highest power of the polynomial is four (q = 5), the contact pressure distribution of Equation (5.5) can be expressed as:

$$p_c(x) = A'X \tag{5.8}$$

where $A' = [a_1 \quad a_2 \quad a_3 \quad a_4 \quad a_5]$, and $X = [\bar{x}^4 \quad \bar{x}^3 \quad \bar{x}^2 \quad \bar{x} \quad 1]'$, where $\bar{x} = x/(1m)$ and x is the longitudinal coordinate in meter (m). When inflation pressure p_l is constant, the elements in matrix A are expressed as functions of the value of the normal load F_z alone:

$$a_i = K_i'F\,;\ (i = 1, 2, 3, 4, 5) \tag{5.9}$$

where $K_i' = [k_{i1} \quad k_{i2} \quad k_{i3} \quad k_{i4}]$ (i = 1, 2, 3, 4, 5); $F = [\bar{F}_z^3 \quad \bar{F}_z^2 \quad \bar{F}_z \quad 1]'$, where $\bar{F}_z = F_z/(1N)$ and F_z represents the normal load in Newton (N) acting on the tire. The vector A can thus be expanded as:

$$A = KF \tag{5.10}$$

where K=$[K_1^t \quad K_2^t \quad K_3^t \quad K_4^t \quad K_5^t]^t$, is a (5×4) matrix containing the vectors K_i (i = 1, ..., 5). Each row of the matrix K, K_i^t (i = 1, 2, 3 4, 5), is a polynomial function in p_l, as expressed in Equation (5.7), and can be written as

$$K_i = W_i P, \qquad (i = 1, \ldots, 5) \tag{5.11}$$

where

$$K_i = \begin{bmatrix} k_{i1} \\ k_{i2} \\ k_{i3} \\ k_{i4} \end{bmatrix}, \quad W_i = \begin{bmatrix} w_{11} & w_{12} & w_{13} & w_{14} \\ w_{21} & w_{22} & w_{23} & w_{24} \\ w_{31} & w_{32} & w_{33} & w_{34} \\ w_{41} & w_{42} & w_{43} & w_{44} \end{bmatrix}_{(i)}, \quad P = \begin{bmatrix} \bar{p}_l^{\,3} \\ \bar{p}_l^{\,2} \\ \bar{p}_l \\ 1 \end{bmatrix} \tag{5.12}$$

where the matrices W_i (i = 1, ..., 5) are the final objective matrices that are used to obtain the coefficients a_i (i = 1, 2, 3, 4, 5), $\bar{p}_l = p_l/(1psi)$ and p_l represents the value of the inflation pressure in psi. The value of i is equal to the number of coefficients a_i contained in the series. When all the matrices W_i are known, the terms in a_i can be obtained using the prescribed procedure. The resulting polynomial, expressed as a function of the values of the inflation pressure, normal load and position along the contact patch, can be used to predict the 2-D tire-road contact pressure distributions for given inflation pressure and normal load. The polynomial function can be expressed in the following manner:

$$(\bar{p}_c(x)) = \sum_{i=1}^{q} \sum_{j=1}^{r} \sum_{l=1}^{s} w_l \cdot (\bar{p}_l)^{s-l} \cdot (\bar{F}_z)^{r-j} \cdot (\bar{x})^{q-i} \tag{5.13}$$

where $\overline{p}_c(x) = p_c(x)/(1Pa)$, $\overline{p}_l = p_l/(1psi)$, $\overline{F}_z = F_z/(1N)$ and $\overline{x} = x/(1m)$ are the normalized contact pressure, inflation pressure, normal load and the longitudinal coordinates, while q, r and s take on values of 5, 4 and 4, respectively. The procedure for formulating the contact pressure polynomial is illustrated in Figure 5.11, in which the matrices W_i, the inflation pressure p_l and the normal load are used as the input data.

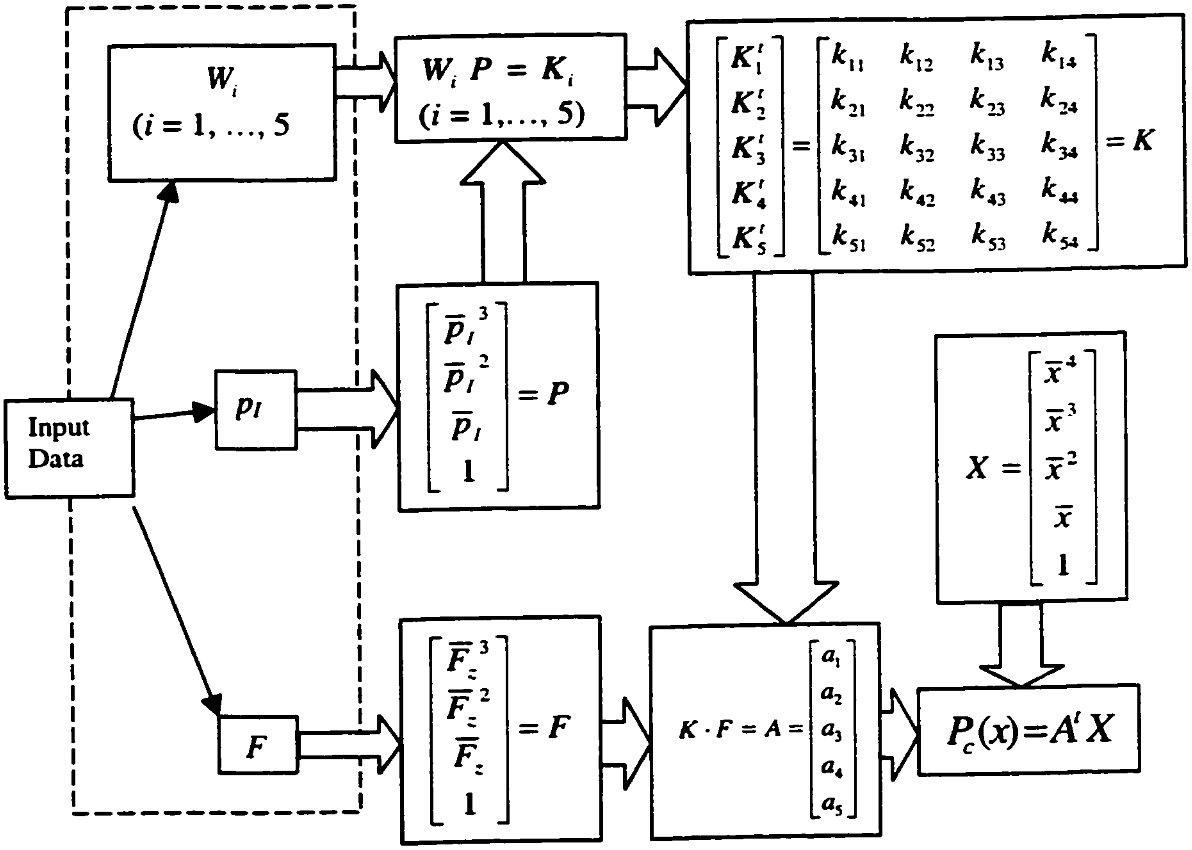

Figure 5.11: Procedure for estimating the contact pressure distribution as a function of the normal load and inflation pressure.

The matrices W_i are used in conjunction with the previously constructed column vector P containing the given value of the inflation pressure to derive the column vector

K_i. The K_i (i = 1, 2, 3, 4, 5) are further employed to construct the matrix K. The dot product of the matrix K and the column vector F containing the given value of the normal load yields the coefficients a_i and thus the column vector A. The objective function $p_c(x)$ is finally achieved by the dot product of A' and the column vector X containing the coordinate x.

5.5 DISCUSSION OF THE RESULTS

The 3-D pressure fields derived from the finite element model of a 12.5R22.5 truck tire are analyzed to formulate matrices W_i. The matrices W_i (i = 1, 2, 3, 4, 5) are derived as following:

$$W_1 = \begin{bmatrix} 0 & 0 & -1.54e-06 & 2.32e-04 \\ 0 & 0 & 0.1177 & -20.88 \\ 0 & 0 & -1.76e+03 & 4.02e+05 \\ 0 & 0 & 7.57e+06 & -8.6e+08 \end{bmatrix}$$

$$W_2 = \begin{bmatrix} -1.85e-11 & 7.32e-09 & -9.26e-07 & 3.67e-05 \\ -3.80e-07 & -2.29e-05 & 0.018 & -1.04 \\ 0.0606 & -15.35 & 1.17e+03 & -2.87e+04 \\ -559.7 & 1.55e+05 & -1.4e+07 & 3.85e+08 \end{bmatrix}$$

$$W_3 = \begin{bmatrix} 0 & 0 & 4.20e-08 & -6.27e-06 \\ 0 & 0 & -3.50e-03 & 0.624 \\ 0 & 0 & 53.166 & -1.33e+04 \\ 0 & 0 & -2.383e+05 & 2.65e+07 \end{bmatrix}$$

$$W_4 = \begin{bmatrix} -1.04e-12 & 2.85e-10 & -2.51e-08 & 7.11e-07 \\ 9.33e-08 & -2.57e-05 & 2.28e-03 & -6.66e-02 \\ -2.30e-03 & 0.63894 & -56.96 & 1.702e+03 \\ 8.5577 & -2.37e+03 & 2.09e+05 & -5.89e+06 \end{bmatrix}$$

$$W_5 = \begin{bmatrix} 0 & -2.45e-11 & 4.96e-09 & -2.45e-07 \\ 4.69e-08 & -1.19e-05 & 9.61e-04 & -2.51e-02 \\ -2.53e-03 & 0.7012 & -63.55 & 1.93e+03 \\ 28.45 & -8.17e+03 & 7.72e+05 & -2.4e+07 \end{bmatrix} \qquad (5.14)$$

The polynomial functions, described in Equations (5.8) and (5.13), are then derived and the estimates of contact pressure distribution are obtained using the procedure illustrated in Figure 5.11, where the required inputs are the values of the inflation pressure and the normal load with units of psi and N, respectively.

Figure 5.12 illustrates the estimated contact pressure distributions at the tire-road interface of the selected tire for inflation pressure ranging from 552.2 to 828.4 kPa (80 to 120 psi), and various values of the normal load, ranging from 5 kN to 45 kN. The estimated pressure distributions corresponding to specific normal loads (20, 30 and 40 kN) and 80 psi, 100 psi and 120 psi inflation pressures are presented in Figure 5.13. It is observed that increasing the normal load significantly increases the length of the contact patch for constant inflation pressure, but increasing the inflation pressure affects the footprint length only slightly for a constant normal load. Under light normal load and high inflation pressure, the contact pressure peaks occur in the vicinity of the central point of the contact patch. The pressure peaks, however, tend to shift towards front and rear edges of the contact patch, under high normal loads or low inflation pressures.

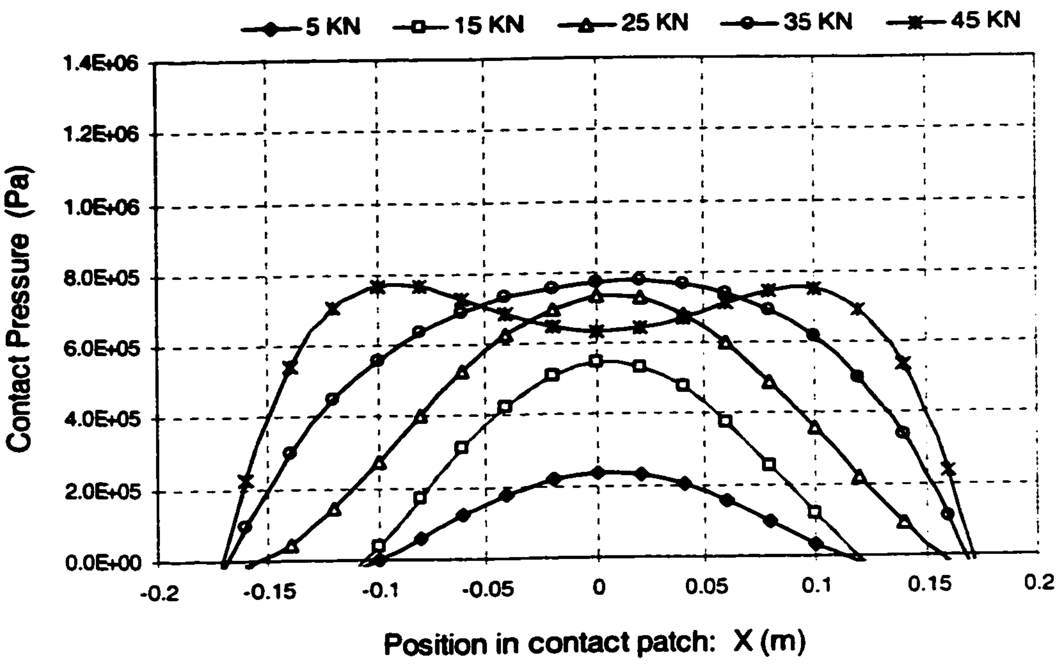

Figure 5.12(a): Contact pressure distributions estimated from the proposed polynomial for different normal loads; p_i = 80 psi.

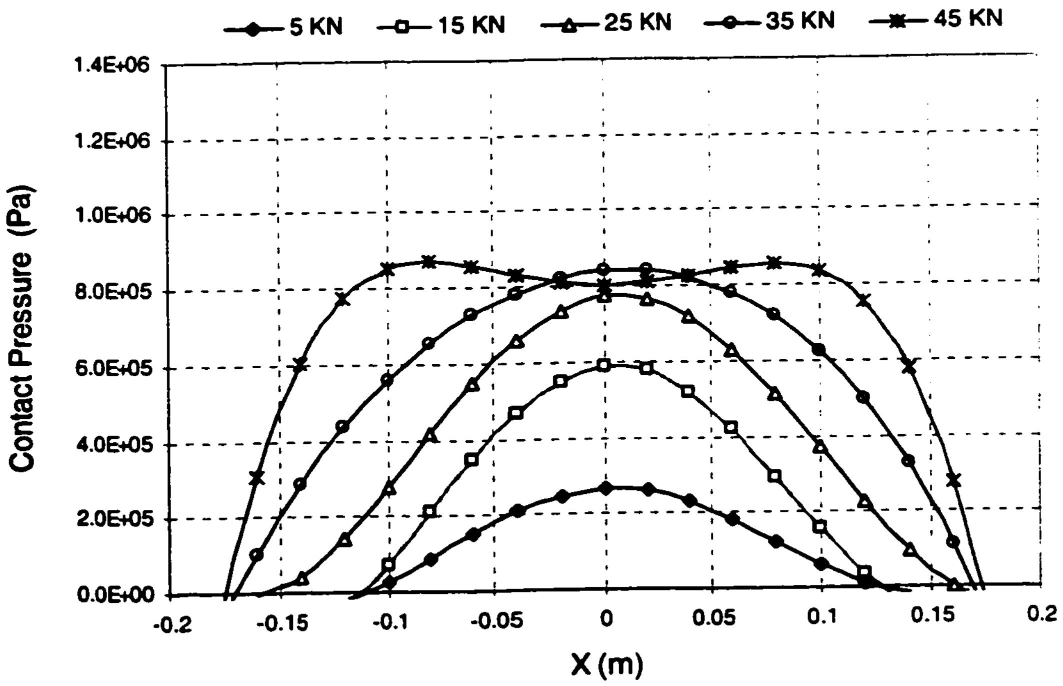

Figure 5.12(b): Contact pressure distributions estimated from the proposed polynomial for different normal loads; p_i = 90 psi.

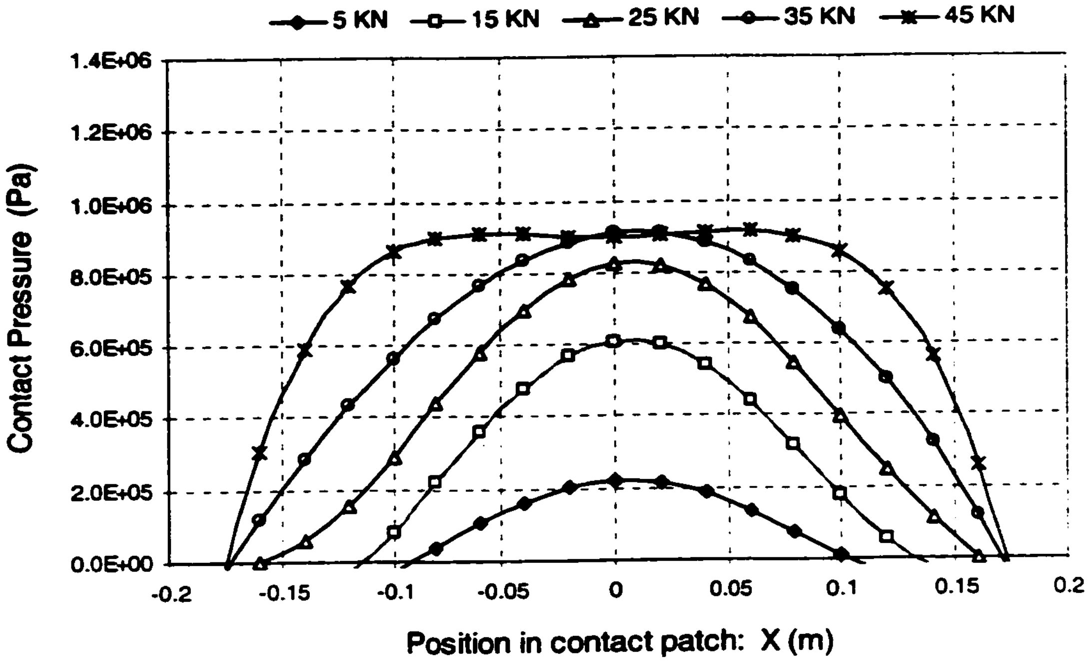

Figure 5.12(c): Contact pressure distributions estimated from the proposed polynomial for different normal loads; $p_i = 100$ psi.

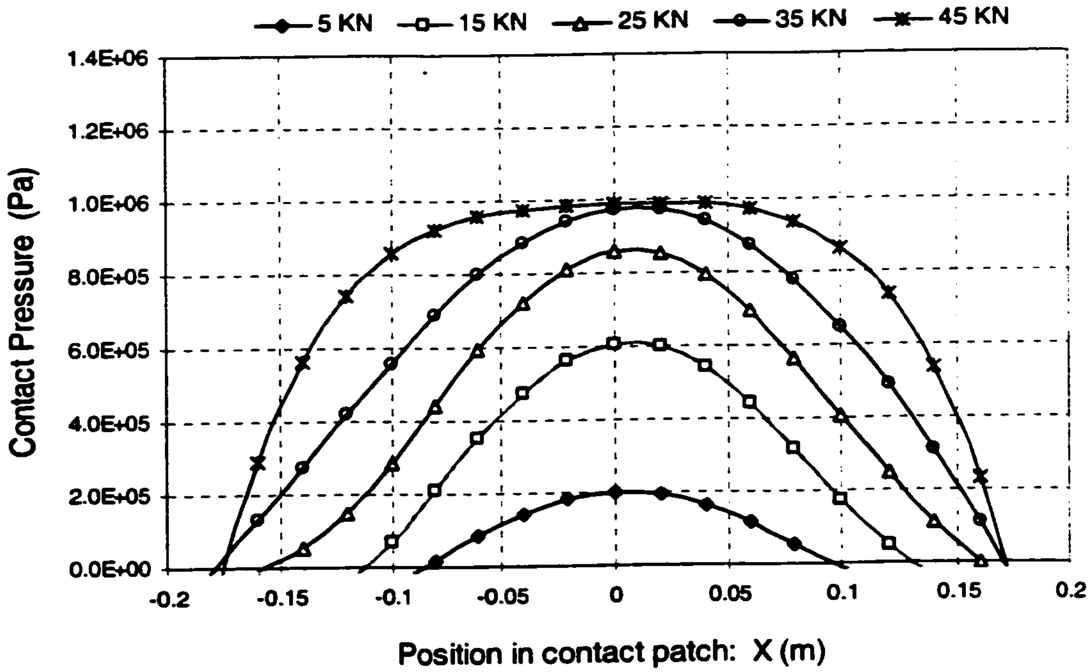

Figure 5.12(d): Contact pressure distributions estimated from the proposed polynomial for different normal loads; $p_i = 110$ psi.

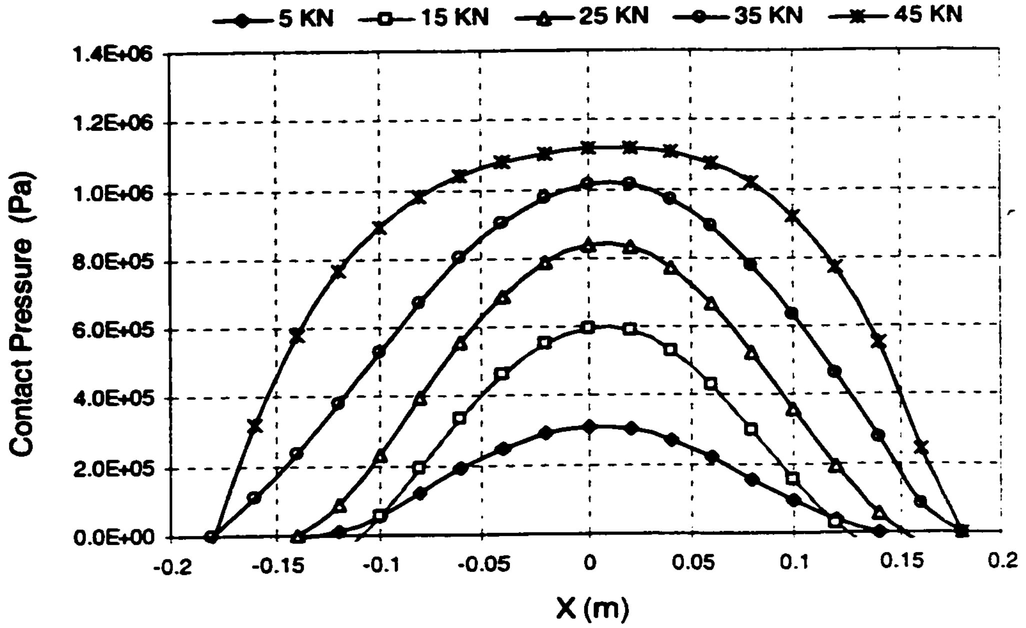

Figure 5.12(e): Contact pressure distributions estimated from the proposed polynomial for different normal loads; p_l = 120 psi.

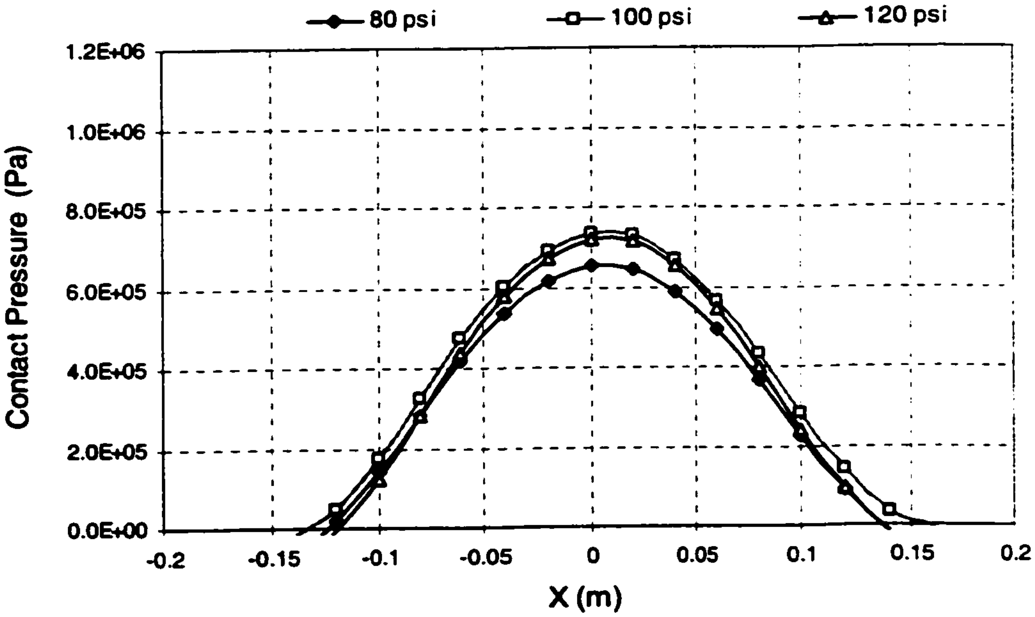

Figure 5.13(a): Contact pressure distributions estimated from the proposed polynomial for different inflation pressures; F_z = 20 kN.

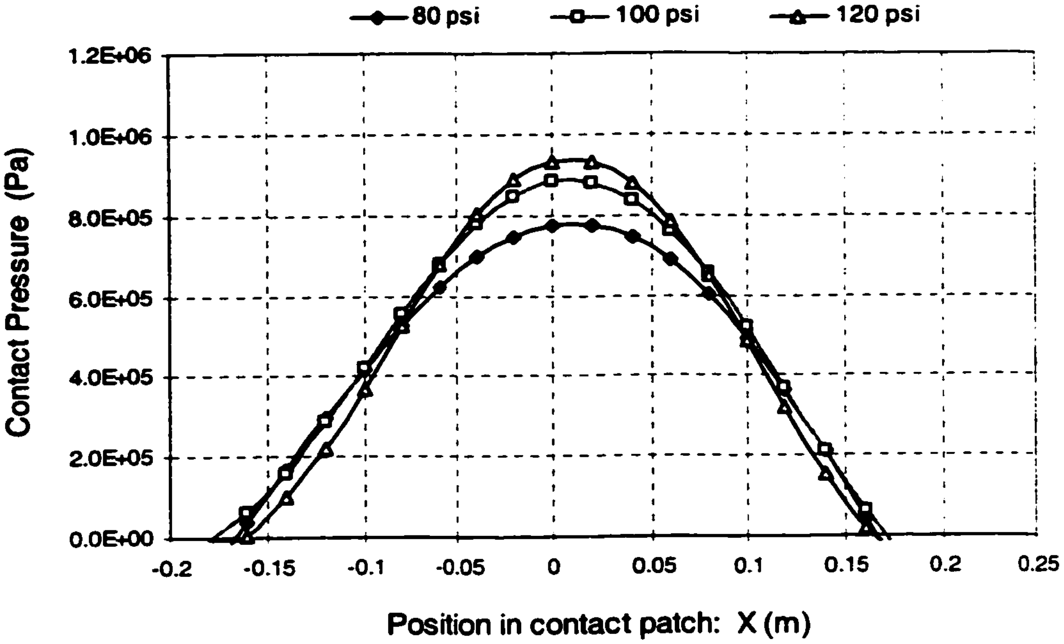

Figure 5.13(b): Contact pressure distributions estimated from the proposed polynomial for different inflation pressures; $F_z = 30$ kN.

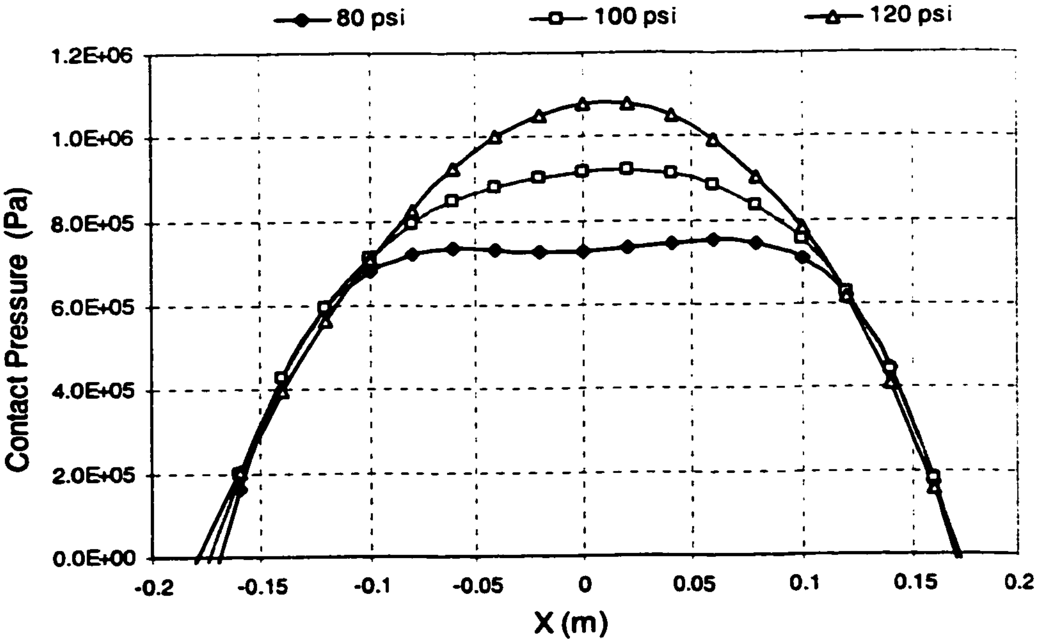

Figure 5.13(c): Contact pressure distributions estimated from the proposed polynomial for different inflation pressures; $F_z = 40$ kN.

Under a lower normal load (20 kN), the variations in p_l exhibit relatively small effect on the contact pressure-distribution and the pressure peak, as shown in Figure 5.13(a). The estimated contact pressure distribution is thus less sensitive to variations in the inflation pressure ranging from 80 psi to 120 psi, when normal load is less than 20 kN. Under a large normal load (above 30 kN), the variations in p_l influence the contact pressure distribution in a significant manner. Lower inflation pressure results in a rapid shift of the contact pressure peaks to the two edges of the contact patch. A higher inflation pressure yields nearly constant contact pressure distribution around the central point of the contact patch. Such observations in the contact pressure distribution have also been reported by Sakai [131] and Browne et al. [141].

It should be emphasized that the proposed polynomial function, and thus the results presented in Figures 5.12 and 5.13, are derived on the basis of the 3-D contact pressure fields computed from a finite element model of a truck tire. While the geometric parameters are taken from the cross-section of the tire, the material properties are estimated from the data reported in various published studies [5, 125, 129, 171-172]. In view of such estimated parameters, the results presented in this study are considered to describe the tire-road interface pressure distribution in a qualitative manner. The validity of the proposed polynomial is examined by comparing the estimated data with those derived from the finite element tire model and Equation (5.3) for different inflation pressure and normal load conditions, as shown in Figure 5.14. The results show reasonably good agreement between the estimated and computed contact pressure distributions. The estimated results also show reasonably good agreement with the reported experimental data by Browne et al. [141].

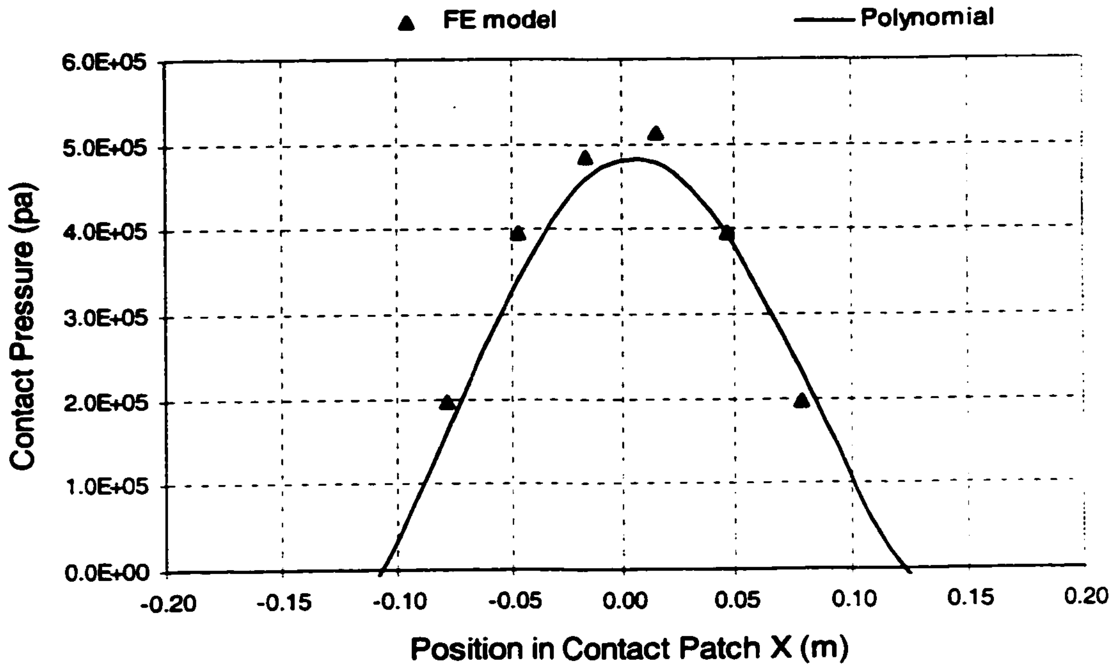

(a)

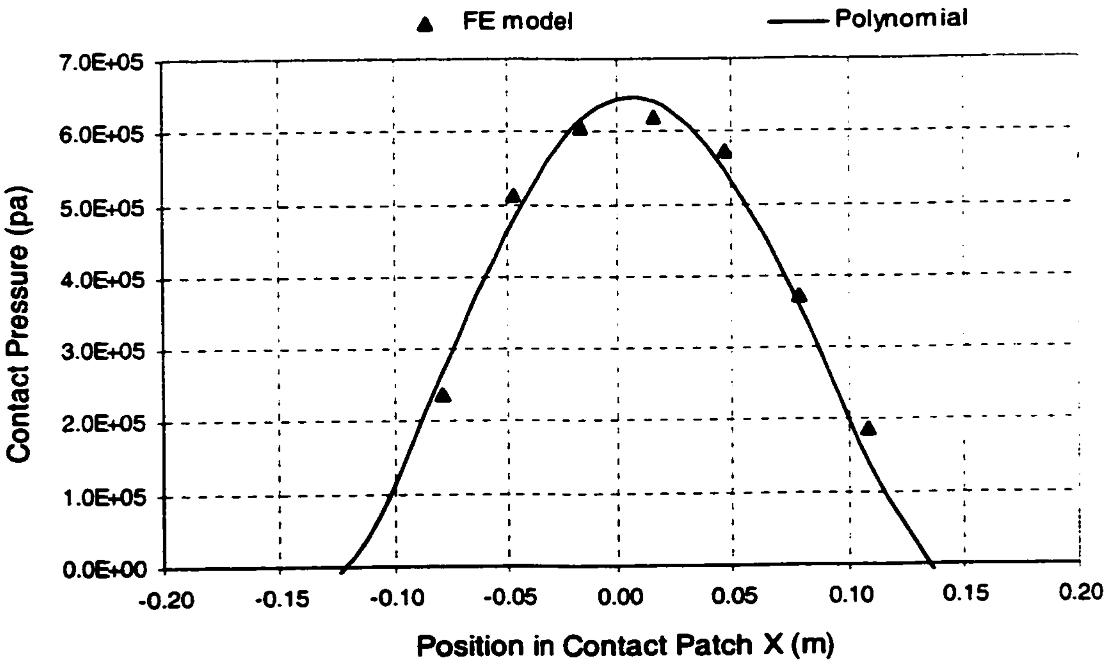

(b)

Figure 5.14: Comparison of the estimated contact pressure distributions with those derived from the FE model; p_l = 621.3 kPa: (a) F_z = 11.2 kN; (b) F_z = 17.4 kN; (c) F_z = 31.1 kN; and (d) F_z = 46.1 kN.

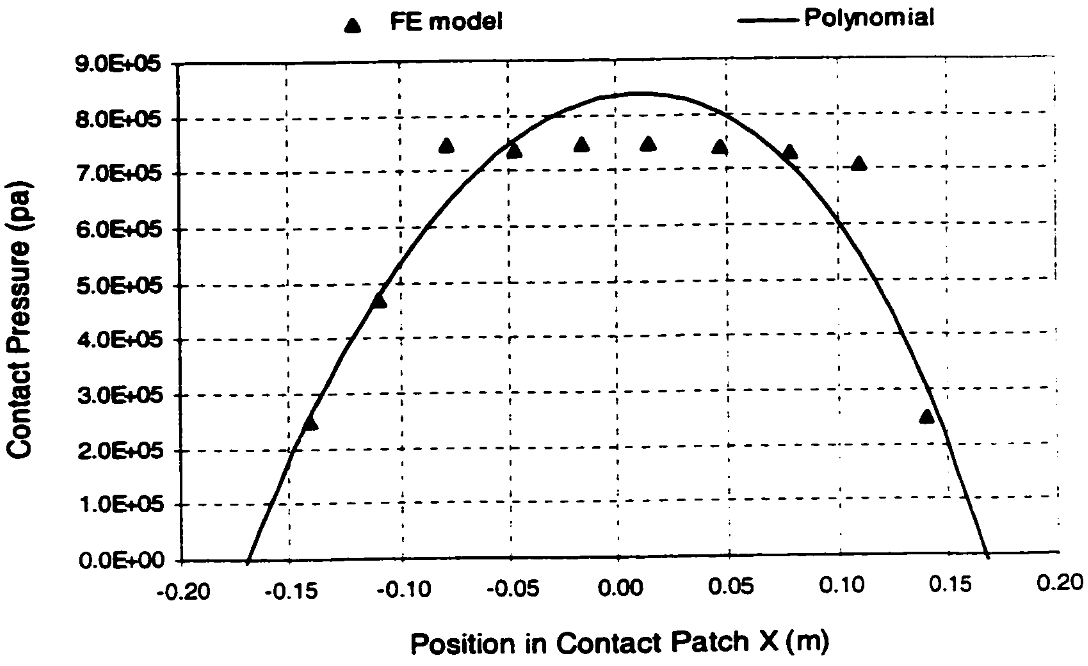

(c)

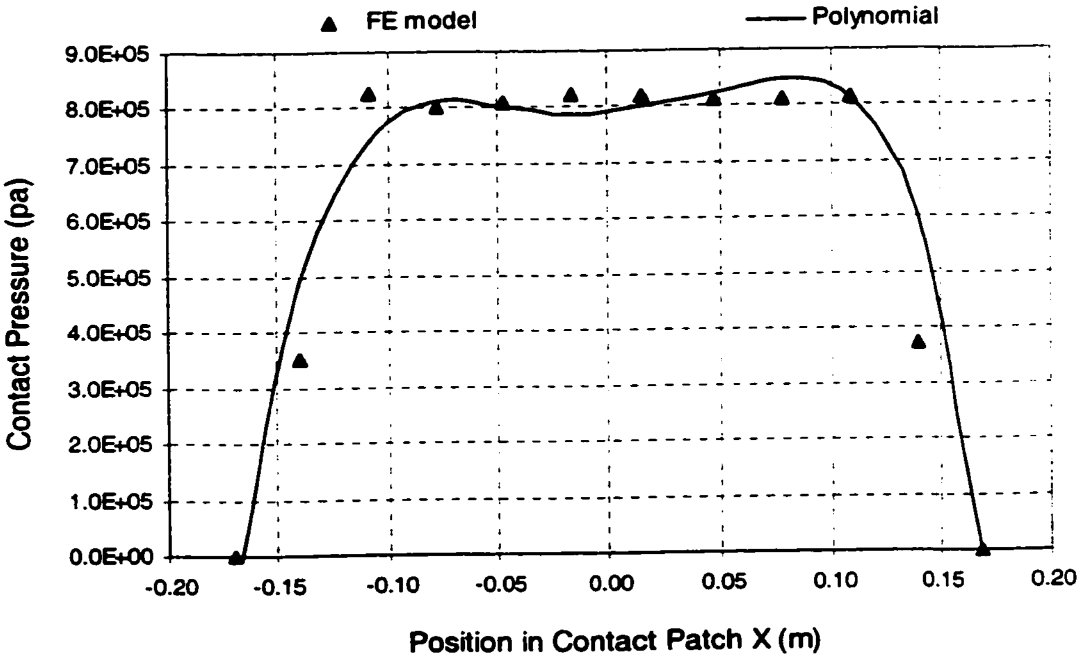

(d)

Figure 5.14: Comparison of the estimated contact pressure distributions with those derived from the FE model; p_l = 621.3 kPa: (a) F_z = 11.2 kN; (b) F_z = 17.4 kN; (c) F_z = 31.1 kN; and (d) F_z = 46.1 kN. (Continued)

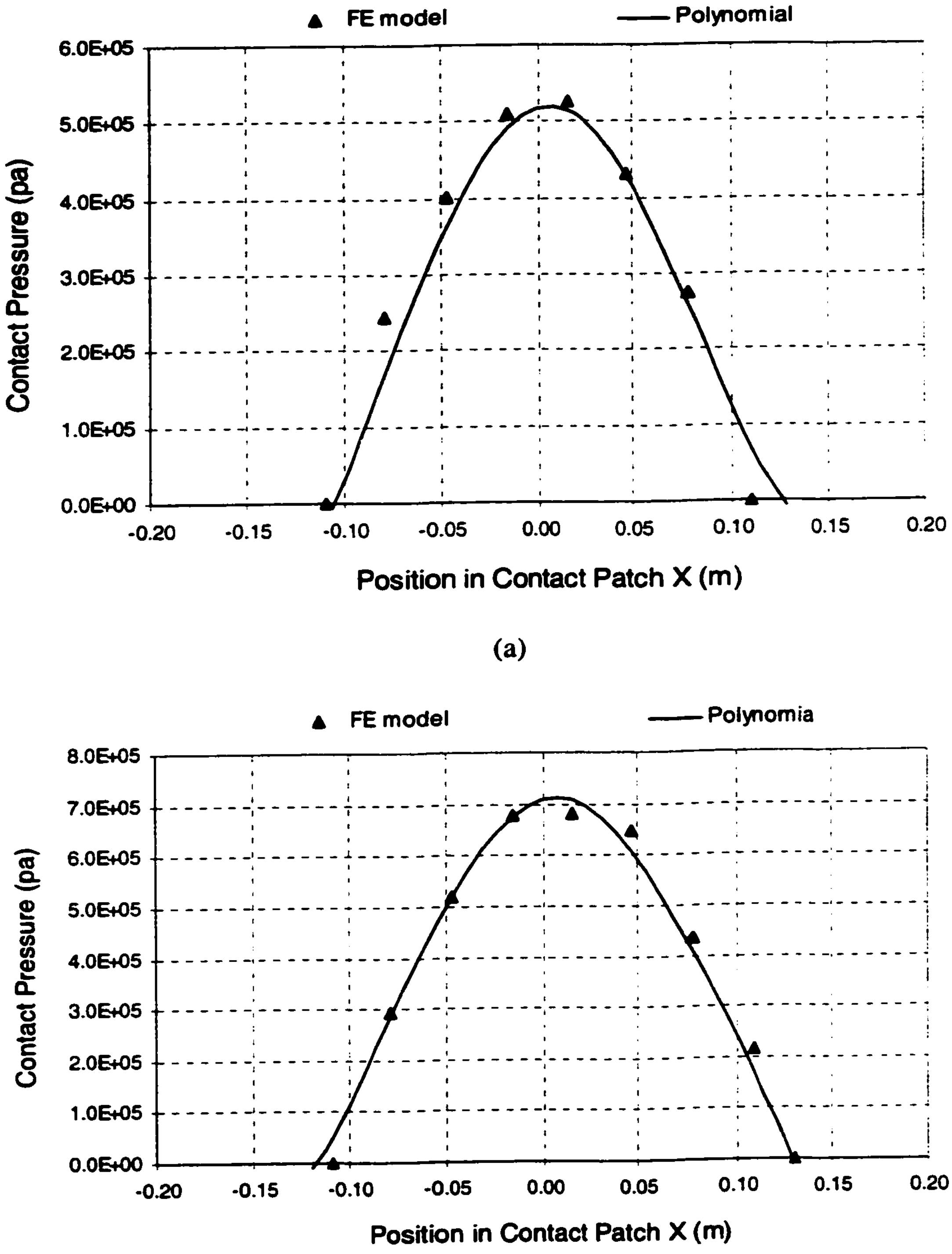

(a)

(b)

Figure 5.15: Comparison of the estimated contact pressure distributions with those derived from the FE model; p_l = 759.3 kPa: (a) F_z = 11.6 kN; (b) F_z = 19.4 kN; (c) F_z = 34.7 kN; and (d) F_z = 46.4 kN.

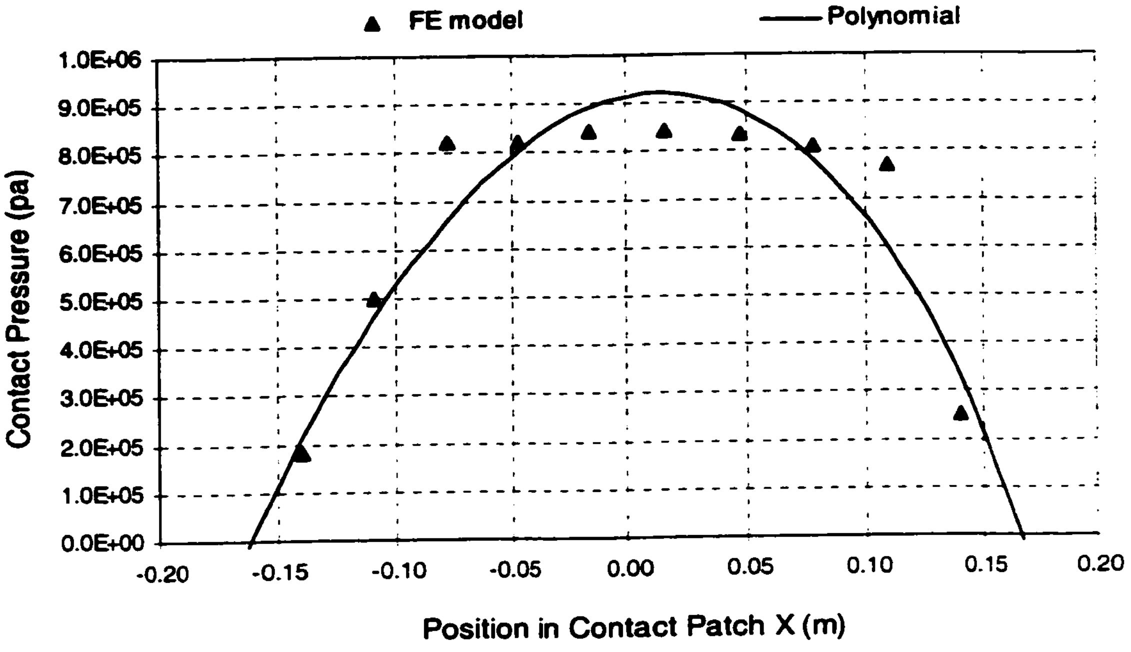

(c)

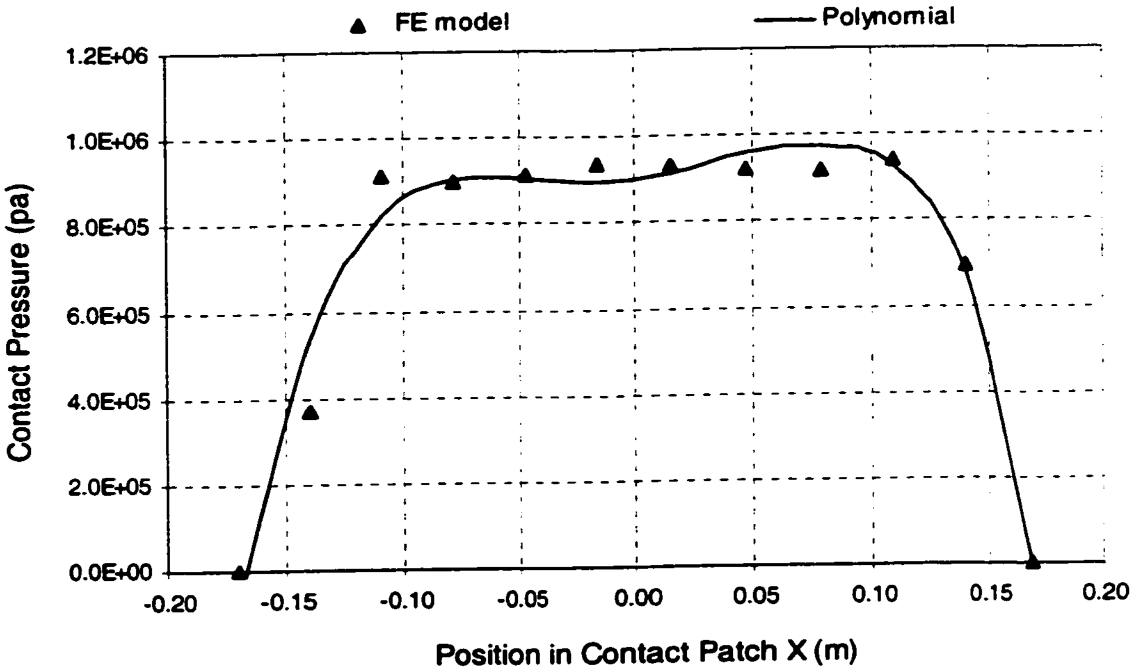

(d)

Figure 5.15: Comparison of the estimated contact pressure distributions with those derived from the finite element model; p_l = 759.3 kPa: (a) F_z = 11.6 kN; (b) F_z = 19.4 kN; (c) F_z = 34.7 kN; and (d) F_z = 46.4 kN. (Continued)

5.6 SUMMARY

A computational methodology is proposed to derive an estimate of the 2-D tire-road contact pressure distribution in the tire plane as a function of the normal load, inflation pressure and the longitudinal coordinate along the contact patch. A polynomial function in the normal load, inflation pressure and coordinate of the local contact point is developed on the basis of the contact pressure field data derived from the finite element model of a truck tire. The principle of equivalent work is applied as a basis to reduce the 3-D contact pressure field into the 2-D pressure fields in the wheel plane of the tire. The resulting 2-D contact pressure distribution is described by a polynomial function using the curve fitting techniques. The polynomial function is applied to obtain estimates of the 2-D contact pressure distribution in the wheel plane at the tire-road interface corresponding to different normal loads and inflation pressures. A comparison of the estimated contact pressure distributions with those derived from the FE model revealed reasonably good validity of the proposed estimation function. The estimated results also revealed reasonably good qualitative agreement with the data reported in the published studies. The proposed methodology can be applied to obtain an estimate of the contact pressure distribution on the basis of resultant point-contact force, inflation pressure and normal load.

The validated tire model is analyzed to estimate its vibration modes and natural frequencies in the following chapter. The vibration modes and the natural frequencies for the radial truck tire with different inflation pressures are analyzed incorporating the pre-stress effects and the nonlinearities. The effects of the individual structural parameters on the tire's natural frequencies are also investigated.

CHAPTER 6 MODAL ANALYSIS OF A TRUCK TIRE BASED ON A NONLINEAR FINITE ELEMENT TIRE MODEL

6.1 INTRODUCTION

The vibration modes and the natural frequencies of a tire inherently determine the tire's dynamic response properties concerning the transmission of disturbances from the tire footprint to the vehicle, critical rotational speed, noise generation, etc. Consequently, the analysis of tire vibration characteristics has played an important role in predicting the vehicle behavior in terms of ride comfort and noise generation [3, 156]. Considerable efforts have been made to conduct both experimental [21, 25, 156] and theoretical studies [28, 40, 157-161] on the vibration characteristics of the pneumatic tires. The majority of the works, however, assume that the symmetric and anti-symmetric motions of the wheel-tire system are uncoupled and can be studied separately [28, 40, 160-161]. Moreover, the tire structure is normally simplified as a circular ring on an elastic foundation to facilitate the analytical formulation of the vibration problems. The tire structure, such as the rubber, textile and steel cords, constituent anisotropy and nonlinear properties of material could not be taken into account. These models thus do not reflect the complexity of a real tire and the majority of them can only provide the in-plane tire vibration characteristics.

Some other tire vibration related works have been performed based on simple finite element models using membrane or shell elements [159]. The most advanced FE models are mainly based on the linear analysis of the multi-layered system, assuming small deformations of the anistropic layers and thus could not properly incorporate the large nonlinear deformations due to the inflation pressure and the axle load [160, 162].

Very few of the reported models are capable of generating three-dimensional deflection modes of the tire, with appropriate consideration of the nearly incompressible property of rubber, the anisotropic property of the multi-layered system and the structural features. The vibration behavior of a pneumatic tire depends not only upon its structural and material properties, but also on the operating load and inflation pressure. The free vibration characteristics of a given tire are thus expected to be load and pressure-dependent. While the load- and pressure-dependent deflection modes have not been reported, the contributions due to the anisotropic property of the belt layers have been mostly ignored.

In this chapter, the free vibration behavior of the truck tire is carried out through the analysis of the finite element tire model described in Chapter 3. The vibration modes and frequencies of a radial truck tire with different inflation pressures are analyzed incorporating the pre-stress effects and the nonlinearities. The effects of variations in the individual structural parameters on the load and pressure-dependent natural frequencies of a radial truck tire are also investigated. The structural parameters considered in the modal analysis are the cord angles in each layer, total number of belt layers and the amount of twisted cords per unit width of each individual layer, which are related to the configuration and anisotropic material properties of the belt layers.

6.2 METHOD OF ANALYSIS

The nonlinear FE tire model developed in Chapter 3 is employed to perform the modal analysis of an inflated truck tire, which is treated as a pre-stressed structure. The analysis is initiated by conducting a static analysis under a given inflation pressure. The results are analyzed to derive the pre-stress effects of the static loading of the nonlinear tire model for the given inflation pressure and the load. A modal analysis of the inflated tire is then carried out upon incorporating the pre-stress effects derived from the static analysis. The free-vibration analysis of the undamped tire structure is performed using the classical eigenvalue problem:

$$[K]\{\Phi_i\} = \omega_i^2[M]\{\Phi_i\} \tag{6.1}$$

Where $[K]$ = stiffness matrix

$\{\Phi_i\}$ = mode shape vector (eigenvector) corresponding to mode i

ω_i = natural circular frequency corresponding to mode i

$[M]$ = mass matrix

The Block Lanczos method [173], which uses the sparse matrix solver and is considered suitable for solution of large symmetric eigenvalue problems, is used to achieve rapid convergence. A static analysis of the model is initially performed under a given inflation pressure to define the stiffness matrix corresponding to the specific pre-stress condition. The modal analysis of the finite element model is then performed to determine the free vibration properties of the pre-stressed tire. The mass matrix is formed using the lumped mass approximation, which can result in a shorter run time and lower memory requirements. The density of the tread rubber material in the tire is obtained based on the data reported by Oh et al. [172]. The average densities of the carcass and belt layers are estimated from the density data of the rubber, the steel cords and the volume ratios occupied by the components in each individual layers. The estimated densities of the tread rubber, plies and the rubber in the plies are illustrated in Table 6.1.

Table 6.1: Estimated densities of rubber, plies and the rubber in the plies

	Tread rubber	Rubber in belt ply	Rubber in carcass ply	Belt ply	Carcass ply
Density ρ (kg/m^3)	1164	1190	1190	1910	1810

The other data related to the material properties, e.g., Young's modulus, tension and shear response characteristics, etc., are estimated based upon the data reported in various published studies [5, 125, 129-130, 172]. The parameters describing the model geometry were selected from the measurements performed on a 12.5R22.5 truck tire. The Table 6.1 together with Table 3.1 to 3.7 summarizes the material and structure parameters of the cord-reinforced rubber plies employed in the tire model. In view of the estimated material properties, the results derived from the modal analysis are considered to describe the tire vibration characteristics in a qualitative manner. The application of the model in conjunction with adequately measured material properties of layers in belts and carcass casing are expected to yield a quantitative modal analysis of a specific tire.

The frequency below which the tire inertia effects may be neglected must lie well below the lowest natural frequency of the tire, which is estimated as 20 Hz for the road vehicle tires [3]. In the high frequency range, considered as higher than 30 Hz, tires exhibit a number of natural frequencies associated with the in-wheel plane and out-of-wheel plane motions, and continuously distributed vibrations of the side walls and the tread band [3]. The in-plane and out-of-plane motions corresponding to a specific mode may be coupled, and the deformation pattern may involve complicated three-dimensional mode shapes, which are different from the results reported in the studies mentioned earlier. The experimental studies performed on pneumatic tires have shown that the amplitude ratio of the hub oscillation to the sinusoidal platform oscillation is relatively small, when the excitation frequency exceeds 110 Hz [21]. The measured resonant peaks were observed to lie in the 60-80 Hz frequency range for the radial tires. The highest resonant frequency of the pneumatic tires is thus considered to be well below 100 Hz, which is also considered to be the cut-off frequency for vibration transmission by the automobile suspension [15]. The highest frequency for the mode extraction in the current study is assumed as 112 Hz. At higher frequencies a rolling tire may exhibit a standing wave phenomenon, which necessitates complex tire dynamic analyses and is thus not included in this study.

In addition to the inflation pressure, the most important structural parameters affecting the vibration characteristics of a tire are the cord angles in belt layers, total number of layers in the belt and the amount of cord ends per unit width of each layer. Since the belt layers containing different cord angles are essential in stabilizing the tire casing in radial direction and are in a highly stressed state, these anisotropic-property-related parameters have direct influence on the vibration properties of an inflated tire. The effects of the structure-related parameters on the vibration modes of the tire with 690.3 kPa (100 psi) inflation pressure are thus evaluated to enhance on understanding of the tire vibration behavior.

6.3 TIRE MODE SHAPES

While a number of studies have been reported on the high frequency motions of the tires [3], the majority of the studies are limited to the motions in the wheel plane and are based on the ring or membrane models. These models thus could not be used to study the effects of the anisotropic property of the multi-layered system on the vibration characteristics of the tires. The nonlinear finite element tire model developed in this study is analyzed, and the vibration modes and the corresponding natural frequencies below 112 Hz are extracted. Table 6. 2 summarizes the natural frequencies associated with the extracted nine modes of the tire model. The nominal parameters for the analysis are considered to be 690.3 kPa (100 psi) inflation pressure, four layers in the belt, 22 degrees cord angle in each layer and 4 cord ends per centimeter in the width of each layer.

Table 6.2: The tire natural frequencies associated with the extracted nine modes

Mode Numbers	1	2	3	4	5	6	7	8	9
Frequencies (Hz)	42.11	45.12	47.00	67.30	67.87	86.25	97.62	98.94	110.86

Figure 6.1(a) to 6.1(i) illustrate the deflection modes of the candidate tire corresponding to the extracted modes. The first deflection mode corresponding to the lowest natural frequency of 42.11 Hz, exhibits translational motions of the tire along the transverse direction, as shown in Figure 6.1(a). The deflection mode 2 (f_2 = 45.12 Hz) contains mainly a rotational motion of the tire around the wheel axle as shown in Figure 6.1(b). The deflection mode corresponding to mode 3 (f_3 = 47 Hz) exhibits rotational or twisting oscillation of the tire around an axis in the wheel plane crossing the tire center. The vibration mode shape corresponding to the frequency of 67.3 Hz reveals relatively complex deformation pattern caused by the twisting of the tire. The portions in the opposite two halves of the tire displace outwards from the wheel plane, while the other opposite portions of the tire tend to oscillate backwards out of the tire plane.

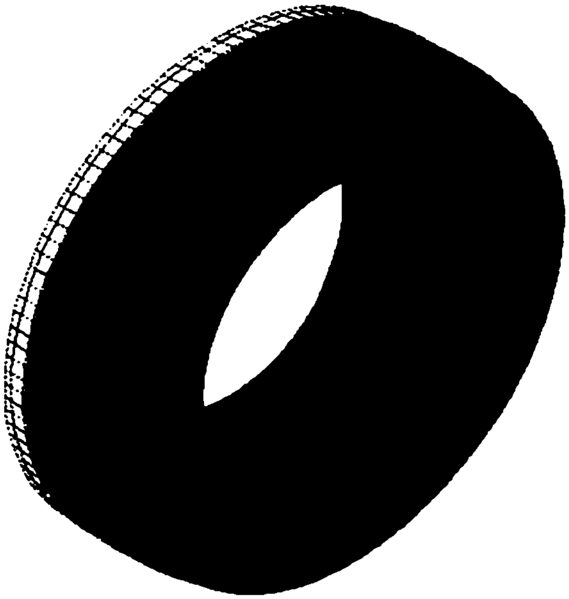

(a) Mode 1

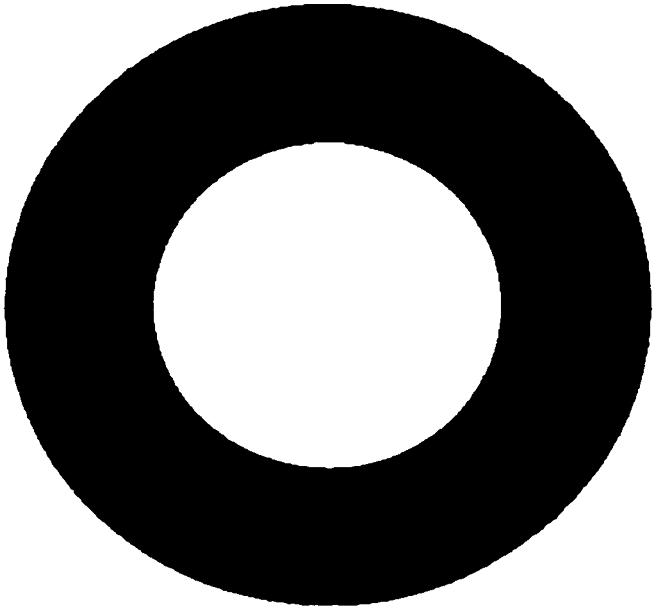

(b) Mode 2

*Figure 6.1: Deflection modes of the tire model: (a) first mode, $f_1 = 42.11$ Hz; and (b) second mode, $f_2 = 45.12$ Hz.

**Note: The deflection modes are extracted from the tire model with the nominal parameters;* $p_t = 690.3$ *kPa (100 psi).*

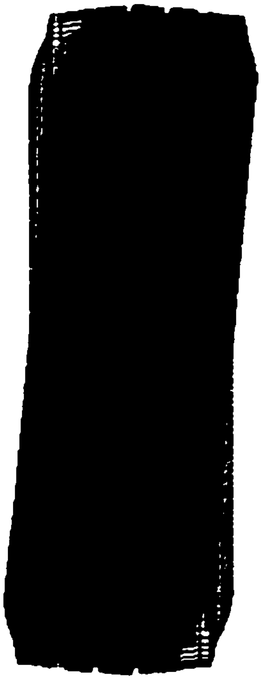

(c) Mode 3

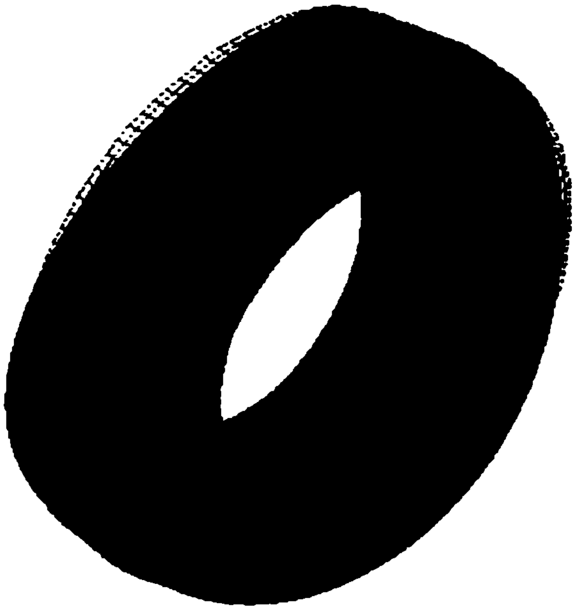

(d) Mode 4

*Figure 6.1: Deflection modes of the tire model: (c) third mode, $f_3 = 47.0$ Hz; and (d) forth mode, $f_4 = 67.3$ Hz. (Continued)

**Note:* *The deflection modes are extracted from the tire model with the nominal parameters;* $p_t = 690.3$ *kPa (100 psi).*

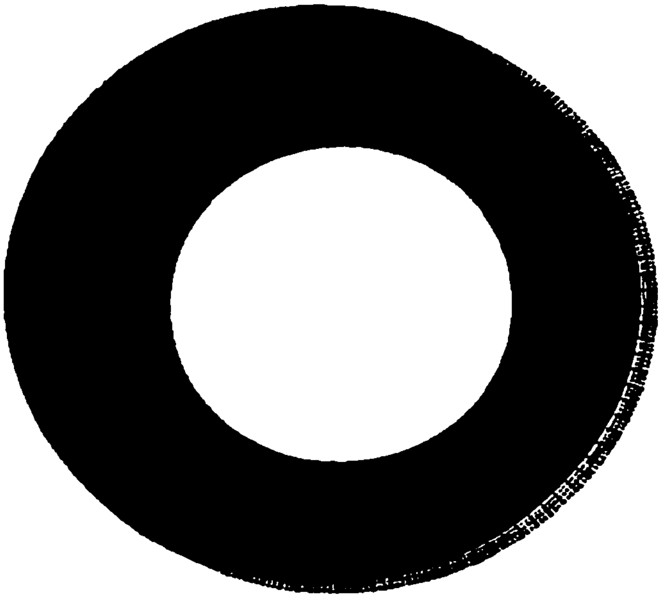

(e) Mode 5

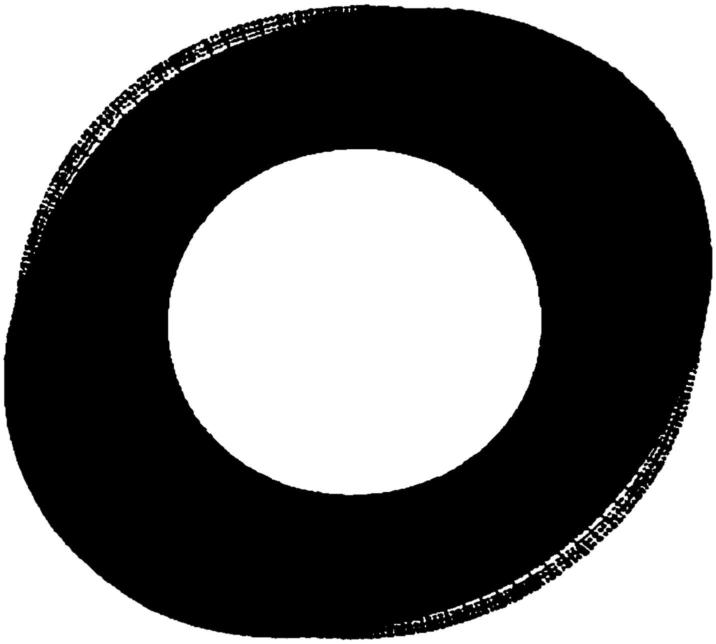

(f) Mode 6

*Figure 6.1: Deflection modes of the tire model: (e) fifth mode, $f_5 = 67.87$ Hz; and (f) sixth mode, $f_6 = 86.25$ Hz. (Continued)

**Note:* *The deflection modes are extracted from the tire model with the nominal parameters; $p_t = 690.3$ kPa (100 psi).*

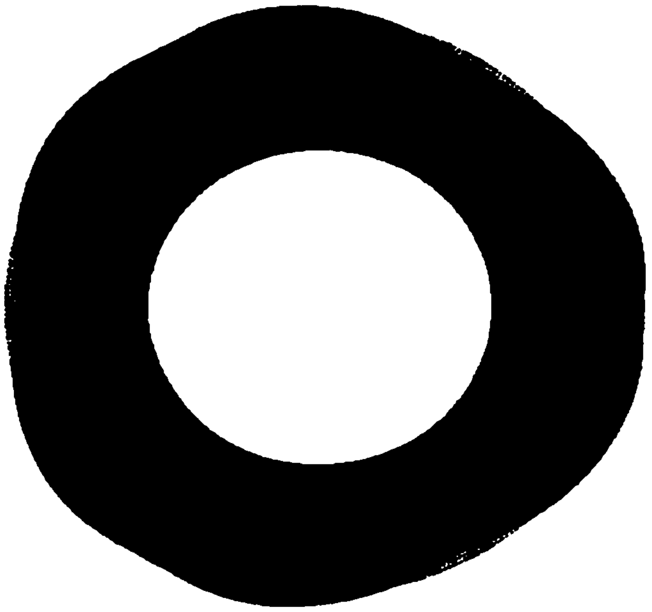

(g) Mode 7

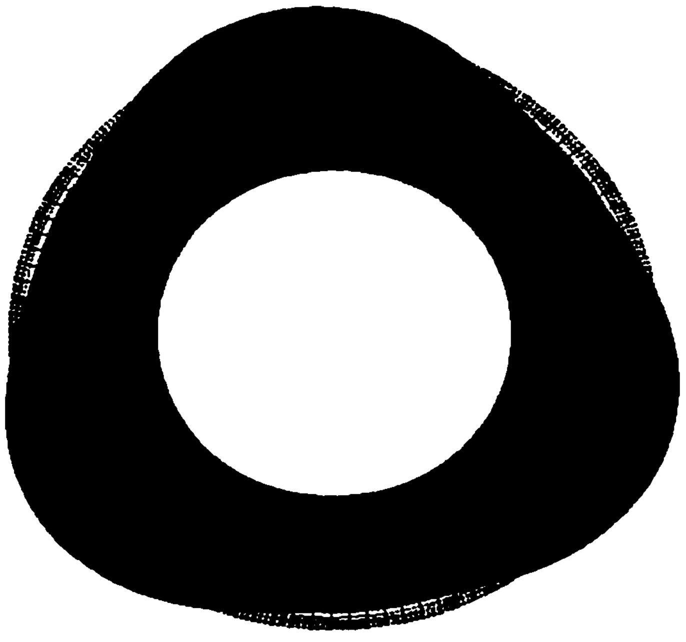

(h) Mode 8

*Figure 6.1: Deflection modes of the tire model: (g) seventh mode, f_7 = 97.62 Hz; and (h) eighth mode, f_8 = 98.94 Hz. (Continued)

**Note: The deflection modes are extracted from the tire model with the nominal parameters; p_t = 690.3 kPa (100 psi).*

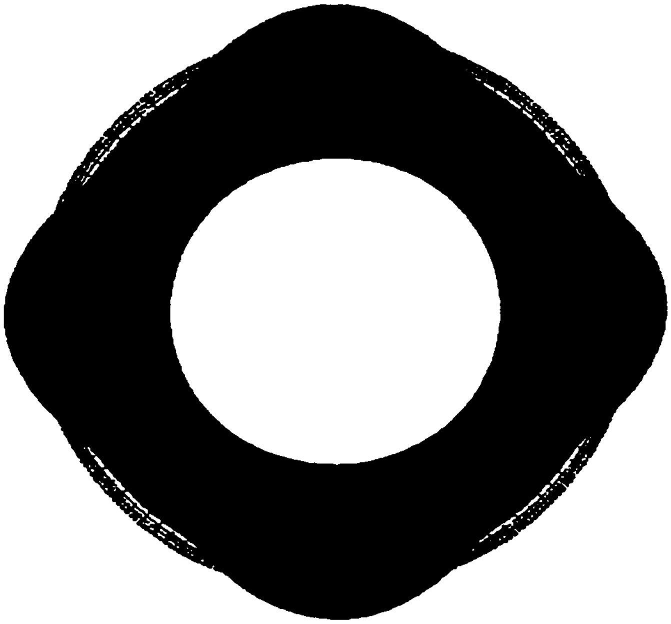

(i) Mode 9

*Figure 6.1: Deflection modes of the tire model: (i) ninth mode, f_9 = 110.86 Hz. (Continued)

**Note: The deflection modes are extracted from the tire model with the nominal parameters; p_t = 690.3 kPa (100 psi).*

The deflection mode 5 (f_5 = 67.87 Hz) describes a vibration motion causing the compression of nearly one half of the carcass and expansion of the other half. The motion is observed to be symmetric about a central axis in the wheel plane. Under the oscillation mode 6 (f_6 = 86.25 Hz), the deformed tire assumes an oval form, as illustrated in Figure 6.1(f). This vibration mode involves the extension motion in opposite directions along a central axis and compressive motion along the opposite axis. The maximum deflections are observed to occur in the crown areas. The two involved axes along which the motions occur are in the wheel plane and are vertically crossed at the tire center. In the seventh mode (f_7 = 97.62 Hz), the tire appears twisted along the toroidal centerline and may suggest the presence of a standing wave with the most complicated deflection shapes among all the considered modes. The deflections mode 8 (f_8 = 98.94 Hz) and mode 9 (f_9 = 110.86 Hz) show more complex deformation patterns, with corner rounded triangular and quadric shapes in their side views, respectively. The vibration modes 7 to 9 are considered to be most likely associated with the standing waves. The results reveal that tire side-wall vibration modes or the side-wall deformations, which are ignored by the in-plane models, such as the ring on elastic foundation type models, play a very important role in tire vibration. Most of the three-dimensional mode shapes presented in this study, however, have not been reported in the literature, with the exception of the modes 5, 6, 8 and 9. Zhang, et al. predicted the tire modes using LS/DYNA3D and presented the side views of the deformation patterns. The deflection modes derived in this study corresponding to these modes show patterns that are similar to those reported by Zhang et al. [162].

Figure 6.2 illustrates the deformation modes and the corresponding frequencies of the tire model analyzed by Zhang et al. [162]. The results show the presence of only one torsional and three belt-bending free vibration modes in the frequency range below 120 Hz. The study also identified five additional free vibration modes in the frequency range above 160 Hz, as illustrated in Figure 6.3. The deflection patterns of the computed modes 5 (f_5 = 67.87 Hz), 6 (f_6 = 86.25 Hz), 8 (f_8 = 98.94 Hz) and 9 (f_9 = 110.86 Hz) are observed to be similar to those reported by Zhang et al., corresponding to the frequencies 57.6, 81.1, 113.3 and 142.2 Hz. Considerable differences, however, can be observed between the predicted and the reported frequencies corresponding to these modes. This may be attributed to the different structural and geometric parameters and the material properties employed in the two studies.

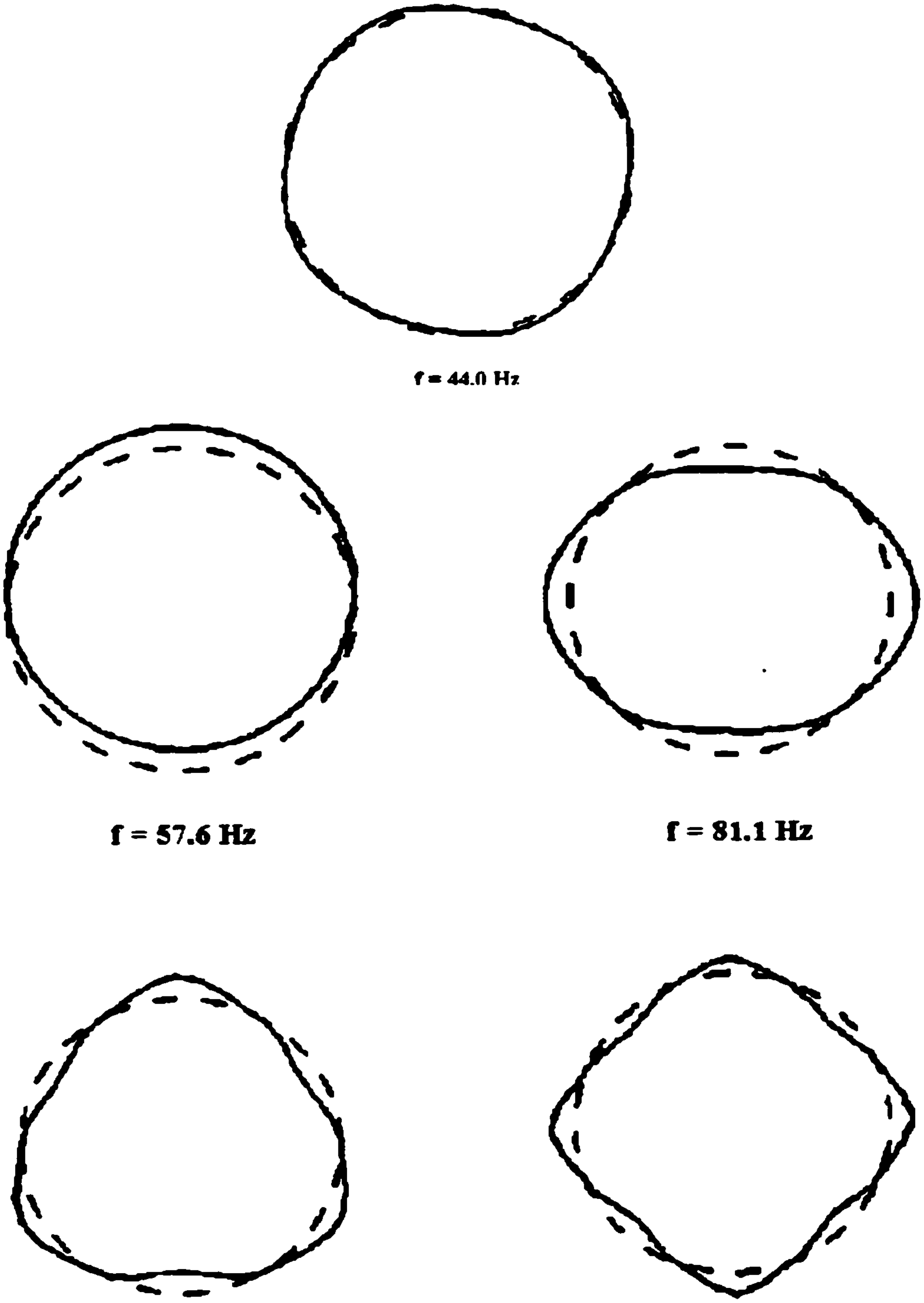

f = 44.0 Hz

f = 57.6 Hz

f = 81.1 Hz

f=113.3 Hz

f = 142.6 Hz

Figure 6.2: Tire free vibration modes as reported in reference [162].

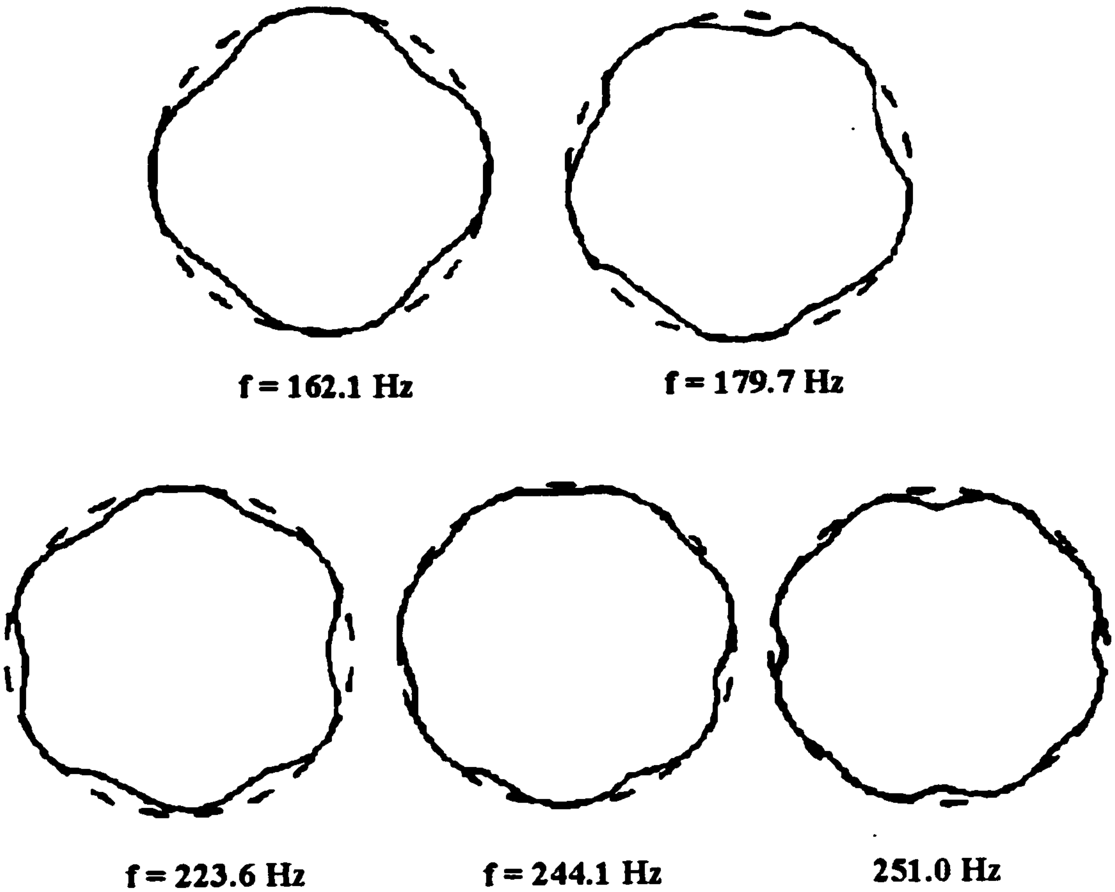

f = 162.1 Hz f = 179.7 Hz

f = 223.6 Hz f = 244.1 Hz 251.0 Hz

Figure 6.3: New free vibration modes as reported in reference [162].

6.4 INFLUENCE OF DESIGN PARAMETERS ON THE TIRE NATURAL FREQUENCIES

The cord angles in the belt layers, total number of layers in the belt and number of cord ends per unit width of each layer, are among the most important structural parameters of a tire. In addition to the inflation pressure, the belt layers containing different cord angles are essential in stabilizing the tire casing in radial direction and are the primary factors affecting the stiffness characteristics of a tire. These anisotropic-property-related parameters have direct influence on the vibration property of a loaded tire, which have not yet been reported.

The effects of the above parameters on the vibration characteristics are investigated individually for a tire with 100 psi (690.3kPa) inflation pressure. The selected parameters are varied within a relatively small range, except for the number of layers in the belt, such that the resulting influence on the mode shapes is relatively small. The variations in the selected parameters, however, are considered to be sufficiently large to illustrate their effects on the natural frequencies of an inflated tire. The subsequent study is thus focused on the analysis of the effects of variations in the inflation pressure and the individual structural parameters on the natural frequencies rather than the mode shapes of the tires.

6.4.1 Effect of the Cord Angle

Among the various design parameters, the cord angle plays a significant role in determining the anisotropic property of each layer and thus the behavior of a radial tire. The stiffness characteristics of the belt layers and thus the tire, in circumferential, radial and axial directions, are primarily dependent on the orientation of the cords in the individual layers. The natural frequencies of the tire are identified through analysis of the tire models with three different cord angles: 18, 22 and 26 degrees. The cord angles are designated as $+\theta$, $-\theta$, $+\theta$ and $-\theta$, respectively, beginning from layer 1, which is nearest to the tread rubber block. Figure 6.4 illustrates the influence of cord angle on the natural frequencies of the tire associated with the first three vibration modes. The effect of variations in the cord angle on higher mode natural frequencies is illustrated in Figure 6.5.

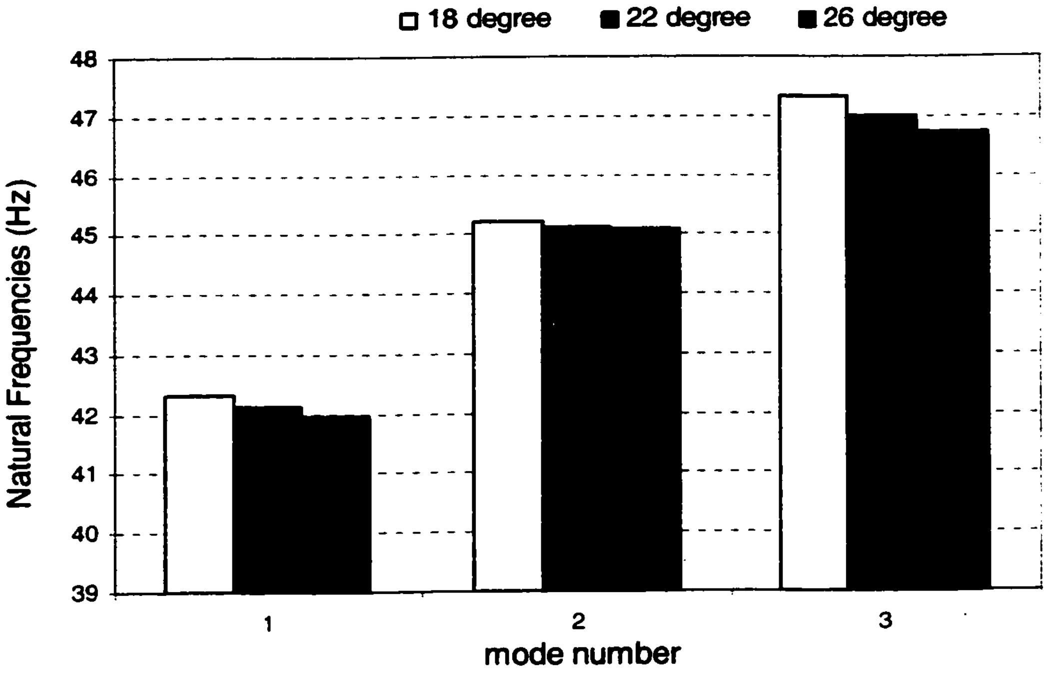

Figure 6.4: Effect of cord angle on the first three natural frequencies of a truck tire; $p_i = 690.3$ kPa (100 psi).

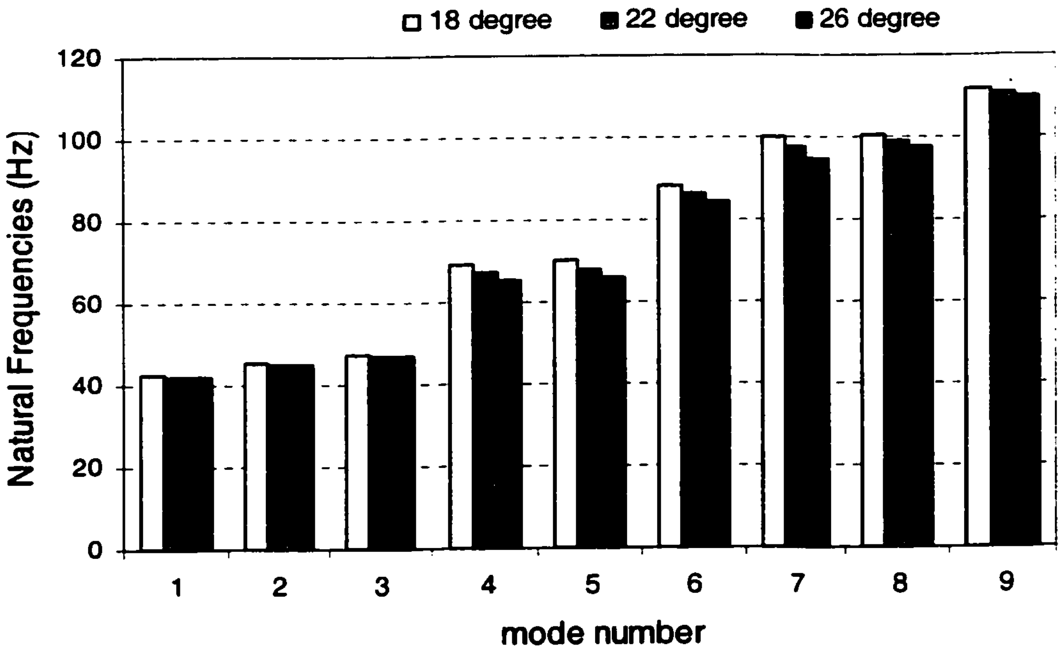

Figure 6.5: Effect of cord angle on the first nine natural frequencies of a truck tire; $p_i = 690.3$ kPa (100 psi).

It can be observed that the increase in the cord angle yields a distinct but small decrease in the first three natural frequencies and relatively larger reduction in the natural frequencies associated with the higher modes of vibration. An increase in the cord angle leads to lower stiffness of the belt layers in the circumferential direction and thus yields lower natural frequencies. The first three modes primarily involve the translational motion in the axial (lateral) direction, rotational motion about the tire center in the wheel plane and the oscillation about an axis in the wheel plane crossing the tire center, other than the motions associated with the circumferential direction. The influence of variations in the cord angles on these modes is thus relatively small. The modes corresponding to higher natural frequencies, however, are associated with motions that include major components in the circumferential direction of the tire. The influence of the variations in the cord angle on the natural frequencies above 60 Hz is therefore slightly larger. It is concluded that relatively larger cord angles help to reduce the natural frequencies of a tire in its service, especially those associated with higher modes in the 60 to 112 Hz range.

6.4.2 Effect of the Number of Belt Layers

The number of belts used in a radial tire affects its rigidity in all the directions and thus the vibration properties in a considerable manner. The belt layers provide high rigidity to the tread against distortion, and affect the rate of tread wear and rolling resistance. Assuming identical geometry and material properties of each individual layer, the use of fewer belts could adversely influence the tire stability and the use of too many belts, on the other hand, could directly affect the weight and the cost. The modal analysis of the tire is performed by varying the total number of belt layers embedded in the crown area from 3 to 5, while the thickness of each layer and the total thickness of the tire in the thickness direction are kept unchanged. The effect of the variations in the number of belt layers on the natural frequencies is illustrated in Figure 6.6 and 6.7.

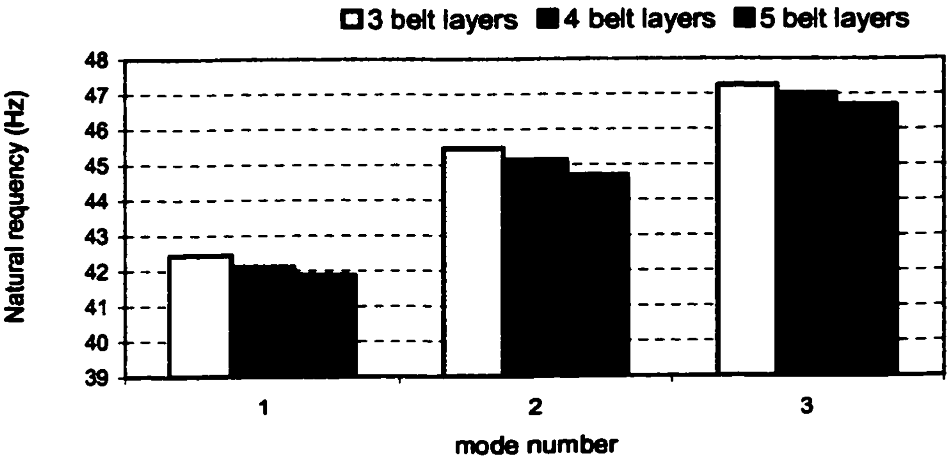

Figure 6.6: Effects of variation of number of layers in the belt on the first three natural frequencies of a truck tire; p_I = 690.3 kPa (100 psi).

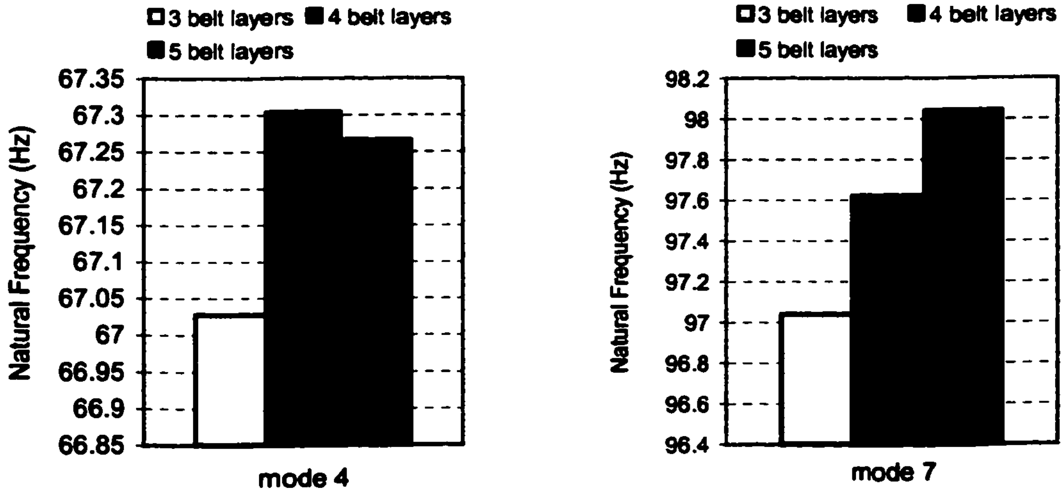

(a) (b)

Figure 6.7: Effects of number of belt layers on the natural frequencies; p_I = 690.3 kPa (100 psi): (a) mode 4 and (b) mode 7.

Figure 6.6 illustrates the influence of number of belt layers on the first three natural frequencies of the inflated tire. As the number of belt layers increases from 3 to 5, the first three natural frequencies decrease only slightly. Similarly, majority of the higher mode frequencies tend to decrease as the number of layer varies from 3 to 5, except those for the modes 4 and 7 (Figure 6.7). The reduction in the natural frequencies due to increasing number of layers in the belt may be attributed to the fact that more belt layers stiffen the crown area but soften the side-wall, which experiences larger deformations and yields lower natural frequencies. Mode 4 involves the bending and twisting movements of the tire around the axles in the wheel plane and its frequency is largely associated with the stiffness characteristics of the body layers in the side-wall. Consequently, the natural frequency f_4 increases as the number of layers increases from 3 to 4 and then decreases slightly as the number of layers further increases from 4 to 5 as illustrated in Figure 6.7(a). Mode 7 possesses the most complicated mode shape among the considered modes and its frequency increases with increase in the number of layers, as shown in Figure 6.7(b), since the involved movements in this mode are closely associated with the bending and twisting motions of the belt layers.

6.4.3 Effect of the Cord Ends per Centimeter (epc)

The amount of cord ends per centimeter (epc) along the width of each individual layer determine the longitudinal and transverse Young's modulus of the layer and thus the stiffness characteristics of a tire in all the directions, when the thickness of the layer is constant. The Young's modulus of each layer, which primarily determines the tire vibration properties, can be determined by the volume ratio of the cords relative to the rubber matrix and their material properties in the composite layer. The effects of varying epc on the material properties, such as the Young's modulus and Poisson's ratio, can be estimated by the Halpin-Tsai equations [130], when the volume ratio of the cords and rubber matrix in the belt and their individual material properties are known. Hence, the study of the effects of material properties of the layers on the vibration characteristics of an inflated tire can be performed by investigating the influence of varying the value of epc, as illustrated in Figure 6.8.

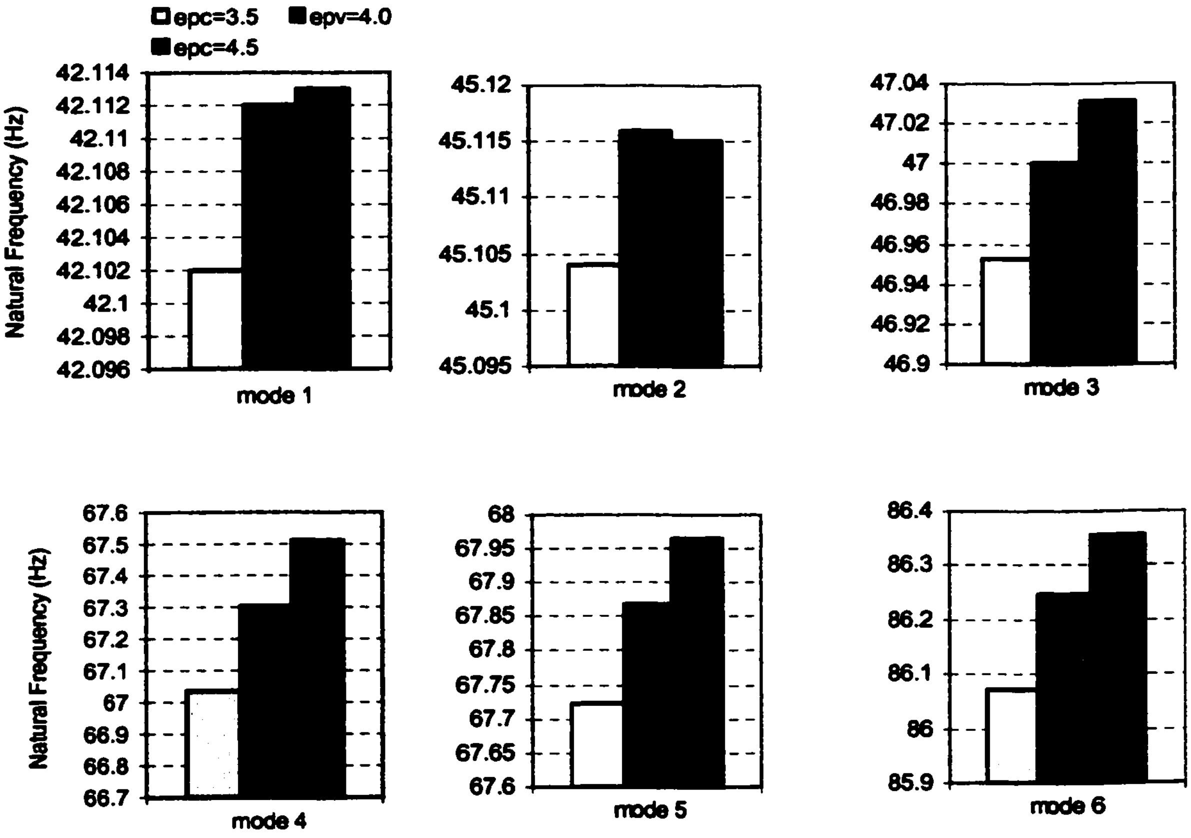

Figure 6.8: Effects of the amount of cord ends per centimeter (epc) on the first nine natural frequencies of a truck tire; p_I= 690.3 kPa (100 psi).

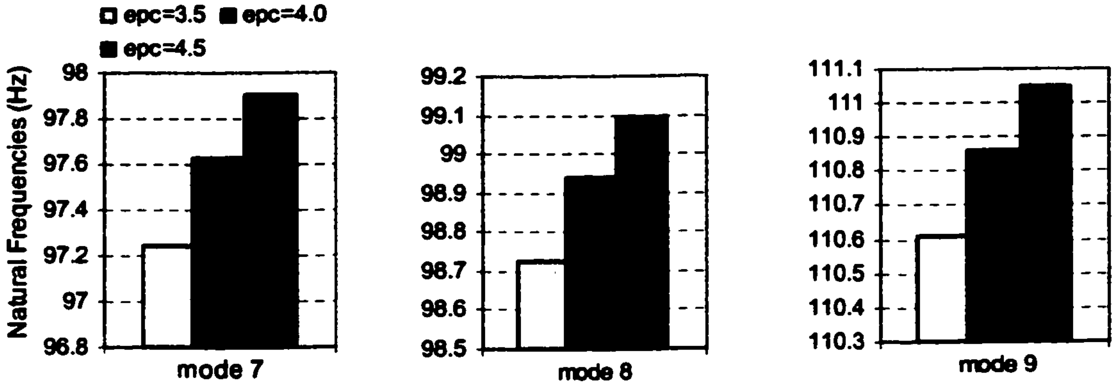

Figure 6.8: Effects of the amount of cord ends per centimeter (epc) on the first nine natural frequencies of a truck tire; $p_I = 690.3$ kPa (100 psi). (Continued)

Figure 6.8 illustrates the effects of varying the value of epc on the first nine natural frequencies of the considered tire with four belt layers, 22 degree cord angles in each layer and 690.3 kPa (100 psi) inflation pressure. The results reveal that the variations in value of the epc have distinct influence on all the natural frequencies below 112 Hz. Increasing the value of epc yields monotonic increases in all the frequencies, except for f_2, which increases as the epc value varies from 3.5 to 4 and then drops slightly with further increase in the value of epc from 4 to 4.5, as illustrated in Figure 6.8. This may be attributed to the fact that mode 2 involves mainly the rotational movement of the tire around the axle and the related frequency is largely dependent on the stiffness of the side-walls rather than that of the belt.

6.4.4 Effect of the Inflation Pressure

The stiffness properties of a tire are strongly related to the inflation pressure as evident from the normal load-deflection characteristics presented in Chapter 3. The free vibration properties of a given tire are thus expected to depend upon the inflation pressure. The stiffening effects due to the inflation pressure significantly affect the stiffness of a tire in all the directions and thus the vibration characteristics of the tire considerably. Figure 6.9 illustrates the influence of varying the inflation pressure on the first nine natural frequencies of the tire with four belt layers, 22 degree cord angle and an epc value of 4 in each layer. The results reveal that all the natural frequencies increase as the inflation pressure increases from 552.2 kPa (80psi) to 828.4 kPa (120 psi). An increase in the inflation pressure, in general, results in a reduced aligning stiffness due to relatively smaller contact patch, and tends to increase the lateral and camber stiffness of a tire [42].

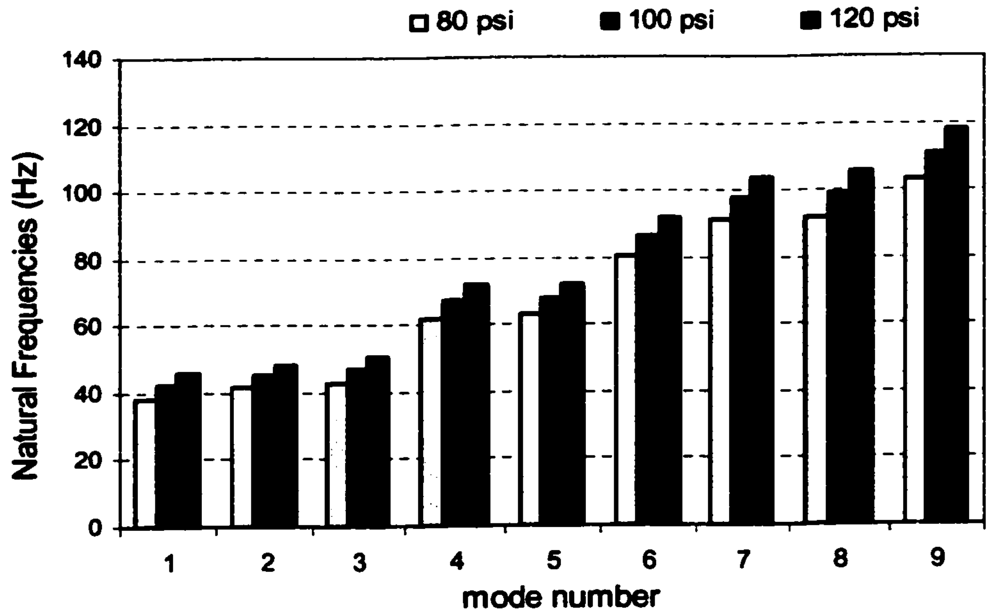

Figure 6.9: Effect of inflation pressure on the natural frequencies of the tire model.

The percent change in the natural frequencies due to variations in the inflation pressure is illustrated in Figure 6.10. The results reveal that increasing the inflation pressure from 100 to 120 psi yields 6.1-8.5 % increases in the first nine natural frequencies and that decreasing in inflation pressure from 100 to 80 psi results in 6.6-9.5

% reduction in all the natural frequencies. The variation in the inflation pressure has large effects on the natural frequencies associated with mode 1 and 3, but relatively small influence on the other modal frequencies. The results further reveal nearly symmetric percent change in the natural frequencies due to the variations in the inflation pressure relative to p_l = 100 psi (690.3 kPa). While a lower inflation pressure is desirable to achieve improved ride quality arising from the reduced inherent natural frequencies, it may deteriorate the tire life due to enhanced tearing and cracking caused by the large deformations developed in the tire-road contact patch, increase in self-aligning torque and squeal. The selection of an optimal inflation pressure for a given tire needs a more elaborate study involving other performance measures, such as tire-road interactions, temperature effects, noise generation, and ride and handling properties of the vehicle.

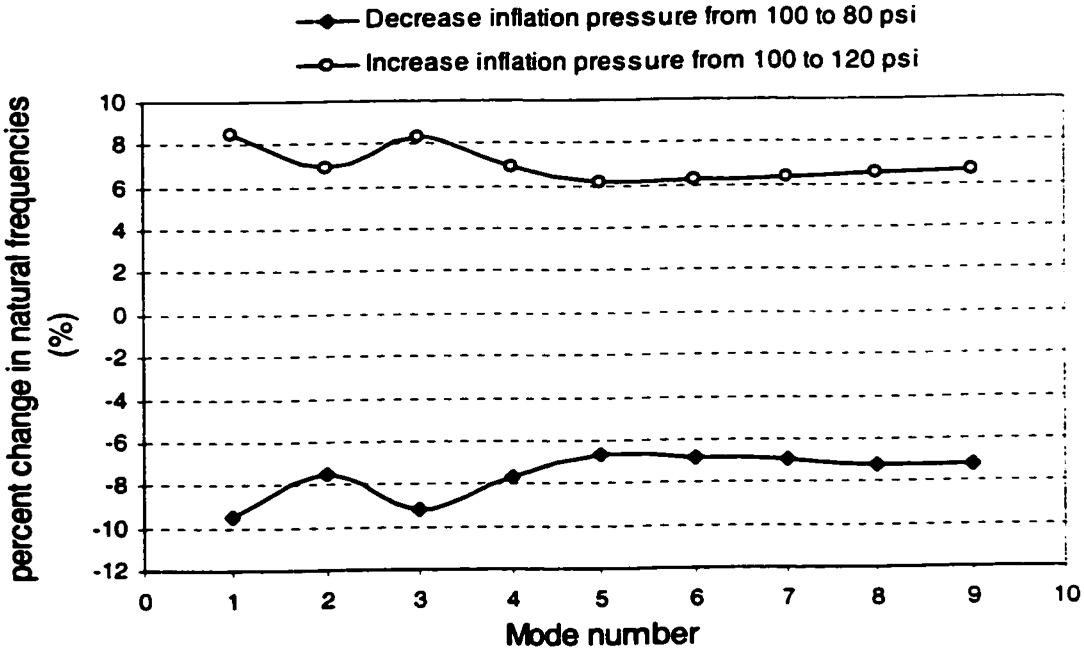

Figure 6.10: Percent change in the first nine natural frequencies of the tire model due to the variation in inflation pressure.

6.4.5 Modal Analysis of the Tire Model Using the Selected Parameters

The nonlinear finite element tire model is analyzed to investigate the mode shapes and natural frequencies of the tire using the selected parameters derived from the parametric study conducted in Chapter 4. The mode shapes of the tire model developed using the selected parameters are extracted and illustrated in Figure 6.11. A comparison of these mode shapes with those extracted from the nominal tire model (Figure 6.1) reveals similar deflection patterns for modes 1, 2, 3, 6 and 9. The remaining mode shapes of the model with selected parameters, however, differ considerably from those extracted for the nominal parameter model. The mode 4 illustrates a vibration motion of the tire with one half of the tire shrinking and the other half expanding in the lateral direction, symmetric about the wheel plane. The deflection modes 5, 7 and 8 reveal motions similar to those seen in modes 4, 8 and 7, respectively, of the tire model with nominal parameters. The differences in the natural frequencies between the modes of tires using the selected and nominal parameters are illustrated in Figure 6.12. The results reveal almost insignificant differences in frequencies f_1 and f_5. The tire model with selected parameters yields higher natural frequencies f_2, f_3, f_7, f_8 and f_9, and slightly lower natural frequencies f_4 and f_6.

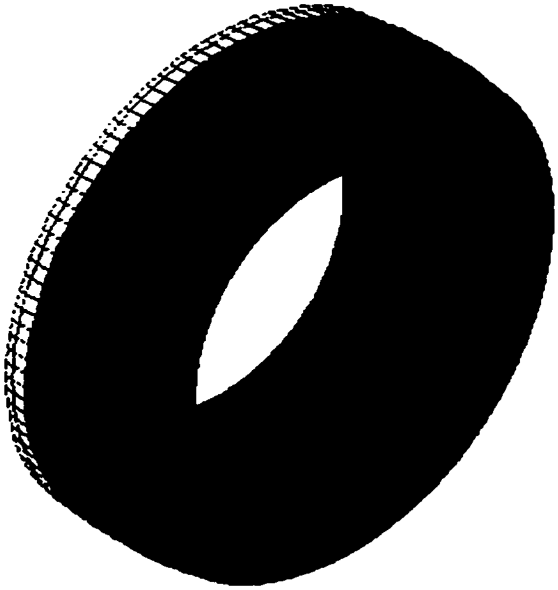

(a) Mode 1

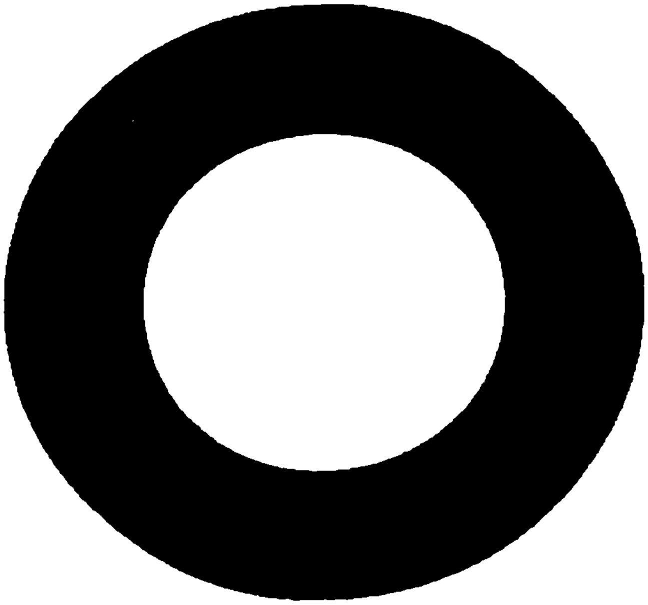

(b) Mode 2

*Figure 6.11: Deflection modes of the tire model: (a) first mode, f_1 = 42.61 Hz; and (b) second mode, f_2 = 46.47 Hz.

**Note: The deflection modes are extracted from the tire model using the selected parameters; p_t = 690.3 kPa (100 psi).*

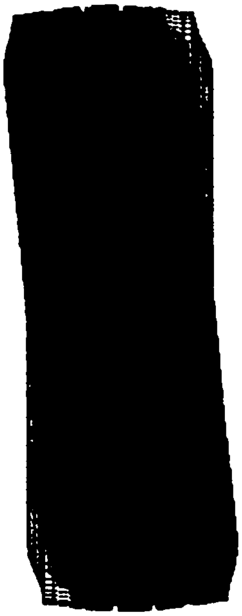

(c) Mode 3

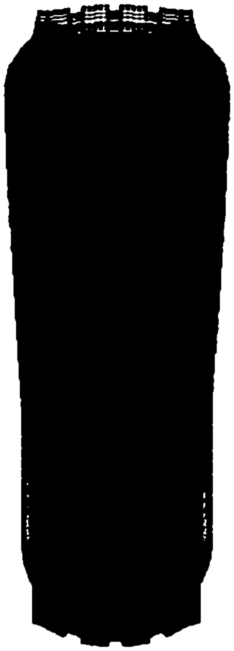

(d) Mode 4

*Figure 6.11: Deflection modes of the tire model: (c) third mode, f_3 = 48.02 Hz; and (d) forth mode, f_4 = 66.63 Hz. (Continued)

**Note: The deflection modes are extracted from the tire model using the selected parameters; p_i = 690.3 kPa (100 psi).*

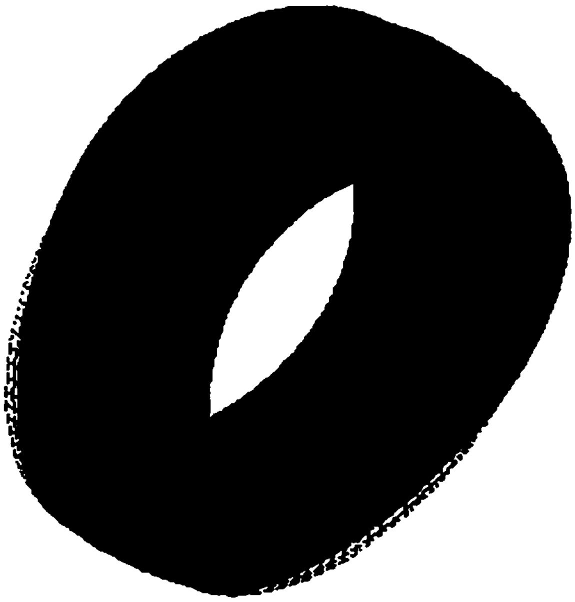

(e) Mode 5

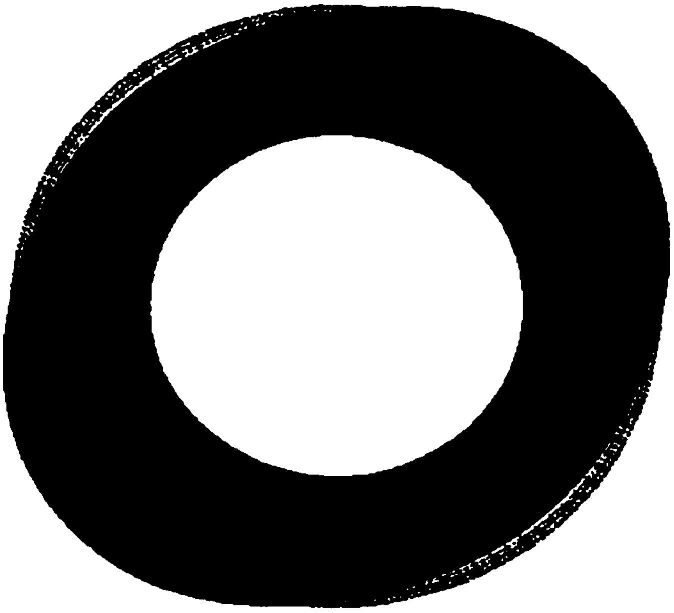

(f) Mode 6

*Figure 6.11: Deflection modes of the tire model: (e) fifth mode, f_5 = 68.86 Hz; and (f) sixth mode, f_6 = 85.54 Hz. (Continued)

**Note: The deflection modes are extracted from the tire model using the selected parameters; p_t = 690.3 kPa (100 psi).*

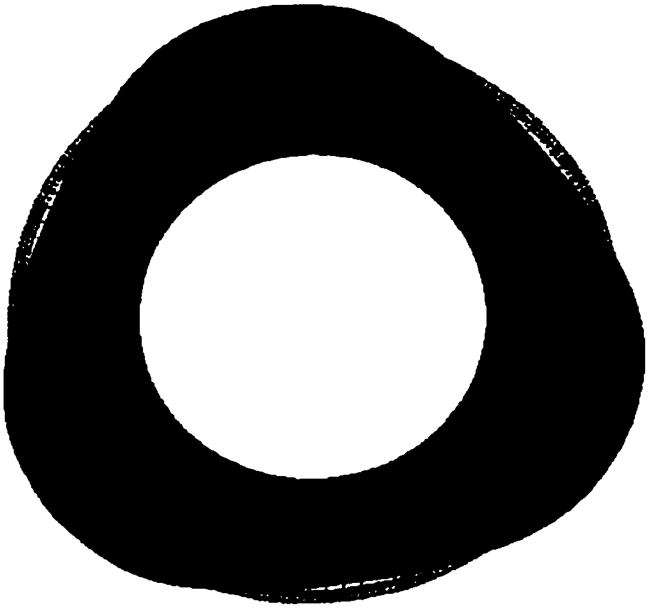

(g) Mode 7

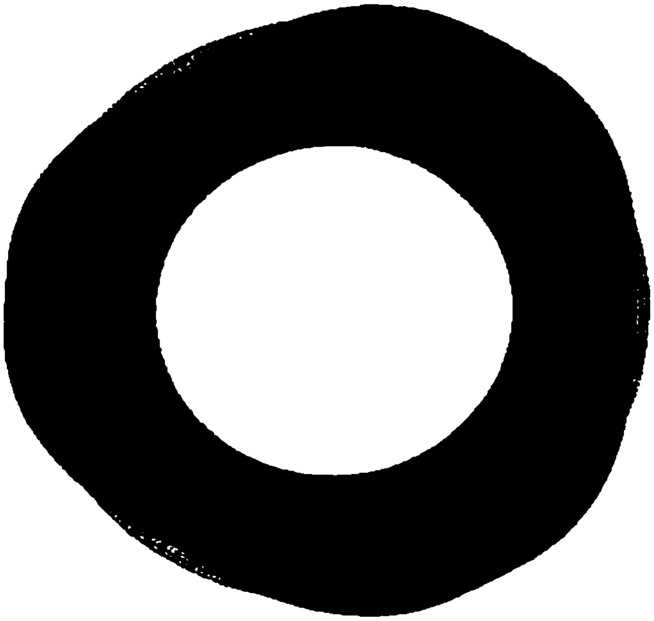

(h) Mode 8

*Figure 6.11: Deflection modes of the tire model: (g) seventh mode, f_7 = 99.84 Hz; and (h) eighth mode, f_8 = 100.64 Hz. (Continued)

**Note: The deflection modes are extracted from the tire model using the selected parameters; p_t = 690.3 kPa (100 psi).*

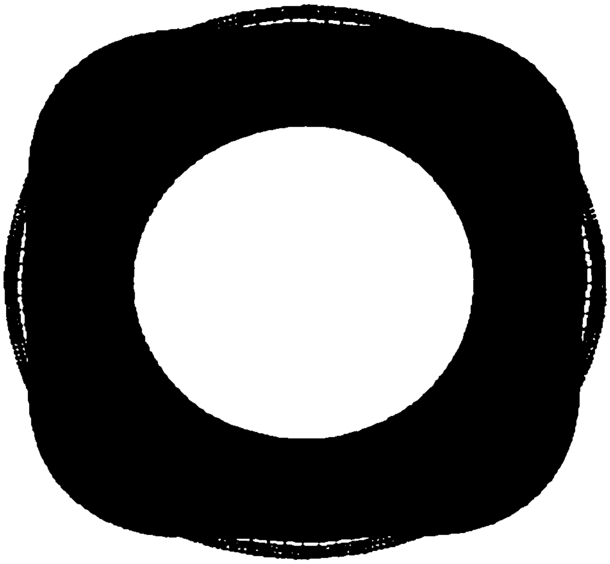

(i) Mode 9, f_9 = 114.5 Hz

*Figure 6.11: Deflection modes of the tire model: (i) ninth mode, f_9 = 114.5 Hz. (Continued)

**Note: The deflection modes are extracted from the tire model using the selected parameters; p_i = 690.3 kPa (100 psi).*

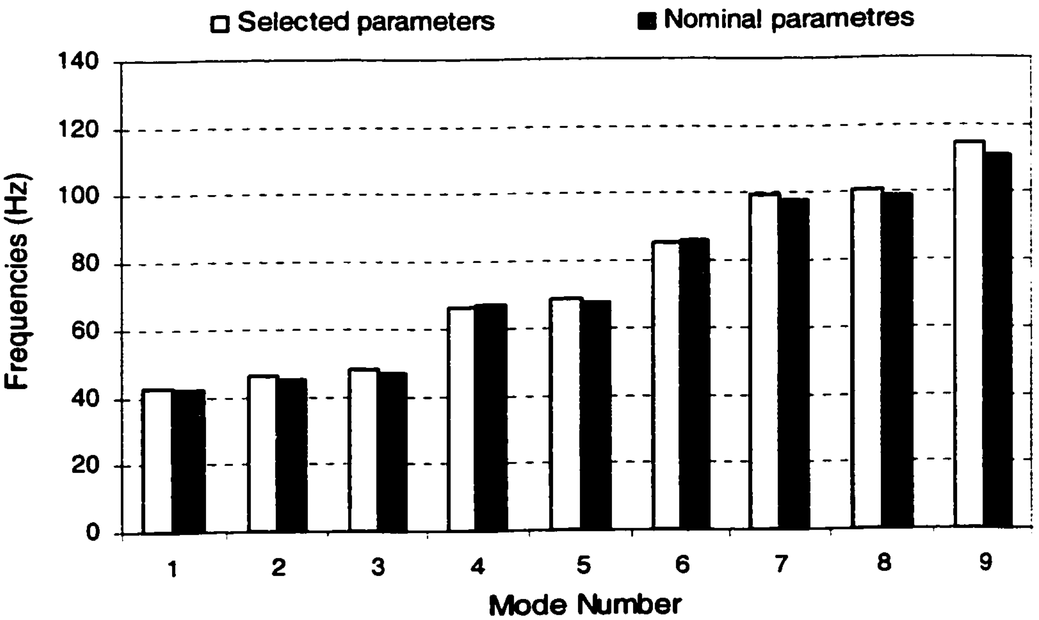

Figure 6.12: Comparison of the natural frequencies of the tire model based upon the selected and nominal parameters; p_i= 690.3 kPa (100 psi).

6.5 SUMMARY

The effects of variations in the inflation pressure and the anisotropic property related structural parameters on the natural frequencies and deflection modes of the inflated tire are investigated through modal analysis of the nonlinear tire model. The results show that the variations in the cord angle can have notable effects on the natural frequencies above 60 Hz and relatively small influence on the lower frequencies. Increasing the cord angles in the layers yields a decrease in the natural frequencies in the considered range. The number of cord ends per unit width in each layer has considerable effect on the natural frequencies. Increasing the value of epc yields higher values of the natural frequencies in almost all of the considered modes. Increasing the number of layers in the belt yields lower natural frequencies f_1, f_2, f_3, f_5, f_6, f_8 and f_9 but higher frequencies f_4 and f_7. An increase in the inflation pressure results in significant increase in all the natural frequencies. The mode shapes of the tire using the selected parameters based on the parametric study performed in Chapter 4 are extracted and discussed. The differences between the tire model based upon the selected nominal parameters are also investigated and discussed.

CHAPTER 7 CONCLUSIONS AND RECOMMENDATIONS FOR FUTURE WORK

7.1 MAJOR HIGHLIGHTS OF THIS INVESTIGATION

In this thesis, a detailed and efficient nonlinear finite element model of a pneumatic truck tire is developed to investigate the deformation, stress and strain fields under different static loads. The finite element model is validated and analyzed to investigate the inter-ply shear interactions in the belt layers, the contact pressure distribution in the tire-road interface, and the mode shapes and natural frequencies. The analyses are conducted with following objectives:

- To propose a more desirable set of structural and geometric parameters that can lead to lower maximum shear stresses in the belt layers for a tire in service.
- To propose an effective analytical procedure to estimate the 2-D tire-road contact pressure distribution as a function of the inflation pressure and normal load to enhance the point-contact models in the ride and pavement damage analyses.
- To perform the free vibration analysis and investigate the influence of variations in the anisotropy-related parameters on the tire natural frequencies.

Portion of the research results have been accepted as a few journal articles and conference papers [174-178].

7.1.1 Development of the Nonlinear Finite Element Tire Model

A nonlinear finite element model of a radial truck tire is developed using the commercial software, ANSYS®, to analyze the tensile stress distributions, deformation fields and the inter-ply shear stresses as a function of the normal load. The tire model is established based on the considerations of the geometry, and orientations of the cords in belts and carcass layers, stacking sequence of different layers and large deformations of the multiple layers in order to predict the interactions between the plies. The model incorporates the nearly incompressible property of the tread rubber block and anisotropic material properties of the layers. The influence of normal load and thus the tire deflection on the above response parameters are discussed. The validation of the model is examined by comparing the computed tire load-deflection characteristics and the footprint geometry with the measured data in a qualitative manner.

7.1.2 Parametric Study: Inter-ply Shear Stresses

The developed FE tire model is employed to perform a parametric study on the maximum shear stresses generated in the belt layers of a truck tire. The parametric study incorporates the geometric and anisotropic material properties of the individual layers in the multi-layered system, and the orientations of the cords in different layers. The parameters considered concerning the geometry of the tire include the aspect ratio, rim radius and tread depth. The parameters related to structural features and material properties of individual layers in the belts, such as cord angle, total number of belt layers under the crown and number of twisted cords per unit width of an individual layer, are further considered. The influence of these parameters on the maximum shear stresses developed in individual belt layers are investigated for a non-rolling radial truck tire with 100 psi (690.3 kPa) inflation pressure, and 20 and 30 mm normal deflections. The results are used to derive a more desirable set of structural parameters so that the maximum stresses within the loaded tire body can be reduced. The maximum inter-ply shear stresses computed using proposed set of parameters is compared with those derived corresponding to nominal parameters considered in the study.

The parameters are varied over a practical range, such that the variations pose negligible effects on the load-deflection characteristics of the tire. The variations, however, are considered to affect the maximum shear stresses in the layers. Hence the presented results and the conclusions from the analysis for constant deflection condition can be considered valid for nearly constant load conditions, which describe more realistic loading situations of a in-service tire.

7.1.3 Estimation of 2-D Contact Pressure Distribution

A methodology to estimate the tire-road contact pressure distribution in the wheel plane as a function of the inflation pressure and normal load for a truck tire is proposed. The modeling process is based on the 3-D pressure fields obtained through the nonlinear static stress analysis of the FE tire model. The 3-D pressure fields are analyzed to derive 2-D contact pressure distribution using the equivalent work as the basis. Curve fitting techniques are applied to derive a polynomial function to describe the contact pressure distribution as a function of the normal load, inflation pressure and coordinate along the contact patch. The polynomial function is then applied to derive an estimate of the contact patch length and contact pressure distribution corresponding to specific values of the resultant tire force and inflation pressure. The validity of the proposed polynomial function is assessed through comparison of the estimated contact pressure with that obtained from the FE tire model.

7.1.4 Modal Analysis

The nonlinear FE tire model is used to conduct a modal analysis of a truck tire. The three dimensional (3D) mode shapes corresponding to natural frequencies below 112 Hz are extracted and the motions associated with each vibration mode of the tire under specific inflation pressures are discussed. The vibration modes and frequencies for a 12.5R22.5 truck tire with different inflation pressure are studied incorporating the pre-stress effects and nonlinearities derived from the static analysis. The effects of variations in the inflation pressure and anisotropic property related structural parameters, such as cord angles and number of cord ends per unit width in each layer and the number of layers in the belt, on the natural frequencies of a radial truck tire are investigated in a qualitative manner. The application of the model in conjunction with the adequately measured material properties of layers in belt and carcass casing is expected to yield a quantitative modal analysis of a specific tire.

7.2 CONCLUSIONS

Based on the studies conducted in this dissertation, the following major conclusions are drawn:

- The majority of the reported FE tire models are primarily based on the linear analysis of the multi-layered system, assuming small deformations of layers and negligible shear interactions between the anisotropic layers.
- From the literature review, it can be concluded that almost no reported model could produce reliable shear stress data for the layers as a function of the tire

load and the influence of various structural and geometric parameters on the shear interactions of a loaded tire have not been investigated.

- Although many studies have derived the contact pressure distributions from various tire models, an effective methodology to estimate 2D contact pressure distributions as a function of the inflation pressure and normal load has not been proposed to enhance the application of point-contact models in pavement damage analyses and vehicle dynamics studies.
- Almost no reported models are available to present the three-dimensional mode shapes and natural frequencies of a tire as function of the anisotropy of the belt layers and the inflation pressure, while considering the nearly incompressible property of the tread rubber block and the structural features of layers.
- The proposed finite element tire model is capable of predicting inter-ply shear stresses between the layers and can be employed to analyze the shear interactions between layers and the fiber forces in individual layers.
- The tire model is validated by comparing the finite element model results with the test data on the normal force-deflection characteristics and the contact geometry over a wide range of normal loads and inflation pressures. The comparisons revealed reasonably good agreements between the model results and the measured data.
- The highest values of the first principal-direction stress appear in the vicinity of the center of the contact patch. The second and third principal stresses have their maximum values in the shoulder areas in the cross section, which is considered

to be resulting from the abrupt changes in the geometry and discontinuities in the material properties associated with the carcass and the belts.

- The tensile stress fields of the belt layers and the corresponding displacements are asymmetric about the circumferential axis, which is attributed to the asymmetric stacking sequence of the layers. The tensile stresses in the carcass layer are distributed nearly symmetrically about the contact patch centerline.
- An increase in the normal load tends to increase the stresses considerably in the elements in the vicinity of the shoulder area. The tensile stresses in belts 4 and 3, located near the carcass layers, are considerably larger than those observed in belts 2 and 1, located near the tread layer.
- The shear stresses derived from the elements in the lateral centerline of the contact patch show that

  (a) The magnitudes of the out-of-tire-plane inter-ply shear stresses (S_{yz}) are over ten times higher than the in-tire-plane stresses (S_{xz}) developed between the belt 4 and the carcass layer;

  (b) The influence of normal load on the S_{xz} is more significant than that on the S_{yz}. The out-of-tire-plane shear stresses S_{yz}, developed between the carcass layer and belt 4, are significantly higher than the corresponding shear stresses generated between the belt layers near the shoulder area.

  (c) The peak values of S_{xz} generated between the belt layers tend to move further away from the center of the contact patch to the outer periphery in the cross-section of the tire when normal load increases.

(d) The peak values of S_{yz} and S_{xz} occurring near the shoulder area may be considered as the main factors causing the delamination damage in the tire.

- High tire-road contact pressures occur at inner side of the inner ribs under light to medium loading (below 15 kN for 621.3 kPa inflation pressure). The pressure peaks, however, tend to shift outward along the lateral direction under higher normal loads.
- The ratio of peak pressures occurring in the outer ribs to those in the inner ribs tends to increase considerably with increase in the normal load.
- Increasing the aspect ratio from 0.77 to 0.91 results in a large increase in the maximum shear stress S_{yz} in layer 2 and a relatively small increase in the maximum shear stress S_{yz} in layer 1, irrespective of the normal load considered. The peak value of S_{yz} in layers 3 and 4, however, decreases with increase in the aspect ratio. The maximum peak shear stresses in the belt layers could be reduced with lower aspect ratio tires.
- Increasing the cord angle from 18 to 26 degrees yields considerably lower peak values of S_{yz} in belt 2, but higher peak values in belts 3 and 4. The peak shear stress in belt 1 decreases with increase in the value of cord angle from 18 to 22 degree, and then increases slightly with further increase in the cord angle from 22 to 26 degrees.
- The computed shear stress S_{yz} fields for the three-layer-belt appear to be similar to those of the layers 1, 2 and 3 of the four-layer-belt. In the case of five-layer-belt, the shear stress fields of S_{yz} in layers 1, 2, 4 and 5 also appear to be similar to those in the layers 1, 2, 4 and 3 for the four-layer-belt case.

- As the number of belt layers increases from 3 to 5, the peak shear stresses S_{yz} in layers 2 and 3 decrease significantly, irrespective of the normal load. The peak value of stress S_{yz} in layer 1 tends to decrease slightly when the total number of belt layers is increased from 3 to 4 and increases slightly with further increase in the number of belt layers. The peak value of stress S_{yz} in layer 4 increases slightly when one more belt layer is added. The addition of the fifth belt layer tends to lower the maximum shear stresses in the layers 1 to 3, and has negligible effect on the peak value of the stress S_{yz} of layer 4. The maximum of the peak shear stress S_{yz} among all the layers are developed in layer 2 and are significantly reduced with increase in the number of belt layers, irrespective of the applied load.
- The variation in the rim radius from 0.26 m to 0.32 m has negligible influence on the peak values of S_{yz} in different belt layers but has significant influence on the peak values of shear stresses S_{xy} and S_{xz} for the considered loading conditions.
- The variations in the tread depth from 3 to 10 mm yield almost insignificant effects on the peak values of S_{yz} and S_{xy} of individual layers. An increase in the tread depth tends to lower the peak shear stress S_{xz} in belt layers under normal deflection of 20 mm, and yields considerably higher values under normal deflection of 30 mm. The design of the tread depth relies on factors other than the shear stresses in multi-layered system, such as heat resistance and wear resistance.

- Increasing the value of epc yields significant increase in the magnitude of the peak shear stress S_{yz} in layer 2, and relatively small increase in the peak shear stresses in all the other layers, irrespective of the normal load. The results reveal nearly linear variation in the maximum shear stresses (S_{yz}) in each belt layer as a function of the values of *epc*. For the simulation conditions considered, a lower value of *epc*, in the 3.5 to 4.5 range, yields a lower peak value of S_{yz} in all the layers.
- Increasing the normal load yields considerable increase in the peak shear stresses S_{yz} in all the layers.
- A more desirable set of these parameters has been proposed to reduce the maximum shear stress developed in the layers of a truck tire under the prescribed loading conditions. The use of the selected set of parameters, yields 35-45% lower values of S_{yz} in belts 2 and 3, and 6-13% lower values of S_{yz} in belts 1, depending upon the normal load. The peak shear stress S_{yz} developed in layer 4, however, increases considerably. The comparison reveals that the highest peak stresses S_{yz} in the belt layers, attained using the selected parameters, are 21.6-23.4%, 18.3-27.9% and 18.6-25.8% lower than those computed for the nominal parameters, under inflation pressures of 690.3, 552.2 and 828.4 kPa, respectively.
- The reductions in the maximum shear stresses S_{yz} are achieved at the expense of relatively higher peak shear stresses S_{xy} and S_{xz}, which is considered acceptable in view of the considerably lower magnitudes of S_{xy} and S_{xz}.

- The three-dimensional contact pressure field derived from the finite element model can be effectively expressed in terms of two-dimensional tire-road contact pressure distribution in the wheel plane as a function of the inflation pressure and the normal load. The proposed function can be conveniently applied to vehicle models for studies on pavement damage potentials and ride quality. The estimated contact pressure distributions show reasonably good agreement with those derived from the finite element model and with the data reported in the published studies.
- Higher contact pressure peaks occur in the vicinity of inner ribs near the central circumferential line, when the normal load is lower than a critical value. The pressure peaks tend to shift towards the outer ribs, when the normal load is increased. The critical value of the normal load increases with increase in the inflation pressure.
- Under light normal load and high inflation pressure, the contact pressure peaks occur in the vicinity of the central point of the contact patch. The pressure peaks, however, tend to shift towards front and rear edges of the contact patch, under high normal loads or low inflation pressures.
- The pressure peaks tend to shift towards the outer ribs from the inner ribs, when the normal load is increased. The ratio of the peak pressure occurring in the outer ribs to that in the inner ribs tends to increase most significantly when the normal load is increased beyond a critical value, specifically for the lower inflation pressures. Under lower inflation pressures, the contact pressure peaks shift to the outer ribs very rapidly with increase in the normal load.

- The length of the contact patch increases significantly with increase in the normal load for constant inflation pressure, but reduces slightly with increase in the inflation pressure under a given normal load.
- Under a lower normal load (20 kN), the variations in p_i exhibit relatively small effect on the contact pressure-distribution and the pressure peaks. Under a large normal load (45 kN), the variations in p_i influence the contact pressure distribution in a significant manner. Lower inflation pressure results in more rapid shifting of the contact pressure peaks to the two edges of the contact patch. A higher inflation pressure yields nearly constant contact pressure distribution around the central point of the contact patch.
- The first three vibration modes of the tire model based upon nominal and selected design parameters involve the translational motion along the axial direction, rotational and oscillatory movements in- and out-of-the-wheel planes, respectively.
- The motions associated with higher frequency modes yield more complex deflection patterns comprising coupled rotational, twisting, oscillatory and bending motions, as well as expansion and shrinking of the carcass along different directions.
- The side views of the deflection patterns associated with some of the modes in the mode 4 to 9 range appear as ovals, triangular and quadrangle with rounded corners. These are most likely attributed to the presence of the standing wave.
- The variations in the cord angles yield significant effect on the natural frequencies above 60 Hz and relatively small influence on the lower mode

frequencies. Increasing the cord angles in the layers yields a decrease in the natural frequencies.

- The number of cord ends per unit width in each layer has considerable effect on the natural frequencies. Increasing the value of epc yields higher values of natural frequencies associated with almost all of the considered modes.
- Increasing the number of layers in the belt yields lower values of natural frequencies f_1, f_2, f_3, f_5, f_6, f_8 and f_9, but higher frequencies f_4 and f_7.
- Increasing inflation pressure results in a significant increase in all the natural frequencies.
- The natural frequencies f_1 and f_5 for the tire model based upon the nominal parameters appear nearly the same as those derived from the model with selected set of parameters. The natural frequencies f_2, f_3, f_7, f_8 and f_9 increase, while the frequencies f_4 and f_6 tend to decrease slightly when the selected tire parameters are used.

7.3 RECOMMENDATIONS FOR FUTURE WORK

The thesis research presents a fundamental nonlinear finite element analysis of a truck tire involving the shear interaction between the belt and carcass layers, the estimation of the contact pressure distribution in the tire-road interface, the mode shapes and natural frequencies. It is recommended to undertake the following future studies to further explore the validation and the application potentials of the proposed concepts and methodologies to facilitate its realization and implementations.

- The frictional force in the tire-road interface may have influence on the shear stress fields developed in the belt and carcass layers of a loaded tire. This influence needs to be investigated.
- The layered elements arranged along the central circumferential line over the contact patch may be employed to analyze the tensile stress distribution in the belt and carcass layers in the vicinity of the contact patch as a function of the normal load and the inflation pressure.
- The model can be modified to explore the possibility of performing transient analysis, by defining a support as a rounded step, which moves at a steady speed towards the statically loaded truck tire. In this way, the maximum dynamic response, in terms of the peak shear stresses in the belt and carcass layers, can be investigated as a function of the speed of a totally braked vehicle moving toward an obstacle on the road. The impact effect on the tire and the axle and thus the vehicle can be investigated.
- The model can be used to incorporate the thermal effects on the stress fields, when the material property as a function of the temperature is known.
- The tire model can be further employed to perform the modal analysis on high frequency (above 112 Hz) properties of the considered tire, concerning the standing wave phenomenon, noise generation, etc.
- Further experimental work need to be conducted to obtain the reliable material properties of the anisotropic belt and carcass layers to perform quantitative analysis of the finite element tire model.

REFERENCES

1 Clark, S. K., *Mechanics of Pneumatic Tires*, U.S. Department of Transportation, NHTSA, Washington D.C., DOT HS805-952, 1981.

2 Bohm, F. and Willumeit, H-P, *Tyre Models for Vehicle Dynamic Analysis*, the second International Colloquium on Tire models for Vehicle Dynamic Analysis, Technical University of Berlin, Feb., 1997.

3 Pacejka, H. B., *Analysis of Tire Properties*, Mechanics of Pneumatic Tires, Chapter 9, edited by Clark, S. K. Washington, DC: U.S. Department of Transportation, 1981.

4 *Tire Science and Technology* Journal, TSTCA, monthly issues.

5 Ridha, R. A. & Clark, S. K., *Tire Stress and Deformation*, Mechanics of Pneumatic Tires, Chapter 7, edited by Clark, S. K. Washington, DC: U.S. Department of Transportation, 1981.

6 Wong, J. Y., *Theory of Ground Vehicles*, Second Edition, A Wiley-Interscience Publication, John Wiley & Sons, Inc., 1993.

7 Ellis, J. R., *Road Vehicle Dynamics*, published by John R. Ellis, Akron, Ohio, USA, 1989.

8 Pacejka, H. B. and Sharp, R. S., *Shear Force Development by Pneumatic Tires in Steady State Conditions: A Review of Modeling Aspects*, Vehicle System Dynamics 20, pp12-176, 1991.

9 Gehman, S. D., *Rubber Structure and Properties*, Mechanics of Pneumatic Tires, Chapter 1, edited by Clark, S. K, US Department of Transportation, Washington, DC, 1981.

10 Bakker, E., Pacejka, H. B. and Lidner, L., *A New Tyre Model with application in Vehicle Dynamics Studies*, 4th Auto-technologies Conference, Monte Carlo, SAE 890087, 1989.

11 Pacejka, H. B. and Bakker, E., *The Magic Formula Tyre Model*, Proceedings 1st Tyre Colloquium, Delft, Oct. 1991, Suppl. To Veh.Sys.Dyn., Vol.21, pp.1-18, 1993.

12 Bakker, E., Nyborg, L. and Pacejka, H. B., *Tyre Modeling for use in Vehicle Dynamics Studies*, SAE 870421, 1987.

13 Tielking, J. T. and Mital, N. J., *A Comparative Evaluation of Five Tire traction Models*, UM-HSRI (University of Michigan, Highway Safety research Institute) Report PF-74-2, January 1974.

14 Bernard, J. E., Segel, L. and Wild, R. E., *Tire Shear Force Generation During Combined Steering and Braking Maneuvers*, S.A.E. paper 770852, 1977.

15 Ridha, R. A. and Theves, M., *Advances in Tyre Mechanics*, Rapra Review Reports, vol.7, No.5, 1994.

16 Hoque, Abul Kalam M. M., *Design Method for a Flexible Pavement with Rubber Tire Chips in Sub-grade*, thesis (M. A. Sc.), Dept. of Civil Engineering, Concordia University, 1995.

17 Henry, J. J. and James C. Wambold (editors), *Vehicle, Tire, Pavement Interface*, Proceedings of the conference on Vehicle, Tire, Pavement Interface sponsored by ASTM Committee E-17 held in Santa Barbara, Calif, Oct. 28, 1990.

18 Marion G. Pottinger and Thomas J. Yager (editors), *The Tire Pavement Interface*, a symposium sponsored by ASTM Committees E-17 on Traveled Surface, Characteristics and F-9 on Tires, Columbus, OH, 5-6, June 1985.

19 Pacejka, H. B. and Fancher, P. S., *Hybrid Simulation of Shear Force Development of a Tire Experiencing Longitudinal and Lateral Slip*, Proc. XIV FISITA Congress, London, 3/78-3/85, 1972.

20 Pacejka, H. B., *In-plane and out-of plane dynamics of pneumatic tires*, Vehicle System Dynamics 10(4-5), 221-252, 1981.

21 Chiesa, A., Obert, L.and Tamburini, L., *High Frequency Vibrations in Tires Under Vertical Perturbation and Their Transmission to the Wheels*, Auto. Engr., 520, 1964.

22 Chiesa, A., and Tangorra, G., *The Dynamic Stiffness of Tires*, Revue gen. Du Caoutchoue 36 (10), 1321, 1959.

23 Rasmussen, R. E., and Cortese, A. D., *Dynamic Spring rate performance of rolling tires*, SAE Paper No. 680408, 1968.

24 Smiley, R. F., and Horne, W. B., *Mechanical Properties of Pneumatic Tires with Special Reference to Modern Aircraft Tires*, NASA Tech. Note 4110, 1958.

25 Chiesa, A., *Vibration Performance Differences Between Tires with Cross-Biased Plies and Radial Plies*, SAE Paper No. 990B, 1965.

26 Barson, C. W., James, D. H. and Morcombe, A. W., *Some Aspects of Tire and Vehicle Vibration Testing*, Proc. IME 182, 3B, 32, 1967-68.

27 Barson, C. W., Gough, V.E., Hutchinson, J. C., and James, D., H., *Tire and Vehicle Vibration*, Proc. IME, Auto. Div., pp. 213, 1964-65.

28 Tielking, J. T., *Plane Vibration Characteristics of a Pneumatic Tire Model*, SAE Paper No. 650492, 1965.

29 Bohm, F., *Mechanik des Gurtelreifens*, ing. Archiv 35, 82, 1966.

30 Fiala, E., and Willowmeit H. P., *Radiale Schwinggungen von Gurtel-Radialreifens*, A.T.Z. 68(2), 33, 1966.

31 Federhofer, K., *Zur Schwingzahlberechnung des dunnwandigen Hohlenreifens*, Ing. Archiv. 10-11, 125, 1939-1940.

32 Dodge, R.N., *Dynamic Stiffness of a Pneumatic Tire Model*, SAE Paper No.650491, 1965.

33 Clark, S. K., *The rolling Tire Under Load*, SAE Paper No. 650493, 1965.

34 Gardner, E. R. and Worswick, T., *Behavior of Tires at High Speed*, I.R.I. 27, 127, 1951.

35 Turner, D. M., *Wave Phenomena in Tires at High Speed*, Third Rubber Tech. Conference London, Trans. I. R. I., June 1954.

36 Drozdov, V. K., et al., *Formation of Stationary waves on Pneumatic Tires at High Rolling Speeds*, Sov. Rubber Tech. 19 (12), 36, 1960.

37 Togo, K., *Standing Wave on Pneumatic Tire at High Speed*, Memoirs of the Defense Academy, Japan, Vol. IV, No. 1, p.43, 1964.

38 Ames, W. F., *Wave Phenomena in Tires*, University of Iowa, Tech. Report 1, 1967.

39 Akasaka, T., and Yamagishi, K., *On the Standing Waves in the Shell Wall of Running Tire*, Trans. Japan Soc. Aer. Space Sc. 11(18), 12, 1968.

40 Soedel, W., *On the Dynamic Response of Rolling Tires According to Thin Shell Approximation*, J. of Sound and Vibration 41, No.2, pp. 233-246, 1975.

41 Dodge, R. N., *Dynamic Stiffness of a Pneumatic Tire Model*, SAE Paper No.650491, 1965.

42 Dixon, J. C., *Tires, Suspension and Handling*, 2nd edition, Publisher: Warrendale, PA: Society of Automotive Engineers; London: Arnold, 1996.

43 Ellis, J. R., Frank, F., and Hinton, B. J., *The Experimental Determination of Tire Model Parameters*, A.S.A.E. Report No. 2, Sept. 1966.

44 Pottinger, M. G. and Fairlie, A. M., *Characteristics of Tire Force and Moment Data*, Tire Science and Technology, TSTCA, 17(1), pp15-51, 1989.

45 Savkoor, A. R., *The lateral flexibility of pneumatic tire and its application to the lateral rolling contact problem*, SAE Paper No.700378, 1970.

46 Wang, Y. Q., Gnadler, R. and Schieschke, R., *Two-Dimensional Contact Area of a Pneumatic Tire Subjected to a lateral Force*, Vehicle System Dynamics, 23, pp. 149-163, 1994.

47 Segel, L., *Basic Linear Theory of Handling and stability of automobiles*, Proceedings of First Course in Advanced Vehicle System Dynamics (Amalfi), ICTS, Rome, pp. 19-87, 1984.

48 Sakai, H., *Theoretical and Experimental Studies on the Dynamic cornering properties of tyres*, International Journal of Vehicle Design, 2(1-4), 1981

49 Sakai, H., *Study on Cornering Properties of Tire and Vehicle*, Tire Science and Technology, TSTCA, 18(3), pp136-196, 1990.

50 Gim, G. and Nikravesh, P. E., *An Analytical Study of Pneumatic Tire Dynamic Properties: part 1-3*, International Journal of Vehicle Design, 11(6), 12(1,2), 1991.

51 Pacejka, H. B., *Wheels*, Farewell Address, Delft Technique University, Delft, Netherlands, May 1996.

52 Sharp, R. S., *On the Accurate Representation of Tyre Shear Forces by a Multi-Radial Spoke Model*, Proc. 11th IAVSD Symposium on the Dynamics of Vehicles on Roads and Tracks, (ed. R. J. Anderson), Swets and Aeitlinger, Lisse, pp528-541, 1990.

53 Sharp, R. S., and EL-Nashar, M. A., *A Generally Applicable Digital Computer Based Mathematical Model for the Generation of Shear Forces by Pneumatic Tires*, Vehicle System Dynamics, Vol.15, No.4, pp. 187-209, 1986.

54 Frank, F. and Hofferberth, W., *Mechanics of the Pneumatic Tire*, Rubber Chemistry and Technology, Vol. 40, No. 1, pp. 271-322, 1967.

55 Ridha, R. A., *Computation of Stresses, Strains and Deformation of Tires*, Rubber Chemistry and Technology, Vol. 53, No. 4, pp. 849-902, 1980.

56 Walter, J. D., *Tire Stress and Deformation*, in Mechanics of Pneumatic Tires, Clark, S. K., ed., Washington, pp. 406-444, 1971.

57 Kulikov, G. M., *Computational Models for Multi-layered Composite Shells with Application to Tires*, Tire Science and Technology, TSTCA, Vol. 24, No. 1, pp. 11-38, January-March 1996.

58 Biderman, V. L., *Computation of Inflated Profile and Stresses in the Elements of Pneumatic Tires Subjected to Internal Pressure*, Moscow, Trans. Scientific Institute of Tire Industry, No. 3, pp. 16-51 (in Russian), 1957.

59 Robecchi, E., and Amici, L., *Mechanics of Pneumatic Tire*, Tire Science and Technology, 1, 290-345, 1973.

60 Nicholson, D. W., *On the Inflated Tire Profile*, Tire Science and technology, v.4, n.3, pp.169-176, August 1976.

61 Grigolyuk, E. I. And Kulikov, G. M., *Methods of Investigation of Multi-layered Composite Shells with Application to Pneumatic Tires*. Scientific and technical Progress in Machine Building, Issue 39, Moscow, (in Russian), 1993.

62 Noor, A. K. and Tanner, J. A., *Advances and Trends in the Development of Computational Models for Tires*, Computers & Structures, Vol. 20, No. 1-3, pp. 517-533, 1985.

63 Tielking, J. T. and Feng, W. W., *The Application of the Maximum Potential Energy Principle to Nonlinear Axisymmetric Membrane Problems*, Journal of Applied Mechanics, 73, pp. 491-496, 1974.

64 Feng, W. W., Tielking, J. T., and Huang, P., *The Inflation and Contact Constraint of a Rectangular Mooney Membrane*, Journal of Applied Mechanics, 73, 979-983, 1974.

65 De Eskinazi, J., Werner, S. and Yang, T. Y., *Contact of an Inflated Toroidal membrane with a flat Surface as an Approach to the Tire Deflection problem*, Tire Science and Technology, TSTCA, Vol. 3, No. 1, pp. 43-61, 1975.

66 Robecchi, E., *Mechanics of the Pneumatic Tire, the Laminar Model under Inflation and in Rotation*, Tire Science and Technology, TSTCA, Vol. 4, pp. 382-438, 1973.

67 Tielking, J. T., McIvor, I. K. and Clark, S. K., *A Modified Linear Membrane Theory for the Pressured Toroid*, J. Applied Mechanics, Vol. 38, pp. 418-422, 1971.

68 Brewer, H. K., *Stresses and Deformations in Multi-ply Aircraft Tires Subject to Inflation Pressure Loadings*, Technical Report AFFDL-TR-70-62, Write-Pattern Airforce Base, Ohio, June 1970.

69 Brewer, H. K., *Tire stress and deformation from Composite Theory*, Tire Science and Technology, TSTCA, Vol. 1, No. 1, pp. 47-76, 1973.

70 Grigolyuk, E. I. And Kulikov, G. M., *Numerical Solution of Problems Involving the Statics of Geometrically Nonlinear Anisotropic Multi-Layered Shells of Revolution*, Mechanics Composite Materials, Vol. 17, No. 3, pp. 294-302, 1981.

71 Grigolyuk, E. I. and Kulikov, G. M., *Analysis of Radial Tires on the Basis of Generalized Timoshenko-type Theory*, Mekhanika Tverdogo Tela, No. 4, pp. 166-174 (in Russian), 1984.

72 Noor, A. K., Andersen, C. M., and Tanner, J. A., *Exploiting Symmetries in the Modeling and Analysis of tires*, Computer Methods Applied Mechanics and Engineering, Vol. 63, No. 1, pp. 37-81, 1987.

73 Grigolyuk, E. I. and Kulikov, G. M., *Effect of Shear Stress Nonuniformity in Modern Tires*, Mechanics Composite Materials, Vol. 22, No. 5, pp. 607-613, 1987.

74 Grigolyuk, E. I. and Kulikov, G. M., *Axisymmetric Deformation of Multi-layered Anisotropic Shells of revolution Subjected to Tangential Loads*, Mekhanika. Kompozitnykh Materialov, No. 4, pp. 484-491. (in Russian), 1992.

75 Kulikov, G. M., *Analysis of Pneumatic Tires on the Basis of Generalized Hypothesis of Broken Line*, Problemy Protchnosty, No. 2, pp. 91-95 (in Russian), 1990.

76 Kulikov, G. M., *Non-axisymmetric Deformation of Multi-layered Anisotropic Shells of Revolution Subjected to Tangential Loading*, Mekhanika Kompozitnykh Materialov, No. 5, pp. 597-602 (in Russian), 1992.

77 Grigolyuk, E. I. and Kulikov, G. M., *General Direction of development of the Theory of Multi-layered Shells*, Mechanics Composite Materials, Vol. 24, no. 2, pp. 231-241, 1988.

78 Noor, A. K. and Burton, W. S., *Assessment of Computational Models for Multi-layered Composite Shells*, Applied Mechanics Reviews, Vol. 43, No. 4, pp. 67-97, 1990.

79 Kulikov, G. M., *Influence of Anisotropy on the Stress State of Multi-layered Reinforced Shells*, Sov. Applied mechanics, Vol. 22, No. 12, pp. 1166-1170, 1987.

80 Zorowski, C. E., and Dunn, S. E., *A Mathematical Model for the Pneumatic Tire*, North Carolina State University, Raleigh, June 1970.

81 Walter, J. D., *Centrifugal Effects in Inflated, Rotating Bias Ply Tires*, Textile Research Journal, 46, 1-7, 1970.

82 Patel, H. P., *Mathematical Analysis of Statically Loaded Pneumatic Tires*, Ph.D. Thesis, North Carolina State University, Raleigh, 1975.

83 Ridha, R. A., Kelsey, S., Cervelli, R. V., and Cadoret, J. E., *Proposal to Supply a Computer program for the Finite Element Analysis of Aircraft Wheel Assemblies*, Report No. VP-1122, The Bendix Corporation, South Bend, Indiana, January 1972.

84 Deak, A. L., and Atluri, S., *The Stress Analysis of Loaded Aircraft Tires*. Interim Report for AFFDL, Mathematical Sciences Northwest, Inc., 1973.

85 Melosh, R. J., *Structural Analysis of Solids*, Journal of the Structural Division, ASCE, 89, No. ST4, 205-224, 1963.

86 Clough, R. W., *Comparison of Three Dimensional Finite Elements*, Proc. Symposium on Application of Finite Element Methods in Civil Engineering, Vanderbilt Univ., pp1-26, November 1969.

87 Ergatoudis, I., Irons, B. M., and Zienkiewicz, O. C., *Curved, Iso-parametric, Quadrilateral Elements for Finite Element Analysis*, International Journal of Solids and Structures, 4, 31-42, 1968.

88 Zienkiewicz, O. C., Irons, B. M., Ergatoudis, J., Ahmed, S., and Scott, F. C., *Iso-parametric and Associated Element Families for Two and Three Dimensional Analysis, Finite Element Methods in Stress Analysis*, TAPIR, Technical University of Norway, Trondhei, Chapter 13, 1969.

89 Adelman, H. M., Catherines, D. S., and Walton, W. C., *Accuracy of Model Stress Calculations by the Finite Element Method*, AIAA, Journal, 8 462-468, 1970.

90 Trinko, M. J., *Ply and Rubber Stresses and Contact Forces for a Loaded Radial Tire*, Tire Science and Technology, TSTCA, Vol. 11, January-December, pp.20-37, 1983.

91 Rothert, H. and Gall, R., On the *Three-dimensional Computation of Steel-Belted Tire*, Tire Science and Technology, TSTCA, Vol. 14, pp. 116-124, April-June, 1986.

92 Chang, J. P., Satyamurthy, K., and Tseng, N., T., *An efficient Approach for Three-dimensional Finite Element Analysis of Tires*, Tire Science and Technology, TSTCA, Vol. 16, pp. 249-273, October-December, 1988.

93 Kim, K. O., Noor, A. K., and Tanner, J. A., *Modeling and Analysis of the Space Shuttle Nose-Gear Tire with Semi-analytical finite Elements*, NASA TP-2977, April 1990.

94 Tanner, J. A., Martinson, V. J., and Robinson, M. P., *Static Frictional Contact of the Space Shuttle Nose Gear Tire*, Tire Science and Technology, TSTCA, Vol. 22, No. 4, October-December 1994.

95 Stubbs, S. M., Tanner, J. A., and Smith, E. G., *Behavior of Aircraft Anti-skid Braking Systems on Dry and Wet Runway Surfaces —A Slip-Velocity-Controlled, Pressure-Bias-Modulated System*, NASA TP-1051, 1979.

96 Tanner, J. A., Dreher, R. C., Stubbs, S. M., and Smith, E. G., *Tire Tread Temperatures During Anti-skid Braking and Cornering on a Dry Runway*, NSNA TP-2009, 1982.

97 Daugherty, R. H. and Stubbs, S. M., *Cornering and Wear Behavior of the Space Shuttle Orbitor Main Gear Tire*, SAE Paper No. 871867, 1987.

98 Daugherty, R. H. and Stubbs, S. M., *Spin-Up Studies of the Space Shuttle Orbitor Main Gear Tire*, SAE Paper No. 881360, 1988.

99 Clark, S. K., and Dodge, R. N., *Heat Generated in Aircraft Tires Under Free Rolling Conditions*, NASA CP-3629, 1982.

100 Clark, S. K., and Dodge, R. N., *Heat Generated in Aircraft Tires Under Braked Rolling Conditions*, NASA CP-3768, 1984.

101 McCarty, J. L. and Tanner, J. A., *Temperature Distribution in an Aircraft Tire at Low Ground Speeds*, NASA TP-2195, 1983.

102 Gardner, I. And Theves, M., *Computer Modeling of a tire Under Cornering Loads, Tire Science and technology*, TSTCA, Vol. 17, No. 2, pp. 86-99, April-June 1989.

103 Faria, L. O., Bass, J. M., Oden, J. T., and Becker, E. B., *A Three-dimensional Rolling Contact Model for a Reinforced Rubber Tire*, Tire Science and technology. TSTCA, Vol. 17, No. 3, pp. 217-233, July-September, 1989.

104 Yavari, B., Tworzidlo, W. W., Bass, J. M., Faria, L. O., Oden, J. T., and Becker, E. B., *Final Report on Tire Modeling by Finite Elements*, COMCO report to NASA Langley Research Center as part of the National Tire Modeling Program under contract No. NASI-18137, 1991.

105 Jeussette, J. P. and Theves, M., *Finite Element Analysis of Tire/Rim Interface Forces Under braking and Cornering Loads*, Tire Science and technology, TSTCA, Vol. 20, No. 2, pp. 83-105, April-June, 1992.

106 Nackenhorst, U., *On the Finite Element Analysis of Steady State Rolling Contact, Proceedings of Contact Mechanics 93*, Southhampton, United Kingdom, 1993.

107 Gall, R., Tkacik, P., and Andrews, M., *On Incorporation of Frictional Effects in the Tire/Ground Contact Area*, Tire Science and technology, TSTCA, Vol. 21, No. 1, pp. 2-22, January-March, 1993.

108 Goldstein, A. A., *Development of a Quasi-Static Rolling Tire Model for Determination of Truck Tire forces and Moments*, Tire Science and technology, TSTCA, Vol. 24, No. 4, pp. 278-293, October-December, 1996.

109 Schaeffer, H. G. and ball, R. F., *Nonlinear Deflections of Asymmetrically Loaded Shells of Revolution*, AIAA Paper, No. 68-292, April 1968.

110 Wunderlich, W., Cramer, H., and Obrecht, H., *Applications of Ring Elements in the Nonlinear Analysis of Shells of Revolution Under Non-axisymmetric Loading*, Computer methods in Applied mechanics and Engineering, Vol. 51, No. 1-3, pp. 259-275, September 1985.

111 Kim, K. O., Tanner, J. A., Noor, A. K., and Robinson, M. P., *Computational Methods for Frictionless Contact With Application to Space Shuttle Orbiter Nose-Gear Tires*, NASA TP-3073, May 1991.

112 Noor, A. K., *On Making Large Nonlinear Problems Small*, Computer Methods in Applied Mechanics and Engineering, Vol. 34, No. 1-3, pp. 955-985, 1982.

113 Noor, A. K., Andersen, C. M., and Tanner, J. A., *Mixed Models and Reduction Techniques for Large Rotation Nonlinear Analysis of Shells of revolution with Application to Tires*, NASA TP-2343, October 1984.

114 Noor, A. K., *Reduction Methods for the Nonlinear Analysis of Symmetric Anisotropic Panels*, International Journal of Numerical Methods in Engineering, Vol. 23, pp.1329-1341, 1986.

115 Noor, A. K., and Peters, J. M., *Nonlinear Analysis of Anisotropic Panels*, AIAA Journal, Vol. 24, No. 9, pp. 1545-1553, September 1986.

116 Noor, A. K., Andersen, C. M., and Tanner, J. A., *Exploiting Symmetries in the Modeling and Analysis of tires*, NASA TP-2649, March 1987.

117 Noor, A. K. and Tanner, J. A., *Advances in Contact Algorithms and their Application to Tires*, NASA TP-2781, April 1988.

118 Gall, R., Tabaddor, F., Robbins, D., Majors, P., Shepherd, W. and Johnson, S., *Some Notes on the finite Element Analysis of Tires*, Tire Science and Technology, TSTCA, Vol. 23, No. 3, pp. 175-188, July-September, 1995.

119 Danielson, K. T., and Noor, A. K., *Finite Element Developed in Cylindrical Coordinates for Three-Dimensional Tire Analysis*, Tire Science and Technology, TSTCA, Vol. 25, No. 1, pp.2-28, January-March, 1997.

120 Storaasli, O. O., Nguyen, D. T., Baddourah, M. A., and Qin, J., *Computational Mechanics Analysis Tools for Parallel-Vector Supercomputers*, Proceedings of the 34th AIAA/ASME/ASCE/AHS/ASC Structures, Structural Dynamics, and Materials Conference, La Jolla, CA 772-778, 1993.

121 Hughes, T. J. R., Ferencz, R. M., and Hallquist, J. O., *Large-Scale Vectorized Implicit Calculations in Solid Mechanics on a CRAY-X-MP/48 Using EBE Preconditioned Conjugate Gradients*, Computer Methods in Applied Mechanics and Engineering, Vol. 61, pp.215-248, 1987.

122 Bathe, K. J., Walczak, J., and Zhang, H., *Some Recent Advances for Practical Finite Element Analysis*, Computers and Structures, Vol. 47, pp. 511-521, 1993.

123 Baddourah, M. A., Storaasli, O. O., Carmona, E. A., and Nguyen, D. T., *A Parallel Algorithm for Generation and Assembly of Finite Element Stiffness and Mass Matrices*, Proceedings of 32nd AIAA/ASME/ASCE/AHS/ASC Structures, Structural Dynamics, and Materials Conference, Baltimore, MD 1547-1553, 1991.

124 Faria L. O., Oden, J. T., Yavari B, Tworzydlo W. W., Bass J M and Becker E B, *Tyre Modeling by Finite Elements*, Tire Science and Technology, TSTCA, Vol. 20, No. 1, p.33-56, 1992.

125 Kim, Y., Saleeb, A. F. and Chang, T. Y. P., *Implementation of Material Stiffness Coefficients in Finite Element Applications to Rubber*, Tire Science and Technology, TSTCA, Vol.22, No.4, pp.223-241, 1994.

126 Nemeth, T., Nandori, F., Sarkozi, L. and Szabo, T., *Application of a Technical Documentation System for deriving New Belt Constructions for Truck Tires*, Tire Science and Technology, TSTCA, Vol. 23, No. 4, Oct.-Dec., pp.266~282, 1995.

127 Wang, T-M., Danial, I. M. and Huang, K., *Stress Analysis of Tire Sections*, Tire Science and Technology, TSTCA, Vol.24, No.4, pp.349~366, Oct.-Dec., 1996.

128 Ridha, R. A., *Analysis for Tire Mold Design*, Tire Science and Technology, TSTCA, Vol. 2, No. 3, p 195-210, 1974.

129 Ford, T. L. and Charles, F. S., *Heavy Duty Truck Tire Engineering*, SAE 34th L. Ray Buckendale Lecture, SP729, 1988.

130 Walter, J. D., *Cord Reinforced Rubber*, Mechanics of Pneumatic Tires, Chapter 3, edited by Clark, S. K, US Department of Transportation, Washington, DC, 1981.

131 Sakai, E. H., *Measurement and visualization of the Contact Pressure Distribution of Rubber Disks and Tires*, Tire Science and Technology, TSTCA, Vol.23, No.4, pp.238~255, Oct.-Dec., 1995.

132 Akasaka, T. and Kabe, K., *Deformation and Cord Tension of a Bias Tire in Contact with the Road,* Tire Science and Technology, TSTCA, VOL.5, No.4, pp.171-201, 1977.

133 Trinko, M. J., *Ply and Rubber Stresses and Contact Forces for a loaded Radial Tire,* Tire Science and Technology, TSTCA, VOL.11, No.1-4, pp.20-37, 1984.

134 Tielking, J. T. *A finite Element Tire Model,* Tire Science and Technology, TSTCA, VOL.11, No.1-4, pp.50-63, 1984.

135 Ridha, R. A., Satyamurthy, K., and Hirschfelt, L. R., *Finite Element Modeling of a homogeneous Pneumatic Tire Subjected to Footprint Loadings,* Tire Science and Technology, TSTCA, VOL.13, No.2, pp.91-110, 1985.

136 Rothert, H., Idelberger, H., Jacobi, W., and Laging, G., *On the Contact problem of Tires, Including Friction,* Tire Science and Technology, TSTCA, VOL.13, No.2, pp.111-123, 1985.

137 Prahakaran, R., *Interactive Graphics for the Analysis of Tires,* Tire Science and Technology, TSTCA, VOL.13, No.3, pp.127-146, 1985.

138 Laging, G. and Rothert, H., *Numerical Results of Tire-Test Drum Interaction.* Tire Science and Technology, TSTCA, Vol. 14, No. 3, pp.160-175, July-September 1986.

139 Akasaka, T., Katoh, M., Nihei, S., and Hiraiwa, M., *Two dimensional Contact Pressure Distribution of a Radial Tire,* Tire Science and Technology, TSTCA, VOL.18, No.2, pp.80-103, 1990.

140 Ishihara, K., *Development of a Three Dimensional Membrane Element for the Finite Element Analysis of Tires,* Tire Science and Technology, TSTCA, VOL.19, No.1, pp.23-36, 1991.

141 Browne, A., Ludema, K. C. and Clark, S. K., *Contact between the Tire and Roadway,* Mechanics of Pneumatic Tires, Chapter 5, edited by S. K. Clark, National Bureau of standards, Monogragh 122, Washington, D.C., 1981.

142 Tanner, J. A., Martinson, V. J., and Robinson, M. P., *Static Frictional Contact of the Space Shuttle Nose-Gear Tire,* Tire Science and Technology, TSTCA, Vol. 22, No. 4, pp.242-272, October-December 1994.

143 Sanders, J. I., Jr., *Nonlinear Theories for Thin Shells*, Q. Applied Mathematics., Vol. 21, No. 1, pp.21-36, April 1963.

144 Budiansky, B., *Notes on Nonlinear Shell Theory*, J. of Applied Mechanics, Transactions of ASME, series E, Vol. 35, No. 2, pp. 393-401, June 1968.

145 Simo, J. C., Wriggers, P., and Tailor, R. L., *A Perturbed Lagrangian Formulation for the Finite Element Solution of Contact Problems*, Computational Methods Appl. Mech. 7 Eng., Vol. 50, No. 2, pp. 163-180, Aug. 1985.

146 Adams, I., *m-Step Preconditioned Conjugate Gradient Methods*, SIAM J. Science. & Statistics Computation, Vol. 6, No. 2, pp.452-463, Apr. 1985.

147 Stein, E., Wagner, W., and Wriggers, P., *Finite Element Postbuckling Analysis of Shells With Nonlinear Contact restraints*, Finite Element Methods for Nonlinear Problems, P. G. Bergan, K. J. Bathe, and W. Wunderlich, Eds., Springer-Verlag, pp. 719-744, 1986.

148 Wriggers, P. and Nour-omid, B., *Solution Methods for Contact Problems*, Rep. No. UCB/SESM-84/09 (Contract N00014-76-C-0013), Dep. of Civil Engineering, Univ. of California, July 1984.

149 Concus, P., Golub, G. H., and O'Leary, D. P., *A Generalized Conjugate Gradient Method for the Numerical Solution of Elliptical Partial Differential Equations*, Sparse Matrix Computations. J. R. Bunch and D. J. Rose, eds., Academic Press, Inc., pp. 309-332, 1976.

150 Froberg, C. E., *Introduction to Numerical Analysis*, second ed., Addison-Wesley Publishing Co., 1969.

151 Noor, A. K. and Kim, K. O., *Mixed Finite Element Formulation for Frictionless Contact problems*, Finite elem. Anal. & Design, Vol. 4, No. 4, pp. 315-332, 1989.

152 Captain, K. M., Boghani, A. B., and Wormly, D. M., *Analytical Tire Models for Dynamic Vehicle Simulations*, Vehicle System Dynamics, Vol. 8, pp. 13-29, 1979.

153 Tielking, John T., *Wide Base Radial Truck Tires: Properties and performance*, Heavy Vehicle Systems (HVS), Int. J. of Vehicle Design (IJVD), Vol.2, No.3/4, pp. 187-207, 1995.

154 Muluka, V., *Optimal Suspension Damping and Axle Vibration Absorber for Reduction of Dynamic Tire Loads*, Master thesis, Dept. of Mech. Eng., Concordia University, Montreal, Quebec, Canada, 1998.

155 Scavuzzo, R. W., Richards, T. R., and Clark, L. T., *Tire Vibration Modes and Effects on Vehicle Ride Quality*, Tire Science and Technology, TSTCA, Vol. 12, No. 1, pp.23-39, 1993.

156 Potts, G. R., Bell, C. A., Charek, L. T., and Roy, T.K., *Tire Vibrations*, Tire Science and Technology, TSTCA, Vol.5, No.4, pp.202-225, 1977.

157 Hunckler, C. J., *The Dynamic Behavior of an Automobile Tire*, Ph.D. Dissertation, Purdue University, 1979.

158 Kung, L. E., Soedel, W., and Yang, T. Y., *Free Vibration of a Pneumatic Tire-Wheel Unit Using a Ring on Elastic Foundation and a Finite Element Model*, Journal of Sound and Vibration, Vol. 107, No. 2, pp. 181-194, 1986.

159 Kao, B. G., Kuo, E. Y., Adelberg, M. L., Sundaram, S. V., Richards, T. R., and Charek, L. T., *A New Tire Model for Vehicle NVH Analysis*, SAE Paper No. 870424, 1987.

160 Huang, S. C., *The Vibration of Rolling Tyres in Ground Contact*, International Journal of Vehicle Design, Vol.13, No. 1, pp. 78-95, 1992.

161 Zegelaar, P. W. A., *Model Analysis of Tire-In-Plane Vibration*, SAE Paper No. 971101, 1997.

162 Zhang, Y., Palmer, T., and Farahani, A., *A Finite Element Tire Model and Vibration Analysis: A new Approach*, Tire Science and Technology, TSTCA, Vol. 26, No.3, pp. 149-172, July-September 1998.

163 Sussman, T. and Bathe, K. J., *A Finite Element Formulation for Nonlinear Incompressible Elastic and Inelastic Analysis*, Computers & Structures, Vol. 26, No. 1/2, pp.357-409, 1987.

164 Bathe, K. J., *Finite Element Procedures*, Englewood Cliffs, N. J., Prentice Hall, 1996.

165 Erwin, K, *Advanced Engineering Mathematics*, seventh edition, Wayne Anderson Publication, John Wiley & Sons, INC., 1993.

166 *Element Library*, Elements Manual, chapter 4, Release 5.5, ANSYS, Inc. Southpointe, 1998.

167 Ebbott, T. G., *An Application of Finite Element-Based Fracture Mechanics Analysis to Cord-Rubber Structures*, Tire Science and Technology, TSTCA, Vol. 24, No. 3, pp. 220-235, July-September 1996.

168 Wu, S. R., Gu, L., and Chen, H., *Airbag Tire Modeling by the Explicit Finite Element Method*, Tire Science and Technology, TSTCA, Vol. 25, No. 4, pp. 288-300, October-December, 1997.

169 Takeyama, T. Matsui, J. and Hijiri, M., *Tire Cord and Cord to Rubber Bonding*, Mechanics of Pneumatic Tires, Chapter 2, edited by Clark, S. K., US Department of Transportation, Washington, DC, 1981.

170 Papoulia, K. D., *Mixed and selective reduced integration procedures in large strain hyper-elastic analysis of nearly incompressible solids*, Computational Mechanics 23, pp. 63-74 © Springer-Verlag, 1999.

171 Gough, V. E., *Structure of the Pneumatic Tire*, Mechanics of Pneumatic Tires, Chapter 4, edited by Clark, S. K, US Department of Transportation, Washington, DC, 1981.

172 Oh, B. S., Kim, Y. N., Kim, N. J., Moon, H. Y., and Park, H. Y., *Internal Temperature Distribution in a Rolling Tire*, Tire Science and Technology, TSTCA, Vol. 23, No. 1, pp. 11-25, January-March, 1995.

173 *ANSYS Structural Analysis Guide*, Release 5.5, ANSYS, Inc. Southpointe, 1998.

174 Zhang, X, Ganesan, R and Rakheja, S., *Nonlinear Finite Element Modeling and Incremental Analysis of a Truck Tire*, accepted for publication in Heavy Vehicle Systems (HVS), Special Series, Int. J. of Vehicle Design (IJVD). (Date of acceptance: 8 May 2000).

175 Zhang, X, Rakheja, S. and Ganesan, R., *Estimation of Tire-Road Contact Pressure Distribution Based on Nonlinear Finite Element Analysis*, accepted for publication in Heavy Vehicle Systems (HVS), Special Series, Int. J. of Vehicle Design (IJVD). (Date of acceptance: 24 May 2000)

176 Zhang, X, Ganesan, R and Rakheja, S., *Influence of Structural and Geometric Parameters on the Inter-Ply Shear Stresses in a Radial Truck Tire*, accepted for publication in Heavy Vehicle Systems (HVS), Special Series, Int. J. of Vehicle Design (IJVD). (Date of acceptance: 4 Dec. 2000)

177 Zhang, X., Rakheja, S. and Ganesan, R., *Stress Analysis of the Multi-Layered System of a Truck Tire*, presented at the 20th Annual Conference on Tire Science and Technology, Akron, OH, US, 24-25 Apr. 2001.

178 Zhang, X., Ganesan, R. and Rakheja, S., *Influences of Structural Parameters on the Maximum Inter-Ply Shear Stresses in a Loaded Truck Tire*," accepted for oral presentation at the Third Canadian International Composites Conference, Montreal, Quebec, Canada, 21-24 Aug. 2001. (Date of acceptance: 3 Jan. 2001)